IPP-Report

Max-Planck-Institut für Plasmaphysik

Damm, H.

Upgrade of the Wendelstein 7-X Thomson Scattering Diagnostic to Study Short Transient Plasma Effects – A Demonstration on Pellet Injection for Stellarator Fuelling

IPP 2018-13
Juni 2018

Upgrade of the Wendelstein 7-X Thomson Scattering Diagnostic to Study Short Transient Plasma Effects

- A Demonstration on Pellet Injection for Stellarator Fuelling -

M A S T E R - T H E S I S

Submitted for the Degree
Master of Science in Physics

University of Greifswald
Faculty of Mathematics and Natural Sciences - Department of Physics

Max-Planck-Institute for Plasma Physics

Submitted 2nd May 2018 by Hannes Damm
Born on 16th December 1991 in Erfurt, Germany

1st Supervisor

PD. Dr. habil. Andreas Dinklage
Max-Planck-Institute for Plasma Physics
Wendelsteinstr. 1
17489 Greifswald

2nd Supervisor

Prof. Dr. Andre Melzer
Faculty of Mathematics and Natural Sciences
Department of Physics
Felix-Hausdorff-Str. 6
17489 Greifswald

Advisor

Dr. Ekkehard Pasch
Max-Planck-Institute for Plasma Physics
Wendelsteinstr. 1
17489 Greifswald

Acknowledgements

Far to rarely I took the time to thank the people who did support me finally finishing my university studies with this thesis. A list of these people and their various contributions might be even longer than the thesis, itself. Therefore, I tried to focus on the ones who have been directly involved in this work and hope the skipped ones can forgive me.
First and foremost, I would like to express my sincere gratitude to my advisor Dr. Ekkehard Pasch. More than anything else, I value his incessant endeavour to support my work and my scientific career without ever putting his own interests first. I would like to thank him for sweeping any difficulty that he could out of my way, and for accepting to advice me, carrying out this thesis. Equally, I would like to thank my academic supervisor PD. Dr. habil. Andreas Dinklage who made this thesis possible in the first place. His eye for the details and his sense for the whole picture as well as our fruitful discussions helped to refine this thesis a lot. Furthermore, I appreciated the effort of my university supervisor Prof. Dr. Andre Melzer to visit me at the Max-Planck-Institute for Plasma Physics and inspect my research-work "in situ". I would like to extend my gratitude to him and the Physics Department audit committee, which he presides, as well as to Prof. Dr. Robert Wolf, as representative for the Stellarator Heating and Optimization Division, for the great opportunity to carry out my master thesis in cooperation between the University of Greifswald and the Max-Planck-Institute.
My particular thank deserves Dr. Jürgen Baldzuhn who, regardless his always tight schedule, repeatedly did find some time to share his immense knowledge on pellet physics with me. Furthermore, I cannot be thankful enough for the countless hours Dr. Evan Scott spend on trying to correct my picture of English grammar, i.e. punctuation, and I am not sure whether or not he finally succeeded. Speaking of colleagues, I have to mention Dr. Felix Warmer who I share an office with. He stayed with me through the ups and downs that such a master thesis comes with. In our office, we discussed all possible and impossible problems of modern plasma physics, not uncommonly on weekends or public holidays, and during that time he became a good friend of mine. In this context, I additionally want to mention Dr. Golo Fuchert and Dr. Sergey Bozhenkov for the interesting discussions on Thomson scattering and the small tricks and tips for the subsequent data analysis. They helped me accomplishing my thesis at least as much as the individually, by hand adjusted interferometry data provided by Dr. Kai-Jakob Brunner.

Beside all the other colleagues within the institute, at JET, and LHD, who never got tired answering my questions, emails, and phone calls, I would like to honer the important work done by the technicians, engineers, and programmers, which, in my opinion, is not always appropriately acknowledged. Namely, I want to point out Jens Meineke who (not only) helped me a lot with the CAD pictures found in this thesis, Torsten Bluhm who was very helpful setting-up the software back-end of the energy monitors as well as Beate Kursinski, Benjamin Hor, and Karsten Lehmann who keep the Thomson scattering diagnostic going.
Most importantly, I want to express my honest love to my wife Camille Marie Damm. I am thankful for her constant support and infinite patience, whenever I came home late again. I am deeply grateful to my fellow student, "groomsmaid", and simply best friend Carola Wirth for always being at my side (and for pushing me trough the whole bachelor's and half the master's degree). And finally, I would like to thank my parents who raised me to the curious human being that I am today and never stopped supporting me in everything I do.

For their financial support during my whole studies in the form of a scholarship, I am grateful to the "Hans-Böckler"-Foundation. Furthermore, I would like to thank the "EUROfusion consortium" for the received support, i.e. for the "FuseNet Master student internship support" received during my studies at JET and the University of Oxford.

Declaration

I hereby certify that this thesis is entirely my own work unless otherwise stated. No sources or aids other than those mentioned have been used. Parts that are in letter or spirit taken from other sources, including secondary literature, are labelled accordingly, mentioning the original source.
The author gives his permission to publish this thesis or parts of it quoting the source consequently. In case of doubt, please contact the author via e-mail.

hannes.damm@ipp.mpg.de.

Place, Date

Hannes Damm

Abstract

Thomson Scattering is a method to provide spatially resolved electron temperature and density profiles in magnetic confinement fusion experiments like Wendelstein 7-X (W7-X). Requiring high laser power, Thomson scattering of plasma electrons is usually conducted with pulsed laser systems. This stroboscopic measurement results in a time comb of data points. Short, unpredictable plasma events, e.g. due to instabilities, cannot be studied systematically on timescales faster than the inverse repetition frequency of the laser system. The main intention of this work was to develop and implement a new operational mode for the Thomson scattering diagnostic allowing for the measurement of such events. This required both a fast sequence of multi laser pulses and the synchronization of the laser pulses with the event of interest.

To fulfil the first requirement, the so-called "burst mode" of Nd:YAG lasers was utilized. It provides a finite number of consecutive laser pulses with low temporal spacing. The realisation at W7-X provides four consecutive pulses with the timings $t_1 = 0\,\mu s$, $t_2 = 100\,\mu s$, $t_3 = 600\,\mu s$, and $t_4 = 700\,\mu s$ on a 5 Hz basis.

To meet the second requirement, a fast trigger scheme was developed. It allows for firing the Thomson scattering lasers with a certain variability from their regular time comb to match the events. The trigger scheme includes a logic circuit which was developed to keep the variation from the time comb within certain margins. The margins were chosen such that the average thermal loads in the laser are sustained to avoid causing damage to the lasers.

The diagnostic upgrade introduced in the course of this thesis combines the two aforementioned techniques, the fast event trigger and the burst mode. They build a system which made it possible to study unpredictably occurring, short transient plasma effects.

As a part of this work, the burst mode was optimized to match the diagnostic's requirements. A particular focus was set on the qualification of safe operation of the laser and all optical components. Furthermore, calibration methods for the new system were compared.

The qualified operational mode was employed to study transient plasma temperature and density profile evolution in the ablation and deposition process of cryogenic hydrogen pellets injected into the plasma. A total number of 25 individual pellet events has been analysed.

Different pellet injection geometries were investigated to contribute to the assessment of drift effects in pellet fuelling. The drift velocities obtained ($\approx 1000\,m/s$)

match the predictions from the HPI2 code [1] (1000 - 4000 m/s) which was developed to model the behaviour of single pellets injected into a plasma.
In addition, density profile changes occurring on slow (100 ms) and fast (100 µs) timescales could be distinguished. Deeper penetration of the pellets than predicted by the code was experimentally verified on time scales of < 1 ms; a penetration depth of 60 % of the plasma radius was measured as compared to the 25 % depth predicted by HPI2. Deeper penetration of later pellets in a pellet series, arising from the cooling of the plasma edge by previous pellets, has also been observed. Moreover, core fuelling effects on a transport timescale (> 2.3 ms) were identified. The code predicts different fuelling efficiencies for different injection geometries. In contrast, the experimental results have shown that the fuelling efficiency is independent of the pellet injection geometry. As opposed to hydrogen gas fuelling, pellet injection was found to allow for centrally-dominated plasma fuelling.

Contents

Introduction

Since the beginning of mankind, the guest for convenience and prosperity has led to the development of tools and facilities. First and foremost, natural resources like wind and water (beside animals) were used to power tools like wind- and watermills and ships when muscle-driven tools no longer produced sufficient output. Ever since the industrial revolution of the late 18th century, these resources could not meet the rapidly increasing demand for energy; therefore, burning fossil fuels became more and more predominant. Although these energy resources gave access to accelerated technological advancement and raised the standard of living, their usage was accompanied by a crucial drawback: the hitherto stored carbon was oxidized during combustion, producing dramatist amounts of carbon dioxide (CO_2), that were subsequently released into the atmosphere.

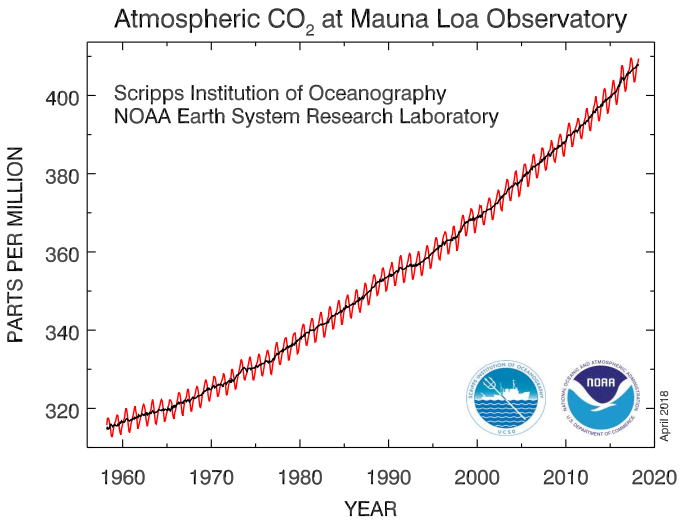

Fig. 0.0.1.: Monthly mean atmospheric CO_2 at Mauna Loa Observatory, Hawaii. The CO_2 data (red curve) are reported as a dry mole fraction defined as the number of molecules of carbon dioxide divided by the number of molecules of dry air (in ppm) [2].

The CO_2 content of earth's atmosphere stayed well below 300 ppm for 20 000 years before 1800 ([3] p. 448). In the last decades, the CO_2 level suddenly rose, exceeding 400 ppm as shown in fig. 0.0.1. According to the greenhouse theory of climate change [4], this alarming increase of CO_2 (besides other anthropogenic gases emitted like nitrous oxide (N_2O) or methane (CH_4)) leads to an increase of the atmosphere's temperature known as "global warming" or "climate change".

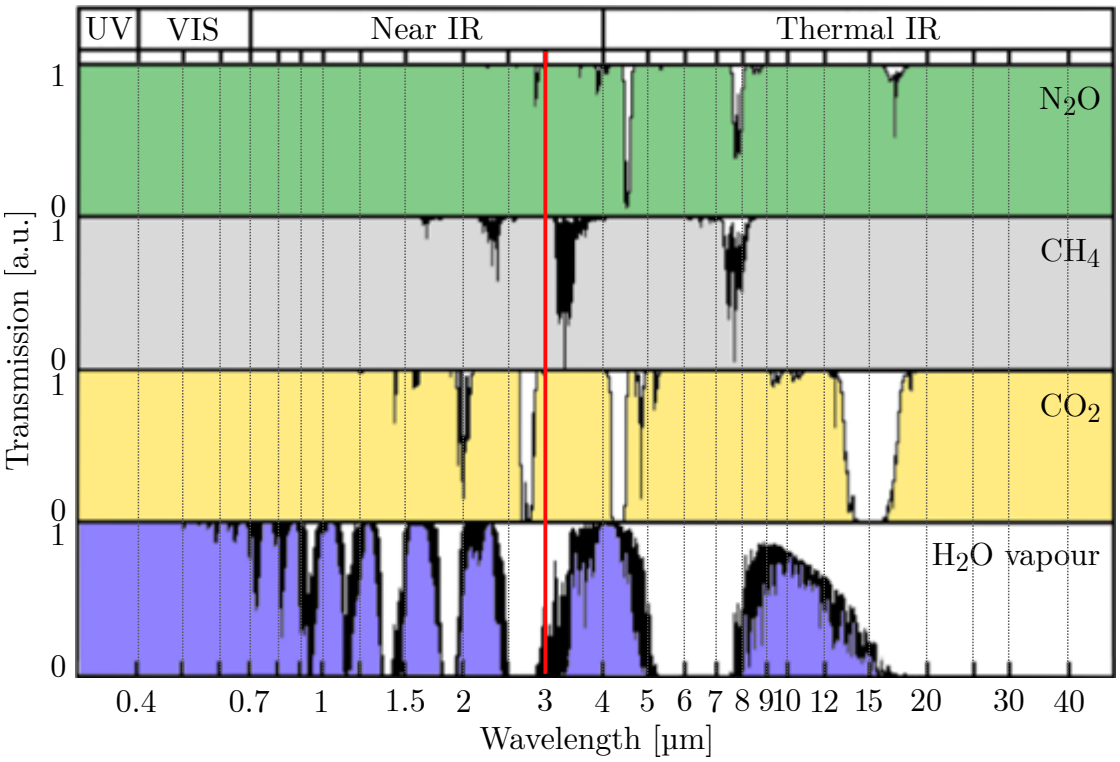

Fig. 0.0.2.: Transmission of electromagnetic waves through different gases for wavelengths in the range of UV (ultra violet) - VIS (visible) - IR (infrared) indicated by the coloured areas below the black curves. Spectral data taken from [5].

The incoming solar radiation's wavelength mainly lies below 3 µm (indicated by the red line in fig. 0.0.2) whereas the back-body radiation of the earth's surface occurs above the red line in the IR range. Therefore, the incoming solar radiation is transmitted through the atmosphere with almost no disturbance, heating up the earth's surface. The resulting thermal radiation cannot easily escape the atmosphere due to its longer wavelength ($\gtrsim 3\,\mu m$). This is because most of the wavelength interval above 3 µm is not transparent due to the H_2O vapour absorption. The increase of the aforementioned gases, especially CO_2, partially blocks the remaining

intervals as can be seen from fig. 0.0.2. The increased radiation insulation is the main driver of anthropogenic climate change.
The Intergovernmental Panel on Climate Change (IPCC) is a United Nations scientific body providing an objective, scientific view on climate change and its political and economic impacts. In its last synthesis report [6] the IPCC states:

> *"Continued emission of greenhouse gases will cause further warming and long-lasting changes in all components of the climate system, increasing the likelihood of severe, pervasive and irreversible impacts for people and ecosystems. Limiting climate change would require substantial and sustained reductions in greenhouse gas emissions which, together with adaptation, can limit climate change risks."*

The IPCC does not only analyse the current situation and mention climate change's impacts and their likelihood; it also provides possible mitigation scenarios. The most effective interventions according to the report [6] could be made in the transportation, industry and electricity generation sectors. In Germany the fraction of fossil energy sources for those sectors were 95 %, 83 %, and 59 %, respectively, in 2016 [7], while they were causing 13.8 %, 16.8 %, and 25.7 % of the global CO_2 emission in 2010 [6]. This equates to more than half of the total greenhouse gas emission in 2010 and is likely to increase further. To reduce the anthropogenic greenhouse gas emission and fight global warming and its catastrophic impacts, it is necessary to find alternatives to fossil energy sources. The current alternatives suffer from high spatial requirements (wind, solar, water), low social acceptance (wind, nuclear fission), or possible persistent radioactive contamination and long-term storage issues (nuclear fission).
A non-renewable (but on human timescales infinite available) energy source is provided by nuclear fusion. Today the only place in our solar system where fusion is happening on a relevant scale is the core of the sun. The largest contributions to sun's mass of $(1.988\,55 \pm 0.000\,25) \times 10^{30}$ kg [8] are from hydrogen (73.5 %) and helium (24.9 %) [9]. The high temperature in the sun's core region leads to a full ionization of the atoms, forming a "plasma", and the high mass pressure leads to frequently occurring collisions between the plasma particles of which a certain fraction results in a fusion reaction. *"A plasma is a quasineutral gas of charged and neutral particles which exhibits collective behaviour."* (e.g. [10] p. 3). In the sun's case, the proton-proton chain reaction is the most dominant fusion reaction with respect to the total energy output. In the first step, two protons collide. Under the aforementioned conditions some of the protons have high enough kinetic energy to tunnel trough the electrostatic Coulomb barrier and get close enough for the strong force, an attractive force that is stronger than Coulombs force across very short distances (<2.5 fm), to come into play. Through these collisions the two nuclei fuse

together and form a single nucleus; this process is called fusion. The fusion of the hydrogen cores generates a deuterium nucleus (= one proton + one neutron), a positron, and a neutrino. Next, the deuterium core and another proton fuse to $^3He^{2+}$ (helium-3 core = two protons + one neutron), emitting a gamma photon; finally, two ^{3}He cores fuse to two protons and form one $^4He^{2+}$ (helium-4 core = two protons + two neutrons). The helium-4 core is sightly lighter than the four protons together. This mass defect can be explained by the increasing binding energy per nucleon shown in fig. 0.0.3, and, according to Einstein's formula $E = mc^2$, releases a certain amount of energy.

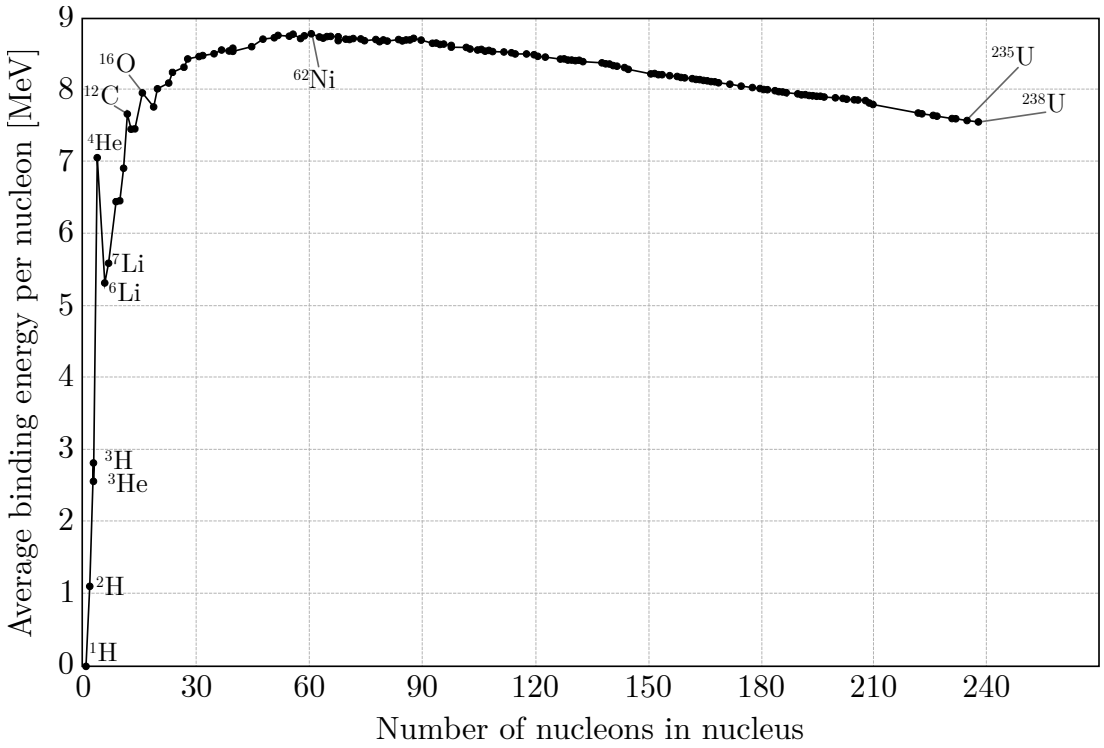

Fig. 0.0.3.: Binding energy per nucleus. Nuclear data taken from [11].

As can be seen, the fusion of hydrogen (^{1}H) to helium-4 (^{4}He) releases several MeV of energy that is partially converted into kinetic energy of the involved particles and partially into the energy of the gamma photon. The significant difference in binding energy per nucleon is what makes fusion the most effective energy source within reach. Even for nuclear fission employed in fission power plants, where ^{235}U (uranium) is split into ^{139}Ba (barium), ^{95}Kr (krypton), and a neutron, the released energy per nucleon is much smaller as explained by the smaller binding energy increment per nucleon for those nuclei (cf. fig. 0.0.3). For chemical reactions, like

burning fossil fuels, the released energy per molecule is orders of magnitude smaller. For instance, the reaction of a carbon atom and an oxygen molecule forming a carbon dioxide molecule releases $\approx 5\,\mathrm{eV}$ [12].
Unfortunately it is not possible to gravitationally confine a plasma on earth and no known material could withstand the sun's core temperature. Therefore, it is necessary to make use of scientific knowledge and find solutions to these difficulties. A very promising approach is to magnetically confine a fusion plasma in a toroidal configuration. The charged plasma particles are bound to magnetic field lines by the Lorentz force as is explained in section 1.1.1. To avoid losses, the magnetic field lines bend, forming self-closing tori. The magnetic field gradient of such configurations leads to charge separation resulting in an electric field. This again introduces a radial particle drift towards the outer edge of the torus as will be explained in section 1.1.5. A poloidal magnetic field component applying a twist to the field lines can compensate these drifts. Different concepts were developed to generate the poloidal magnetic field realised by the two leading experimental setups the "tokamak" [13] and the "stellarator" [14]. While tokamaks use an induce toroidal plasma current which in turn creates a poloidal magnetic field, stellarators twist the magnetic field around itself along the torus using complex three-dimensional coil-setups.
However, the proton-proton chain reaction is not the most suitable fusion reaction for reproduction on earth due to its low fusion cross-section. The probability for a fusion reaction to occur is in proportion to its fusion cross-section. The fusion of deuterium (^{2}H or D) and tritium (^{3}H or T) is currently the best candidate for future fusion power plants.

$$\mathrm{D} + \mathrm{T} \rightarrow {}^4\mathrm{He} + \mathrm{neutron} + \mathrm{energy}.$$

The D-T fusion cross-section peaks at $10^2\,\mathrm{keV}$, exceeding all other possible fusion reactions' cross-sections in this temperature interval [15]. Additionally, the potential binding energy step is still large (cf. fig. 0.0.3). Both deuterium and tritium are easily accessible. The first is a stable isotope of hydrogen with a natural occurrence of $0.015\,\%$ [16] which, given the large amounts of hydrogen as part of water molecules in Earth's oceans, will suffice for millions of years of fusion energy. Although tritium is an unstable hydrogen isotope with a half-life of approx 12 years [15], and hence not naturally occurring, it can be produced from lithium (Li), which is very abundant on Earth, and could be used for fusion energy production for thousands of years [17]. Depending on the neutron kinetic energy, two reaction regimes are possible:

$$^{6}\mathrm{Li} + \mathrm{neutron} \rightarrow {}^{4}\mathrm{He} + \mathrm{T} + \mathrm{energy},$$
$$^{7}\mathrm{Li} + \mathrm{neutron} \rightarrow {}^{4}\mathrm{He} + \mathrm{T} + \mathrm{n} - \mathrm{energy}.$$

Due to the finite size of fusion plasmas on Earth, a pedestal region must exist connecting the hot plasma with the cooler surroundings; this means a temperature gradient must exist as well. One of the major challenges of today's fusion research is to shape this gradient region such that the vessel walls are not harmed from the close by plasma; and the core plasma is not disturbed by the plasma-wall interactions at the edge regions. The high temperatures sufficient for fusion reactions to occur are only reached in the core regions of the plasma. Therefore the fuel, deuterium and tritium, which is diluted by the fusion reaction, needs to be replenished.
Unfortunately, the magnetic confinement not only prevents the inner particles from escaping the plasma, but also it hinders outer charged particles from penetrating the plasma. This makes the refuelling of the plasma core very difficult. A promising technique is the injection of cryogenic fuelling pellets as described in sections 1.4 and 2.2 [18]. Pellet injection fuelling has already been performed in previous experiments conducted on large plasma machines like ASDEX Upgrade and JET [19, 20]. However, the work done so far has been mainly dedicated to Tokamak experiments. To establish effective and reliable pellet fuelling schemes for stellarator plasmas, it is necessary to fully understand the physics behind the injection process and the subsequent particle deposition within the plasma. Significant differences are expected due to the different magnetic field setup.
One of the main goals of Wendelstein 7-X (W7-X) [21], a large state-of-the-art stellarator plasma experiment established in Greifswald, Germany in 2015, is to achieve high performance steady-state plasmas and hence to reach and sustain high plasma core densities. It has been equipped with several diagnostics, one being the Thomson scattering system (cf. section 2.3). Its ability to radially measure temperature and density makes it a particularly favourable system to study the pellet injection process. Nevertheless, a limitation is the low repetition frequency of the standard Thomson scattering system of 10 Hz, which is much too low for the very short timescales during which the pellet processes take place (≤ 1 ms).

The aim of this thesis is to develop an upgrade of the Wendelstein 7-X Thomson scattering diagnostic which allows for the study of short transient plasma effects. The chosen approach is based on the so-called "burst-mode" operation of a pulsed laser synchronized to pellet injection experiments for stellarator fuelling. Both techniques, event-synchronized Thomson scattering and burst-mode Thomson

scattering, were previously demonstrated at other magnetic confinement fusion experiments individually [22, 23], whereas in the course of this thesis both were combined in one system.
The theoretical background of pellet injection and the general plasma physics necessary in this context are given in the 1st chapter as well as a short introduction to laser physics relevant to the burst mode operation of the Thomson scattering laser system. The general feasibility of non-uniform laser triggering for event-synchronization are derived employing the general heat equation to assess the thermal-temporal limits given by the laser setup.
The current setup of both the W7-X pellet injector and the Thomson scattering diagnostic are introduced in chapter 2 after the W7-X plasma experiment and its main machine parameters were described.
The event trigger system developed as part of this work allows for the Thomson diagnostic to run in burst mode with the temporally-short fast-repetitive bursts to be triggered by occurring plasma events. This system is presented in chapter 3 with a focus on the implementation of the pellet trigger signal and a subsequent study of the Thomson scattering laser's performance in burst-mode operation. In the second half of the 3rd chapter, the absolute density calibration of the new operation mode and the verification of its ability to measure the effects for which it has been designed is shown.
Finally, in chapter 4 selected data from event-triggered burst mode measurements are presented. The excellent dataset obtained using the burst mode system allowed for the comparison of the experimental results and the theoretical predictions. An analysis of the effects of serial pellet injection and different injection geometries as well as a comparison of pellet fuelling and gas fuelling is performed. In this context, observations of the particle transport timescale currently dominating W7-X plasmas are presented.
The essential diagnostic development achievements and physics findings obtained within this work are summarised and evaluated in the conclusions in chapter 5 accompanied by a brief outlook to the further applications and improvements of the "event-triggered burst-mode Thomson scattering system".

1. Theoretical Background

The deliberations and experiments presented in this thesis pertain various fields within physics. To put everything in the correct context, an overview of the main theoretical concepts will be given in this chapter. At first, the concepts of magnetic confinement plasma physics relevant to this thesis will be discussed. The derivations mainly follow the High Temperature Plasma Physics lecture by Prof. Dr. Thomas Sunn Pedersen held in 2017 at the University of Greifswald, published in [24]. Thereafter follow the physics principles of pulsed high power laser systems, and the proposed diagnostic's upgrade is illuminated from the theoretical side. An assessment of the expected operational limits is performed employing the general heat equation. A separate section is devoted to the well-established understanding of the Thomson scattering process and its diagnostic application including the main post-processing steps necessary to obtain the electron temperature and density. Finally, the basic mechanisms of pellet injection in hot magnetically confined plasmas are outlined together with simulated predictions to be compared to the later measurements.

1.1. Introduction to Plasma Physics

1.1.1. Charged Particle Motion in Electromagnetic Fields

The forces on a particle of charge q and mass m moving in an electromagnetic field can be combined to form an equation of motion commonly known as Lorentz force equation [10].

$$m\frac{\mathrm{d}\boldsymbol{v}}{\mathrm{d}t} = q\left(\boldsymbol{E} + \boldsymbol{v} \times \boldsymbol{B}\right), \tag{1.1.1}$$

with
$\boldsymbol{v}$ ... particle velocity,
$\boldsymbol{E}$ ... electric field vector and
$\boldsymbol{B}$ ... magnetic flux density.

$\boldsymbol{F} = q\boldsymbol{E}$ describes the force resulting from the electric field whereas $\boldsymbol{F} = q\boldsymbol{v} \times \boldsymbol{B}$ results from the magnetic field. In the absence of an electric field ($\boldsymbol{E} = 0$) and if the background magnetic field can be assumed to be constant ($\boldsymbol{B} = B_0\boldsymbol{e_z}$), the equation of motion reduces to an ordinary differential equation. Without loss of generality the direction of the magnetic field was choosen to be parallel to $\boldsymbol{e_z}$. After application of the cross product, equation 1.1.1 then yields:

$$\begin{aligned}
\frac{\mathrm{d}v_\mathrm{x}}{\mathrm{d}t} &= \frac{|q|\,B_0}{m}v_\mathrm{y}, \\
\frac{\mathrm{d}v_\mathrm{y}}{\mathrm{d}t} &= \frac{-\,|q|\,B_0}{m}v_\mathrm{x}, \\
\frac{\mathrm{d}v_\mathrm{z}}{\mathrm{d}t} &= 0.
\end{aligned} \tag{1.1.2}$$

The solution is known to be a harmonic wave and can be written as:

$$\begin{aligned}
x &= \frac{v_\perp}{\omega_\mathrm{c}}\sin(\omega_\mathrm{c}t + \delta) + x_\mathrm{gc}, \\
y &= \frac{v_\perp}{\omega_\mathrm{c}}\cos(\omega_\mathrm{c}t + \delta) + y_\mathrm{gc}, \\
z &= v_\parallel t + z_\mathrm{gc}.
\end{aligned} \tag{1.1.3}$$

Where δ is an arbitrary phase shift and $v_\perp$ and $v_\parallel$ are the resulting particle velocity

components with respect to the magnetic field direction. Thus two motions can be distinguished: a parallel motion along the field line ($\boldsymbol{e_z}$-direction) and a circular motion perpendicular to $\boldsymbol{e_z}$. The particle hence appears to be "pinned" to a field line, orbiting it in a so-called "gyro motion". The axis of this motion, defined by the initial coordinates x_{gc}, y_{gc}, and z_{gc} as well as the direction $\boldsymbol{e_z}$, is called the "guiding centre" accordingly. The frequency of the gyration:

$$\omega_{\mathrm{c}} = \frac{|q|\, B_0}{m}, \tag{1.1.4}$$

is called the "cyclotron frequency" or "gyrofrequency" and its radius:

$$r_{\mathrm{L}} = \frac{v_\perp}{\omega_{\mathrm{c}}} = \frac{m v_\perp}{|q|\, B_0}, \tag{1.1.5}$$

is know as the "Larmor radius" or "gyroradius".

1.1.2. Magnetic Flux and Rotational Transform

As has been mentioned in the introduction, the magnetic field in tokamaks and stellarators is neither straight nor constant. This is why the particles experience several drift forces discussed in a subsequent section. In fact the field lines are both circularly bent and twisted. Therefore, it is convenient to introduce a torus coordinate system, which reflects this geometry. The magnetic field $\boldsymbol{B}$ can be separated into two components in this coordinate system as shown in fig. 1.1.1. Poloidal quantities point in direction of the poloidal angle Φ_{pol} and toroidal quantities point in direction of the toroidal angle Φ_{tor}. The poloidal and toroidal component of the magnetic field are denoted as $\boldsymbol{B}_{\mathrm{pol}}$ and $\boldsymbol{B}_{\mathrm{tor}}$, respectively. The magnetic flux Ψ passing trough a surface S is defined as the surface integral of the normal component of the magnetic field $\boldsymbol{B}$ passing through that surface:

$$\Psi = \iint_{\mathrm{S}} \boldsymbol{B} \cdot \mathrm{d}\, \boldsymbol{S}. \tag{1.1.6}$$

Accordingly, Ψ_{pol} denotes the flux, which is introduced by the poloidal component of the magnetic field, $\boldsymbol{B}_{\mathrm{pol}}$, passing trough a toroidal cross section of the torus and Ψ_{tor} is introduced by the toroidal component of the magnetic field, $\boldsymbol{B}_{\mathrm{tor}}$, passing trough a poloidal cross section of the torus. The measure for the amount of twist of the magnetic field lines around the torus is called the "rotational transform" and is defined as:

$$t = \frac{1}{2\pi}\frac{\mathrm{d}\Psi_{\mathrm{pol}}}{\mathrm{d}\Psi_{\mathrm{tor}}}, \tag{1.1.7}$$

which can be paraphrased as the number of poloidal transits per single toroidal transit of a field line on a toroidal flux surface.

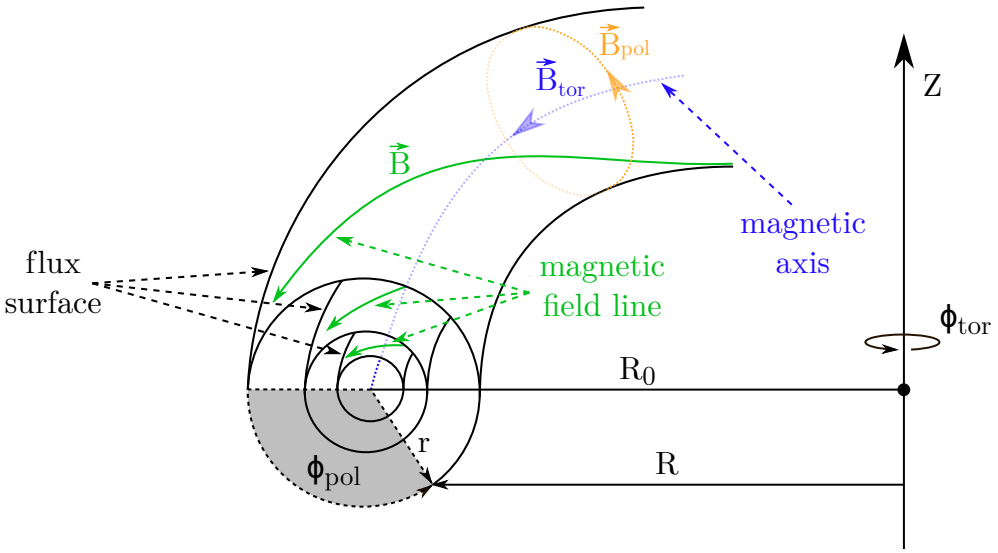

Fig. 1.1.1.: Introduction of poloidal and toroidal direction on the example of a selection of nested flux surfaces in a toroidal magnetic field configuration. Z, R, r, Φ_{pol}, and Φ_{tor} are coordinates of the toroidal coordinate system. R_0 is the major radius of the tori and r the minor radius of each individual torus. Toroidal and poloidal quantities are denoted by "tor" and "pol", respectively.

In in W7-X ι is close to 1 but usually chosen such that rationales (m/n with $m, n \in \mathbb{N}$) are avoided which means that the field lines are not self-closing for a finite number of toroidal turns. One field line rather spans a toroidally shaped so called "magnetic flux surface". These flux surfaces contain a constant amount of total magnetic flux $\Psi = \Psi_{\mathrm{pol}} + \Psi_{\mathrm{tor}}$. In the case of W7-X, due to its complex 3D magnetic field, the shape of the toroidal flux surface cross section changes from bean-like to triangular five times in one toroidal revolution. The innermost surface, containing zero flux, is called the "magnetic axis", and the outermost surface the "last closed flux surface" (LCFS), which is the boundary of the confined plasma region. The flux surfaces can be labelled from 0 (magnetic axis) to 1 (LCFS). With the assumption that transport phenomena perpendicular to these flux surfaces are much slower than parallel ones, physics parameters such as density, temperature,

etc., are constant on flux surfaces. The underlying assumption can be explained by the gyration of charged plasma particles along the field lines. By implication, the gyro motion allows free streaming of the particles along the field lines implying long mean free paths and thus fast transport. Perpendicular to the field lines, or flux surfaces, no free propagation is possible for charged particles. Therefore, the particles can only spread through collisions. In the purely classical approach, the mean free path for these random walk like collisions is of the order of the gyroradius and according to the neoclassical theory about an order of magnitude higher ([10] pp. 188). Nevertheless, the particle velocity parallel to the field lines exceeds the velocity perpendicular to them, depending on the exact plasma conditions, by a factor of 10^8 - 10^{10} [25].

1.1.3. Temperature, Density, and Pressure

The density of a plasma is usually described by a number density $n_\alpha = N_\alpha/V$, where N_α is the particle number and V the reference volume; α indicates the particle species. The index $\alpha = \mathrm{e}$ denotes the electrons and $\alpha = \mathrm{i}$ the ions. If multiple ion species occur within the plasma, a further distinction can be made. The plasma temperature of each species, is normally quoted in electron volts (eV) as $k_\mathrm{B}T_\alpha$ including k_B, the Boltzmann constant ($(8.617\,330\,3 \pm 0.000\,005\,0) \times 10^{-5}\,\mathrm{eV/K}$) [15], and e the elementary charge ($(1.602\,176\,620\,8 \pm 0.000\,000\,009\,8) \times 10^{-19}\,\mathrm{C}$) [15]. The notation is convenient in a hot fusion plasma where the particles usually are Maxwell-Boltzmann-distributed [26], which, for instance, allows the application of the ideal gas pressure in the form [10]:

$$p_\mathrm{plasma} = \sum_\alpha n_\alpha k_\mathrm{B} T_\alpha. \tag{1.1.8}$$

If a plasma of pressure p_plasma is confined within a finite volume by a magnetic field, as in a fusion device, a pressure gradient corresponding to a force $\boldsymbol{F} = \nabla p_\mathrm{plasma}$ must exist. In the plasma fluid model this can be expressed by the low frequency magnetohydrodynamics equilibrium equation [27]:

$$\nabla p_\mathrm{plasma} = \boldsymbol{j} \times \boldsymbol{B}, \tag{1.1.9}$$

where $\boldsymbol{j} = (\nabla \times \boldsymbol{B})/\mu_0$ is the plasma current with $\mu_0 = 4\pi \times 10^{-7}\,\mathrm{H/m}$ [15] being the magnetic constant or vacuum permeability. From this equation it can be seen that ∇p_plasma must be perpendicular to $\boldsymbol{B}$, meaning $\boldsymbol{B} \cdot \nabla p_\mathrm{plasma} = 0$. The only 3D topology satisfying this criterium is a torus, which is the reason why it was chosen

to be the geometry of most magnetic confinement fusion experiments.
A commonly employed measure for the quality of the plasma confinement by a particular magnetic field in fusion science is the ratio of the mean plasma pressure to the magnetic field pressure [10]:

$$\beta = \frac{\langle p_{\mathrm{plasma}} \rangle}{p_{\mathrm{mag}}}, \tag{1.1.10}$$

where $p_{\mathrm{mag}} = B^2/2\mu_0$.

1.1.4. Debye Shielding

In plasma physics, the Debye length λ_{D} [28] is a measure for the range of the electrostatic effects of the internal plasma (or any external) charge carriers. The corresponding Debye sphere is a volume whose radius is the Debye length. Within one Debye length, the electric potential $\Phi(\boldsymbol{r})$ of a particular charge carrier in the plasma will decrease in magnitude by $1/e$ (with e being the irrational Euler's number) corresponding to a perfect electrical screening on length scales $\ll \lambda_{\mathrm{D}}$. A plasma's Debye length can be obtained by combining Poisson's equation [29] with the Maxwell-Boltzmann-distribution to the Poisson-Boltzmann equation for a electrically neutral system:

$$\varepsilon_0 \nabla^2 \Phi(\boldsymbol{r}) = -\sum_{\alpha=1}^{N} q_\alpha n_\alpha \exp\left(-\frac{q_\alpha \, \Phi(\boldsymbol{r})}{k_{\mathrm{B}} T}\right), \tag{1.1.11}$$

where $\varepsilon_0 = 1/\mu_0 \mathrm{c}^2$ [15] is the electric constant or vacuum permittivity with c $= 299\,792\,458\,\mathrm{m/s}$ [15] being the vacuum speed of light. In the high-temperature limit, $q_\alpha \, \Phi(\boldsymbol{r}) \gg k_{\mathrm{B}} T$, which usually applies to fusion plasmas, the exponential in equation 1.1.11 can be Taylor expanded:

$$\exp\left(-\frac{q_\alpha \, \Phi(\boldsymbol{r})}{k_{\mathrm{B}} T}\right) \approx 1 - \frac{q_\alpha \, \Phi(\boldsymbol{r})}{k_{\mathrm{B}} T}. \tag{1.1.12}$$

Now the Debye length can be identified as the characteristic length scale in the linearised Poisson-Boltzmann equation:

$$\nabla^2 \Phi(\boldsymbol{r}) = \frac{1}{\varepsilon_0} \left(\sum_{\alpha=1}^{N} \frac{q_\alpha^2 n_\alpha}{k_{\mathrm{B}} T}\right) \Phi(\boldsymbol{r}), \tag{1.1.13}$$

$$\lambda_{\mathrm{D}} = \sqrt{\frac{\varepsilon_0 k_{\mathrm{B}} T}{\sum_{\alpha=1}^{N} q_\alpha^2 n_\alpha}}\,. \tag{1.1.14}$$

1.1.5. Particle Drift Motions

Drifts arising from general external forces $\boldsymbol{F}$ can be discussed in a general manner by replacing the electric field $\boldsymbol{E}$ in equation 1.1.1 by $\boldsymbol{F}$:

$$m\frac{\mathrm{d}\boldsymbol{v}}{\mathrm{d}t} = q\left(\boldsymbol{F} + \boldsymbol{v} \times \boldsymbol{B}\right). \tag{1.1.15}$$

The velocity can be split into parallel and perpendicular components with respect to the guiding centre. Whereas the drifts along the field lines do not cause particle drifts and hence do not need to be compensated, the perpendicular drifts are of major interest.

$$m\frac{\mathrm{d}\boldsymbol{v_{\mathbf{d}}}}{\mathrm{d}t} = q\left(\boldsymbol{F}_\perp + \boldsymbol{v_{\mathbf{d}}} \times \boldsymbol{B}\right). \tag{1.1.16}$$

Without loss of generality $\boldsymbol{B} = B_0\boldsymbol{e_{\mathbf{z}}}$ and $\boldsymbol{F}_\perp = F_{\mathrm{x}}\boldsymbol{e_{\mathbf{x}}} + F_{\mathrm{y}}\boldsymbol{e_{\mathbf{y}}}$ can be chosen. Applying the cross product, the components of equation 1.1.16 become:

$$\begin{aligned}
\frac{\mathrm{d}v_{\mathrm{x}}}{\mathrm{d}t} &= \frac{B_0}{qm}\left(v_{\mathrm{y}} + \frac{F_{\mathrm{x}}}{qB_0}\right),\\
\frac{\mathrm{d}v_{\mathrm{y}}}{\mathrm{d}t} &= \frac{B_0}{qm}\left(v_{\mathrm{x}} - \frac{F_{\mathrm{y}}}{qB_0}\right),\\
\frac{\mathrm{d}v_{\mathrm{z}}}{\mathrm{d}t} &= 0.
\end{aligned} \tag{1.1.17}$$

The fractions F_{x}/qB_0 and F_{y}/qB_0 relate to the x- and y-components of the drift velocity respectively. With F_{x}, F_{y}, q, and B_0 being constant, the drift velocity $\boldsymbol{v}_{\mathrm{d}}$ must also be constant, and $\mathrm{d}\boldsymbol{v_{\mathbf{d}}}/\mathrm{d}t = 0$. Applying another cross product with $\boldsymbol{B}$ from the right and using the vector identity $(\boldsymbol{a} \times \boldsymbol{b}) \times \boldsymbol{c} = \boldsymbol{b} \cdot (\boldsymbol{a} \cdot \boldsymbol{c}) - \boldsymbol{a} \cdot (\boldsymbol{b} \cdot \boldsymbol{c})$ equation 1.1.16 now yields:

$$0 = \boldsymbol{F}_\perp \times \boldsymbol{B} + q\left(\boldsymbol{B} \cdot \cancelto{0}{(\boldsymbol{v}_\mathrm{d} \times \boldsymbol{B})} - \boldsymbol{v}_\mathrm{d} \cdot B^2\right). \tag{1.1.18}$$

With $\boldsymbol{v}_\mathrm{d} \perp \boldsymbol{B}$ the first term in the brackets equals zero, and the general drift velocity is given by:

$$\boldsymbol{v}_\mathrm{d} = \frac{\boldsymbol{F}_\perp \times \boldsymbol{B}}{qB^2} \tag{1.1.19}$$

To obtain the most relevant single particle drifts in toroidally confined plasmas, the particular force simply needs to be inserted into equation 1.1.19. The two drifts discussed throughout the thesis arise from the gradient of the magnetic field $\nabla\boldsymbol{B}$ and the electric field $\boldsymbol{E}$ introduced by the charge separation created from the $\nabla\boldsymbol{B}$-drift. If the perpendicular force does not linearly depend on q (as in the case of $\nabla\boldsymbol{B}$), positively and negatively charged particles will drift in opposite directions. These drifts are the reason why a poloidal magnetic field was introduced which, by twisting the field lines around the torus, might compensate for the drifts. Moreover, the exact same drifts will be relevant for the charge separation in "plasmoids" and the resulting $\boldsymbol{E} \times \boldsymbol{B}$-drift discussed in section 1.4.

The two corresponding drift velocities are:

$$\begin{aligned} \nabla\boldsymbol{B}\text{-drift:} \qquad & \boldsymbol{v}_{\nabla\boldsymbol{B}} = \frac{-\boldsymbol{\mu}\nabla\boldsymbol{B} \times \boldsymbol{B}}{qB^2}, \\ \boldsymbol{E} \times \boldsymbol{B}\text{-drift:} \qquad & \boldsymbol{v}_{\boldsymbol{E}\times\boldsymbol{B}} = \frac{\boldsymbol{E} \times \boldsymbol{B}}{B^2}. \end{aligned}$$

The magnetic moment $\boldsymbol{\mu}$ is defined as $(mv_\perp^2/2B)\boldsymbol{e}_\mu$ [10].

For stellarators, it has been theoretically predicted that particle drifts result in hollow density profiles [30] caused by neoclassical thermo-diffusion. Unfortunately, the plasma core is the region where fusion will most likely occur, and thus the fusion of the fuel itself dilutes the plasma core even further. Therefore, developing central particle fuelling techniques is vital for the practicality of toroidal magnetic confinement devices as future fusion power plants.

1.2. Laser Physics

The general physics behind LASERs (Light Amplification by Stimulated Emission of Radiation) explained by Einsteins Quantum Theory of Radiation [31] and the quantum physics picture of the atomic model provide the basis for this chapter. The specific case of a Nd:YAG laser system will be briefly introduced followed by considerations on different laser operation modes and an assessment of the thermal conditions in a laser rod.

1.2.1. Nd:YAG Lasers

Neodymium-doped yttrium aluminum garnet (short Nd:YAG) crystals have been employed as lasing medium first in 1964 by J. E. Geusic *et. al.* [32]. The lasing medium consists of neodymium^{3+} - ions embedded in a transparent $Y_3Al_5O_{12}$ crystal lattice.

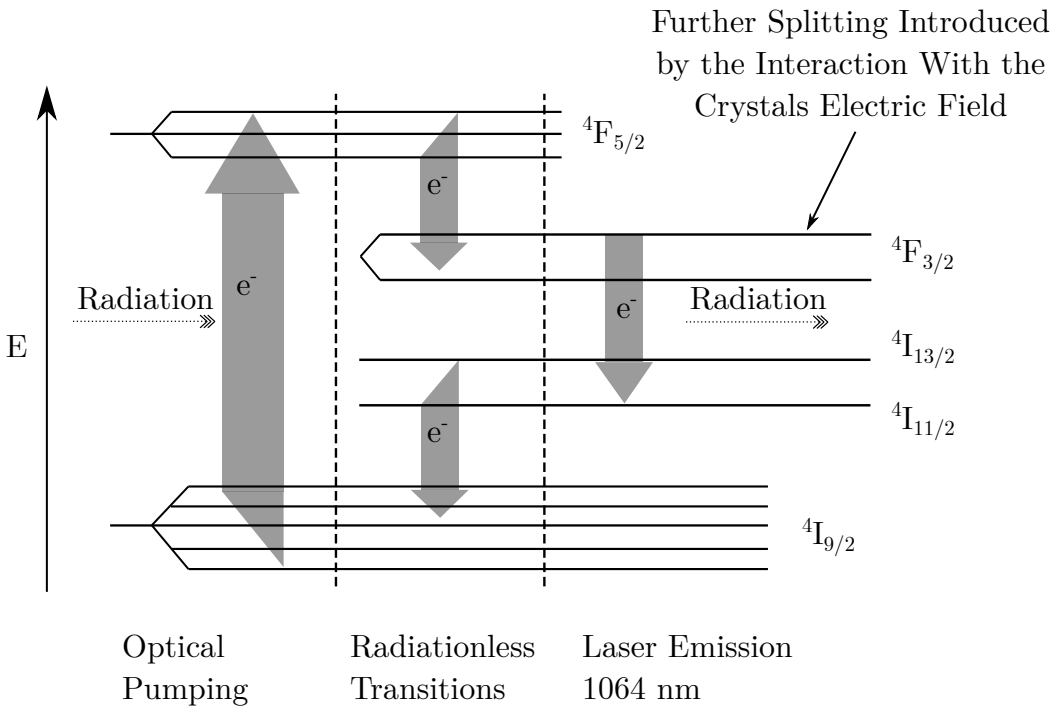

Fig. 1.2.1.: Optical transitions in an Nd^{3+} - ion used to emit $\lambda = 1064\,\text{nm}$.

Neodymium builds an ideal four level laser system for the optical transitions shown in fig. 1.2.1. After being excited by the incident pump-radiation the electrons in the pump level $^4F_{5/2}$ relax quick, radiation less and with high efficiency to the upper laser level $^4F_{3/2}$. The $^4F_{3/2}$ level is meta-stable ($\tau = 230\,\mu s$). It cannot relax quickly to the ground state $^4I_{9/2}$ or other ^4I-levels, because in the crystals field the electric dipole mechanism ($\Delta l \stackrel{!}{=} \pm 1$) is forbidden [33]. Nevertheless, it relaxes by stimulated emission into the lower laser level $^4I_{11/2}$, emitting a photon with $\lambda = 1064\,nm$. The lower laser level, like the pump level, undergoes a fast, non-radiative decay into the ground state $^4I_{9/2}$. The $^4I_{9/2}$ level consists of 5 sub-states and the $^4F_{5/2}$ level of 3 sub-states introduced by the electron orbit interaction with the crystal electric field. This increases the efficiency of the pumping, because several wavelength are accepted (i.e. 808 nm, 869 nm and 885 nm [33]).
A typical setup of a high power Nd:YAG laser is shown in fig. 1.2.2:

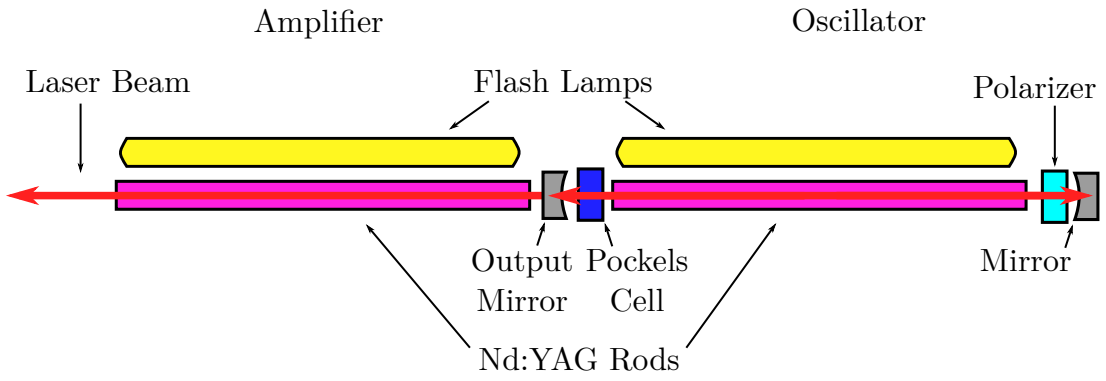

Fig. 1.2.2.: Schematic setup of a Nd:YAG laser.

The flash lamps, or occasionally diode lasers, are used as optical pumps. In the oscillator stage of a pulsed Nd:YAG laser the laser light is generated and released after applying a high voltage to the Pockels cell. The cell is equivalent to a Q-switch, selecting the polarization direction of the polarizer and hence allowing successful lasing between the two mirrors only if it is "open". To increase the power output, one or more amplification stages are usually introduced thus spreading the incident thermal power load from the flash lamps to multiple rods. With this setup, as in the case of the W7-X Thomson scattering diagnostic lasers, typical figures are 0.5 - 2.5 J of energy per pulse, $\approx 10\,ns$ pulse length and repetition frequencies of 10 - 20 Hz.
The timing between the components displayed in fig. 1.2.2 must be set carefully. It has a huge influence on the laser beam and pulse properties and could, if set incorrectly, destroy the laser. According to the physics explained above, the

population inversion in the oscillator Nd:YAG rods in our case is introduced by the absorption of pump light emitted from the oscillator flash lamps for 200 µs. After reaching its maximum at about 215 µs after the start of the flash lamp pulse, the Pockels cell opens and the lasing in the oscillator begins. At this moment, the population inversion in the amplifier Nd:YAG rod needs to be at its maximum to gain maximum energy outputs. Therefore, the amplifier flash lamps are triggered simultaneously with the oscillator flash lamps. If the energy of the laser pulse has to be reduced, the trigger of the amplifier flash lamp and hence the population inversion of the amplifier rod can be delayed. Additionally it is possible to reduce the flash lamp voltage, which reduces the intensity of their radiated light and therefore excite fewer electrons to the pump levels. The general timing, without taking amplification stages into account, is shown in fig. 1.2.3:

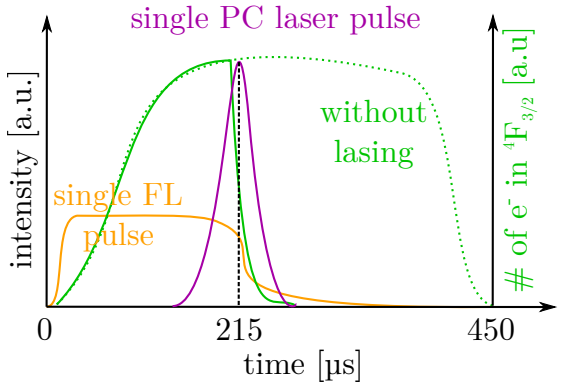

Fig. 1.2.3.: Timing for a single laser pulse emitted from a pulsed Nd:YAG laser without amplifier. The Pockels cell (PC) laser pulse duration in this figure does not scale to the flash lamp (FL) and the population inversion duration.

Only if the interplay between the different components is well adjusted, keeping important parameters like the above mentioned thermal loads in a safe range, will the laser operate in a stable regime. The thermal conditions in the laser greatly affect properties like the beam pointing stability and the beam profile as discussed in section 3.3.

1.2.2. Burst-Mode Operation

A special operation mode featuring short trains of multiple pulses emitted by a laser in a very short time interval is called “burst mode”. One technique to achieve burst-mode operation for Nd:YAG lasers is the reduction of the repetition frequency by a factor of two, replacing the single flash lamp pulse cycle by two cycles. The minimum delay between two pulses is therefore limited by the duration of a flash lamp discharge. Another more complex option is to extract two or more pulses from a single flash lamp cycle during the time the flash lamp is still pumping the laser as shown in fig. 1.2.4.

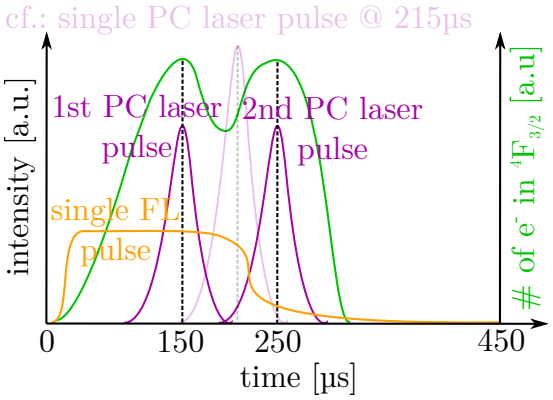

Fig. 1.2.4.: Timing for two laser pulses (double Pockels cell (PC) pulse) emitted from a pulsed Nd:YAG laser. The Pockels cell (PC) laser pulse durations in this figure do not scale to the flash lamp (FL) and population inversion duration. The former single PC pulse is displayed semi-transparent for comparison.

Via this method, the energy of the single FL pulse is split to the multi pulses as indicated by the intensity decrease. The original single PC laser pulse intensity is displayed semi-transparent for comparison. The amount of pulses generated by this method is in principle not limited. Nevertheless the reduction of the individual pulse energies is an expensive trade off for additional pulses. This is why two pulses are used in general. The maximal delay between such pulses is limited by the population inversion lifetime and the flash lamp discharge duration.
The average thermal conditions in the laser rod stay the same for both methods. For the first method, the reduction from the half repetition frequency is compensated by the double flash lamp pulse. The second method does not affect the thermal conditions at all because the second pulse is not generated by a separate flash. By combining the two methods, a pulse train of typically four pulses emitted

from one laser, as shown in figure 1.2.5, is possible. With respect to the temporal boundary conditions a robust operation regime had to be found and qualified not to exceed operation limits causing harm to the laser and beam path components of the diagnostic. This systematic study is presented in section 3.3) although the optimized timings will be used in this section for illustration purpose already.

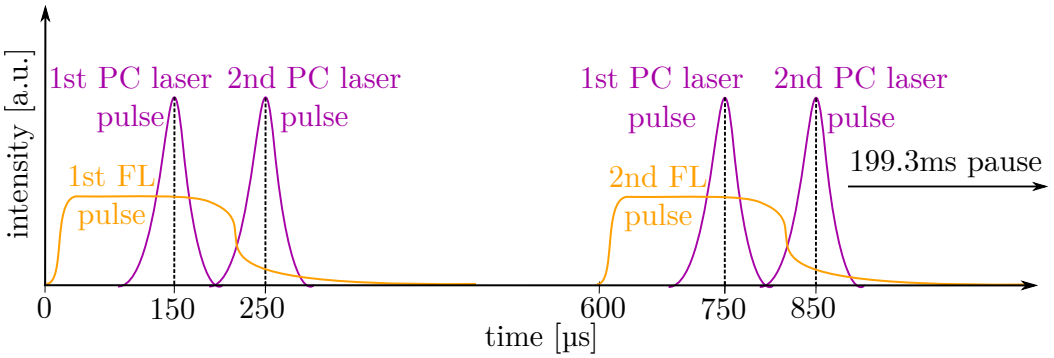

Fig. 1.2.5.: Burst pulse train emitted by one laser combining flash lamp (FL) and Pockels cell (PC) double pulses.

With the three available W7-X Thomson scattering lasers, this pattern can be extended to a train of 12 pulses with uniform increment of 100 µs as shown in fig. 1.2.6. It will provide Thomson scattering data with a repetition frequency of 10 kHz for the duration of 1.2 ms based on a 5 Hz repetition frequency. Many combinations of burst and non-burst modes and timings could be set for different requirements utilizing three lasers. These pulse trains must be synchronized with fast, randomly occurring events. The general feasibility of this aim will be demonstrated in the next section.

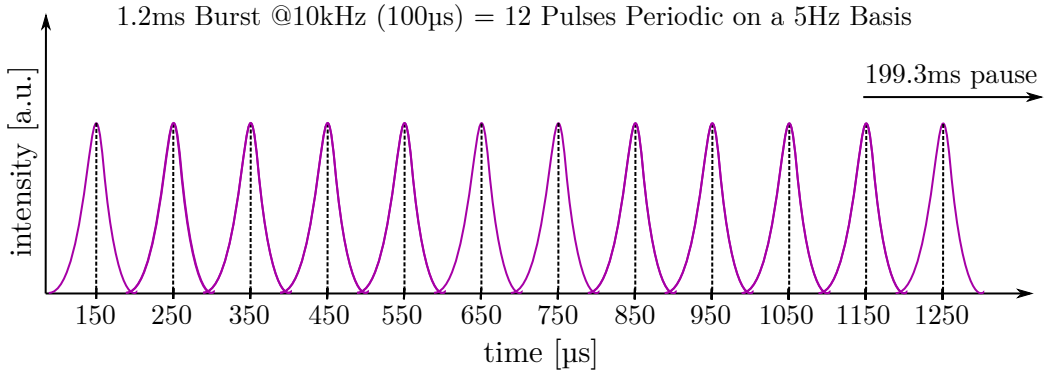

Fig. 1.2.6.: Pulse train for combined three-laser burst-mode operation.

1.2.3. Thermal Limits of Non-Uniform Laser Pulse Triggering

The unpredictability of occurring events (like the pellet injection - given its huge jitter) require contentiously operating diagnostics with high temporal resolution or, as in the case of low repetition frequency measurements like Thomson scattering, triggers that match the timing of the events. But even if a good trigger can be found, it is not trivial to implement it within a diagnostic. In the case of the Thomson scattering system, it is not possible to take a measurement only when the event occurs. As an "operational diagnostic", the Thomson scattering system is required for the safe operation of W7-X. Additionally, the lasers need a consisted repetition frequency to achieve stable thermal conditions; the heat up alone takes several seconds. At the first glance it does not seem possible at all to trigger the Thomson scattering system using fast events. For pellets with a nominal repetition frequency of $\approx 30\,\mathrm{Hz}$ and a jitter in the range of $1/30\,\mathrm{Hz}$, a deviation of about 30 ms from the regular Thomson timing would be necessary in a time interval of the same scale. To circumvent the restrictions given by the thermal conditions of the laser, the slow nature of thermal processes is exploited. If one could show that the thermal conditions in the laser remain similar for the required deviation from the regular Thomson timings, the design of a (pellet) event-triggered Thomson scattering diagnostic becomes possible. To access the thermal processes in the Nd:YAG rods, the following appraisal was utilized:

The thermal energy in an arbitrary volume (for example a volume element of a Nd:YAG rod):

$$E(t) = \int_{\mathrm{V}} \rho c \cdot T(\boldsymbol{x}, t)\,\mathrm{d}\boldsymbol{x} \tag{1.2.1}$$

where
$\rho \ldots$ mass density,
$c \ldots$ specific heat capacity,
$T(\boldsymbol{x}, t) \ldots$ temperature, time and space dependent,

changes by the heat flux density $\boldsymbol{q}(\boldsymbol{x}, t)$ entering or leaving trough its surface ∂V:

$$\frac{\partial E_{\mathrm{in}}}{\partial t} - \frac{\partial E_{\mathrm{out}}}{\partial t} = \oint_{\partial \mathrm{V}} \boldsymbol{q}(\boldsymbol{x}, t) \cdot \hat{\mathbf{n}}\,\mathrm{d}(\partial V), \tag{1.2.2}$$

where $\hat{\mathbf{n}}$ is the normal vector of the surface ∂V.

In the case of the hot Nd:YAG rod, $\frac{\partial E_{\text{in}}}{\partial t}$ and $\frac{\partial E_{\text{out}}}{\partial t}$ of neighbouring volume elements cancel. The temperature of the surrounding air is less than the rod's temperature during laser operation. According to the second law of thermodynamics [34], the heat flux into the rod, and therefore $\frac{\partial E_{\text{in}}}{\partial t}$, goes to zero in-between the flash lamp flashes. This means equation 1.2.2 can be rewritten as:

$$-\frac{\partial E}{\partial t} = \oint_{\partial \text{V}} \boldsymbol{q}(\boldsymbol{x}, t) \cdot \hat{\mathbf{n}} \, \mathrm{d}(\partial V). \tag{1.2.3}$$

Note: $\frac{\partial E_{\text{out}}}{\partial t} = \frac{\partial E_{\text{total}}}{\partial t} = \frac{\partial E}{\partial t}$.

After applying Gauss's law, equation 1.2.3 can be written as:

$$\frac{\partial E}{\partial t} = -\int_{\text{V}} \nabla(\boldsymbol{q}(\boldsymbol{x}, t)) \, \mathrm{d}\boldsymbol{x}, \tag{1.2.4}$$

which can be combined with the temporal derivation of equation 1.2.1:

$$\begin{aligned} \int_{\text{V}} \rho c \cdot \frac{\partial T(\boldsymbol{x}, t)}{\partial t} \, \mathrm{d}\boldsymbol{x} &= -\int_{\text{V}} \nabla(\boldsymbol{q}(\boldsymbol{x}, t)) \, \mathrm{d}\boldsymbol{x}, \\ 0 &= \int_{\text{V}} \rho c \cdot \frac{\partial T(\boldsymbol{x}, t)}{\partial t} \, \mathrm{d}\boldsymbol{x} + \int_{\text{V}} \nabla(\boldsymbol{q}(\boldsymbol{x}, t)) \, \mathrm{d}\boldsymbol{x}, \\ 0 &= \int_{\text{V}} \left(\rho c \cdot \frac{\partial T(\boldsymbol{x}, t)}{\partial t} + \nabla(\boldsymbol{q}(\boldsymbol{x}, t)) \right) \mathrm{d}\boldsymbol{x}. \end{aligned} \tag{1.2.5}$$

Therefore $\rho c \cdot \frac{\partial T(\boldsymbol{x}, t)}{\partial t} + \nabla(\boldsymbol{q}(\boldsymbol{x}, t)) = 0$ applies to all volume elements.

With Fourier's law of heat conduction [35], $\boldsymbol{q}(\boldsymbol{x}, t) = -\kappa \nabla T(\boldsymbol{x}, t)$, where κ is the thermal conductivity, the **General Heat Equation** results as follows:

$$\begin{aligned} \frac{\partial}{\partial t} T(\boldsymbol{x}, t) - \nabla \left(\left(\frac{\kappa}{\rho c} \right) \nabla T(\boldsymbol{x}, t) \right) &= 0, \\ \frac{\partial}{\partial t} T(\boldsymbol{x}, t) - \frac{\kappa}{\rho c} \Delta T(\boldsymbol{x}, t) &= 0. \end{aligned} \tag{1.2.6}$$

Including heat sources or sinks, as in the case of the Nd:YAG rod, the right hand side of equation 1.2.6 would not be zero. As explained, the rod is warmer than the surrounding air after a sufficient number of flash lamp flashes introduced a quasi-stationary equilibrium. Therefore, the zero is replaced with a pure sink term in-between the flash lamp flashes (which usually would be sources). In cylindrical coordinates, and assuming cylindrical symmetry ($T(\varphi) = const.$) for the rod, the General Heat Equation becomes:

$$\frac{\partial}{\partial t}T(r,z,t) - \frac{\kappa}{\rho c}\left(\frac{1}{r}\frac{\partial}{\partial r}\left(r\frac{\partial}{\partial r}T(r,z,t)\right) + \frac{1}{r}\frac{\partial^2}{\partial z^2}T(r,z,t)\right) = \text{sink term.} \quad (1.2.7)$$

Multiplying by $\left|\cdot\frac{r^2\rho c}{\kappa}\right.$:

$$\frac{r^2\rho c}{\kappa}\frac{\partial}{\partial t}T(r,z,t) - r\frac{\partial}{\partial r}\left(r\frac{\partial}{\partial r}T(r,z,t)\right) + r\frac{\partial^2}{\partial z^2}T(r,z,t) = \text{sink term}, \quad (1.2.8)$$

the term in front of $\frac{\partial}{\partial t}T(r,z,t)$ can be identified as a typical time constant for the heat flowing out of the rod in-between two flash lamp flashes.
The characteristic length of a 3-D object describing its general shape can be defined as ratio between volume and surface. For the Nd:YAG rod, which is a thin cylinder of finite length, the ratio gives:

$$\frac{V_{\text{rod}}}{\partial V_{\text{rod}}} = \frac{\pi r_{\text{rod}}^2 L_{\text{rod}}}{2\pi r_{\text{rod}} L_{\text{rod}}} = \frac{r_{\text{rod}}}{2} \quad (1.2.9)$$

Thus the characteristic time constant for the rods is:

$$\tau_{\text{thermal}} = \frac{r_{\text{rod}}^2 \rho c}{4\kappa} \quad (1.2.10)$$

The W7-X Thomson scattering laser rods have radii of 6.35 mm in the oscillator and up to 12 mm in the amplifiers. A YAG crystal has a density of $\rho \approx 4.56 \times 10^6\,\text{g/m}^3$, a thermal conductivity of $\kappa \approx 12.9\,\text{W/mK}$ and a specific heat capacity of $c \approx 0.59\,\text{Ws/gK}$ [36]. These values give a τ_{thermal} on the order of 1.9 - 7.5 s.
This demonstrates that the flash lamp pulses can be non-uniformly distributed

with variations tens of milliseconds, keeping the total number of pulses constant within several hundred milliseconds. This fundamentally allowed the design of the event-triggered (burst-mode) Thomson scattering diagnostic as described in this thesis.

1.3. Overview on Thomson Scattering Physics and Diagnostic Application

Thomson scattering is a well-established non-pertubative experimental technique used to determine the velocity distribution (temperature) and density of plasma electrons [37] and is employed at most state-of-the-art magnetic confinement plasma experiments [38, 39, 40, 41, 42]. The underlying principle is the scattering of photons by the plasma particles. The derivations in this subsection mainly rely on the book "Principles of Plasma Diagnostics" by I. H. Hutchinson [37].
As mentioned in the introduction, a plasma in general shows collective behaviour. Nevertheless, on length-scales smaller than the Debye length λ_D (cf. equation 1.1.14), this generalization does not hold. Therefore, usually two cases are distinguished: "coherent", or "collective", Thomson scattering and "incoherent" Thomson scattering. In the former case, the scattering of the light from the particles within a Debye sphere will add-up coherently since there is negligible phase difference between them. In the later case, the phase difference between photons scattered by particles within the sphere is large, which is why it is called incoherent Thomson scattering. It applies in the case when $k_s\lambda_D \ll 1$, where k_s is the absolute value of the wave vector $\boldsymbol{k}_s$ of the scattered wave introduced in fig. 1.3.1.

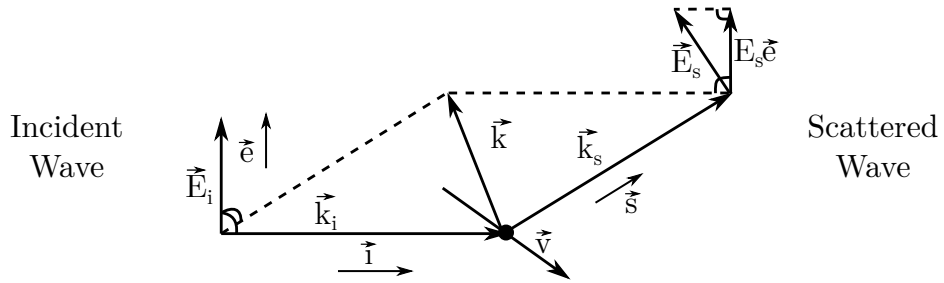

Fig. 1.3.1.: Vector diagram for the Thomson scattering of an electromagnetic wave, linear polarized perpendicular to the scattering plane ($\boldsymbol{E}_i \perp \boldsymbol{s}$; $\boldsymbol{E}_i \perp \boldsymbol{i}$ always), by a single particle (taken from [37] - modified). $\boldsymbol{E}$ is the electric field of the wave and $\boldsymbol{e}$ its direction. The wave vectors are denoted by $\boldsymbol{k}$, and $\boldsymbol{v}$ is the velocity of the plasma particle. The indices i and s indicate quantities of the incident and scattered waves, respectively, and so do $\boldsymbol{i}$ and $\boldsymbol{s}$ indicate their directions.

In an experimental setup, incoherent Thomson scattering can be observed by a particular selection of the observation direction (i.e. perpendicular to the $\boldsymbol{e}$-

direction) and an appropriate probing wave's wavelength and polarization. The high-power Q-switched Nd:YAG lasers, introduced in section 1.2.1, emit linear polarized light that can be set perpendicular to the scattering plane as shown in fig. 1.3.1. Their wavelength, $\lambda = 1064\,\mathrm{nm}$, which relates to the wave vector by $|\boldsymbol{k}| = 2\pi/\lambda$, lies in the desired range for the plasmas of interest for this thesis. The subsequent described processes focus on incoherent Thomson scattering in the aforementioned geometry, and thus allow for a treatment of the particles as free particles, excluding collective plasma effects. Moreover, usually only the electrons contribute to the scattering by the plasma, which can be explained employing an electromagnetic picture of the scattering process. Free charged particles start oscillating if they experience the forces arising from the electric and magnetic fields of an incident electromagnetic wave. The equation of motion for this process has been introduced earlier as the Lorentz equation 1.1.1. The acceleration and deceleration of the charge in the direction of the electric field of the incident wave, $\boldsymbol{E}_\mathrm{i}$, results in electromagnetic dipole radiation which builds the scattered wave. The radiated (scattered) field $\boldsymbol{E}_\mathrm{s}$, for the above described case, can be expressed in terms of the incident field ([37] p. 276):

$$\boldsymbol{E}_\mathrm{s} = \left[\frac{\mathrm{r_e}}{r}\boldsymbol{s} \times (\boldsymbol{s} \times \boldsymbol{E}_\mathrm{i})\right]_\mathrm{ret.}. \tag{1.3.1}$$

Note that the right hand side needs to be evaluated at retarded time $t' = t - |\boldsymbol{r} - \boldsymbol{r'}|/c$, which is the time when the field began to propagate from where it was emitted at point ($\boldsymbol{r'}$) to an observer at $\boldsymbol{r}$, indicated by the square brackets. The classical electron radius $e^2/4\pi\varepsilon_0 \mathrm{m_e c^2} = (2.817\,940\,322\,7 \pm 0.000\,000\,001\,9) \times 10^{-15}\,\mathrm{m}$ [15] is denoted by $\mathrm{r_e}$, with $\mathrm{m_e}$ ($(9.109\,383\,56 \pm 0.000\,000\,11) \times 10^{-31}\,\mathrm{kg}$ [15]) being the electron rest mass.
From Poynting's theorem [43] it follows that the power P per unit area A carried by the electromagnetic wave is:

$$P = \varepsilon_0 \mathrm{c} \left|E^2\right|, \tag{1.3.2}$$

which can be combined with equation 1.3.1 to derive the power scattered per unit angle with respect to the incident wave's field. For this purpose the solid angle, defined as the area segment A of a sphere divided by the radius r of the considered sphere, $\Omega = A/r^2$, is employed:

$$\frac{\mathrm{d}P_\mathrm{s}}{\mathrm{d}\Omega} = \mathrm{r_e^2} \sin^2(\varphi) \varepsilon_0 \mathrm{c} \left|E_\mathrm{i}^2\right|. \tag{1.3.3}$$

The factor of $\sin^2(\varphi)$ arises from the angular distribution of power radiated by an electric dipole. The ratio between incident and scattered power, given as $\mathrm{r_e^2}\sin^2(\varphi)$, integrated over all solid angles can be interpreted as the effective size of an electron for scattering. The total power it scatters in all directions (all solid angles) is equal to the power of the incident wave that would fall on a disc of area:

$$\int \mathrm{r_e}\sin^2(\varphi)\,\mathrm{d}\Omega = \int_0^{2\pi} \mathrm{r_e^2}\sin^2(\varphi)\cdot 2\pi\sin(\varphi)\,\mathrm{d}\varphi = \frac{8\pi}{3}\mathrm{r_e^2} = \sigma_{\mathrm{Th}}, \tag{1.3.4}$$

which is commonly known as the total "Thomson scattering cross section" σ_{Th}.
Due to the much larger mass of the ions (containing one proton at least) as compared to the electrons, the ion acceleration is negligible as is the ion scattering ($\mathrm{m_p/m_e} \approx 2000$; $\mathrm{m_p} = (1.672\,621\,898 \pm 0.000\,000\,021) \times 10^{-27}\,\mathrm{kg}$ [15]).
At $\lambda = 1064\,\mathrm{nm}$ the energy of one photon (hc/λ, where h denotes the Planck constant $(4.135\,667\,662 \pm 0.000\,000\,025) \times 10^{-15}\,\mathrm{eV\,s}$) is 1.1653 eV, whereas the rest energy of an electron is 511 keV [15]. Therefore, the change in the electron's momentum introduced by the scattering process can be neglected, and it can be seen that Thomson scattering is a non-pertubative process. Nevertheless, momentum conservation ($\boldsymbol{k} = \boldsymbol{k}_\mathrm{s} - \boldsymbol{k}_\mathrm{i}$) as well as energy conservation ($hc/\lambda_\mathrm{s} = hc/\lambda_\mathrm{i} + \boldsymbol{kv}/2\pi$) in general must apply for the elastic scattering process. The formulation of the energy conservation law indicates that the wavelength of the scattered light depends on the velocity of the electron.
As discussed earlier, for the case of incoherent Thomson scattering, the particle phases are uncorrelated, and thus the powers scattered from multiple electrons add incoherently. Applying this summation for a volume V of length L, as shown in fig. 1.3.2, the ratio between scattered and incident power yields:

$$\frac{P_\mathrm{s}}{P_\mathrm{i}} = \frac{8}{3}\pi\mathrm{r_e^2}n_\mathrm{e}L, \tag{1.3.5}$$

where n_e is the number of electrons per unit volume, commonly referred to as electron density in plasma physics. This is how Thomson scattering can provide a measure of a plasma's electron density. Evaluating the fraction $P_\mathrm{s}/P_\mathrm{i}$ for typical electron densities of the order of $10^{20}\,\mathrm{electrons/m^3}$ and a typical length of the scattering volume of the order of $10^{-2}\,\mathrm{m}$ (limiting the achievable spatial resolution of the Thomson scattering diagnostic), the scattered power is found to be a factor of 10^{-10} smaller than the incident power. The significant difference is explained by the small value of the Thomson scattering cross section, which is about $10^{-30}\,\mathrm{m^2}$, and is why high power lasers need to be employed for Thomson scattering measurements.

Several experimental considerations need to be taken into account to maintain a sufficient signal-to-noise ratio as discussed later in this section.

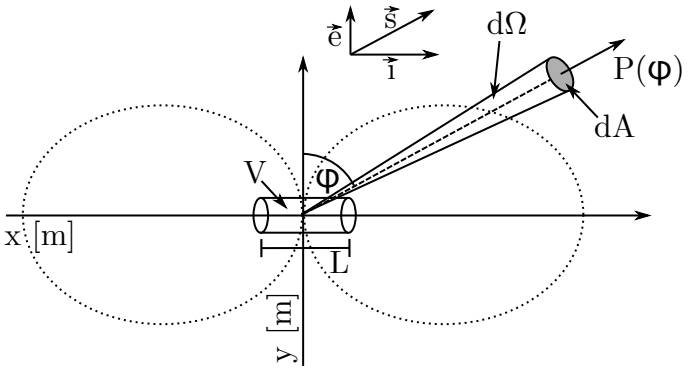

Fig. 1.3.2.: Schematic of the Thomson scattering setup, including a polar plot of the angular distribution of power (dotted spheres) radiated by a single electric dipole in the scattering volume V of length L. The power $P(\varphi)$ has the shape of the function $\sin^2(\varphi)$. The directions of the incident wave and its electric field, as well as the direction of the scattered wave, are denoted by $\boldsymbol{i}$, $\boldsymbol{e}$, and $\boldsymbol{s}$, respectively. The differential solid angle $\mathrm{d}\Omega$ is indicated by the cone around the dashed line and $P_\mathrm{s}(\varphi)$ is the angle dependent scattered power integrated over the differential area $\mathrm{d}A$.

Now that the principle mechanism to obtain the electron density from Thomson scattering has been discussed, the second quantity, the electron temperature T_e, will be reviewed. Referring to the energy conservation principle of the scattering process $hc/\lambda_\mathrm{s} = hc/\lambda_\mathrm{i} + \boldsymbol{k}\boldsymbol{v}/2\pi$, note the dependence of the scattered wave's wavelength λ_s on the electron velocity $\boldsymbol{v}$. The average kinetic energy of the particles in a system, and hence their velocity, can be used to define the temperature of the system, at least if the system is in local thermal equilibrium where the particles are Maxwell-Boltzmann distributed. As mentioned in section 1.1.3, this is usually the case in magnetic confinement plasma experiments (Note: Close to the location of the plasma heating this simplification might not hold.). The Maxwellian electron velocity distribution is the product of the electron's velocity distribution in the three spacial directions, each of which are Gaussian distributions [44] with standard deviation $\sqrt{k_\mathrm{B}T_\mathrm{e}/m_\mathrm{e}}$. In the specific case of the plasma electrons gyrating along the magnetic field lines, strictly speaking, two (in general) different temperatures exist: the temperature parallel and the temperature perpendicular to the field lines. The subsequent discussion focuses on the perpendicular component only since it is the component which is analysed by the W7-X Thomson scattering diagnostic due to its observation geometry perpendicular to the magnetic field lines. (Note: This

is the direction of highest scattered power given the polarization of the probing wave perpendicular to the scattering plane, as can be seen from fig. 1.3.2, which is for practical reasons the most favourable observation angle regarding the small ratio of scattered to incident power.)
Monochromatic light scattered by multiple plasma electrons gives a spectrum that is broadened due to the Doppler effect [45] arising from the thermal motion of each individual electron in a simple classical picture. This motion results in a shift of the incident wave's wavelength as seen by the electrons and in a shift of the re-emitted wave's wavelength observed in the resting diagnostic reference frame. The aggregation of all singe electron scattering processes yields a scattered spectrum depended on the electron velocity distribution. The width of the spectrum can be used to derive the mean temperature if the dependence of the spectrum's shape on the temperature is known. Under conditions typical of magnetic confinement plasmas, the temperature of the electrons is several keV, meaning they need to be treated relativistically rather than classically. As a result the radiated spectra are not only Doppler-broadened, but, for instance, blue-shifted as well. This blue shift results from the "headlight effect" known from special relativity theory. The effect is understood recalling the doughnut-like $\sin^2(\varphi)$ shape of the scattered power. This shape must always remain the same in the electron frame of reference as shown in fig. 1.3.3 (a).

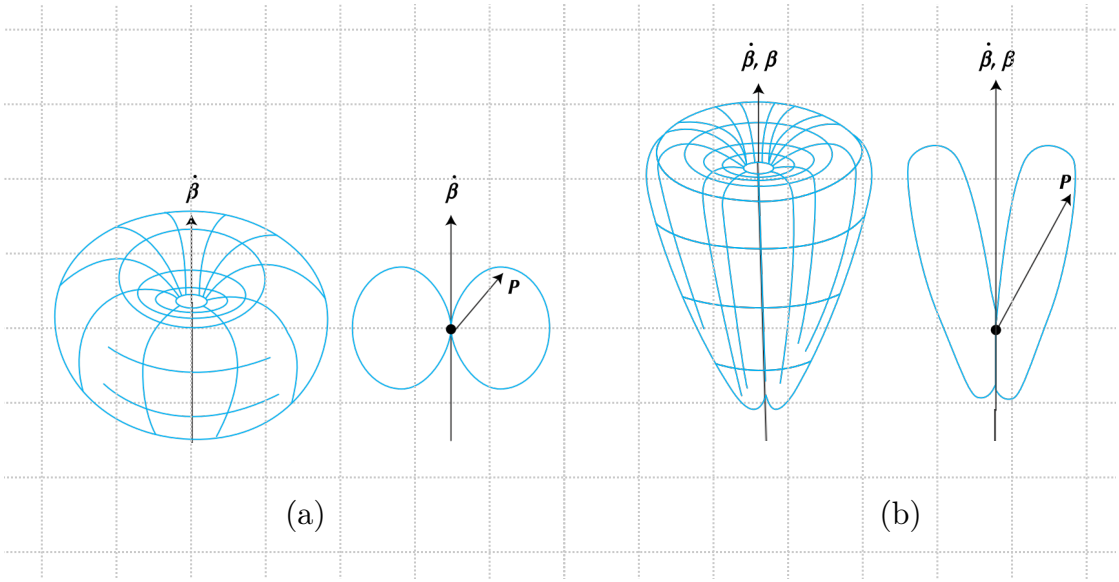

Fig. 1.3.3.: The angular variation of the power P radiated by an accelerated charge and its poloidal cut. (a) Stationary charge; (b) charge moving with $\boldsymbol{\beta} \parallel \dot{\boldsymbol{\beta}}$, where $\boldsymbol{\beta} = \boldsymbol{v}/\mathrm{c}$ and $\dot{\boldsymbol{\beta}}$ is the first time derivative of $\boldsymbol{\beta}$ (taken from [46] - modified).

At relativistic velocities the motion of the electron deforms this doughnut shape (seen in the rest frame of reference) noticeably as shown in fig. 1.3.3 (b). From this figure it becomes clear that, in the resting frame of the observer, the power scattered along the direction of the electron velocity increases while it decreases for the opposite direction. Therefore, the electrons moving fast towards the observer contribute more to the spectrum than the electrons moving away with the same speed, which resulting in the aforementioned blue-shift.
In a real setup the observable scattered power will always be limited to some fraction emitted in a certain solid angle given by the observation optics; moreover, the transmission through the employed optical components is usually wavelength dependent. Therefore, both an absolute (density), and a relative (spectral) calibration of the Thomson scattering system are necessary, as will be discussed later in this section. To determine the scattering spectrum (Thomson spectrum) a so called "polychromator" setup can be employed (the technical implementation of the W7-X polychromators can be found in section 2.3). The idea is to split the observed wavelength range in a few spectral intervals of known width and sensitivity employing spectral filters. For different temperatures different fractions of the Thomson spectrum lie within these intervals as shown in fig. 1.3.4.

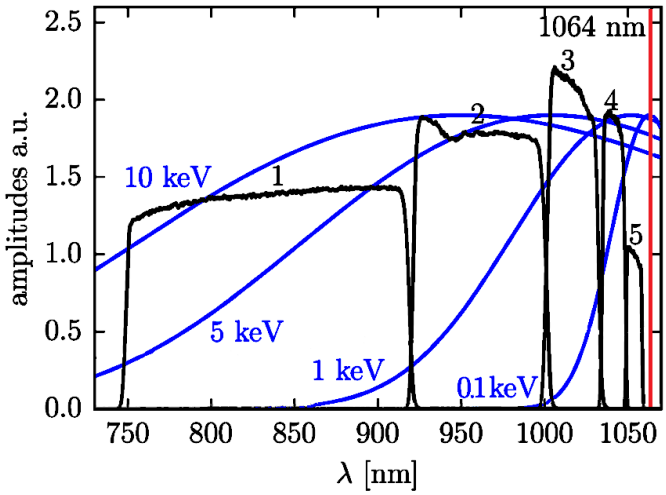

Fig. 1.3.4.: Filter curves (black) resulting from the spectral calibration. Thomson scattering spectra (blue) of 1064 nm incident light (red line) are given for temperatures of 0, 1, 5 and 10 keV (taken from [47] - modified).

Therefore, the signal detected in each channel by a photo diode beyond the spectral filter can be employed to reconstruct the distribution of scattered light by comparing the relative signal fractions. The amplitude of the spectrum scales to the electron density. The signal detected by a spectral channel can be expressed as [48]:

$$D_{\mathrm{TH}}^{(i,j)} = c_{\mathrm{geom}}^{(i)} P_{\mathrm{i}}\, n_{\mathrm{e}}^{(i)} \sigma_{\mathrm{Th}} \int \tau^{(i,j)}(\lambda)\, S(\lambda,\, T_{\mathrm{e}}^{(i)},\, \varphi^{(i)})\, \mathrm{d}\lambda, \tag{1.3.6}$$

where:
(i) ... index for the spatial position of the scattering volume,
(j) ... index for the spectral channel,
P_{i} ... incident laser power,
σ_{Th} ... Thomson scattering cross section for a single electron,
$\varphi^{(i)}$ ... scattering angle for each position,
$\tau^{(i,j)}(\lambda)$ ... spectral transmission of the interference filters as a function of the wavelength λ.

Naito *et.al.* gives an analytical approximation of the spectral density function $S(\lambda,\, T_{\mathrm{e}}^{(i)},\, \varphi^{(i)})$ [49, 50] for the most common measurement configuration, where both the incident and the observed light polarization are perpendicular to the scattering plane (which applies for W7-X); the exact solution in any configuration would be given by the integral of the electron distribution. The "(1,1) approximation" of Naito's formula [49, 50] yields a reliable fit (error $\leq 0.1\,\%$) to the exact solution for temperatures up to 30 keV, which is significantly more than can be normally expected for W7-X plasmas. To evaluate $D_{\mathrm{TH}}^{(i,j)}$ with respect to the quantities of interest, the electron density n_{e} and the electron temperature T_{e} calibration measurements are needed. The spectral transmission of the interference filters as a function of wavelength $\tau^{(i,j)}(\lambda)$ ... can be determined by a "spectral calibration" described in detail in [47]. The filter curves resulting from the spectral calibration are shown in fig. 1.3.4. In order to determine the "geometric factor" $c_{\mathrm{geom}}^{(i)}$, a technique called "Raman calibration" as first proposed in [51] can be applied. For this purpose the signal of the spectral lines $\lambda_{\mathrm{Ra}}^{(J)}$ from Raman scattering of the probe laser light in nitrogen (N_2) at a known temperature (T_{N_2}=300 K) and density n_{N_2} (100 mbar for the results shown here and in section C) is measured in situ with the polychromator setup. The Raman spectrum consists of multiple narrow lines due to $J \rightarrow J-2$ transitions of the N_2 molecule, where J is the rotational quantum number. The Raman signal D_{Ra} is given by [48, 47]:

$$D_{\mathrm{Ra}}^{(i,j)} = c_{\mathrm{geom}}^{(i)} P_{\mathrm{i}}\, n_{N_2} \cdot \sum_J \sigma_{\mathrm{Ra}}^{(J)}\, f^{(J)}\, \frac{\lambda_{\mathrm{Ra}}^{(J)}}{hc}\, \tau^{(i,j)}\left(\lambda_{\mathrm{Ra}}^{(J)}\right), \tag{1.3.7}$$

where:
$f^{(J)}$ ... fractional population of the upper Raman energy state,
$\sigma_{\mathrm{Ra}}^{(J)}$ ... according Raman scattering cross section for a single N_2 molecule.

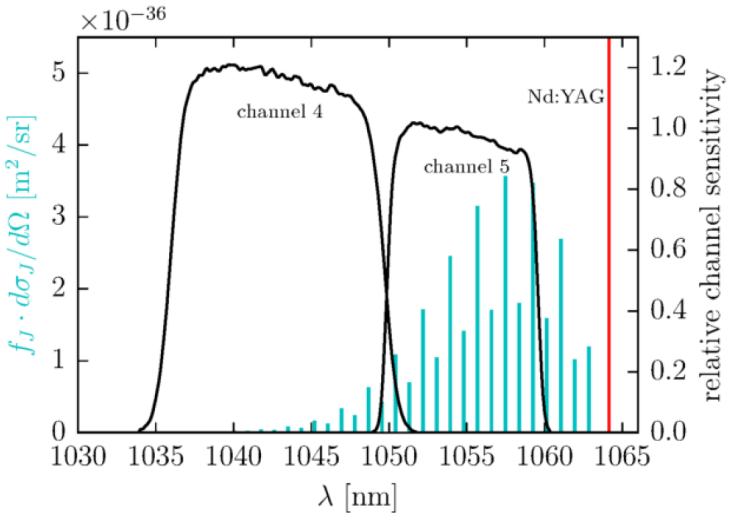

(a) Effective cross sections of the Nitrogen Raman lines at 300 K including the relative level populations (cyan) are overlaid with typical spectral curves of two Thomson channels.

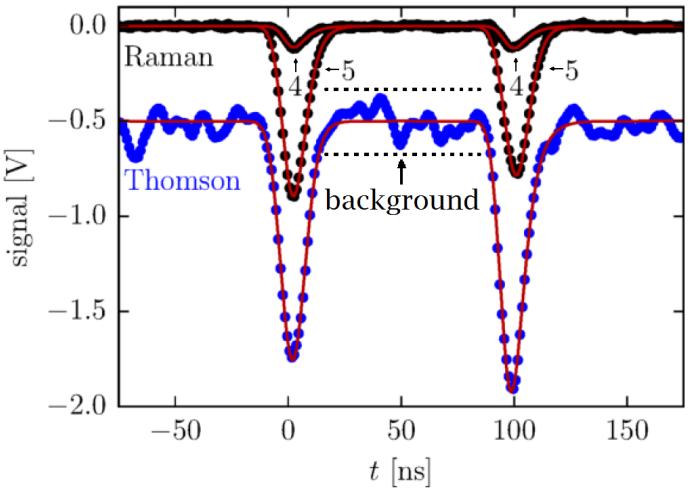

(b) Raman signals for the channels 4 and 5 at nitrogen pressure 100 mbar, and $E_\ell = 1\,\mathrm{J}$. For comparison a Thomson signal (channel 1, $T_e \approx 6\,\mathrm{keV}$, $n_e \approx 1.3 \times 10^{19}\,\mathrm{m}^{-3}$, and $E_\ell = 1.5\,\mathrm{J}$) is shown with an offset of $-0.5\,\mathrm{V}$. The red curves indicate the according fits.

Fig. 1.3.5.: Raman scattering calibration (taken from [47] - modified).

The intensity of the lines is well known for fixed densities and laser energies and hence the expected diode signal per polychromator channel. Therefore, by comparing the measured signal with the theoretical prediction, $c_{\mathrm{geom}}^{(i)}$ can be calculated. The Raman lines lie within only 2 of the 5 spectral channels of the W7-X polychromators (channel 4 and channel 5). The Raman lines including the relative level populations as well as representative examples of their Raman calibration signals are shown in fig. 1.3.5 (a) and (b), respectively. For the analysis performed in section C, only the signal from channel 5 is employed, because the other one is very small. In fig. 1.3.5 (b) every curve shows 2 signal peaks because 2 scattering volumes are merged to one polychromator each, as will be explained in section 2.3. A typical Thomson scattering signal is shown in the figure for comparison. The red lines illustrate fits to the experimental data. The fluctuations between the dashed lines in fig. 1.3.5 (b), indicated as "background", need to be significantly smaller than the actual Thomson scattering signal to reliably fit the signal, itself. The total signal, detected by an individual spectral channel j at position i, contains the summation of the Thomson scattering signal D_{Th}, all types of plasma radiation D_{plasma} (bremsstrahlung, electron synchrotron radiation, etc.), and noise D_{noise}. Noise, for instance, arises from the photo diode's dark current, the analogue–digital converter discretization steps, and the amplification of the signal. Accordingly, the signal-to-noise ratio for each individual channel can be defined as:

$$\mathrm{SNR} = \frac{D_{\mathrm{Th}}}{D_{\mathrm{plasma}} + D_{\mathrm{noise}}}. \tag{1.3.8}$$

To reconstruct the distribution of the scattered light (and hence the velocity distribution or temperature), as well as the signal intensity (hence electron density), the time integral of the fitted Thomson signal is determined for all channels, and the relative signal fractions are subsequently compared. From the relative signal levels the most likely scattering spectrum is determined. Ideally, this process would result in the original spectrum, as shown in fig. 1.3.4. Nevertheless, the reconstruction of the scattering spectrum can fail for different reasons, thereby limiting the experimentally available measurement range:

- insufficient SNR, i.e. due to low laser energy (Note: The burst mode reduces the laser pulse energy by roughly a factor of 2.),
- similar signal in all channels due to a very broad spectrum, i.e. for high temperatures (cf. fig. 1.3.4),
- zero signal in the lower channels, i.e. for low temperatures (cf. fig. 1.3.4).

The careful analysis of the experimental limits of the W7-X Thomson scattering system [47] revealed the diagnostic's ability to reliably provide electron and temperature profiles, obtained from the arrangement of multiple scattering volumes along the radial direction of a poloidal plasma cross section, for a wide range of different plasma conditions. It is able to determine electron temperatures in the range of 10 eV to 10 keV, although the errors only remain reasonable ($\lesssim 10\,\%$) within 1 - 5 keV. Both the lower and upper density limits are given by the experimentally achievable densities in W7-X rather than by limitations of the Thomson scattering diagnostic, itself. Nevertheless, the diagnostic allows for precise electron density measurements from $2 \times 10^{18}\,\mathrm{m}^{-3}$ up to $5 \times 10^{20}\,\mathrm{m}^{-3}$ [52]. For the burst mode operation regime of the lasers, the observable density range (i.e. the lower threshold) had to be reviewed, because the laser energy per pulse was reduced. It turned out that, for all shots analysed, the Thomson scattering signal could be fitted sufficiently even in burst mode operation. One should note that the bisected pulse energy was partially compensated by the high densities achieved during pellet injection when the burst mode was usually applied.

1.4. Basic Mechanisms of Pellet Injection

As mentioned in the introduction, the injection of cryogenic pellets, is one of the most promising ways to fuel the plasma in magnetic confinement experiments. In contrast to other techniques like gas fuelling applied to the plasma edge, pellets may penetrate deep beyond the LCFS and hence deliver the fuel where it is required, which is the plasma core, as discussed earlier. A pellet can generally be described as a portion of solid matter. The cryogenic pellets employed for plasma fuelling usually have a cylindrical shape with some millimetre length and diameter. In the case of W7-X they consist of frozen hydrogen and will be closer described in section 2.2. Beside plasma fuelling, pellets can be employed for plasma stability controlling i.e. pacing of edge localized modes [53]. A short overview of the widely accepted current understanding of pellet injection physics, mainly based on the work of B. Pégourié *"Review: Pellet injection experiments and modelling"* [54], is introduced for the terminology in this thesis.
When a pellet is injected into a plasma, two main phases can be distinguished: the ablation phase and the subsequent deposition or homogenization phase. Even though both phases occur simultaneously to a great extent, they are usually treated separately. Ablation refers to the interaction of the pellet with the background plasma, resulting in the pellet's complete sublimation after a certain time within the plasma. This gradual sublimation produces a cloud of neutral particles that surrounds the pellet. The cloud temporarily shields the pellet from further interaction with the background plasma and hence from further ablation (neutral gas shielding [55]). While the pellet continues travelling in the direction of injection, the cloud is heated further, ionizes, and forms a so-called "plasmoid" that further increases the shielding (plasma shielding [55]). The plasmoid containing of charged particles is stopped by the Lorentz force and detaches from the pellet.

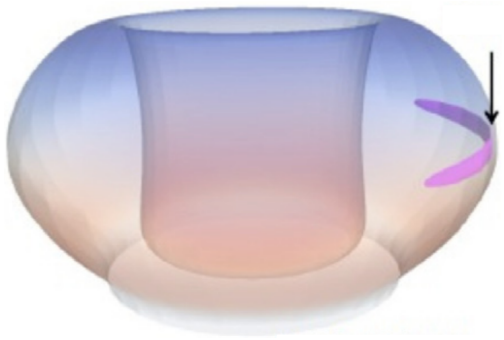

Fig. 1.4.1.: Three dimensional illustration of a plasmoid (indicated by the arrow) in a toroidal plasma experiment (taken from [56]).

A schematic of such a plasmoid in a toroidal plasma is shown in fig. 1.4.1. As soon as the pellet leaves the shielded region it is again exposed to the background plasma particles and starts forming a new cloud, whereas the detached plasmoid starts drifting and distributing its particles within the plasma, which is called deposition, since these processes lead to the deposition of the pellet particles. The plasmoid's electrons and ions spread along the magnetic field lines around the torus. Due to the different masses and temperatures, the expansion velocity along the field lines is at least one order of magnitude larger for electrons than for ions ($v_{\parallel\ \mathrm{ions}} \approx 10^5\,\mathrm{m/s}$), but is limited by the electric fields arising from charge separation. Therefore, the temperature on flux surfaces equilibrates rather quickly while this equilibration occurs slower between flux surfaces. Furthermore, the plasmoid electrons and ions start separating to the top and bottom due to the $\nabla \boldsymbol{B}$-drift arising from the toroidal background plasma's $\boldsymbol{B}$-field gradient. This then leads to an electrical field, which in turn introduces an $\boldsymbol{E} \times \boldsymbol{B}$-drift of the plasmoid as whole in the direction of $-\nabla \boldsymbol{B}$, since the $\boldsymbol{E} \times \boldsymbol{B}$-drift does not depend on the particle charge. This drift is implied by $v_{\boldsymbol{E}\times\boldsymbol{B}}$ in fig. 1.4.2. Note: Unlike in tokamaks, $-\nabla \boldsymbol{B}$ does not always points outwards in radial direction due to the complex magnetic field geometry of stellarators. The drift direction thus depends on the exact toroidal position, and therefore, changes along the toroidal extension of the plasmoid.

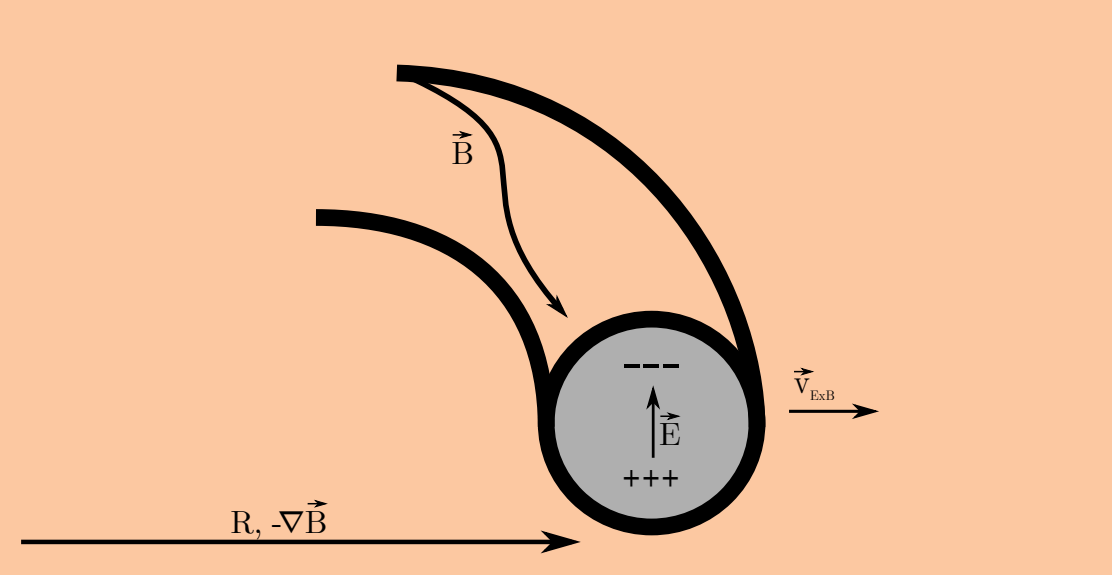

Fig. 1.4.2.: Physical mechanisms underlying the plasmoid $\boldsymbol{E} \times \boldsymbol{B}$-drift. The plasmoid's cross section is displayed in grey surrounded by the background plasma (orange).

Due to its drift, the plasmoid passes several flux surfaces each of which featuring different temperatures and densities. The temperatures on the flux surfaces are

always higher than the temperature of the plasmoid whereas the densities are always lower before the plasmoid arrives. The collisions between the plasmoid particles and the plasma particles lead to a further increase in plasmoid temperature and dilution in density until thermal and density equilibria with the background plasma are reached, which denotes the end of the existence of the plasmoid as such.
By the expansion along field lines and the field line twist, it can happen that, after a finite number of toroidal turns (i.e. one turn for $\iota \approx 1$), the positive and negative regions of the plasmoid reconnect, short-circuiting its charge separation and reducing the value of the internal electric field. This hinders the plasmoid's $\boldsymbol{E} \times \boldsymbol{B}$-drift significantly, if not completely stops it. The same applies if the plasmoid has spread around the torus poloidally.
On much slower but simultaneous timescales, the particle diffusion perpendicular to the flux surfaces occurs. It causes the decay of the local density peak which was introduced at a certain radial position by the ablation and deposition of the pellet material. This equilibration of the density takes between 100 ms and 1 s [30].

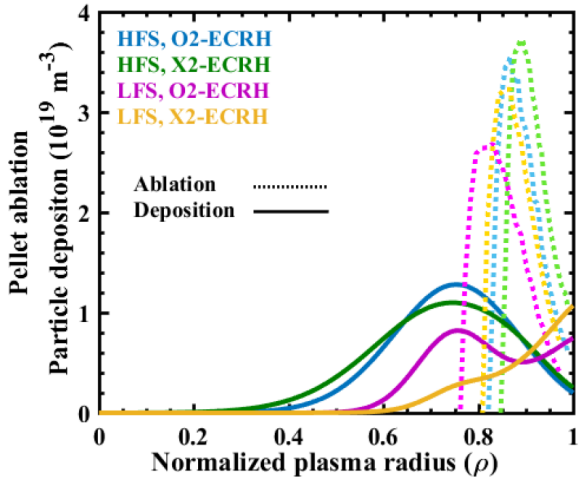

Fig. 1.4.3.: Pellet ablation (dotted) and particle deposition (solid) profiles for HFS (high field side) and LFS (low field side) injections into W7-X calculated with HPI2. In all cases the assumed pellet velocity is 250 m/s, pellet content is 1.9×10^{20} atoms (length = 2 mm, diameter = 1.5 mm), and the magnetic field is in standard configuration (taken from [57]). The starting temperature and density profiles are shown in fig. 1.4.4.

To model the injection of cryogenic pellets into plasma experiments several codes have been developed. One of them is the "HPI2" (Hydrogen Pellet Injection 2) code [1]. It was mainly written by B. Pégourié *et al.* [1] for tokamaks and adapted for the W7-X stellarator by F. Köchl and N. Panadero *et al.* [57]. The code was

developed to simulate the ablation of a cryogenic hydrogen, deuterium, or tritium pellet, or mixtures of thereof. Additionally it is able to calculate the evolution of the resulting pellet cloud and considers all known mechanisms involved in the plasmoid drift. The below mentioned numbers for the specific conditions applicable for W7-X plasmas were obtained employing the HPI2 code.
To obtain the HPI2 ablation and deposition density profiles shown in fig. 1.4.3, typical (artificial) W7-X ion and electron density and temperature profiles (shown in fig. 1.4.4) were fed into the code.
Note: The difference between the ECRH (electron cyclotron resonance heating) X2- and O2-mode will be introduced in section 4.1. The terminology of "high-field" and "low-field" side historically origins from tokamak experiments, where the magnetic field at the inboard side of the torus is higher than at the field at the outboard side. Although this is not the case at all toroidal positions of a stellarator (due to its complex 3D magnetic field geometry, as stated earlier), the terminology was adapted by the community and high-field side (HFS) and low-field side (LFS) are uses synonymous to inboard and outboard side.

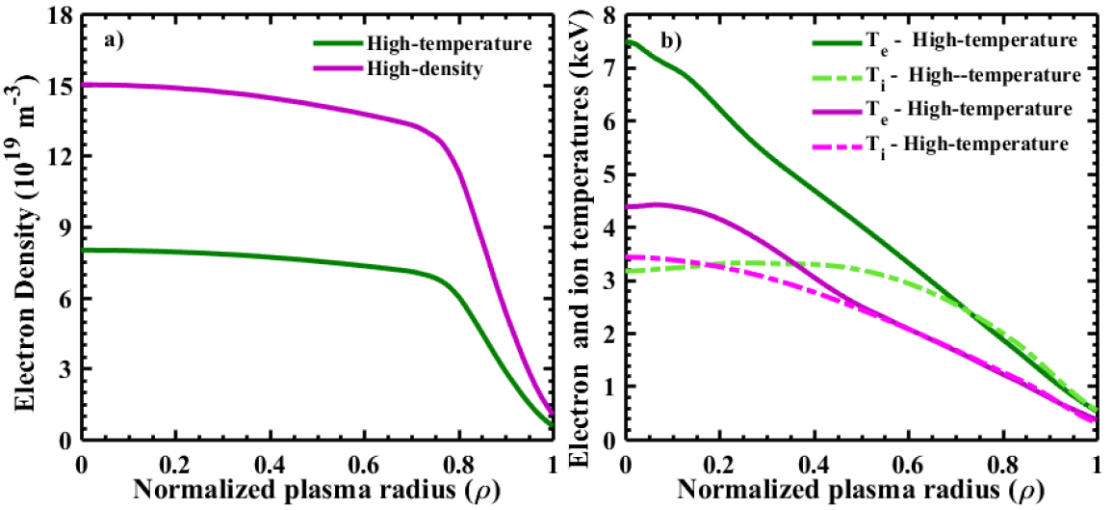

Fig. 1.4.4.: Profiles of a) electron density and b) electron and ion temperature, corresponding to high-temperature (ECRH in X2-mode) and high-density (ECRH in O2-mode) scenarios in W7-X (taken from [57]).

Given the 0.53 m minor plasma radius of W7-X, to which the abscissa in fig. 1.4.3 and 1.4.4 was normalized, the penetration depth of the pellet is roughly 10 cm for all cases while the deposition depth varies. The HFS deposition reaches up to ≈ 30 cm whereas the LFS deposition ends at ≈ 20 cm. For LFS pellets the peak electron density increase in general is lower and parts of the material were pushed out of the plasma which can be explained by the discussed drifts. Why similar drift

effects cannot be observed for the HFS remains unclear, since the radial extension of the cloud should as well result in a drift away from the plasma centre, at least for the fractions of the HFS plasmoid material extending to inboard-side located $-\nabla \boldsymbol{B}$ regions.
The ablation process takes 400 µs, assuming a pellet velocity of 250 m/s (design value of the W7-X pellet injector [58]). The deposition profiles shown were calculated at 0.735 ms after injection. The drift speed of the ablated cloud is calculated to be 1 - 4 km/s, which would result in a maximal 1000 µs drift duration for HFS pellets at the Thomson scattering diagnostic toroidal position of the plasma, assuming the plasmoid would drift through the whole plasma of ≈ 1 m diameter before it reaches the plasma edge. Therefore, the total absolute particle deposition (ablation + drift) must happen within ≤ 1.4 ms even though radial redistribution might continue up to 0.5 s due to particle diffusion [59]. The peak density increase that could be observed by the Thomson scattering diagnostic is expected to be of the order of $10^{19}\,\mathrm{m}^{-3}$ as shown. The fraction of the pellet particle content deposed within the LCFS nears 100 % for the HFS pellets and is expected to be significantly lower for LFS pellets according to the deposition profiles. At the end of its deposition phase, the cloud's radial extension and length parallel to the field lines are 0.4 m and 25 m at maximum, respectively. This means that the calculations performed yield, that the plasmoid would not cover a full W7-X toroidal circumference before it equilibrates with the background plasma [60]. While the subsequent parallel expansion goes with $\mathrm{v}_{\parallel\,\mathrm{ions}}$, the expansion along the poloidal direction of a flux surface is slower by roughly a factor of one over the aspect ratio of the corresponding flux tube,

$$\epsilon_\mathrm{t} = \frac{\text{W7-X major radius}}{\text{flux tube minor radius}}, \tag{1.4.1}$$

in the case of W7-X ($\iota \approx 1$).

2. The Wendelstein 7-X Stellarator and the Diagnostics Relevant for this Thesis

This chapter is starting off with a basic introduction to the plasma experiment, to which this work is applied; the Wendelstein 7-X stellarator. Thereafter, the preceding theoretical considerations on Thomson scattering and pellet injection introduced in the 1st chapter will be completed by the technical descriptions provided for both systems as set up at Wendelstein 7-X. Details important to the developed (pellet) event-trigger system are pointed out, such as the newly implemented fast laser energy monitor and the photo diode which provides the pellet ablation signal employed as an event trigger.

2.1. The Wendelstein 7-X Stellarator

Wendelstein 7-X is a plasma experiment operated by the Max-Planck-Institute for Plasma Physics in Greifswald since 2015. With its 30 m^3 plasma volume, it is (together with LHD [61]) the largest stellarator experiment in the world. It was built *"to demonstrate the suitability of fusion devices of the stellarator type for a power plant"* [62]. The main device parameters are shown in table 2.1.1.

Tab. 2.1.1.: Wendelstein 7-X technical data [62].

Parameter	**Value**
Major plasma radius	5.5 m
Minor plasma radius	0.53 m
Magnetic field	up to 3 T (2.5 T achieved)
Pulse length	up to 30 min (30 s achieved)
Plasma heating	up to 14 MW (6 MW achieved)
Plasma volume	30 m^3
Plasma particle amount	5 - 30 mg
Plasma species	hydrogen, deuterium, helium
Plasma density	up to 3×10^{20} /m^3

During the past campaigns only hydrogen and helium were employed as working gases; however deuterium plasmas are planed for the post-2020 campaigns. The maximum pulse length at present is on the order of 30 s but will be extended after an active cooling system is installed for the plasma facing components that are currently inertially cooled. The magnetic field in W7-X is generated by a set of 50 superconducting non-planar coils. Additional planar coils might be used for field corrections. A schematic from a CAD model (Computer Aided Design) of the Wendelstein 7-X main torus including the outer vessel/ports (grey), the planar coils (orange), and the non-planar coils (green-grey) as well as some parts of the support structure (purple) is shown in fig. 2.1.1. The plasma is implied by the translucent yellow-red torus. In the foreground some parts of the Thomson Scattering diagnostic are displayed (cyan). The subsequent fig. 2.1.2 shows the torus from above. The locations of the diagnostics introduced in this chapter, the pellet injector and the Thomson scattering diagnostic, are indicated.

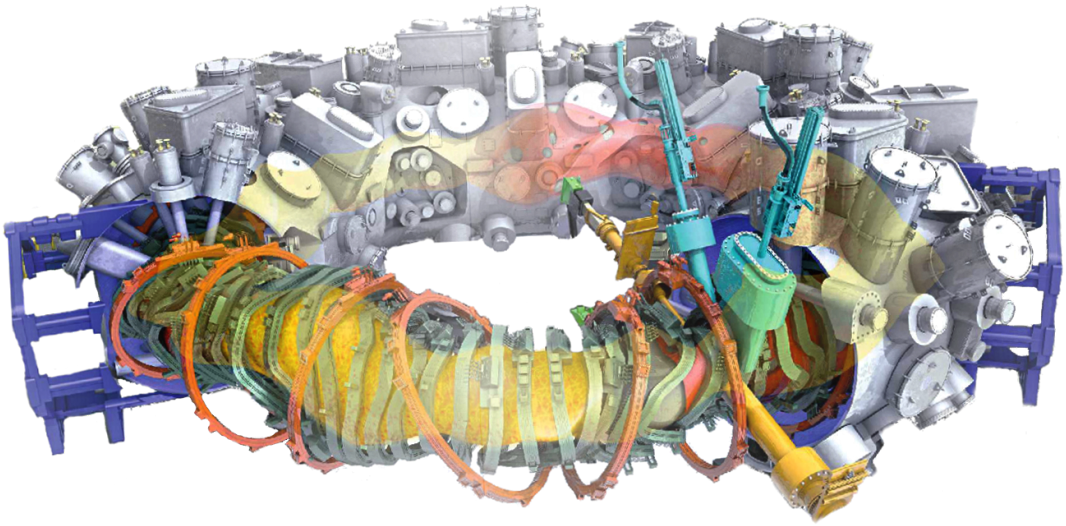

Fig. 2.1.1.: CAD schematic of the W7-X Torus (taken from [63] - modified).

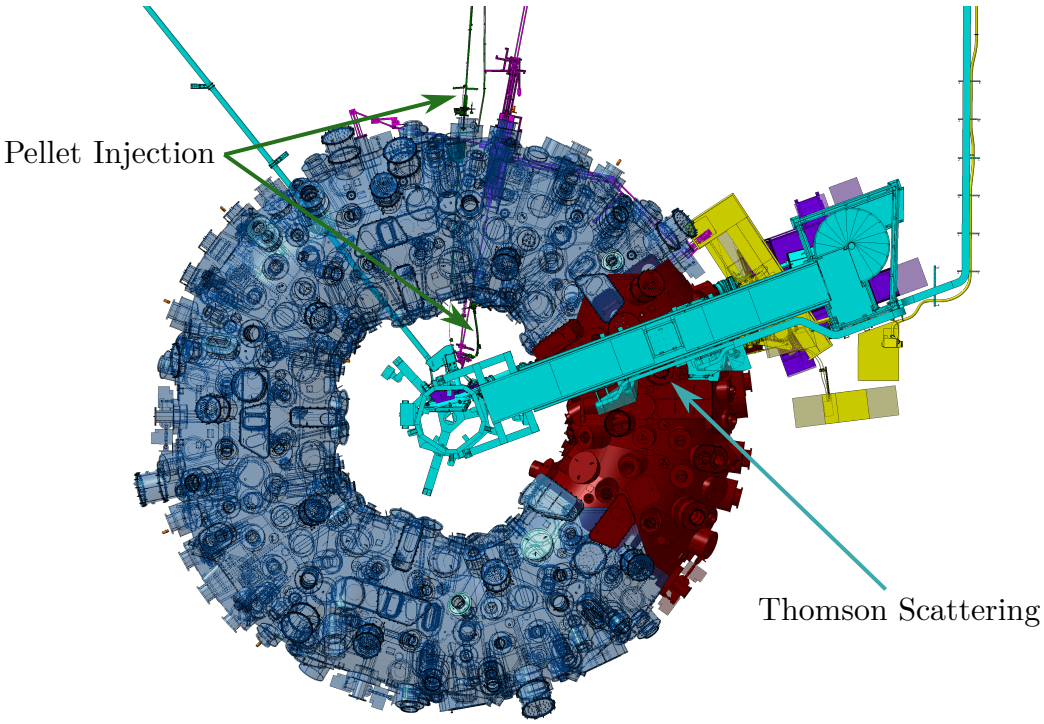

Fig. 2.1.2.: Top view of the CAD Torus. The locations of the pellet injector and the Thomson scattering diagnostic are indicated.

2.2. The Pellet Injector of Wendelstein 7-X

For the pellet injection system at W7-X, the ASDEX Upgrade blower gun has been borrowed and adapted [64]. A schematic of the gun is shown in fig. 2.2.1. It was designed to produce pellets from hydrogen (H_2), deuterium (D_2) or a mixture of both. For the experiments performed at W7-X so far, only hydrogen was used. The cylindrical pellets of 2 mm diameter and 2 mm length are accelerated by pressurized helium as propellant gas. A high velocity is desired to deposit the pellet material deep in the plasma. With the given setup, velocities up to 250 m/s can be achieved. In a test mock-up, repetition rates in the range of 2 - 50 Hz were tested [58]. Above 10 Hz, pellet delivery efficiencies of about 90 % were reached, with the delivery efficiency being defined as the ratio of pellets leaving the launcher to the number of expected pellets.

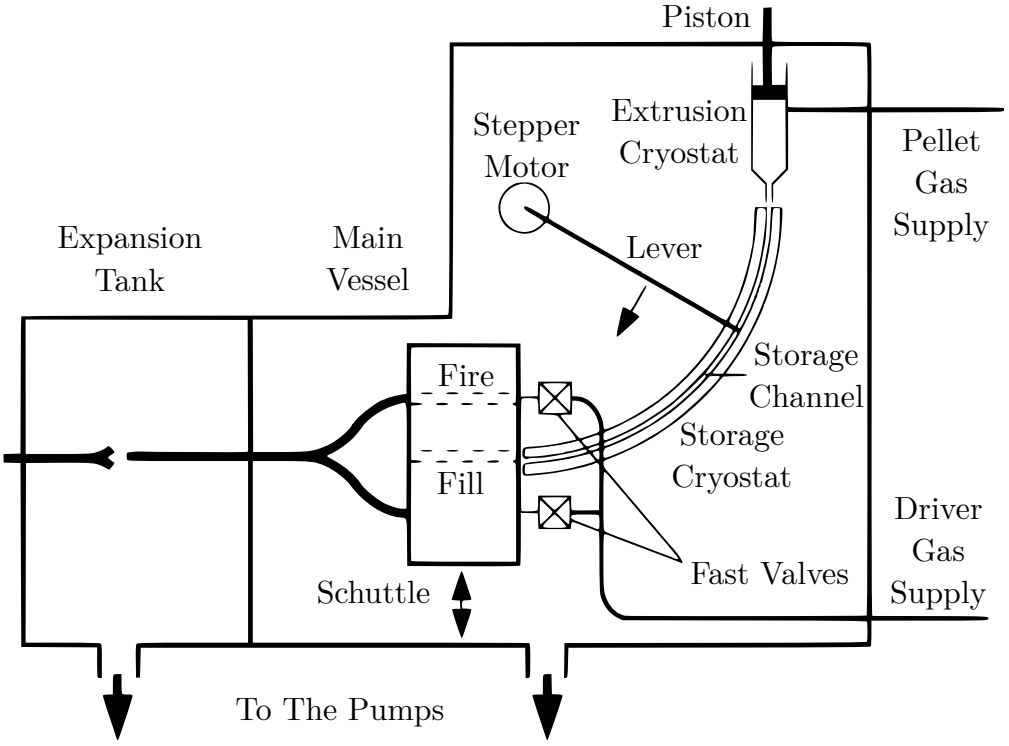

Fig. 2.2.1.: The ASDEX Upgrade blower gun schematic (taken from [64]).

The function of the blower gun can be described as follows: The extrusion cryostat is cooled by liquid helium to a temperature of 4 K. Inside, gaseous hydrogen is

frozen to form a thin layer of solid hydrogen covering the cryostat wall. Next, the cryostat temperature is slightly increased to allow for a pneumatic piston to push scraped-off ice through a nozzle at the bottom of the cryostat. The hereby generated thin rod of compressed hydrogen ice slides into the storage cryostat, where it can be kept for about 10 minutes at 10 K. The length of the storage channel limits the extension of the ice rod generated in one run and hence the number of pellets available. Less than 62 pellets can be generated from a rod of 124 mm maximal length, taking losses at both ends into account. The lever comes into play when the stored ice is to be injected into the experiment. It then cuts the rod below the extrusion cryostat and pushes it towards the shuttle, which has two holes to fit the tip of the ice rod as implied by the dashed lines in fig. 2.2.1. The shuttle slides up and down defining the later injection frequency, cutting the ice into pieces. Alternately one pellet is fired from the filled hole while filling the other hole with the next pellet. To fire a pellet, the fast helium valve opens releasing a short pulse of propellant gas.
Unlike in pneumatic guns, the pellet gains momentum not mainly from the propellant but rather from the evaporation of its own material by contact with the warmer helium. Consequently some of the initial pellet mass is lost during the acceleration process. A back-illuminated photograph, as shown in fig. 2.2.2, taken at the exit of the blower gun captures the size of the pellet (roughly 2 mm length and 1.5 mm diameter) after the generation and acceleration procedure:

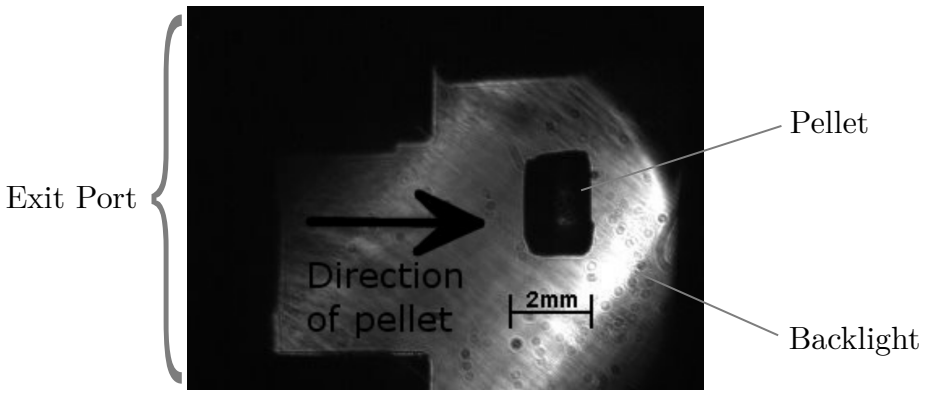

Fig. 2.2.2.: Pellet leaving the blower gun (image taken from [58] - modified).

The overall setup is illustrated by fig. 2.2.3. For W7-X the blower gun injector is meant to inject pellets from both the high- and low-field side. This operation is different to ASDEX Upgrade, where the pellet injector was only employed for low-field side injection. In the case of high-field side injection the pellet needs to circumvent the torus. This results in a more complex geometry for the high-field

side injection tube including several bends with radii of about 1 m and a much longer distance to cover compared to the short straight low-field side tube. Both tubes are made of stainless steel with the inner surface being electro polished to minimize the surface roughness. The wall thickness is 1 mm and the inner diameter 8 mm. Because the tube is not actively cooled, the larger diameter compared to the pellet size allows the pellet to benefit from the Leidenfrost effect [65] and slip through the tube with negligible friction, thus avoiding strong erosion. A detailed analysis of the different factors affecting the erosion was performed [58], coming to the result that the impact of the chosen tube geometry plays only a minor role at the given pellet speed of $\leq 250\,\mathrm{m/s}$. Microwave diagnostics delivered by the Oak Ridge National Laboratory have been implemented, highlighted by the red circles in fig. 2.2.3. They consist of a microwave cavity which changes its resonance frequency if a dielectric pellet passes trough. The amplitude of the cavity response relates to the pellet mass whereas the width is determined by the pellet velocity [66].

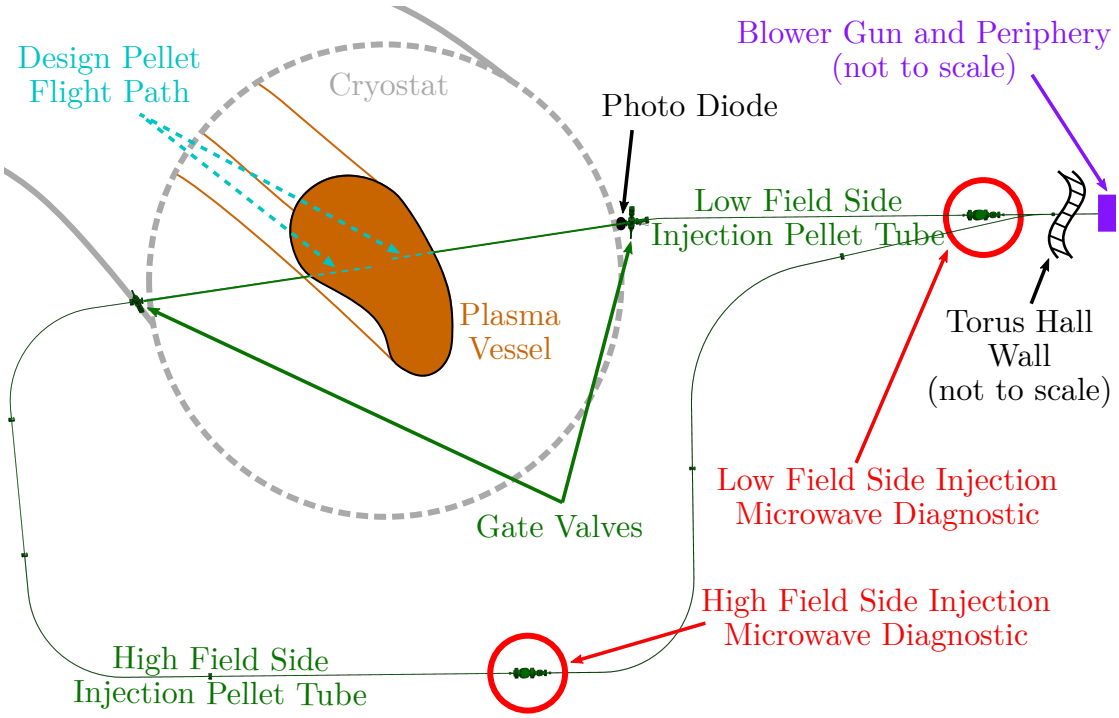

Fig. 2.2.3.: The W7-X pellet injection system including poloidal cross sections of the cryostat and the plasma vessel, schematic.

The figure shows the location of the PIN photo diode "9741-1" from the manufacturer "LOT" which detects the H_α radiation of both HFS and LFS pellets and provides a trigger signal when the pellet enters the plasma. The gate valves

depicted above can be shut to select one side for pellet injection only.

Given the fact that erosion does not greatly depend on the tube geometry at the utilized pellet velocities, it is possible to estimate the erosion as a function of guiding tube length. In the best case a pellet contains 3.30×10^{20} protons (0.55 mg) at the exit of the blower gun, 2.55×10^{20} protons after 8.3 m guiding tube (LFS microwave diagnostic) and 1.84×10^{20} protons after 16.7 m (HFS microwave diagnostic).

A fit to these numbers provides the function:

$$\frac{N_{\text{protons}}}{10^{20}} = 3.496 \times 10^{-4} l^2 - 9.326 \times 10^{-2} l + 3.3, \tag{2.2.1}$$

where l is the distance along the guiding tube in meters.

Applying this to the total tube length of 15 m for the LFS and 29 m for the LFS, the pellet proton number decreases to:

$$\begin{aligned} N_{\text{LFS}} &\lesssim 2.0 \times 10^{20}, \\ N_{\text{HFS}} &\lesssim 0.9 \times 10^{20}, \end{aligned} \tag{2.2.2}$$

as a very rough estimate holding for the best cases only, i.e. assuming that perfect pellets leave the blower gun and that they are not broken into pieces during their travel in the guiding tube.

Assuming $\approx 22\,\text{m}^3$ of the $30\,\text{m}^3$ W7-X plasma volume is filled with uniform density (in reality the density distribution shows a gradient towards the edge), one would expect a maximum density increase of:

$$\begin{aligned} \Delta N_{\text{LFS}} &= 7.0 \times 10^{18}\,\text{m}^3 \text{ per pellet}, \\ \Delta N_{\text{HFS}} &= 3.6 \times 10^{18}\,\text{m}^3 \text{ per pellet}. \end{aligned} \tag{2.2.3}$$

This approximation will be taken as references for the analysis performed later.

2.3. The Thomson Scattering System of Wendelstein 7-X

The Thomson Scattering Diagnostic of W7-X, as schematically displayed in fig. 2.3.1, is optimized to measure electron temperatures between 20 eV and 10 keV and electron densities from $2 \times 10^{18}\,\mathrm{m}^{-3}$ up to $5 \times 10^{20}\,\mathrm{m}^{-3}$ [52]. It currently employs three Nd:YAG high power lasers "SplitLight2500" from the manufacturer "InnoLas Laser GmbH" which are located in a room outside the radiation shielding of the WX-7 "torus hall". The wavelength of the linearly polarized laser light (perpendicular to the scattering plane) is $\lambda = 1064\,\mathrm{nm}$ and the repetition frequency of each laser is 10 Hz. The typical pulse duration is 10 ns, and the energy per pulse ranges between 0.6 J and 2.50 J. Pulses of the individual lasers can be triggered either with delays to provide higher total repetition frequencies or simultaneously to increase the pulse energy.
Most of the main components of the experiment are placed in the torus hall. During operation the torus hall needs to stay closed and access is restricted due to radiation safety. Therefore, all components in the torus hall need to be operated remotely.

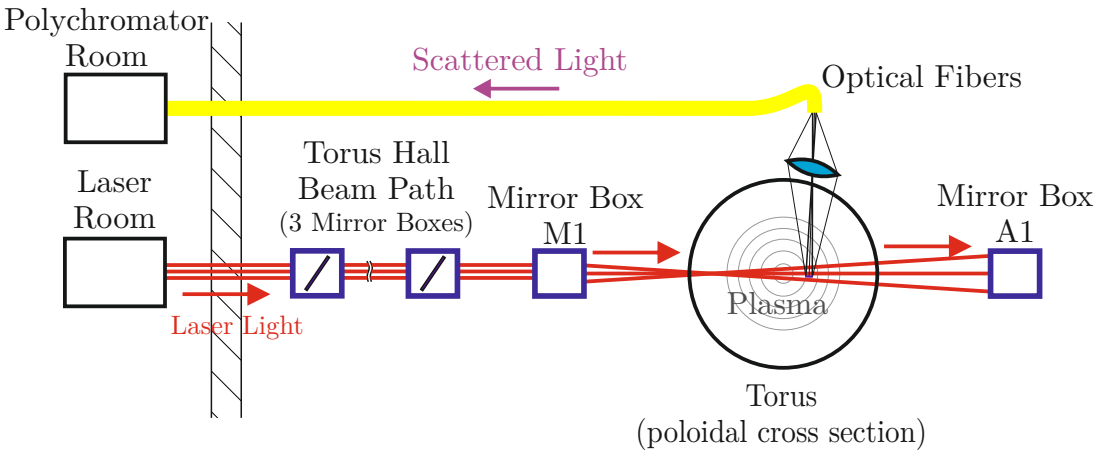

Fig. 2.3.1.: Schematic setup of the W7-X Thomson scattering diagnostic.

In the figure, the torus hall shielding wall is implied by the striped area in between the double dash. In the mirror boxes the optical components, like mirrors and lenses, of the system are mount.
From the laser room containing the three lasers and the control periphery, the laser beams are guided into the torus hall. The set of mirrors used for this purpose

consists of several different high-reflection, high-power sustaining dielectric layers deposited on quartz substrates. For the current campaign large rectangular mirrors were ordered to fit multiple beams but were not delivered in time nor with sufficient quality. Therefore only the round two-inch diameter mirrors from the preceding campaign were available, fitting one of the three beams only.
After leaving mirror box M1 the laser light enters the torus trough a window mounted at the Brewster angle relative to the laser beam polarisation to avoid reflection of the laser light at the surface of the window. In the plasma vessel the light gets scattered by the plasma electrons before it leaves the torus at the opposite side and is dumped outside the vacuum vessel in mirror box A1.
All components of the Thomson scattering diagnostic including the mirror boxes, are mounted either to optical tables directly connected to the ground or to a special structure called the "Thomson bridge". Thus the whole system is mechanically decoupled from the vacuum and cryostat vessels, ensuring optical stability.

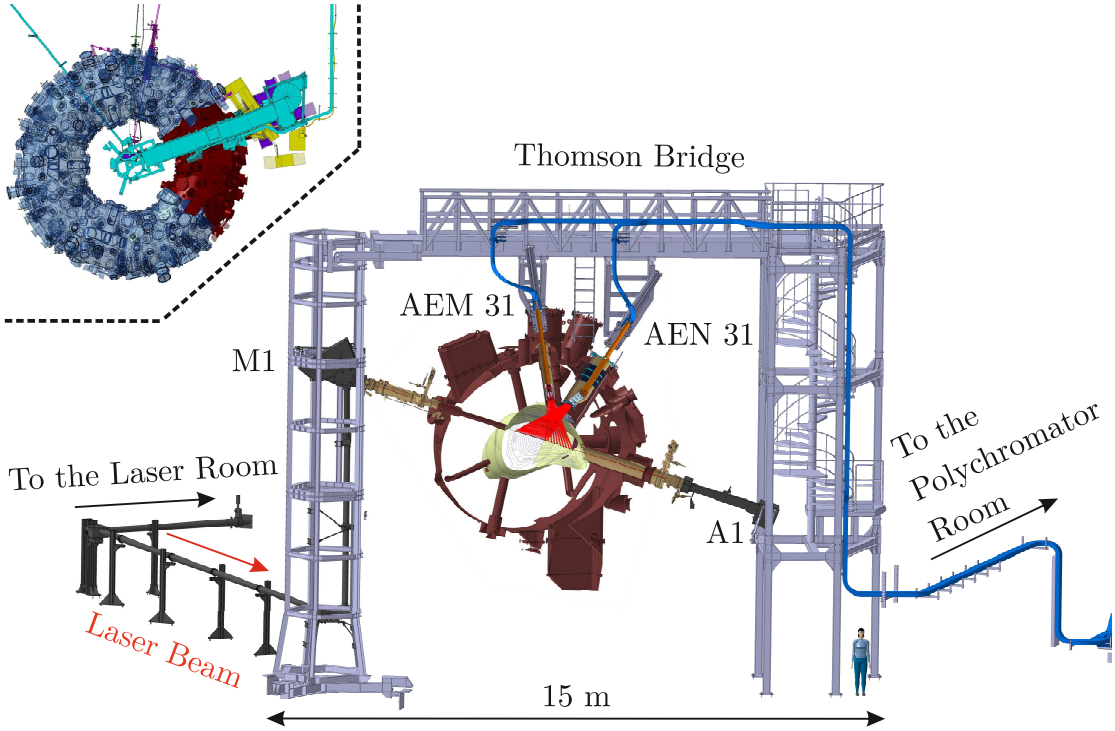

Fig. 2.3.2.: CAD model of the W7-X Thomson scattering diagnostic (poloidal cut at the angle $\phi_{\mathrm{tor}} = 27.2°$ where the Thomson scattering takes place). The torus (upper left corner) shows the segment in which the Thomson scattering diagnostic is situated (red) from above.

In fig. 2.3.2 a CAD model of the real setup is shown. The scattered light is collected into optical fibers with the optics in the AEM 31 and the AEN 31 port. Each fiber bundle observes a specific scattering volume. (The scattering volumes available during the the current campaign cover the outer half of the plasma, employing the AEM 31 optics only.) They are illustrated by the blue boxes overlying the magnetic flux surfaces of the "Standard Configuration", cut at the toroidal location of the Thomson Scattering diagnostic ($\phi_{\mathrm{tor}} = 27.2°$), as shown in fig. 2.3.3.

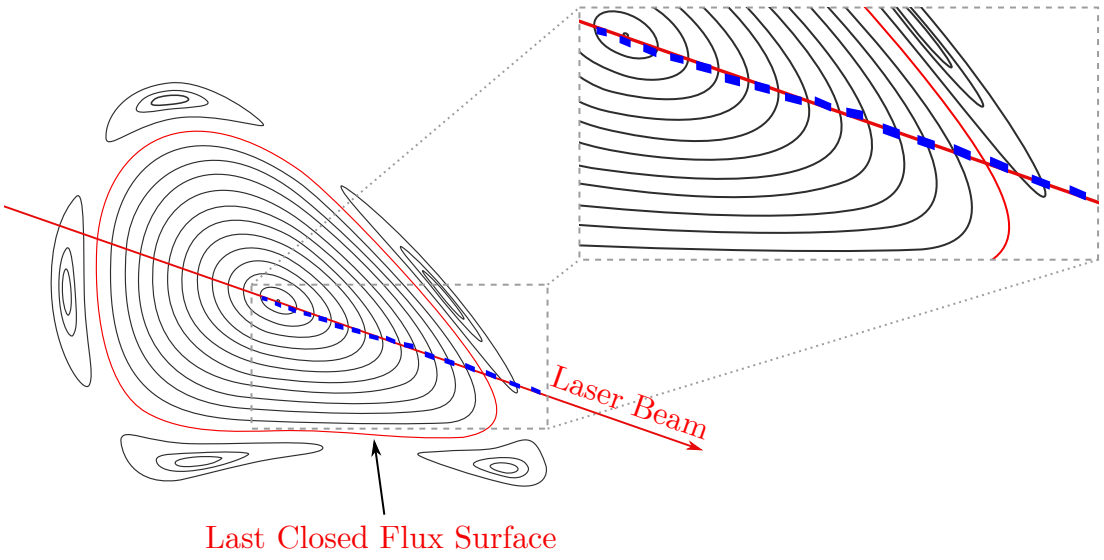

Fig. 2.3.3.: Poloidal cross sections of the magnetic flux surfaces and magnetic islands of the W7-X Standard Configuration cut at $\phi_{\mathrm{tor}} = 27.2°$. The blue boxes illustrate the location of the 16 available scattering volumes in OP1.2a.

The positions of the scattering volumes were surveyed in the real setup and integrated in the CAD model. The slight deviations from the laser path do only result in minor changes of the measured temperatures and densities since the offset is almost parallel to the magnetic flux surfaces on which the aforementioned quantities remain constant. The spacial resolution, defined as the distance between the centres of the scattering volumes (optically projected to the laser line), ranges from 3 cm in the core to 8 cm at the edge in real space coordinates. The toroidal angle of $\phi_{\mathrm{tor}} = 27.2°$ was chosen for the Thomson scattering diagnostic because it relates to a region of large flux surface expansion, where higher spacial resolution can be archived. (Note: The shape of the flux surface cross section toroidally varies from bean-like (high flux surface compression) to triangular (high flux surface expansion)

in the W7-X stellarator magnetic field.)
The scattered light is transferred to the polychromator room outside the torus hall by fibers, where polychromators split the spectrum of the light into five wavelength ranges (750 - 920 nm, 920 - 1000 nm, 1000 - 1035 nm, 1035 - 1051 nm, and 1051 - 1061 nm) [47]. The light detection is performed with temperature-stabilized avalanche photodiodes of the type "Excelitas c30956eh". The setup of a W7-X polychromator is shown in fig. 2.3.4.

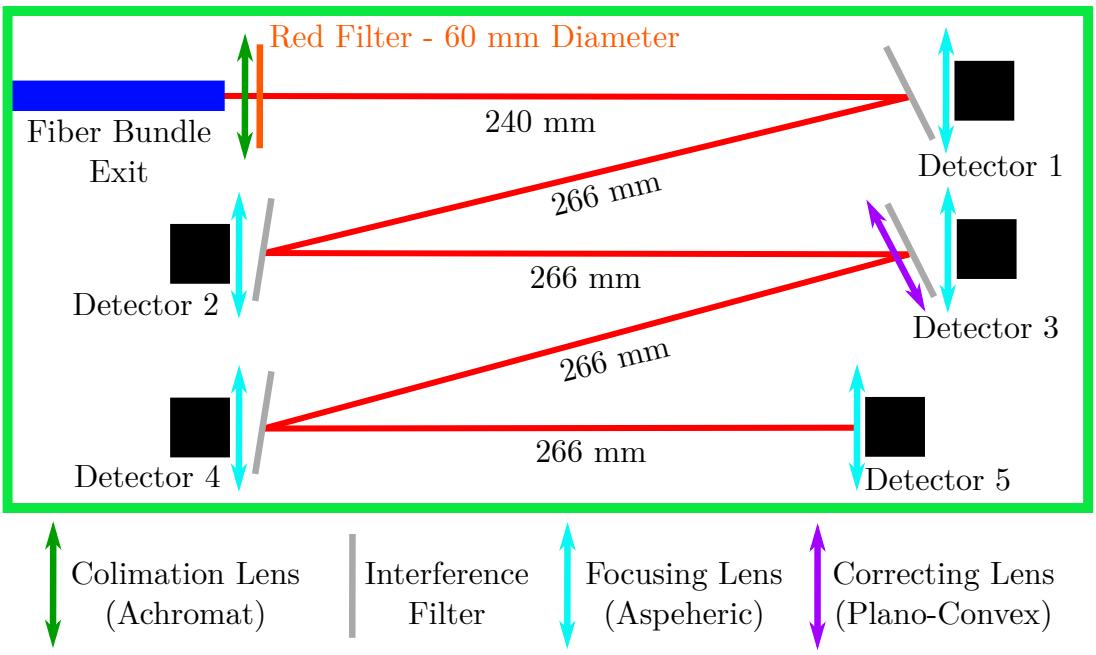

Fig. 2.3.4.: Schematic setup of the W7-X Thomson scattering polychromators.

Two fiber bundles of different length (57 m and 77 m) each, representing two different scattering volumes, are merged to the same polychromator. The additional 20 m fiber introduces a delay to separate the two signals from the two different scattering volumes in time such that the signal from these individual volumes can be analysed by one polychromator. This reduces the number and hence the costs for the polychromators by a factor of two. Nevertheless it results in a (tolerable) increase in the noise level arising from the integration of background plasma emission of two volumes, rather than only one.
Stray light to the polychromators is reduced by dumping the laser beam three meters beyond the last scattering volume and perpendicular to the vessels output port. Additionally, the spectral filters in the polychromators provide a suppression of the laser wavelength by six orders of magnitude.

The avalanche diodes behind the spectral filters (Detector 1-5) output an electrical signal which is amplified and digitized, removing the constant background via an AC filter. The ADC (analogue digital converter) "SP Devices ADQ-14" used provides 14 bit resolution with a sampling rate of 1 GSample/s.
Later, the time-resolved digital scattering signals are used to reconstruct both the electron density and temperature. For the reconstruction, the process explained in section 1.3 is applied.
In fig. 2.3.5 the A1 mirror box of the Thomson scattering system is shown. It is the last mirror box of the system which lies beyond the plasma. In this box the laser beam is not only dumped but also monitored with respect to its alignment position and pulse energy.

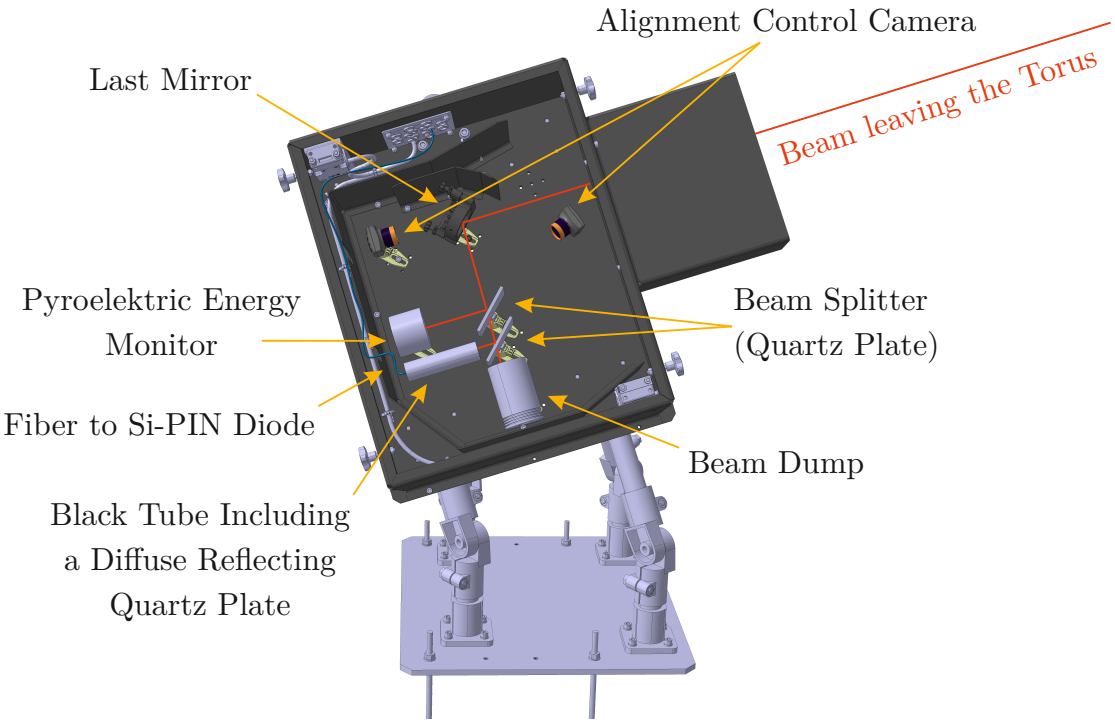

Fig. 2.3.5.: Setup of the A1 mirror box including the beam dump, the two different energy monitors, the last mirror, and two cameras installed later for beam alignment control.

For the purpose of energy monitoring fractions of the laser light are separated from the beam employing quartz plates as beam splitters right before the beam dump. The fractions irradiate a ceramic-coated pyro-electric energy sensor "PEM45K-USB" (short PEM) from "Sensor- und Lasertechnik" and, via optical fiber, a 18 V biased

Si-PIN diode of type "PDSIU500FC1D-W-0" from "PL-LD Inc.". The resulting diode voltage can be employed as energy monitor signal too.
The PEM of 4.5 cm diameter is absolutely calibrated and larger than the laser beam diameter (2.5 cm), thus small variations of the beam position do not affect the measurement. At the same time the large sensor limits the repetition frequency to $\approx 10\,\mathrm{Hz}$ due to the necessary thermal equilibrium that needs to be reached for the whole sensor surface ahead of the subsequent measurement. In contrast to this the PIN diode is very small (active area of $500\,\mu\mathrm{m}^2$) which allows for readout frequencies up to $\approx 600\,\mathrm{MHz}$ as stated by the manufacturer, but makes it sensitive to small variations of the beam position. Additionally the diode signal needs to be calibrated relative to another monitor.
To reduce stray light to the energy monitoring PIN diode, the fiber is located at the end of a black tube. In the centre of the tube, a diffuse reflecting quartz disc is situated to even out intensity fluctuations introduced by the mode structure of the laser beam and interference patterns from the beam splitters. These fluctuations would result in large errors by small variations of the beam position. The diffuse quartz disc enhances the robustness of the "diode-energy-monitor" against errors arising from beam position variations.

3. The Event-Triggered Burst-Mode: Development & Implementation

The subsequent chapter describes the main technical developments achieved in the course of this thesis. It focuses on the development of the event-triggered burst-mode Thomson scattering system, itself, including the following major steps:

- conceptual design, assembly, and commissioning of the event-trigger and a dedicated trigger logic circuit,
- burst mode operation and characterization of the Thomson scattering laser system with respect to operational safety and reproducibility in the real diagnostic setup,
- calibration of the data obtained from the upgraded diagnostic.

Difficulties in this process and the resulting solutions are presented as well as diagnostic data validating the success of the implemented approach. For this purpose several other diagnostics' data, i.e. other density and temperature diagnostics as well as pellet video data, are compared to the Thomson scattering data. Additionally, the abilities of the original Thomson scattering diagnostic are opposed by the upgraded diagnostic's abilities employing experimental data.

3.1. The H_α Pellet Event Trigger

As described in section 1.4, the pellet ablation and deposition processes mainly happen on 1 ms timescales and below. During test operation of the W7-X pellet injection system, the timing of pellets entering the plasma suffers from a large jitter (≈ 30 ms with respect to the blower gun trigger). In combination with the comparably low repetition frequency of both, the pellet injection system and the Thomson scattering diagnostic, it is very unlikely that a Thomson measurement is taken synchronously with a pellet ablation by chance. This is discussed in section 3.4.2, analysing the non-event triggered W7-X shot 20171123.037. Reproducing such a measurement "by chance" several times for a systematic study is obviously impossible. One of the main objectives for this thesis was therefore, to set up a reliable pellet trigger scheme for the Thomson scattering diagnostic.
Originally designed for this purpose was the W7-X "Trigger, Timing and Event System" (TTE-System). It was set up to synchronously trigger all the different processes and diagnostics involved in W7-X, to generate the timestamps for taken data and to receive and distribute triggers to other connected systems within 5 ns accuracy. It would thus be possible to trigger Thomson scattering (and any other diagnostic) to selected events of any kind.
It was planned to distribute the pellet trigger via the TTE system, but the features of sending and receiving event triggers via this system was unexpectedly delayed. Therefore, a customized solution had to be developed. At first, light-gates were taken into account to predict the pellets injection time several milliseconds ahead. This approach failed because, for some unknown reason, the available light-gates were not able to detect the pellets. A different option was the photo diode (see fig. 2.2.3) monitoring H_α light radiated by the pellet material during its ionization process. With this trigger being generated right at the start of the event of interest and with the lasers requiring 150 - 200 µs to build-up population inversion in the Nd:YAG rods (cf. section 1.2.1), it was of high importance to send the trigger the fastest way possible to the lasers considering the pellet process would mainly take place within 1 ms after the H_α radiation started.
To avoid issues with transients induced to a loop, it is not allowed to run a long cable straight from the torus hall to external devices like the Thomson lasers permanently. Therefore, the electrical signal from the photo diode, after appropriate amplification, was converted to an optical signal employing the a fiber optic link ("HEAG171 R" from "Baumer GmbH"). It was sent via an institute-internal fiber network to the Thomson laser room. A connection between the pellet injections switchboard in the torus hall and the one located in the laser room needed to be spliced for this propose. In the Thomson scattering diagnostic laser room, a fiber optic link receiver ("HEAG174" from "Baumer GmbH") converted the signal back to an

electrical signal.
After the successful setup of the transmission path for the trigger, an investigation on the total transit time of the H_α signal was carried out (the results can be found in appendix A). In order to do so, a reference signal was transmitted via a copper cable to the location of the photo diode and back via the optical transmission line. Additionally, the signal was passed trough a logic circuit. The circuit's function and necessity is explained in section 3.2. The delay between the pellets H_α emission start and the signal arriving at the lasers was determined to be $\approx 7.5\,\mu s$ which is neglectable compared to the time the lasers need to reach a sufficient population inversion (150 - 200 µs). The setup therefore should be suitable synchronizing the Thomson measurements to the pellet injection.

3.2. The Trigger Logic Circuit

Pellets are usually injected with frequencies above the 5 Hz repetition frequency of the lasers. Therefore not all pellet triggers can be used to trigger the laser system. Additionally indispensable for any pellet to be measured would be to deviate from the uniform repetition of the lasers to compensate for the jitter in the pellet timings. In principle it is possible to actuate the "External Trigger" interface of the SplitLight2500 lasers for this purpose. This interface has been designed to provide the lasers with an external trigger equivalent to the one provided by the laser's software, e.g. if the lasers were integrated in an autonomous triggering scheme.
Similar to the case of a "burst mode" operation (cf. section 1.2.3), it has been assumed that the thermal conditions in the laser rod should not deviate noticeably if the uniform repetition rate is changed to a non-uniform one, keeping the overall frequency constant. Nevertheless, this has never been performed with the W7-X Thomson diagnostics nor the SplitLight2500 lasers. Therefore, studies where needed to validate the initial assumption and analyse the resulting effects on all included components carefully. This analysis is found in section 3.3. The development of a sufficient trigger system would be needed beforehand and therefore was not implemented by the laser manufacturer, nor commercially available.

The trigger system needed to meet several requirements:

1. provide the uniform standard trigger if no pellet occurs,
2. block external triggers if they occur too close to the regular triggers,
3. accept an external trigger if it occurs in a predefined time slot ("acceptance interval") and block the next regular trigger to maintain the average frequency,
4. block the second and all further external triggers if more than one occurs in the allowed times lot,
5. cover all possible combinations of the former cases.

A visualisation of this set of demands can be found in appendix B.

These requirements were considered developing the logic circuit shown in fig. 3.2.1.

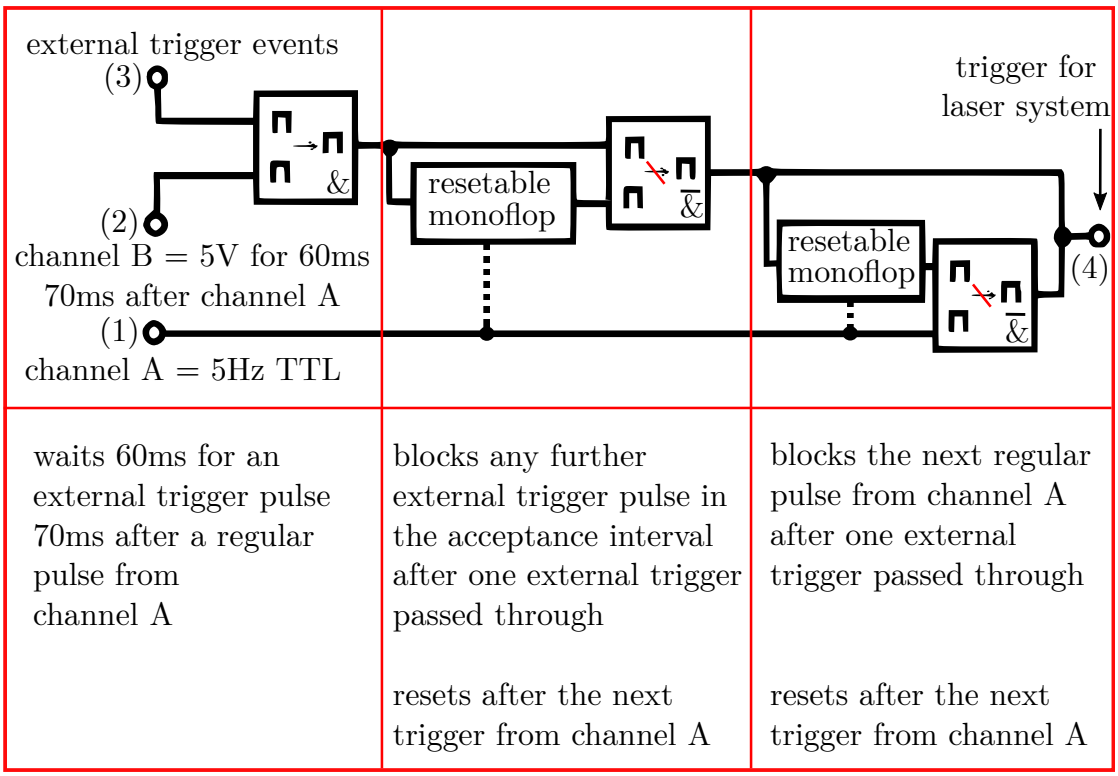

Fig. 3.2.1.: W7-X event trigger logic circuit schematic. The numbers (1)-(4) relate to the signals shown in fig. 3.2.2. Dotted connections are employed to reset the monoflops. The ⊓ in the logic and- (&) and nand- ($\bar{\&}$) chips indicates a logical high state at the input or output. TTL is a standard called "Transistor-Transistor-Logic" which is characterized by 5 V pulse amplitude and 1 ms pulse duration.

The technical circuit, including logic chips and part numbers, can be found in the burst mode manual in the appendix F. It was soldered and later implemented to the event-triggered burst-mode Thomson scattering system. Before the implementation, its functionality was confirmed by extensive laboratory tests. In the subsequent oscilloscope images, results of a validation of the developed circuit are shown. The upper curve (1) represents the 5 Hz "TTL" signal (Transistor-Transistor-Logic) of channel A. The second curve (2) represents channel B which relates to the interval in which triggers are accepted. The third curve (3) is equal to the external trigger events, and the lower curve (4) is the output of the circuit and therefore the trigger for the laser system. The channel A and channel B signals were generated by

"Quantum Plus Pulse Generators Model 9514" from "Schulz Electronic". In fig. 3.2.2 (a) external triggers (3) falling in the acceptance interval are output to (4) and the subsequent regular trigger (1) is bocked. Fig. 3.2.2 (b) shows the case of multiple external triggers (3) falling into the acceptance interval (2). Only the first of them is conducted to the output (4); further external triggers in one acceptance interval as well as the regular triggers (1) are blocked.

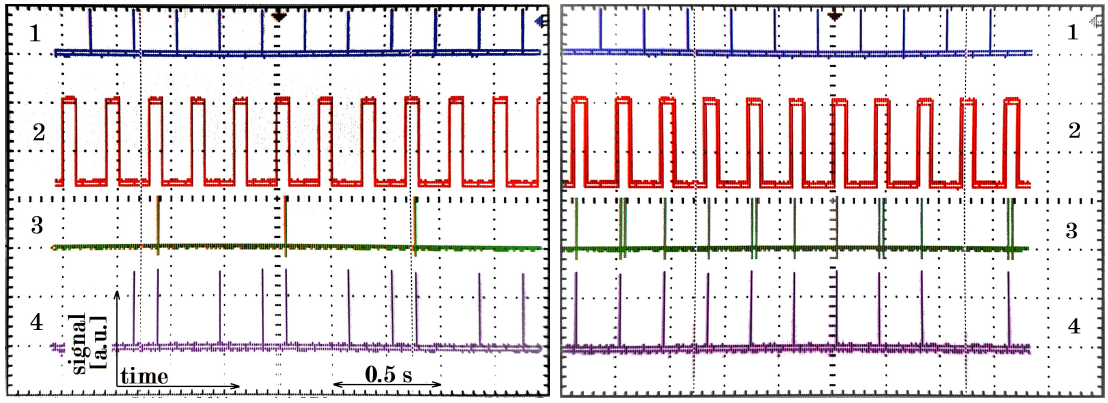

(a) (b)

Fig. 3.2.2.: (a) Regular trigger (1) being blocked in the output (4) after an external trigger (3) occurred in the interval during which external triggers are accepted (2).
(b) Second external trigger (3) in the same acceptance interval (2) being blocked in the output (4). The regular trigger (1) is blocked too.

The developed trigger logic satisfies all requirements from the above list. It is able to trigger the W7-X Thomson scattering system to the unpredictably occurring pellet events, maintaining the average repetition frequency of 5 Hz. To prepare for any kind of further amendment, to safe the acquisition cost for the pulse generators and to achieve greater flexibility in general, it is suggested to replace the circuit with an FPGA (Field Programmable Gate Array) in the future. FPGAs are used to emulate logic circuits and contain an internal clock such that the pulse generators will be obsolete. Moreover they can store multiple logic circuit setups and can be accessed via network. Hardware soldering will be avoided and switching between the normal-mode W7-X Thomson scattering and the event-triggered burst mode will only need a remote user input. This input can be done from the W7-X control room. Therefore, rewiring the whole laser system as described in the burst-mode manual (cf. appendix F) will be unnecessary. For the proof-of-principle provided in this thesis, a hard-wired physical circuit was deemed appropriate.

3.3. The SplitLight2500 Lasers in Burst Mode Operation

As introduced in section 1.2.2 the SplitLight2500 lasers are able to emit bursts of laser pulses which can be interlaced, as demonstrated in fig. 3.3.1:

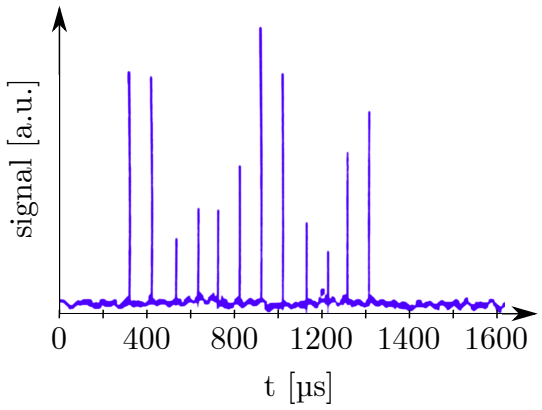

Fig. 3.3.1.: Burst containing 12 pulses of equal distance (100 µs) emitted from three interlaced SplitLight2500 lasers detected by an ordinary photo diode. By this measurement is has been proved, that combining the three diagnostics lasers a burst of 12 equidistant laser pulses with 100 µs spacing can be achieved. The oscilloscope was operated in the peak detection mode where the pulse height does not scale to the energy per pulse to be able to detect the very short pulses on this comparable large timescale.

Nevertheless this feature is rather experimental and not as stable as the regular 10 Hz standard mode; therefore the most important parameters from a diagnostics perspective have been analysed in the laboratory before applying the burst mode to the diagnostic itself.

The aforementioned parameters are:

1. The beam profile - most important for the mirrors which could be destroyed by pockets of high energy density.
2. The beam pointing stability - if the laser were put under mechanical stress, likely to be introduced by varying thermal loads, the beam could be emitted at an unusual angle. Over the long distances of the Thomson diagnostics

beam path this could lead to clipping of the beam at mirror edges and/or other structures as well as the laser beam might miss the scattering volumes at all.

3. The self emission - can be understood as "leakage" of the laser, emitting light even when it was not intended. This should be avoided to not run into troubles with the data acquisition system and to have the full laser energy available for the intended pulses.

4. The energy per pulse - the intensity of the scattered light, and therefore the measured density, scales with the energy of the laser pulses and should be kept constant.

5. The laser induced damage threshold - the laser pulse energy per area irradiated in a certain time interval must remain below this threshold in order to avoid harming the diagnostic's mirrors , the focussing lenses or optical components of the laser, itself.

3.3.1. Beam Profile

In the normal mode, the spatial beam profile shape is "flat", characterized by the ratio of maximum to mean intensity being ≤ 1.1. The profile for different delays between the flash lamp triggers has been analysed for the burst mode. In a separate analysis the double Pockels cell pulse delay range was accessed and found to provide sufficient laser emission between 100 µs and 250 µs. To achieve maximum laser power and sustain the desired 100 µs temporal spacing, the Pockels cell triggers were set at 150 µs and 250 µs and only the flash lamp delay was varied subsequently. If the beam profiles were well-shaped, then both delays were considered appropriate. For a first rough estimate, the laser pulses' burn patterns on photo paper were analysed:

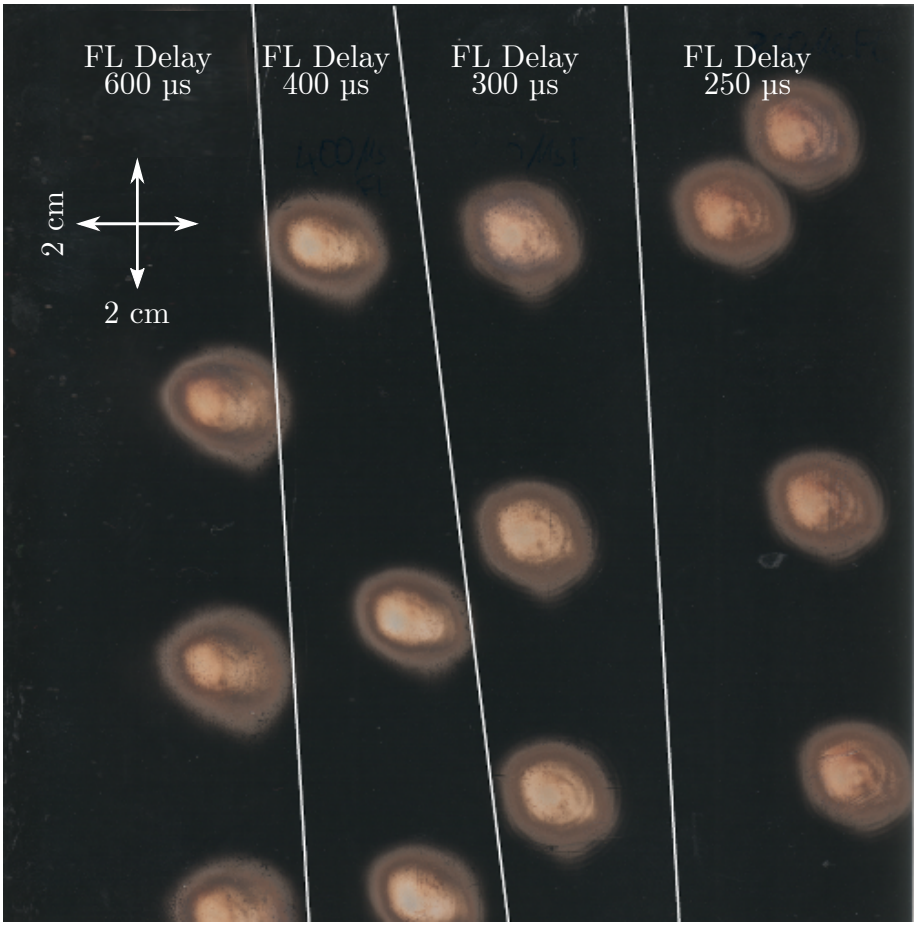

Fig. 3.3.2.: Burn patterns of a SplitLight2500 laser. Brighter colours relate to higher intensities - darker colours to lower intensities. The double flash lamp mode and the double Pockels cell mode were employed simultaneously. Patterns with flash lamp delays of 600 µs, 400 µs, 300 µs, and 250 µs are shown (from left to right, separated by the white lines). The Pockels cell triggers were kept constant at 150 µs and 250 µs. Note: Each spot was produced by the four pulses of one burst.

None of the delays led to a visible hot spot or a misshapen beam profile as seen in fig. 3.3.2. The beam profile shape therefore does not seem to be a limiting factor the burst-mode operation of the diagnostic. This was verified by testing the chosen delays with mirrors used in the real diagnostic.

3.3.2. Beam Pointing Stability

The beam pointing stability denoting the fluctuation of the emittance angle provided by the manufacturer of the SplitLight2500 is designed to be less than ±50 µrad. In the lab, only 15 m beam paths were available without using additional mirrors. The maximum fluctuation should therefore stay below ±0.7 mm at the end of this distance, which was assured to hold for the burst mode too.
In the real diagnostic setup, the beam path is about 40 m such that the beam centre at the beam dump should not deviate more than ±2 mm from its adjusted position. This deviation is considered in the design of the diagnostic and would not perturb the measurements. Nevertheless, it was found later, that the deviation due to thermal drifts independent from the burst-mode operation was much larger and significantly disturbed the measurement (cf. 3.4.1). However, the beam pointing stability of the lasers in burst mode should not be an issue for the reliability of the diagnostic because this drift is not further increased by burst-mode operation.

3.3.3. Self Emission

During the tests it was found that the lower threshold for the flash lamp delay was not the duration of the flash, itself (200 µs), as stated by the manufacturer. For flash lamp delays below 325 µs, several pulses with low energy were emitted spontaneously without intention. It was assumed, that the excitation of the Nd^{3+}-electrons had not sufficiently decayed, since the lifetime of the exited state is 430 µs (cf. section 1.2.1). Whether or not this assumption is true and why the Q-switch opened unintentionally is currently under investigation by the laser manufacturer. For the time being, the appropriate operation of the diagnostic is ensured by keeping the flash lamp delay ≥ 350 µs.

3.3.4. Energy per Pulse

With the oscilloscopes available in the laboratory (Tektronix “TDS 200-Series Digital Real-Time Oscilloscope 071-0492-03”), it was not possible to trigger to the second, third, or fourth pulse in a burst. Therefore, the pulse height (and thus pulse energy) detected by the photo diode could not be investigated with high temporal resolution for each individual pulse. They rather had to be displayed all together on the oscilloscope screen, as shown in fig. 3.3.3.

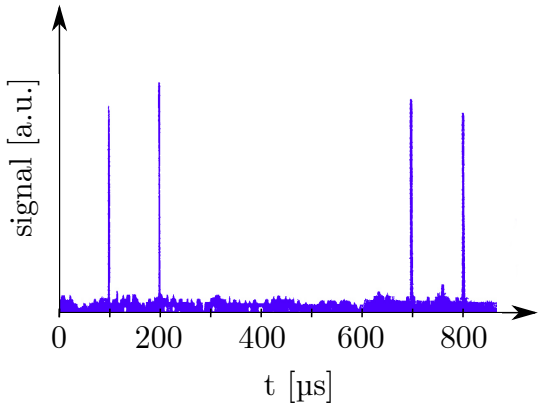

Fig. 3.3.3.: Pulse energy of the four burst pulses averaged over 128 samples.

As the chosen time interval analysed by the oscilloscope is lengthened, the temporal resolution is decreased. For the interval necessary to capture the four burst pulses from one laser, the sampling rate is no longer sufficient to digitize the structure of the for individual pulses of 10 ns duration. Therefore, only sharp peaks could be displayed. The pulse height of the displayed peaks relates to any arbitrary signal amplitude from the temporal evolution of the diode signal which is usually not the maximum value that would scale to the pulse energy.
For a first rough estimate, assuming the deviation between consecutive bursts to be small, the oscilloscope signal was internally averaged over 128 measurements. From this averaging one could compensate somewhat for the low sampling rates. The 128 measurements taken would now be statistically distributed, discretising different instants of time of the temporal evolution of the individual laser pulse diode signals. For these averaged pulses the Pockels cell was adjusted such that the pulses appeared to have a similar height and, therefore, intensity. The result is shown in fig. 3.3.3. This procedure was not the optimal way to fine-tune the energy per pulse, but sufficient for providing an approximation for later optimization.
Anyway, the energy pumped with one flash lamp pulse remains constant even in burst mode. Thus the energy per pulse (subdivided by two Pockels cell pulses) will always be less than that of a single Pockels cell laser pulse. This results in the fact that the components that withstand the normal mode would not be harmed by the burst mode with respect to the energy per pulse.
The energy fluctuation per pulse was reviewed in the real setup, employing the analogue to digital convertor (ADC) “SP Devices ADQ-14” that writes the digitized signal to storage from which the data can be post-processed. This allowed the individual pulses to be distinguished from one another and to be analysed with 1 GS/s sampling rate. This analysis is part of section 3.4.1. The finally chosen burst contains four consecutive laser pulses with ≈ 1 J energy per pulse compared

to the $\approx 1.5\,\mathrm{J}$ energy per pulse of normal mode operation.

3.3.5. Laser Induced Damage Threshold

After analysing the previous parameters defining the general limits of the burst-mode operation and determining that the burst mode should not damage the laser, now the mirrors used in the diagnostic setup were tested. They were originally specified to withstand $10\,\mathrm{J/cm}$ for the normal $10\,\mathrm{Hz}$ mode [67]. Although the energy and the profile of individual pulses of the burst mode are very unlikely to have a different impact on the mirrors, as deduced from the former analysis, the altered timing might have an influence. Indeed, for dielectric layers, a parameter called "laser induced damage threshold" (LIDT) exists. It does not only accounts for the incident energy per unit area, but also for the time interval during which the energy is radiated, much like the physics quantity "power". In the case of dielectric layers, it is the power that can be transmitted via collisions from the electrons to the lattice or the ions of the substrate material. If the incident power exceeds this threshold, the electrons escape and a plasma starts to form. This plasma then better absorbs the incident radiation, causing damage. This process scales with the repetition frequency of the laser. Increasing the frequency from $10\,\mathrm{Hz}$ to $\approx 10\,\mathrm{kHz}$ might therefore be a serious threat to the mirrors. Given the complex physics behind the LIDT, its inspection is rather simple. If the mirror withstands the laser for a geometry similar to the real conditions, the LIDT was not reached. This experiment was conducted and the mirrors were not damaged.

Consequently the burst mode could be implemented in the existing W7-X Thomson scattering diagnostic with no risk for the safe operation of the system.

3.4. Calibration of the Burst-Mode Data

3.4.1. Laser Pulse Energy Normalisation

As mentioned in section 3.3.4 already, the Thomson scattering signal is proportional to the laser energy (cf. equation 1.3.6), which must always be accounted for in post-processing. Unfortunately, it was not possible to find the laser settings for which the burst mode provides perfectly equal energy per pulse due to the limitations of the oscilloscope available in the laboratory. Therefore, the energy of each laser pulse was planned to be monitored during operation. Employing the energy measurements, one could then apply a normalisation factor to the data to adjust to the actual laser energy rather than set it equal for all burst pulses. For the purpose of this monitoring, a fast PIN diode monitoring has been carried out, resulting in the setup described in section 2.3 and shown in fig. 2.3.5.
A typical laser pulse detected with the PIN diode is shown in fig. 3.4.1.

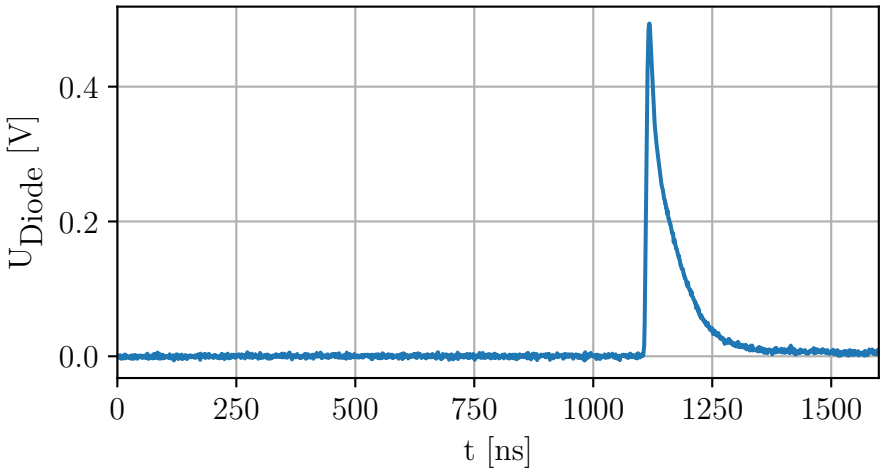

Fig. 3.4.1.: PIN diode signal of a SplitLight2500 laser pulse.

The pulse height and the integral of the signal were compared to the pyroelectric energy monitor signal to determine if one or both provide a reliable monitor for the laser energy. A base-line subtraction was applied to the diode signal beforehand. A resulting measurement taken during W7-X shot 20171109.042 can be found in fig. 3.4.2.

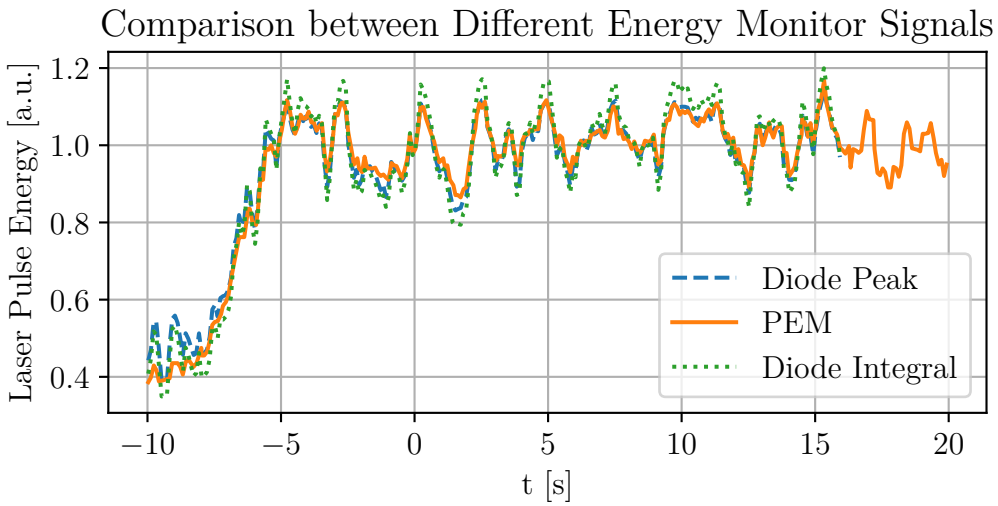

Fig. 3.4.2.: Energy signals from the PEM and the PIN diode, normalised to the respective median values.

From −10 s to −5 s the energy ramp-up of the lasers can be identified. The PEM signal extends some seconds compared to the diode signals because the data acquisition of the diode stops when the plasma discharge ends, whereas the PEM uses an independent data acquisition system. The end of the PEM signal therefore denotes the end of the laser emission. Additionally, a large fluctuation of the mean laser energy after the ramp-up is visible on all monitor signals, although the energy scatter according to the manufacturer is less than 1 %. This is discussed in appendix D.
The three monitor signals agree well, although the integral signal seems to have a somewhat larger deviation from the PEM than the peak signal. Additionally, the integral signal is more sensitive to stray light reflected at various surfaces in the last mirror box (stretching the diode signals' horizontal extension) than the peak signal which indicates the maximal signal measured by the diode at a fixed time point. Accordingly, the signal's peak-height was selected to become the fast energy monitoring signal.
The signals' peak-height linearity in the range provided by the ADCs was measured in the laboratory. The ADCs' range is −1 V to +1 V and an offset can be defined. For the diode no offset was implemented; this reduced the available resolution by 1/2 to 0 - 1 V because the diode signal is always positive. Based on the 14 bits that are usually available, the remaining 8192 discretization levels should still be sufficient. The desired diode output range is 0.5 - 1 V since the energy ramp-up is only of minor interest and the important pulse energy measurements for the data normalisation are taken after it.
Light of different laser energies was analysed with the diode output voltage within

that range, analysing the linearity between laser energy and output voltage. The result of this study is shown in fig. 3.4.3. The measurement simulated real conditions. Therefore a part of the laser light was extracted by a quartz plate and smoothed with a diffuse reflecting quartz disc like in the real setup, which explains the comparably low energy values in the graph.

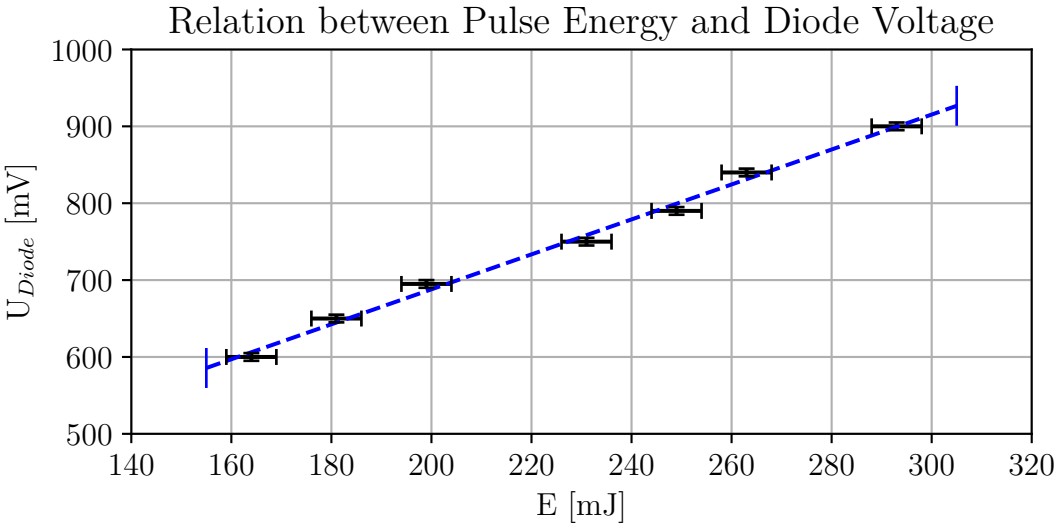

Fig. 3.4.3.: Peak voltage of the PIN diode employed as fast laser monitor.

As desired, the scaling between energy and peak voltage is linear within the uncertainties for the analysed interval. The energy uncertainty was derived from the accuracy of the employed "Scientech" laboratory energy monitor "PHDX50". Since the physics of the scattering process is the same for the burst mode and only the laser energy changes (the density scales linearly with the laser energy), it is now possible to apply a normalisation factor to the burst-mode Thomson data at each timestamp using the fast energy monitor signal. To determine the absolute laser energy from the relative diode peak signal, a comparison to the PEM signal is made.

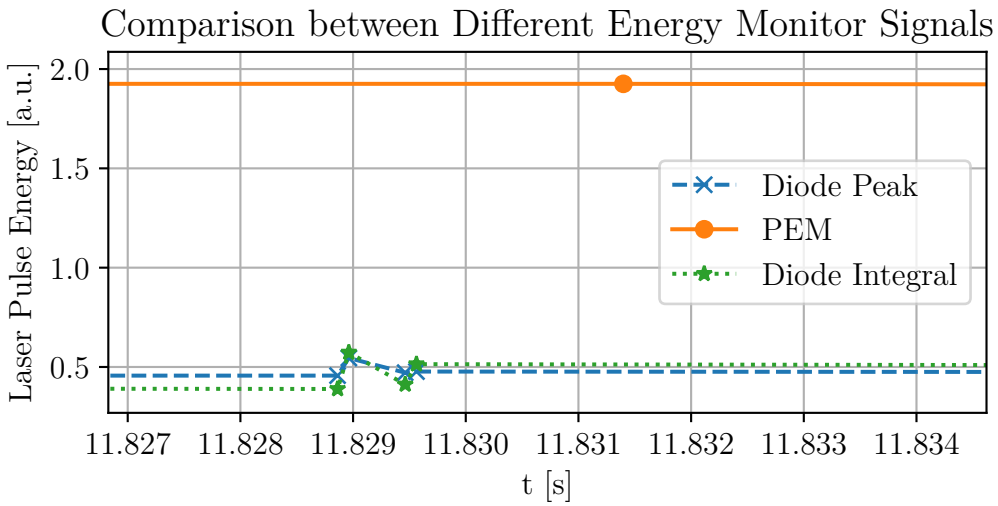

Fig. 3.4.4.: PEM and diode signals for burst-mode operation. The slow PEM integrates over the four burst pulses which are recognized as individual points by the diode. The timestamp of the data point is generated at the end of the integration process which is why the PEM measurement seems to be delayed but it is not.

Since the PEM measurement is integrated over several milliseconds, it is not able to recognize the four burst pulses individually. It therefore sees a sum of the four pulse energies which is consequently about four times higher. Additionally, the plot shows a small energy deviation of the second Pockels cell pulses of each flash lamp cycle (diode points no. 2 and 4). While diode points 1 and 3 (the first Pockels cell pulses of each flash lamp cycle) have the same energy, pulse 2 and 4 deviate from the desired value hence the parameters could not be sufficiently adjusted as explained. From the relative proportions of the four pulses and knowing the absolute energy of the sum of the pulses from the PEM measurement, it is now possible to gain the absolute energy for each pulse. This results in the aforementioned normalisation factor.
To cross-check the reliability of the procedure, the Raman calibration, introduced in section 1.3, was executed during burst-mode operation. After applying the energy normalisation, the Raman signals of the individual burst pulses (1-4) were compared. Given the fix and uniform densities featuring the Raman calibration, the energy normalised Raman scattering signal should be equal for all individual burst pulses. Although the drawn conclusions are quite important in the further course of this thesis, the whole process is rather technical. Therefore, the detailed steps undertaken can be found in appendix C.
The most important finding was, that the energy normalisation introduced a large

signal fluctuation. Without the normalisation, the Raman signals scatter was of the range of the uncertainty of the scattering process itself. Only the mean value of the Raman signals from the individual 1st, 2nd, 3rd, and 4th pulse in the bursts were shifted according to their slightly different energy arising from the insufficient energy balance.
An investigation of the laser beam path in the Thomson scattering mirror boxes yielded a truncation of the laser beam both before the entrance and after the exit of the plasma vessel. As main source of this truncation a thermal drift of the laser beam and its resulting clipping at the edges of optical and mechanical components was identified. It could be greatly reduced by a beam control camera and alignment system installed for this purpose subsequently, and an air conditioner in the laser room, both of which is discussed in appendix D.
These interventions helped to ensure a sufficient fraction of the laser power reached the scattering volumes to perform Thomson scattering measurements. However, the truncation of the beam could never be fully remedied and always varied sightly due to the thermal drift and mechanical vibrations. Thus, the total incident power remains unknown. Under these conditions, an independent calibration of the Thomson scattering density data was impossible.
Therefore, a line-integral of the Thomson scattering density will be adjusted to the line-integrated interferometry density signal for the whole campaign, i.e. for burst- and normal-mode Thomson scattering. This adjustment method is explained in the next chapter.
A general overview of the W7-X interferometer and its functionality is given in *"A New Dispersion Interferometer for the Stellarator Wendelstein 7-X"* by J. Knauer *et. al.* [68].

3.4.2. Thomson Scattering Profile Integration and Calibration to the Interferometer Density

To cross-calibrate the Thomson scattering data to the interferometer density, it was necessary to map the line-of-sight (LOS) from one diagnostic to the other or, as in our case, to transform both in coordinates of "effective radii". An effective radius is defined via the magnetic flux surfaces introduced in section 1.1.2. The flux surfaces can not only be identified by their label number (0 - magnetic axis to 1 - LCFS) but also by their radii. With the coordinate system transformation used by the applied mapping code "VMEC2000" [69] the flux surfaces become cylindrically symmetric, defining the effective radii as follows:

$$r_{\text{eff}} = \sqrt{\frac{A}{\pi}}, \tag{3.4.1}$$

where A is the cross-sectional area of a constant magnetic flux torus. With the assumption that $v_{\parallel} \gg v_{\perp}$, introduced in section 1.1.2, particles move fast along field lines, and therefore density and temperature should equilibrate quick on a flux surface and the corresponding effective radius. Therefore, the electron density from the Thomson scattering and interferometry diagnostics can be compared in the VMEC coordinate system at equal effective radii. The magnetic configuration applied for the mapping is called "EJM" or "Standard Configuration" and is denoted by the VMEC ID "w7x_ref_1". It features the following machine and plasma parameters:

- main coil currents [A]: 15000, 15000, 15000, 15000, 15000, 0, 0,
- net toroidal plasma current [A]: 0,
- magnetic axis field [T]: 2.72,
- toroidal plasma β [%]: 0,
- minor radius [m]: 0.54,
- major radius [m]: 5.51,
- volume inside the LCFS [m^3]: 31.56.

In the real setup and when it comes to pellet injection events, some constrains must be applied to the above mentioned assumptions.

1. As described in section 1.4, the density on a flux surface is far from constant during the pellet ablation and deposition phase.

2. The toroidal plasma β is zero only for the vacuum case. As soon as a plasma is present, the plasma β is a positive number, increasing with for example the plasma density, which likewise increases significantly during pellet injection.
3. Currently, the W7-X Thomson scattering diagnostic only provides data for the outer half of the plasma cross section. To compare these "half profiles" to the interferometry data, mirror-symmetrical "full profiles" are assumed.

Fortunately, the LOS of the Thomson scattering diagnostic and the interferometer are close to each other (<10 cm beam-to-beam distance). Therefore, the poloidal penetration position of the flux surfaces is similar for both diagnostics, keeping the error arising from no. 1 small.
The error introduced by the non-zero plasma β in no. 2 is small as well. The outward shift of the flux surfaces for non-zero β values is the strongest in the centre, where β reaches the highest values due to the high plasma pressure arising from high plasma temperature and density. Additionally, the central tori, corresponding to low r_{eff}, are of small volumes and therefore both the enclosed density and the error from its shift are small.
No. 3 cannot be avoided. Density peaks on the inboard side will not be seen by the Thomson diagnostic but will by the interferometer; peaks on the outboard side will be mirrored in full profiles and subsequently taken into account twice. In combination with the interferometer calibration, this will lead to an artificial up-shift of the density half-profiles for HFS injection and an underestimation of the density half-profiles for LFS injection. This is discussed in section 3.5 & chapter 4.
After mapping both diagnostic LOSs, the Thomson half-profiles were mirrored to produce artificial full profiles and interpolated employing robust univariate splines. The r_{eff} of scattering volumes outside the LCFS were approximated by the shortest point-to-point distance along the r_{eff}-direction because the strict definition of r_{eff} employed by VMEC does not hold outside the LCFS. Next, the fit was line-integrated along the direction of r_{eff} to gain a quantity comparable to the line-integrated measurement of the interferometer. For the purpose of the integration, the interferometer two lines-of-sight (incident and reflected beam) were discretised by 102, equidistant points between vessel entrance and exit in real coordinates. To take into account that they do not pass trough the plasma centre, the r_{eff} interval missed was excluded from the Thomson scattering profile line-integral for each individual beam (the incident and reflected beam cross the vessel at slightly different heights). From the line-integrated density thus obtained and the interferometer line-integrated density, a factor was calculated to be applied to the Thomson profiles for each timestamp in a dataset. As mentioned before, this procedure has several limitations and it was assumed, that the profile shape was unaffected by the truncation of the laser beam.

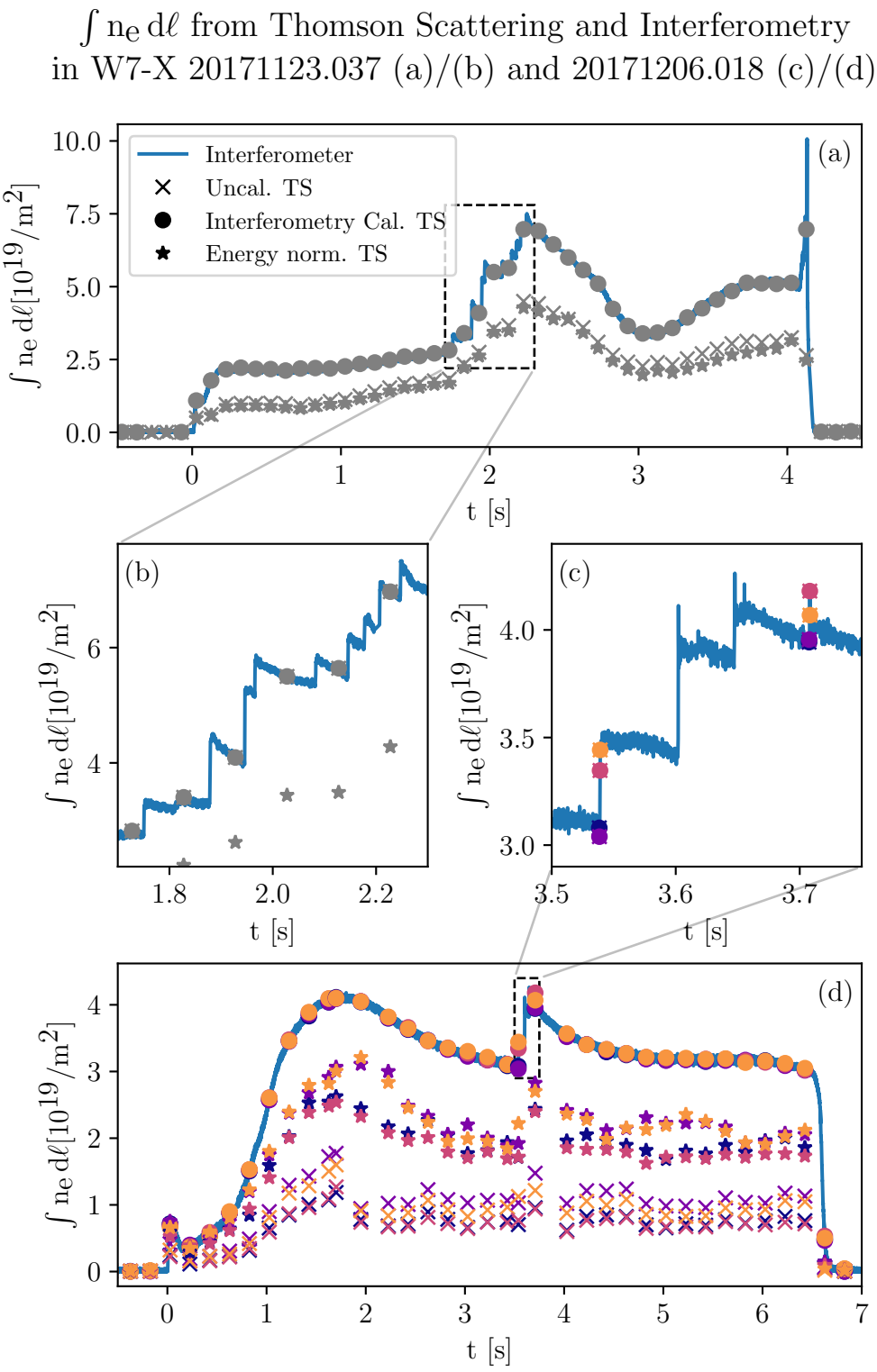

Fig. 3.4.5.: Comparison of the different normalisations/calibrations of the Thomson scattering (TS) data for burst and normal mode. The four pulses of the bursts are indicated in the order of appearance by the colours blue-purple-rose-orange.

To validate this procedure, the temporal evolution of the uncalibrated Thomson line integrals were plotted together with the energy-normalised and interferometry-normalised integrals as well as the interferometry signal itself, as shown in fig. 3.4.5. Visible for both the normal and the burst mode, the uncalibrated Thomson scattering line-integral density does not match the interferometry density before the calibration but fits well after the interferometer calibration procedure.
The interferometry signal employed for the described calibration must be precisely temporally aligned to the Thomson measurement; otherwise, the four burst pulses will not match the density steps introduced by the ablation of the pellet material, and the whole calibration would be inaccurate. Whereas a few milliseconds would not play a role for the usually "slowly" changing line-integrated density, the pellets introduce a very quick (sub-millisecond) and rather massive density change. Out of the set of signals provided by the interferometry group, the "analogue signal" was the only one with the necessary time precision, as is discussed in the next section. It was originally planned as a backup to the regularly standard signal, which in contrast to the analogue signal already includes a "fringe-jump correction" (further discussed in [68]). Unfortunately this standard density signal suffers from a several millisecond jitter arising from its transmission via Ethernet and could therefore not be utilised for the calibration of the Thomson density data obtained during pellet injection. The fringe-jumps therefore needed to be corrected by hand for all burst shots before being able to use the analogue signal instead.
In the normal, non-event triggered operation of the Thomson diagnostic shown in fig. 3.4.5 (a) and (b), for the W7-X shot 20171123.037, pellets are always missed by the non-even-triggered normal-mode Thomson measurements, and no transient profile effects on the sub-millisecond timescale introduced by pellets could be observed. In contrast, from fig. 3.4.5 (c), it is shown, how well the timing of the Thomson measurement was aligned to the pellet injection timing for event-triggered burst-mode operation. A more detailed discussion follows in the next section.
One more observation can be made from fig. 3.4.5 (d): the relative densities for burst pulse 2 and 4 (purple & orange stars - the second Pockels cell pulse each) deviate from 1 and 3 (blue & rose stars - first Pockels cell pulses) even for relatively flat line-integrated densities such as those between 5 - 6 s; this is why only the first and third pulses from a burst will be shown in the following sections. This deviation needs further careful investigation before it can be understood. For instance, the deviation did not appear during the Raman measurements where all four pulses in one burst exhibited similar energy progression (cf. fig. C.0.6) even though their absolute energies were different, which could be corrected by a energy normalisation, if the laser was not truncated.

3.5. Verification of the Event-Triggered Burst Mode's Ability to Detect Pellet Effects

For the new diagnostic to measure the effects introduced to the plasma by a pellet, it needs to satisfy the spatio-temporal boundaries given by this event as well as provide a sufficient radial and density/temperature resolution.
As discussed in section 1.4, the HPI2 code predicts that the ablation and deposition will happen within 1 ms after the injection of the pellet. Additionally some profile redistribution might happen subsequently. Therefore, the 12 planned pulses were distributed evenly spaced with 100 µs clearance to cover a 1.2 ms interval as explained in section 1.2.2. With the loss of 2 out of 3 lasers, the 4 pulses left were situated at 150 µs, 250 µs, 750 µs and 850 µs including the delay arising from the trigger and laser system. This would still allow most of the pellet event to be covered, i.e. as a proof of principle, if the 4 pulses matched the pellet timing.

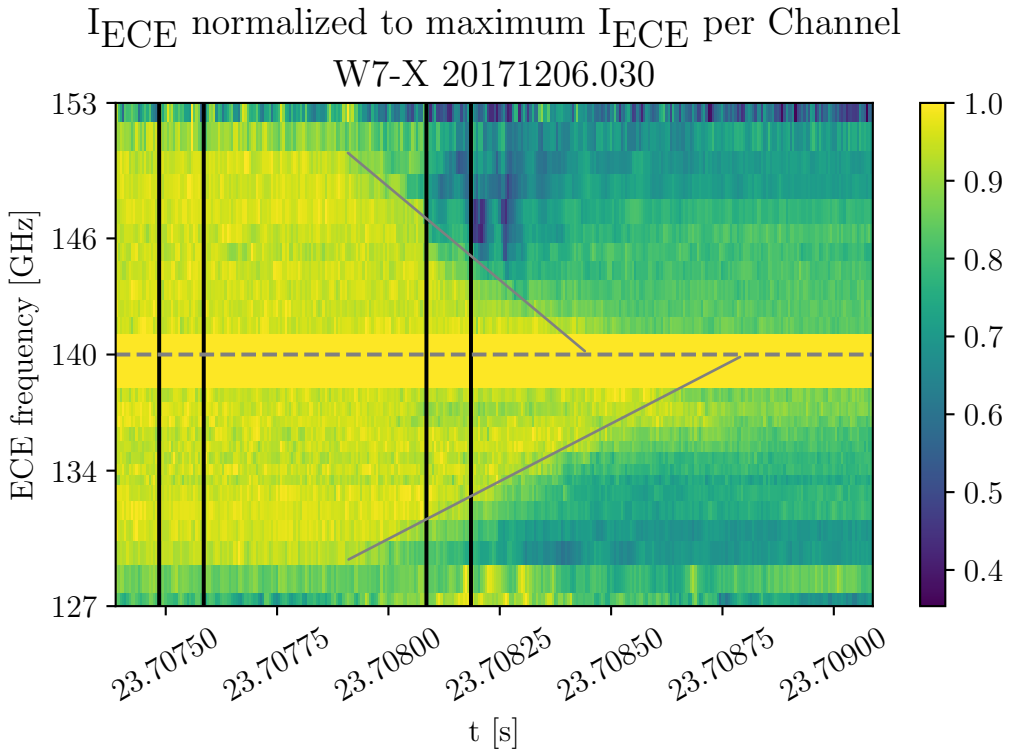

Fig. 3.5.1.: Timing of the burst pulses indicated by the black vertical lines on top of an ECE (electron cyclotron emission) radiation T_e spectrum. The grey lines were added to indicate the asymmetry of the T_e decrease and the frequency range around 140 GHz was faded out.

In fig. 3.5.1 the timing of a HFS pellet-triggered burst of 4 laser pulses (black lines) is compared to the ECE (electron cyclotron emission) temperature spectrum during pellet injection. The ECE data for the frequency range 138 - 141 GHz was not yet calibrated by the ECE group with disturbance caused by the ECRH, and is therefore faded-out in all ECE plots. The dashed line indicates 140 GHz, which is radiated close to the magnetic axis. Higher frequencies are radiated further to the inboard and lower frequencies further to the outboard side of the torus. The propagation asymmetry can be explained by the plasma β increase introduced by the pellet locally reducing the magnetic field and hence the ECE frequency. Each channel is normalized to its maximum in the shown interval to highlight the temporal match between the ECE electron temperature decrease introduced by the pellet and the burst-mode timing. Unfortunately most of the ECE channels were in "cut-off" for LFS pellet injections, at least for the shots analysed. In the cut-off case the density lies above the values for which the plasma is transparent for the ECE radiation. Therefore, a similar analysis could not be performed for LFS pellets. Additionally profiles need to be reconstructed from the spectra first before more careful analysis can be done. The moment the LFS pellet arrives to the plasma is visible as cut-off and hence the ECE spectrum can still be employed to check the quality of the burst-mode timing. As shown in fig. 3.5.2, as a representative example, the burst was sufficiently triggered for LFS pellets as well. Slight fluctuations in the timing found for different pellets might be explained by the pellets' injection side and need further investigation to be fully understood.
The analogue interferometry line-integrated density signal is displayed in fig. 3.5.2 and fig. 3.5.3 likewise. The time of the density increase introduced by the pellet matches with the ECE temperature decrease as well as with the burst-pulse timings. In contrast to the concern that the provided trigger might be too close to the pellet event (cf. section 3.1) the results in fig. 3.5.1, 3.5.2 and 3.5.3, show the trigger was set off several hundred microseconds ahead of the pellet reaching the plasma. Other diagnostics triggered by the H_α-signal experienced the same phenomenon. For the burst-mode Thomson scattering diagnostic, this was a fortunate coincidence providing profile data of the unperturbed plasma, which could later be compared to the pellet-affected profiles.
As discussed and shown in fig. 3.5.2 and 3.5.3, the burst-mode timing was compared for three independent diagnostics (H_α as Thomson scattering trigger, the ECE, and the interferometer diagnostic), validating the successful triggering of the bursts to the moment of pellet injection in W7-X. Additionally it seems like most of the time-interval of the density and temperature change introduced by the pellet is covered. This interval will increase if the three lasers (12 pulses) become available in the next campaign.

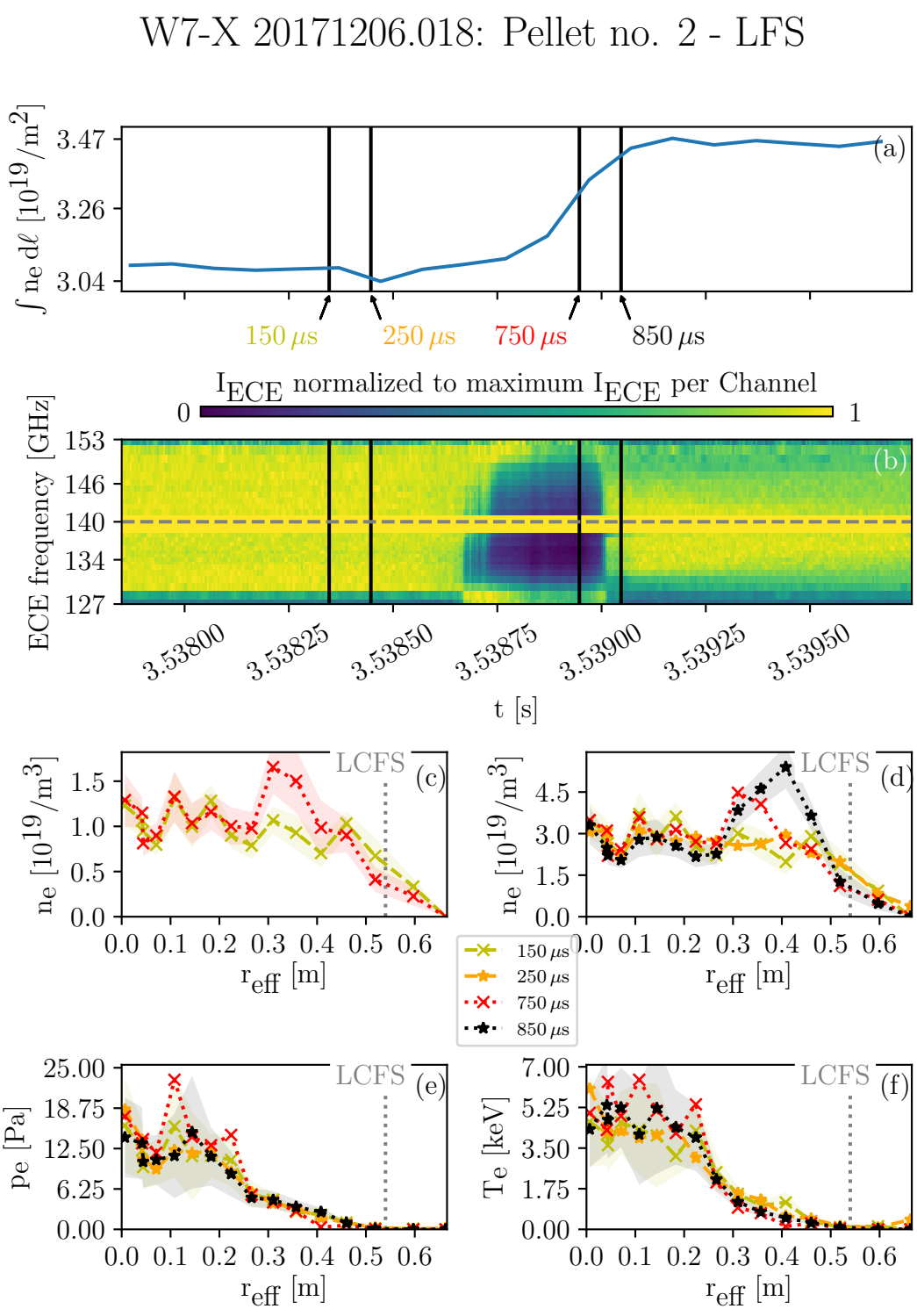

Fig. 3.5.2.: Overview of the electron temperature and density effects of the 2nd pellet injected in W7-X program 20171206.018 from LFS. The energy normalised (c) and the interferometry calibrated (d) density profiles are shown for comparison.

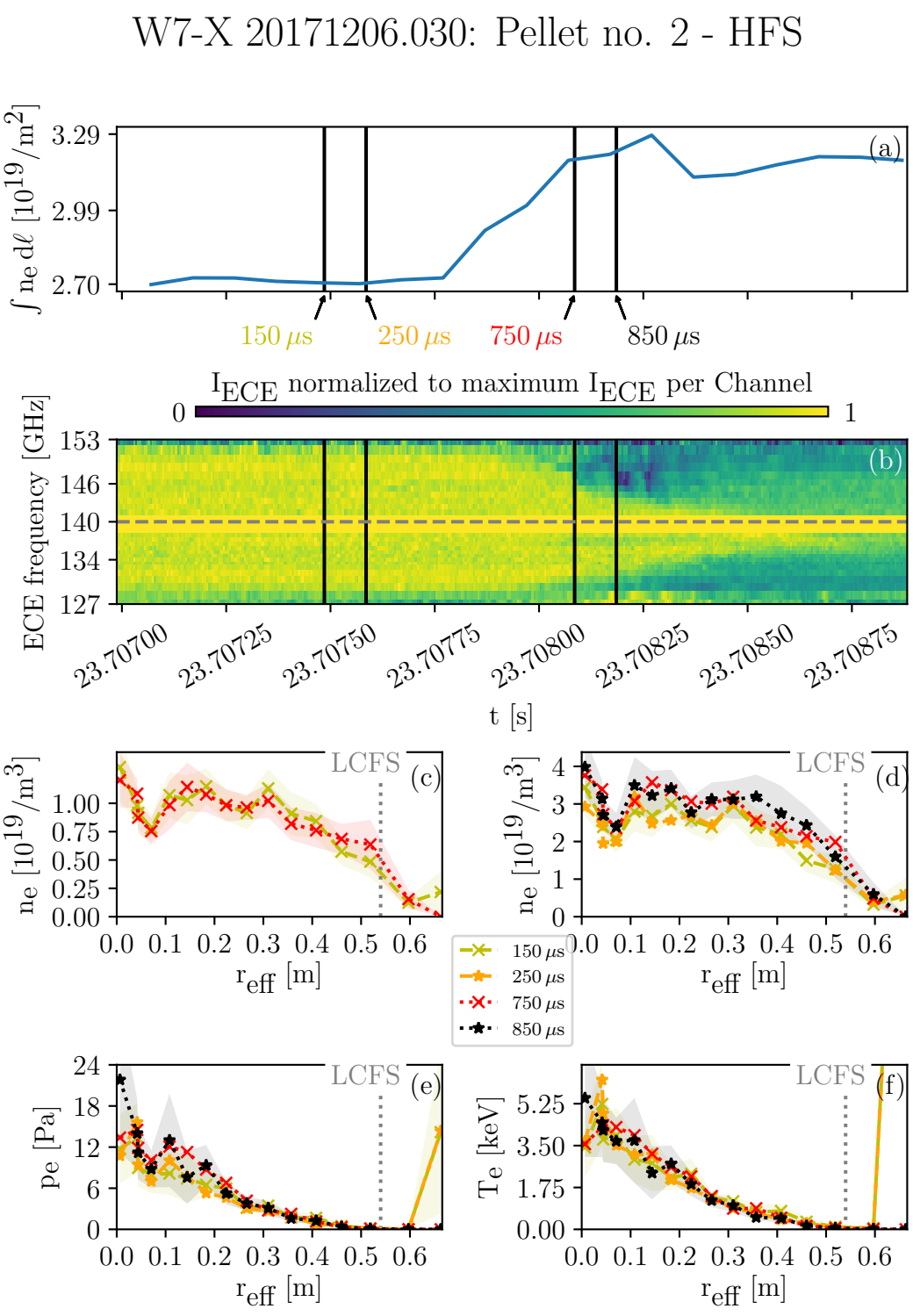

Fig. 3.5.3.: Overview of the electron temperature and density effects of the 2nd pellet injected in W7-X program 20171206.030 from HFS. The energy normalised (c) and the interferometry calibrated (d) density profiles are shown for comparison.

Note: The H_α monitoring diode is sensitive to all sorts of events which cause (sufficient) radiation in a certain wavelength range. This incorrect triggering happened from time to time (cf. fig. 3.4.5 (d) at 1.75 s), but overall rather rarely. An option to reduce this effect significantly would be to install a narrow-band filter transparent only for the H_α line in front of the trigger diode.

After the temporal match, the second parameter analysed was the spacial resolution. As shown in fig. 2.3.3, the spacial resolution at the edge is 8 cm and increases nearer the plasma core. With the pellet cloud expanding up to 40 cm during its deposition phase, it was easily detectable. In fig. 3.5.2 (d) the plasmoid changes it size from ≈ 20 cm at 750 µs after injection to ≈ 40 cm diameter in real space at 850 µs after injection. At the same time, its centre drifts ≈ 10 cm to the outboard side, implying a drift velocity of 1000 m/s. All the measured numbers lie within the intervals predicted by the HPI2 code. The density increase and the penetration depth seem to be larger than predicted for LFS pellets. Unfortunately, for the HFS case, no more than a slight overall increase in density is visible. The following estimate shows that the size of the HFS pellets should be sufficient to introduce a density increase larger than the Thomson scattering error bars. With the assumption of HFS pellets containing 9×10^{19} hydrogen atoms at the arrival at the plasma (cf. section 2.2) deposited within an r_{eff} interval of 20 cm, the density increase would still be larger than the Thomson scattering error, even if the HFS pellets were deposed only in the edge 20 cm where the volume is the largest.

Tab. 3.5.1.: Expected density increase at different radial positions for HFS pellets compared to the typical Thomson scattering error at the same position.

r_{eff} [m]	ΔV [m^3]	Δn_e [$10^{19}\,m^{-3}$]	Thomson error [$10^{19}\,m^{-3}$]
$0.6 - 0.4$	21.7	4.14×10^{18}	2.8×10^{18}
$0.4 - 0.2$	13.0	6.91×10^{18}	2.8×10^{18}
$0.2 - 0$	4.3	2.07×10^{19}	3.0×10^{18}

Therefore, another explanation was needed to understand why no density peak could be identified on the profile, and was given by the toroidal extension of the cloud. As stated in section 1.4, the maximal length of the cloud is 25 m at the end of the homogenization phase. With the Thomson scattering located at 171° in toroidal coordinates and the pellet injection at 231°, the angle between both is 60° and the distance along the magnetic axis is ≈ 6 m given the W7-X major radius of 5.5 m / ≈ 35 m circumference. While in the LFS case the 12.5 m extension of the

cloud (to both sides) is sufficient to reach the Thomson LOS in positive toroidal direction, the HFS cloud would need multiple toroidal revolutions to appear on the outboard half side of the torus that is observed with the current Thomson scattering diagnostic. It can therefore only be detected as an overall density increase rather than a sharp, well-defined cloud because during the revolutions it gets deluded and burred. Additionally, it is questionable whether it arrives on the outer half-profile before the last burst measurement is taken. This depends on the flux surface the cloud passes on its expected inwards drift. Nevertheless, the outer surfaces with larger diameter are passed first and thus it is assumed that the material on these surfaces needs too many toroidal evolutions (ι is close to, but not equal to 1) to arrive in time. On the other hand the clouds drifted through the whole plasma are greatly diluted and hence cannot longer be observed as sharp density peaks on the outboard half-profile. Fortunately, the inboard side of the Thomson scattering diagnostic is currently under preparation and will be available for the next campaign to study HFS pellet injection.

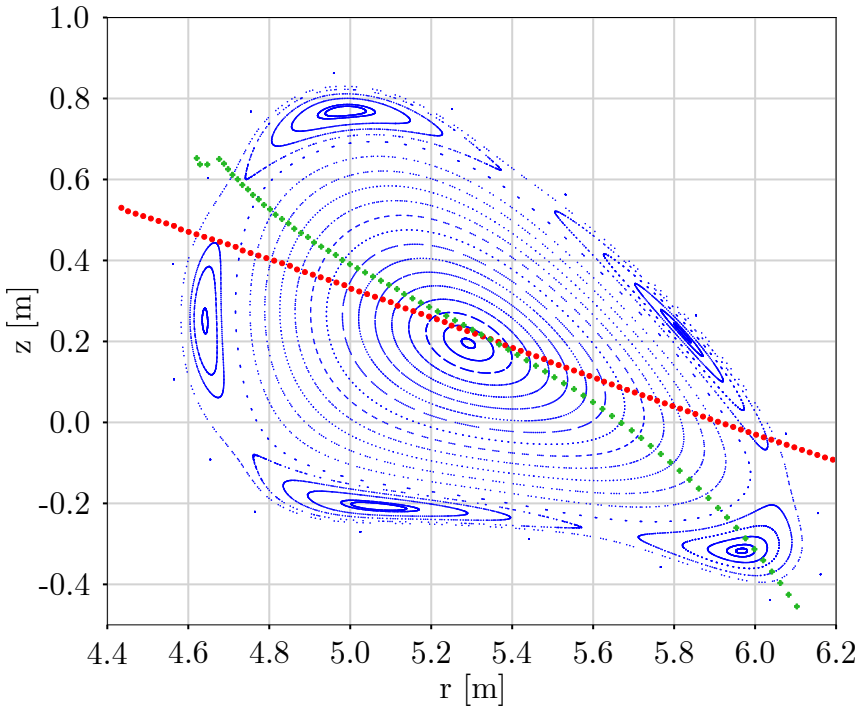

Fig. 3.5.4.: Thomson LOS (red) compared to the pellet injection "line" (green, approximated by the connection between the HFS and LFS injection ports) at a toroidal angle of 171° for the W7-X standard configuration.

One should note that the plasmoids of LFS injected pellets as well could only be observed if they map onto the Thomson LOS while taking the rotational transform

(winding of the magnetic field lines around the torus) into account. This mapping was exemplarily performed for the vacuum standard configuration, which is close to the experimental conditions, for the analysed pellet shots. The non-zero plasma β during operation introduces a moderate outward shift which is largest at the plasma centre. The result of the mapping process is shown in fig. 3.5.4. For this configuration the lines show an adequate agreement, implying that the plasmoid expands up to 40 cm, and the maximal distance between both LOSs is 20 cm. Therefore, the plasmoid would at least overlap with the Thomson scattering LOS. The mapping for different magnetic configurations would result in slight variations of the pellet line, but even for the high ι cases, the deviation from the shown plot is 35 cm at the edge only and decreases toward the centre.
Additionally, the pellets exit the guiding tube with an angular spread of up to 14° [58], which can result in a large deviation from the "pellet line" (green crosses) drawn in fig. 3.5.4. The pellets may therefore fly along the line or appear above or below as shown in images from the LFS pellets at 3.110 s and 3.304 s in W7-X program 20171115.018 in fig. 3.5.5. They were observed with the burst-mode Thomson scattering diagnostic as well and will be analysed in chapter 4.

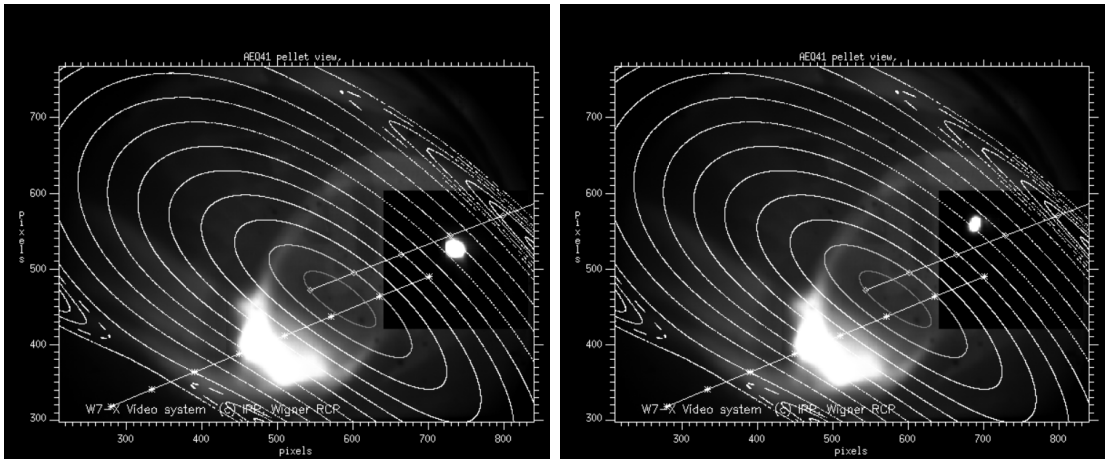

(a) LFS pellet at 3.110 s. (b) LFS pellet at 3.304 s.

Fig. 3.5.5.: Deviation of the LFS pellet flight paths from the designed path indicated by the white line. The image shown is the last frame from a series taken for each LFS pellet in W7-X 201115.018. Only a rectangular region of interest in the right side of the image was actually recorded; the image of the background plasma and the field lines were added for comparison (provided by [70]).

It has been observed that some pellets cross the designed path, which can also be explained by drifts of the cloud material. Nevertheless, a crossing of the Thomson

line of sight cannot be observed with the burst mode, which still has a too low repetition frequency. Fortunately, the interferometry diagnostic has a very similar LOS and is sampled with 100 kHz. Therefore, it is possible to show this effect in fig. 3.5.6 on the line integrated density.

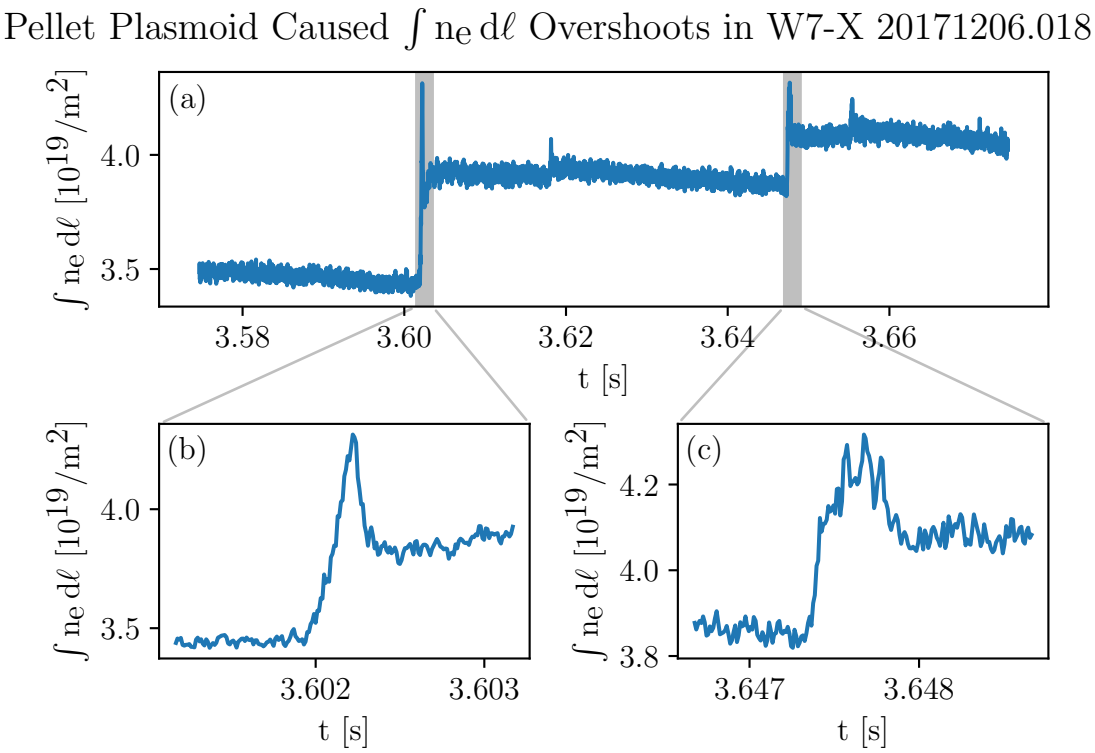

Fig. 3.5.6.: A LFS pellet (b) and a HFS pellet (c) introducing an overshoot in the line integrated density data from the Thomson LOS interferometer.

The discussed circumstances and results prove that the event-triggered burst-mode Thomson scattering diagnostic as developed for this thesis is able to measure transient density and temperature profile effects introduced by pellets injected into W7-X plasmas. The limitations were spotted and can explain the significance of the profile effects, i.e., for HFS injected pellets. It was also possible to verify several predictions made by the HPI2 code. A further discussion of the physics results from Thomson scattering data employing the event-triggered burst mode follows in the next chapter.

4. Brief Overview on Pellet Physics Observed in Burst Mode Operation

In this chapter some results from radial fuelling studies are shown to demonstrate the capabilities of the new event-triggered burst-mode Thomson scattering diagnostic. The short-timescale effects of pellet injection are examined employing the burst measurements. Additionally, inter-burst profile changes were analysed to study the radial evolution after pellet injection. In all cases, HFS and LFS injections were compared whenever data was available. On top of this, a comparison to fuelling with gas puffing was carried out. Finally the "pre-cooling effect", as found for other plasma experiments [71], is shown for W7-X pellet series.
Comparisons between the total fuelling rates determined via the interferometer line-integrated density measurements and the total Thomson profile integration are obsolete because the Thomson profiles were calibrated to the interferometer densities as described in section 3.4.2. Nevertheless, the crucial advantage of the Thomson scattering measurements in comparison to the interferometry is the radial resolution which allows only material within the LCFS to be taken into account for the fuelling studies. The ratio between the predicted pellet particle content at the exit of the guiding tubes (cf. section 2.2) and the density increase within the LCFS was used to calculate the fuelling efficiency. Moreover, it was possible to radially analyse the density changes and validate whether the desired core fuelling could be achieved with a single pellet or with multiple pellets, or with gas fuelling.

4.1. Radial Fuelling on Sub-Millisecond Timescale

For the analysis of fast radial density and temperature changes the pellets injected in programs 20171206.018 at 3.539 s (LFS - 2nd pellet) and 20171206.030 at 28.708 s (HFS - 2nd pellet) were chosen. In section 3.5, the appropriate trigger timing was shown in fig. 3.5.2 and 3.5.3 and the electron temperature, density, and pressure profiles were displayed. In this chapter only the relative density and temperature changes were plotted for better clarity. The error intervals displayed for both, the electron temperature and density obtained from Thomson scattering measurements, denote a 1σ standard deviation from the most likely values obtained from the procedure explained in section 1.3. As an overview some important plasma parameters were plotted for the time interval of the pellet injection. The according overview plots for the entire shot can be found in the appendix, section E.

A LFS Pellet in 20171206.018

The W7-X discharge 20171206.018 was a pure hydrogen discharge heated with the second harmonic extraordinary mode (X2-mode) of 140 GHz microwave radiation. The incident ECRH power during the injection of a mixture of HFS and LFS hydrogen pellets is displayed in fig. 4.1.1. The 2nd of 5 pellets was injected to 20171206.018 at 3.539 s from low field side and observed with the event-triggered burst-mode Thomson scattering diagnostic. (Note: The 1st pellet did not introduce a noticeable density increase to the interferometer density signal but was clearly seen by the H_α monitoring diode.)
As already mentioned in section 3.5, the density increase introduced by the plasmoid is clearly visible 750 µs after the H_α - trigger at $r_{eff} = 0.2 - 0.45$ m with a maximum of $\Delta n_e \approx 1.4 \times 10^{19}\,m^{-3}$ at $r_{eff} = 0.3$ m in fig. 4.1.2. The peak density increases to $\Delta n_e \approx 3.8 \times 10^{19}\,m^{-3}$ and drifts to $r_{eff} = 0.4$ m, 100 µs later, while the radial extension ranges from $r_{eff} = 0.25$ m to $r_{eff} = 0.5$ m by than. These extensions and the according drift velocity (1000 m/s) match to the HPI2 predictions [57, 60] as stated earlier. Even though the ablation of the pellet was not completely finished (cf. 3.5.2), no later measurement was available due to the lack of the second and third lasers. Therefore, the particle input was calculated for the measurement 850 µs after the H_α trigger for all analysed short timescale pellet measurements. To calculate the total number of electrons, the electron density increment, shown in fig. 4.1.2, is integrated radially, assuming the density in the torus slices to be constant between the Thomson scattering volumes. To account for the half-profiles, a factor of 2 was applied to the results. For the LFS pellet shown, the number of electrons deposited within the LCFS was $(2.3 \pm 1.7) \times 10^{20}\,m^{-3}$. The uncertainty

interval was calculated the same way using the difference between upper and lower threshold cut in half. Compared to the estimate provided in section 2.2 ($\Delta N = 2 \times 10^{20}$ electrons per LFS pellet), the result and the corresponding fuelling efficiency $\eta = (115 \pm 85)\,\%$ seem reasonable given the large error.
The radial position of the relative temperature change (compared to the temperature profile 150 µs after the H_α - trigger, which is usually still a few hundred microseconds ahead of the arrival of the pellet) correlates with the location of the density increase. One should note that the constantly applied central ECRH heating probably affects the result. The electron energy W_e in fig. 4.1.1 (d) changes only within the uncertainty interval during pellet injection, indicating the adiabatic nature of the process. This holds for all pellets analysed.

A HFS Pellet in 20171206.030

The W7-X discharge 20171206.030 was a helium discharge until, starting from 23.5 s, 7 hydrogen pellets were injected from HFS. The discharge was heated with the X2-mode of 140 GHz microwave radiation. The incident ECRH power is displayed in fig. 4.1.4. The 2nd pellet was injected to 20171206.018 at 23.707 s and observed with the event-triggered burst-mode Thomson scattering diagnostic.
In contrast to low field side injection, a marked density peak could not be found on the outboard side Thomson profile; nevertheless, a slight overall density increase is noticeable. As mentioned in section 3.5, the increase could be distorted by the calibration to the interferometer and the fact that the Thomson scattering diagnostic only observes one half-profile. A possible effect of a pellet that is only present on the inboard side would therefore be accounted for twice and lead to an overestimation of the density on the outboard half-profile. In fact, the density increment displayed in fig. 4.1.5 results in an increase of $(1.8 \pm 1.6) \times 10^{20}$ electrons in the total electron number within the LCFS (compared to the prediction of 0.9×10^{20} electrons per HFS pellet), giving a fuelling efficiency of $\eta = (200 \pm 178)\,\%$, which seems to be off by a factor of 2.
The relative temperature change is, as for the LFS pellet, negative for $r_{eff} = 0.3\,m$ up to the LCFS as shown in fig. 4.1.6.

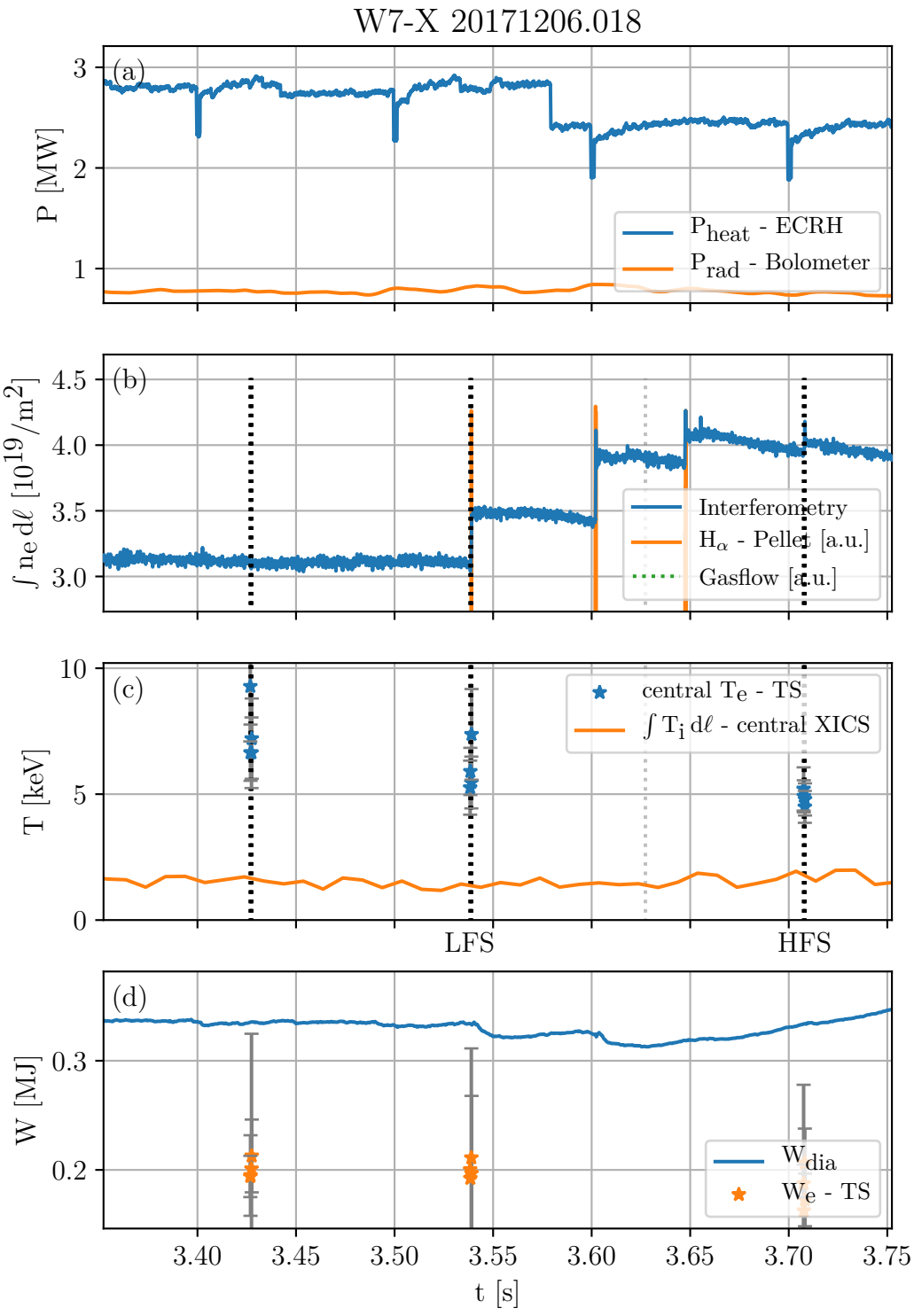

Fig. 4.1.1.: W7-X discharge 20171206.018 overview plot during the pellet injection phase. The dashed black lines indicate the timing of the Thomson scattering measurements; dashed grey lines indicate the uniform standard trigger. If the Thomson scattering diagnostic was triggered by a pellet the lines do not overlap. The pellet injection side is indicated by HFS (high field side) or LFS (low field side). The full overview plot can be found in the appendix.

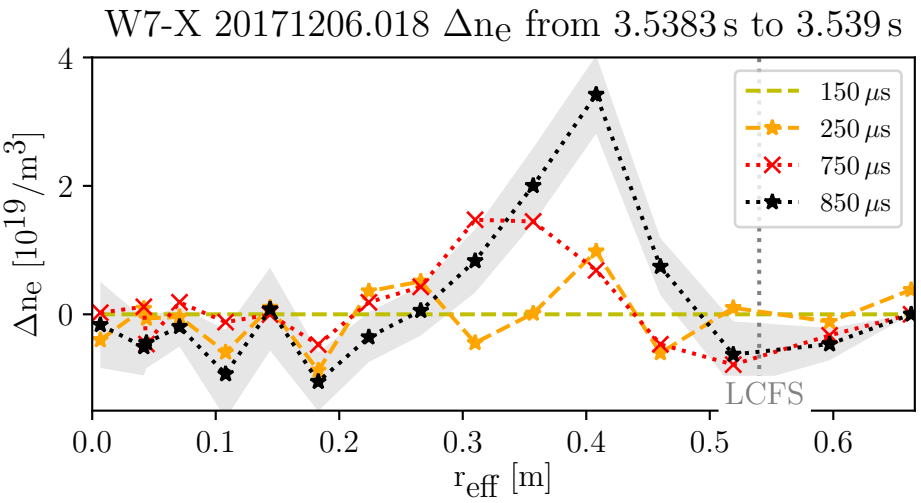

Fig. 4.1.2.: Electron density change induced by the 2nd pellet (low field side) injected during W7-X discharge 20171206.018 relative to the first density profile from the burst.

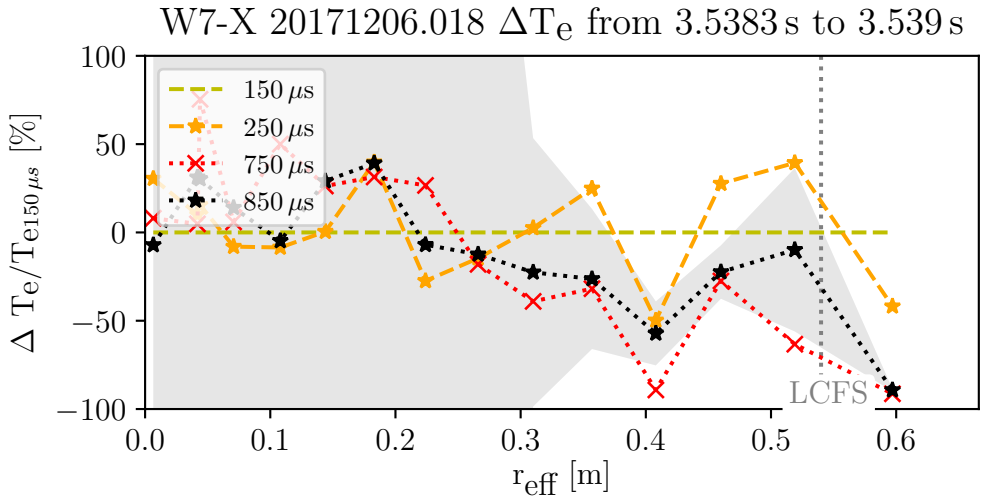

Fig. 4.1.3.: Electron temperature change induced by the 2nd pellet (low field side) injected during W7-X discharge 20171206.018 normalized to the first temperature profile from the burst.

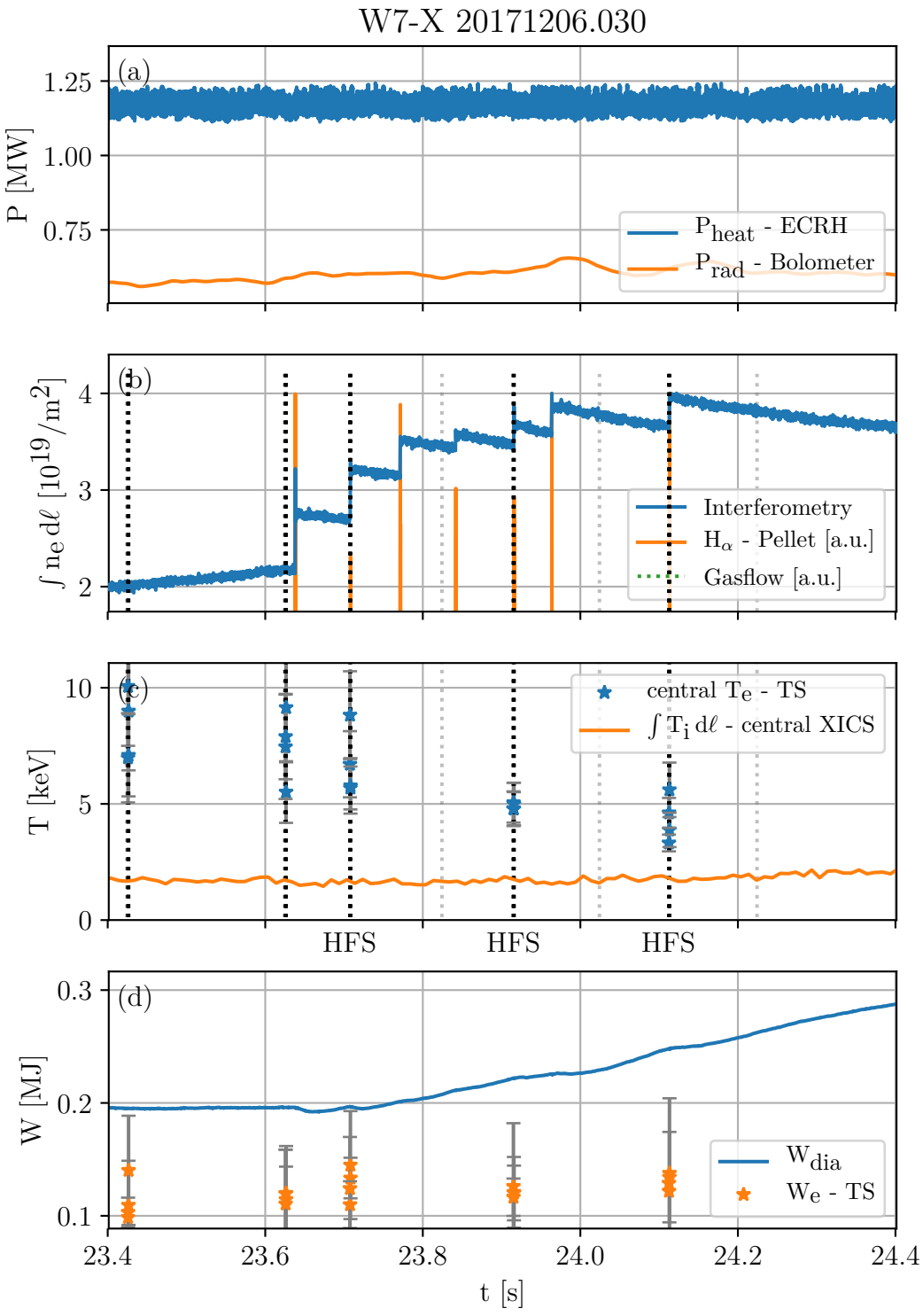

Fig. 4.1.4.: W7-X discharge 20171206.030 overview plot during the pellet injection phase. The dashed black lines indicate the timing of the Thomson scattering measurements; dashed grey lines indicate the uniform standard trigger. If the Thomson scattering diagnostic was triggered by a pellet the lines do not overlap. The pellet injection side is indicated by HFS (high field side) or LFS (low field side). The full overview plot can be found in the appendix.

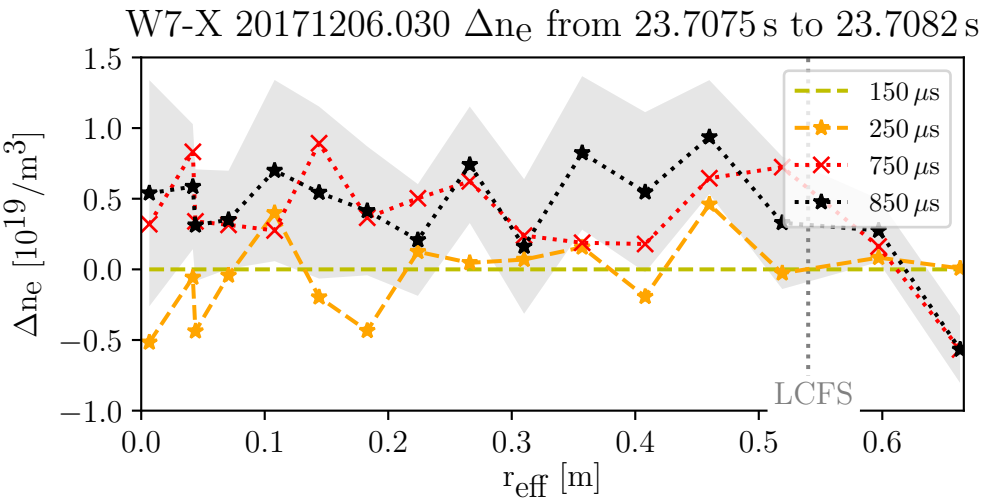

Fig. 4.1.5.: Electron density change induced by the 2nd pellet (low field side) injected during W7-X discharge 20171206.030 relative to the first density profile from the burst.

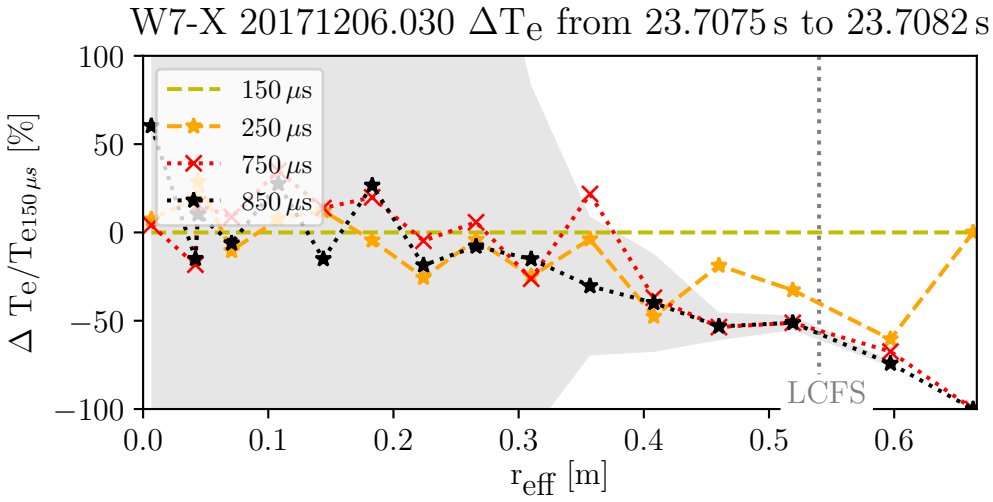

Fig. 4.1.6.: Electron temperature change induced by the 2nd pellet (high field side) injected during W7-X discharge 20171206.030 normalized to the first temperature profile from the burst.

4.2. Radial Fuelling on Multi-Millisecond Timescale

To compare the injection of single pellets to pellet series and gas guff fuelling with respect to the radial particle deposition, the electron density profiles from the first pulse of a burst was compared to the first pulse of the next burst. Those pulses provide Thomson data a few 100 µs ahead of the next pellet injected; therefore, this method provides information about the temperature and density profiles after complete ablation and deposition of the former pellet. Evidence that the aforementioned procedure is valid because the profiles do not change significantly between two pellets will be given in section 4.3.

4.2.1. Single Pellet Fuelling

Fortunately, in W7-X discharges 20171121.025 and 20171206.030, the burst-mode Thomson scattering diagnostic was triggered by the second pellet of the series, which allowed for the comparison of the Thomson scattering data from before the first pellet to the data right before the second pellet. This data can be treated like data from a single pellet, since no change to the background plasma was introduced by a previous pellet.
The first pellet was injected from HFS in 20171206.030 and from LFS in 20171121.025. W7-X 20171121.025 was a pure hydrogen discharge; 13 pellets were injected from both sides. It was heated with the X2-mode of 140 GHz microwave radiation, and was terminated when the density exceeded the absorption cutoff of the X2-mode at $1.2 \times 10^{20}\,\mathrm{m}^{-3}$. The incident ECRH power is displayed in the overview plot of 20171121.025 for the time interval of pellet injection in fig. 4.2.1.
The according overview plot for discharge 20171206.030 can be found in section 4.1 were the shot was used already.

Comparison between single HFS and single LFS pellet

From fig. 4.2.2 and 4.2.3, one can see that core fuelling was achieved, for both the single HFS pellet and single LFS pellet, although the deposition appears to be more (exclusively) central for HFS injection. After $\approx 80\,\mathrm{ms}$ the HFS pellet material had already sufficiently radially equilibrated (as will be discussed in section 4.3) such that the error arising from the exclusive outboard observation of the Thomson scattering diagnostic should not play a role for the case shown in fig. 4.2.3. The calculated $\Delta\mathrm{N}$ is $(1.0 \pm 1.3) \times 10^{20}$ electrons and the fuelling efficiency, η, is $(111 \pm 144)\,\%$, which indeed fits to the expectations within the uncertainties. Interestingly, the fuelling efficiency of the LFS pellet is now slightly too high, even when considering the large error: $\eta = (175 \pm 65)\,\%$, or $\Delta\mathrm{N} = (3.5 \pm 1.3)$ electrons, which needs further investigation. It is possible some impurities were injected together with the actual pellet.
The relative temperature profile change in the time interval between the two pellets is negligible as will be discussed in section 4.4 and therefore not shown.

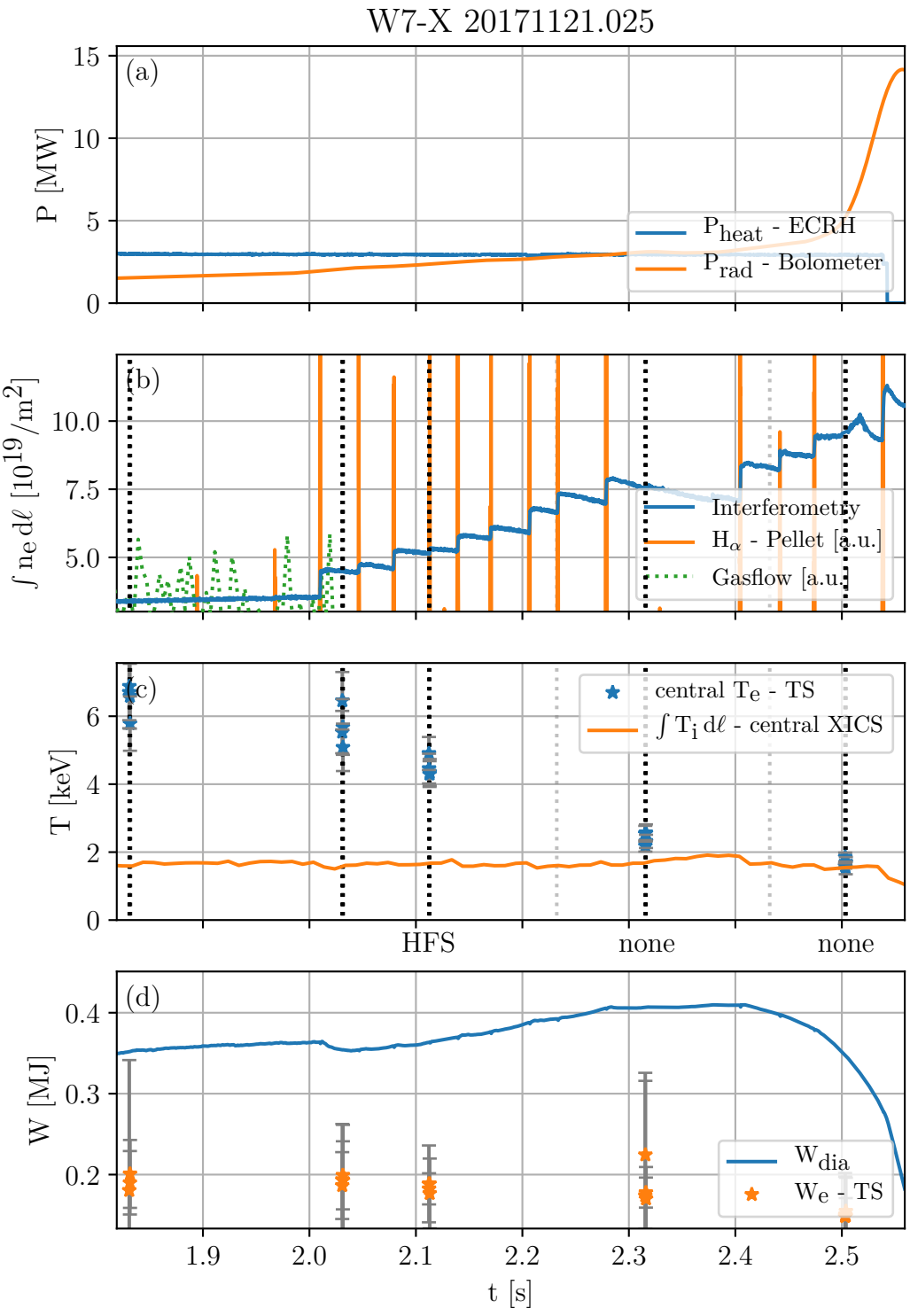

Fig. 4.2.1.: W7-X discharge 20171121.025 overview plot during the pellet injection phase. The dashed black lines indicate the timing of the Thomson scattering measurements; dashed grey lines indicate the uniform standard trigger. If the Thomson scattering diagnostic was triggered by a pellet the lines do not overlap. The pellet injection side is indicated by HFS (high field side) or LFS (low field side). The full overview plot can be found in the appendix.

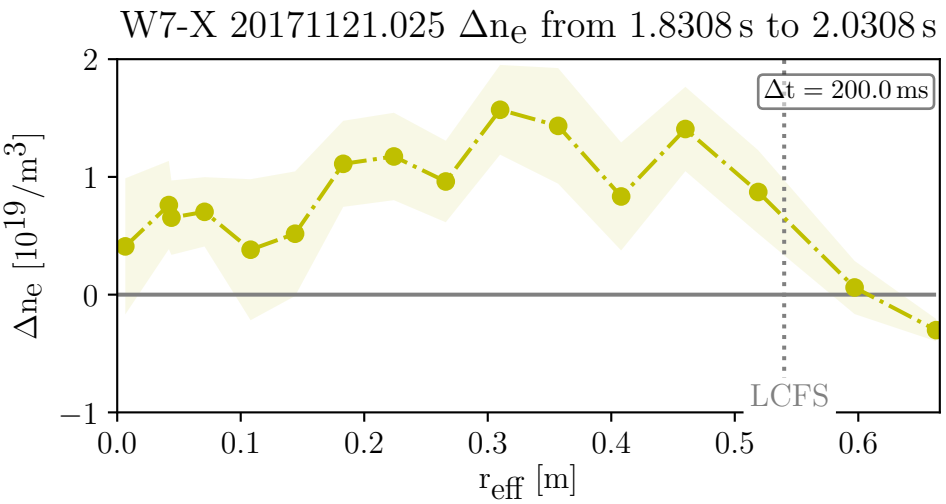

Fig. 4.2.2.: Electron density change induced by the 1st pellet (low field side) injected during W7-X discharge 20171121.025 relative to the first density profile from the burst long before the injection. The time interception between the two Thomson measurements is denoted by Δt.

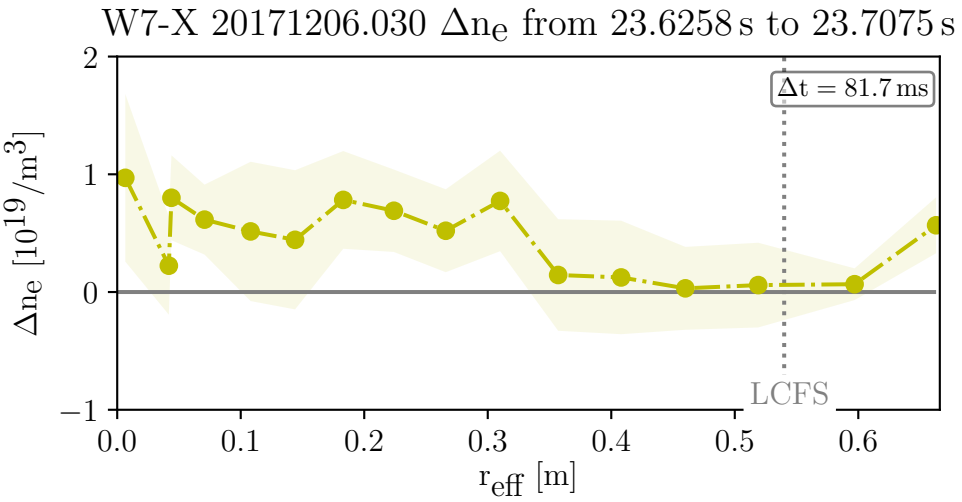

Fig. 4.2.3.: Electron density change induced by the 1st pellet (high field side) injected during W7-X discharge 20171206.030 relative to the first density profile from the burst long before the injection. The time interception between the two Thomson measurements is denoted by Δt.

4.2.2. Fuelling with Pellet Series

The pellet series from W7-X discharges 20171121.025 (mixed HFS and LFS) and 20171206.030 (pure HFS) were further analysed with respect to their radial pellet material deposition. As shown in fig. 4.2.4 and 4.2.7, both discharges' density profiles do not only generally increase but also become rather peaked. This indicates that the pellet material finally was deposited more centrally than the single LFS pellet in particular. This has been observed before in other large stellarator plasma experiments like LHD [71] and can be explained by a deeper penetration of the latter pellets in a series made possible by the cooling of the plasma edge by the earlier pellets. This effect is discussed in section 4.4 in further detail. The predominant cooling of the edge region is clearly visible in the 3D plot of the electron temperature during pellet injection in fig. 4.2.4 and 4.2.7.
To compare the different phases within a pellet series, the density profile change after equilibration is shown in fig. 4.2.5 for (a) the first pellet, (b) the pellets immediately following, and (c) some later pellets of each series and 4.2.6.

A Mixed HFS and LFS Pellet Series in 20171121.025

In contrast to the pure HFS pellet series injected to W7-X discharge 20171206.030 a mixed HFS and LFS series as used in 20171121.025 was chosen because no pure LFS pellet series experiments were conducted in W7-X so far. As already discussed in section 4.2.1, the first LFS pellet's material is mainly deposited in the outer regions of the plasma. After pellet 2 (HFS) and 3 (LFS) the deposition becomes more central and for the pellets 4 - 9 (3 HFS / 3 LFS) a large central density increase is observed as shown in fig. 4.2.5.

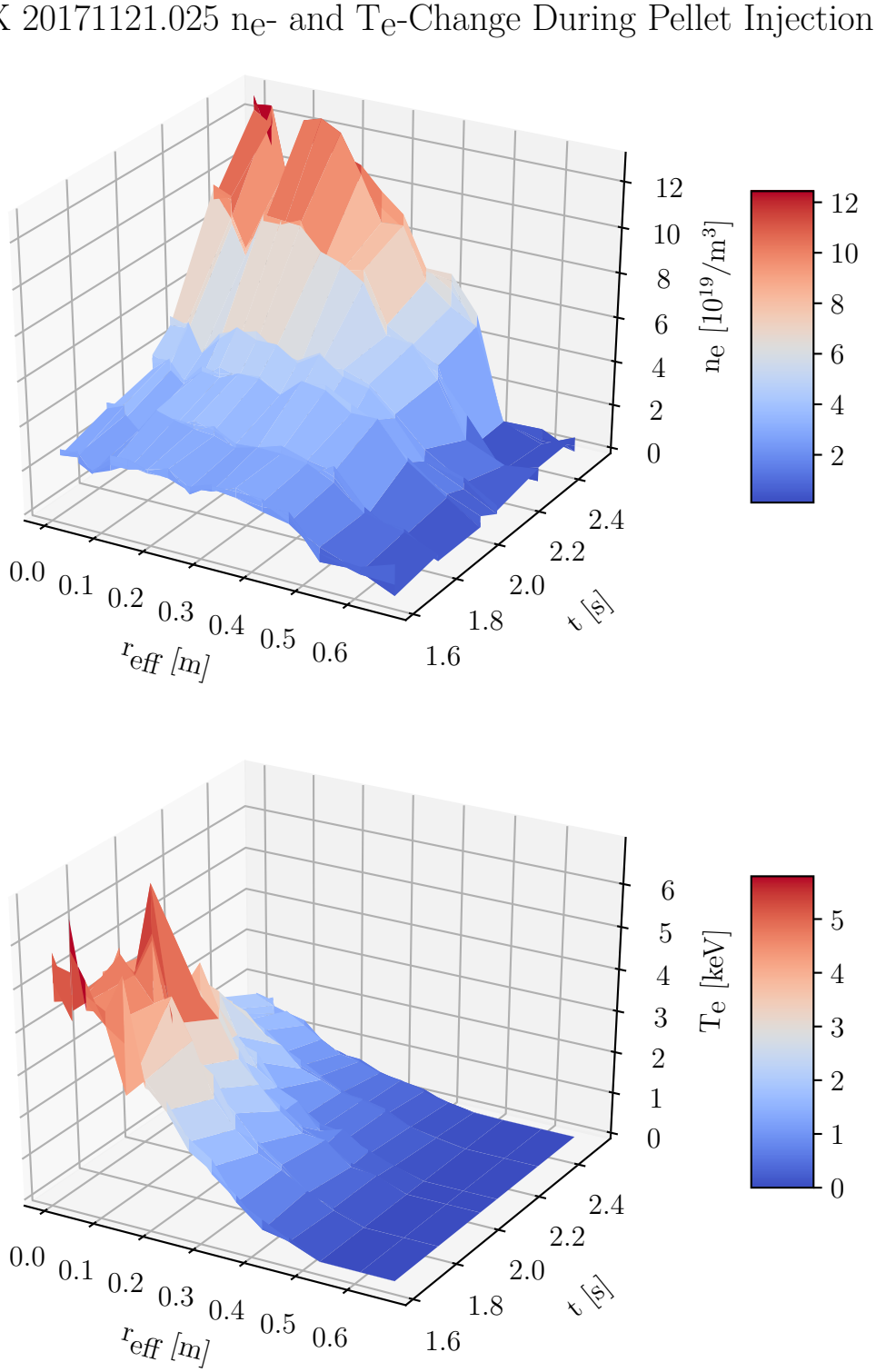

Fig. 4.2.4.: 3D depiction of the electron density and temperature evolution in W7-X discharge 20171121.025 during pellet injection. Temperature spikes outside the LCFS exceeding the central temperature were set to zero.

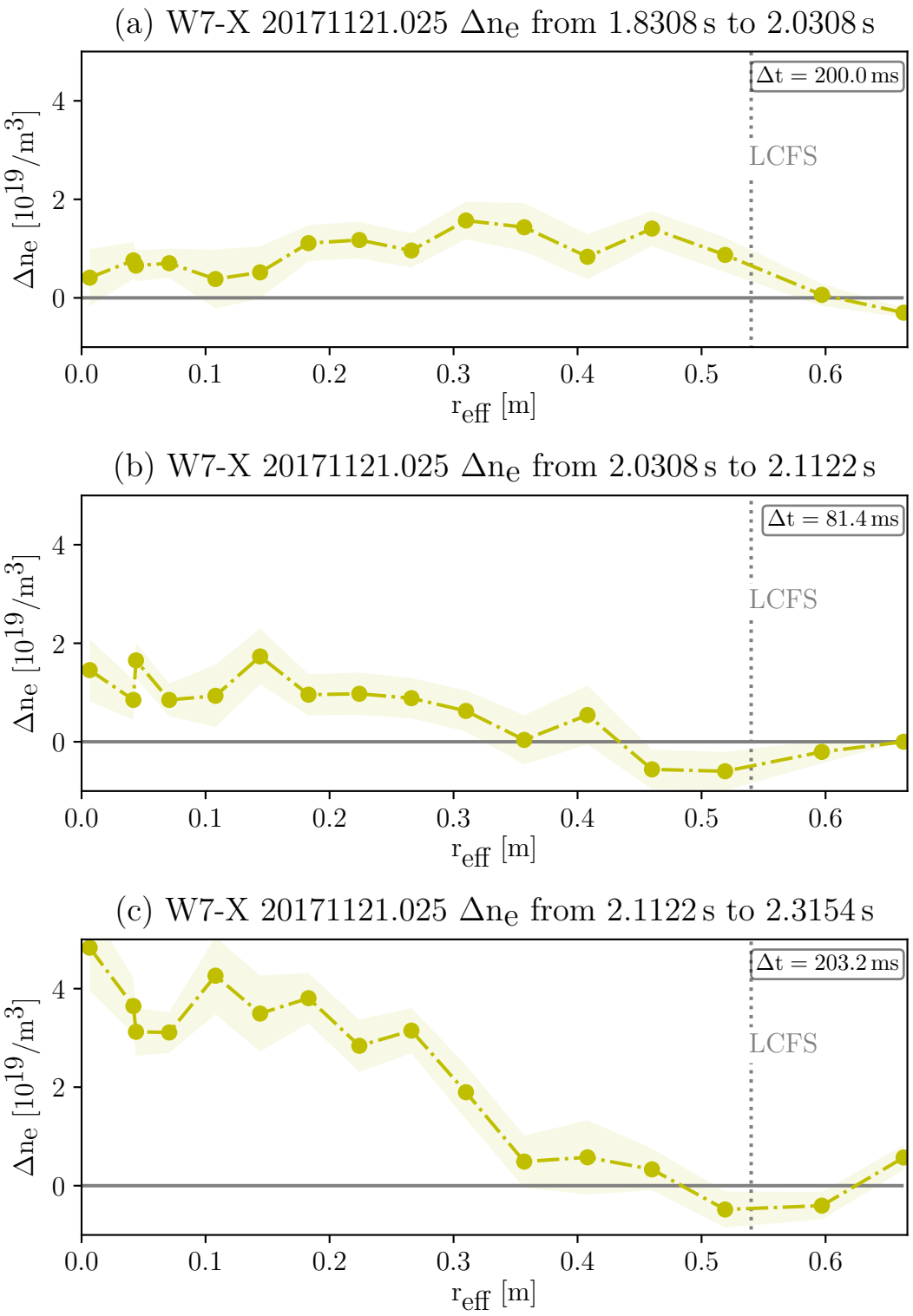

Fig. 4.2.5.: Electron density change in W7-X discharge 20171121.025 introduced by (a) pellet 1/14 (LFS), (b) pellets 2/14 (HFS) and 3/14 (LFS), and (c) pellets 4-9/14 (3 HFS / 3 LFS).

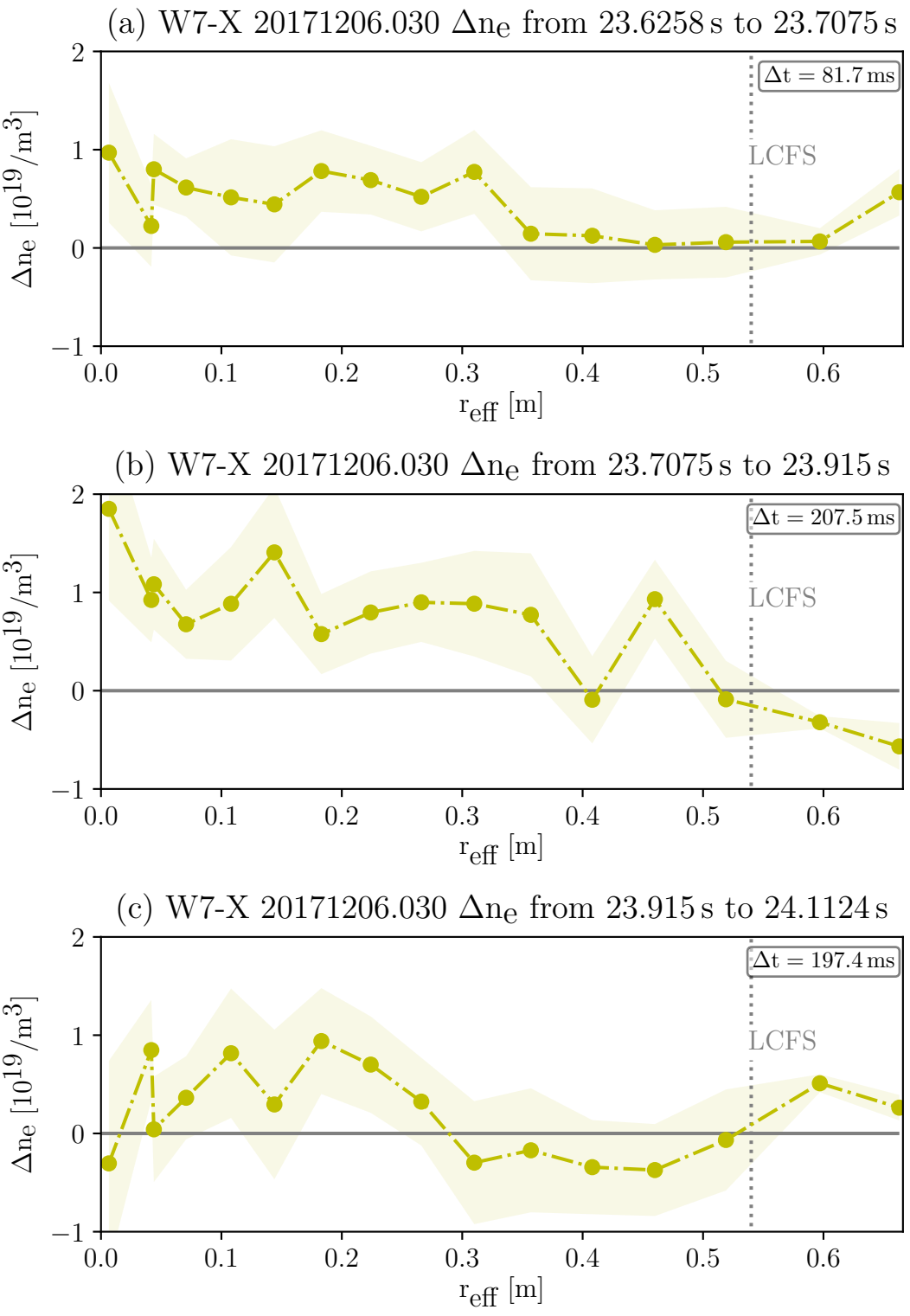

Fig. 4.2.6.: Electron density change in W7-X discharge 20171206.030 introduced by (a) pellet 1/7, (b) pellets 2-4/7, and (c) pellets 5-7/7. The pellets were all injected from HFS.

A Pure HFS Pellet Series in 20171206.030

The density increase per pellet in the pure HFS pellet series is smaller than for the mixed series (note the different ordinate scaling!). This can be explained by the pellet's higher material loss in the longer, stronger bended tube necessary for HFS injection. The material deposition is relatively central from the first pellet on. Why the fuelling efficiency of the 5th - 7th pellet decreases compared to pellet 2 - 4 needs further investigation. For some series, both HFS and mixed ones, it was found that the particle loss between two pellet injections is stronger in later phases of the series even though the penetration of the material on the $\sim 1\,\mathrm{ms}$ timescale does not worsen. An example of this behaviour can be seen in fig. 4.2.10 in the next section where the line integrated density from the interferometry diagnostic stays constant in between the injection of the early pellets of the series but strongly decreases in between the later pellet injections. This is still an open question to the community and needs further investigation.

Another current issue the pellet injection group deals with is the design of a steady-state pellet injector for the post-2020 campaigns. In this context an important question was whether the $\boldsymbol{E} \times \boldsymbol{B}$ - drift in the direction of $-\nabla \boldsymbol{B}$ as theoretically predicted (cf. section 1.4) and observed for tokamak plasma experiments would hinder efficient LFS fuelling in W7-X as well, making HFS pellet injection favourable for steady-state pellet fuelling [72]. From the results shown, sufficient fuelling seems possible from both high and low field sides. Therefore, it can be recommended to design the new steady-state injector to be a pure LFS injector and thus avoid the technical difficulties that accompany the long, high-curvature tubes necessary for HFS injection.

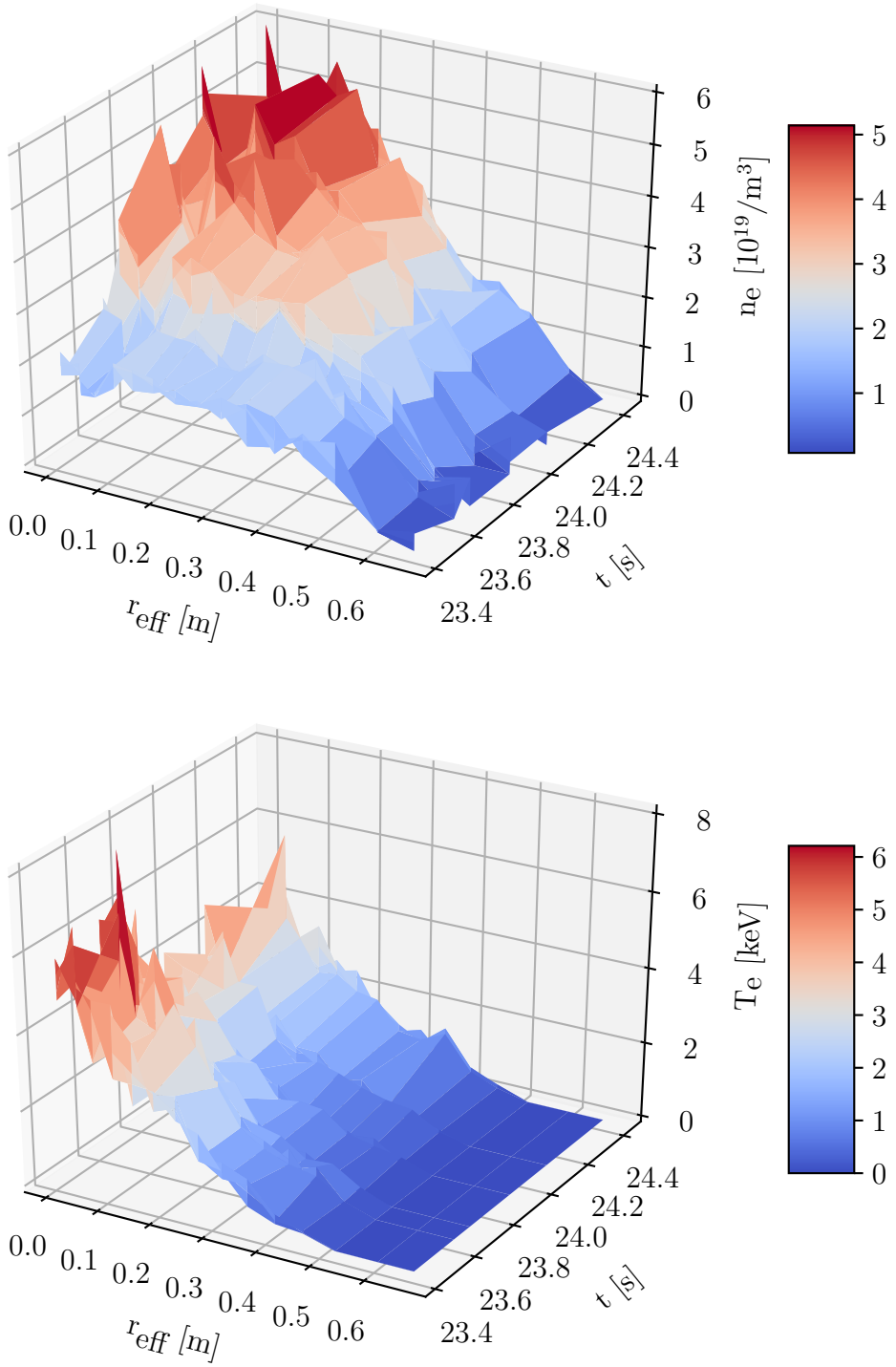

Fig. 4.2.7.: 3D depiction of the electron density and temperature evolution in W7-X discharge 20171206.030 during pellet injection. Temperature spikes outside the LCFS exceeding the central temperature were set to zero.

4.2.3. Comparison to Gas Puff Fuelling

One of the most intuitive and commonly applied fuelling techniques is the injection of gas via gas valves, known as gas puffing or gas fuelling. The W7-X valves are situated at the lower inboard side vessel edge. As the only other fuelling method currently available for W7-X plasmas, it was compared to pellet fuelling. For this purpose, a time interval of W7-X discharge 20171115.038 where the increase of the line-integrated density employing gas fuelling is comparable to the average increase during the subsequent pellet series is used (cf. fig. 4.2.9). The total gas flow is show in all overview plots in sub-figure (b). The density profile change from gas fuelling is rather similar for all values of r_{eff} as shown in fig. 4.2.8.

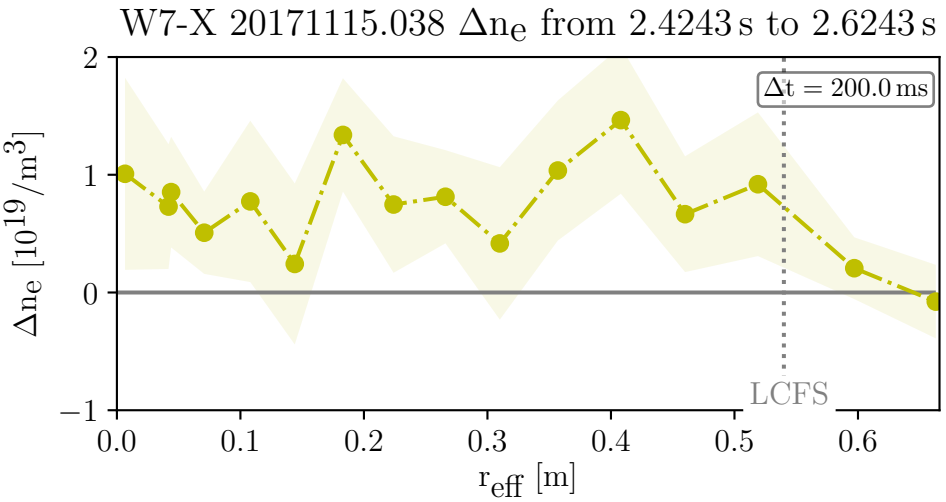

Fig. 4.2.8.: Electron density change in W7-X discharge 20171115.038 introduced by gas puff fuelling. The resulting line integrated density increase in the period shown was comparable to the average increase during the later pellet series.

With respect to the toroidal shape of the plasma, this means that most of the material is deposited in the outer region of the plasma where the volume increment per r_{eff} is larger. In the analysed case, 50 % of the material deposited within the LCFS relates to material that is located at $r_{eff} = 0.4\,m$ and further out whereas, for pellet series, effectively no material was deposited within this region (i.e. only further inward), at least not for the later pellets within the series. Therefore, peaked profiles cannot be introduced by gas puff fuelling but rather by pellet fuelling.
Plasmas with peaked density profiles are desirable because, in addition to several other advantages, they suffer less from strong edge radiation, and can therefore achieve, better performance and higher overall densities.

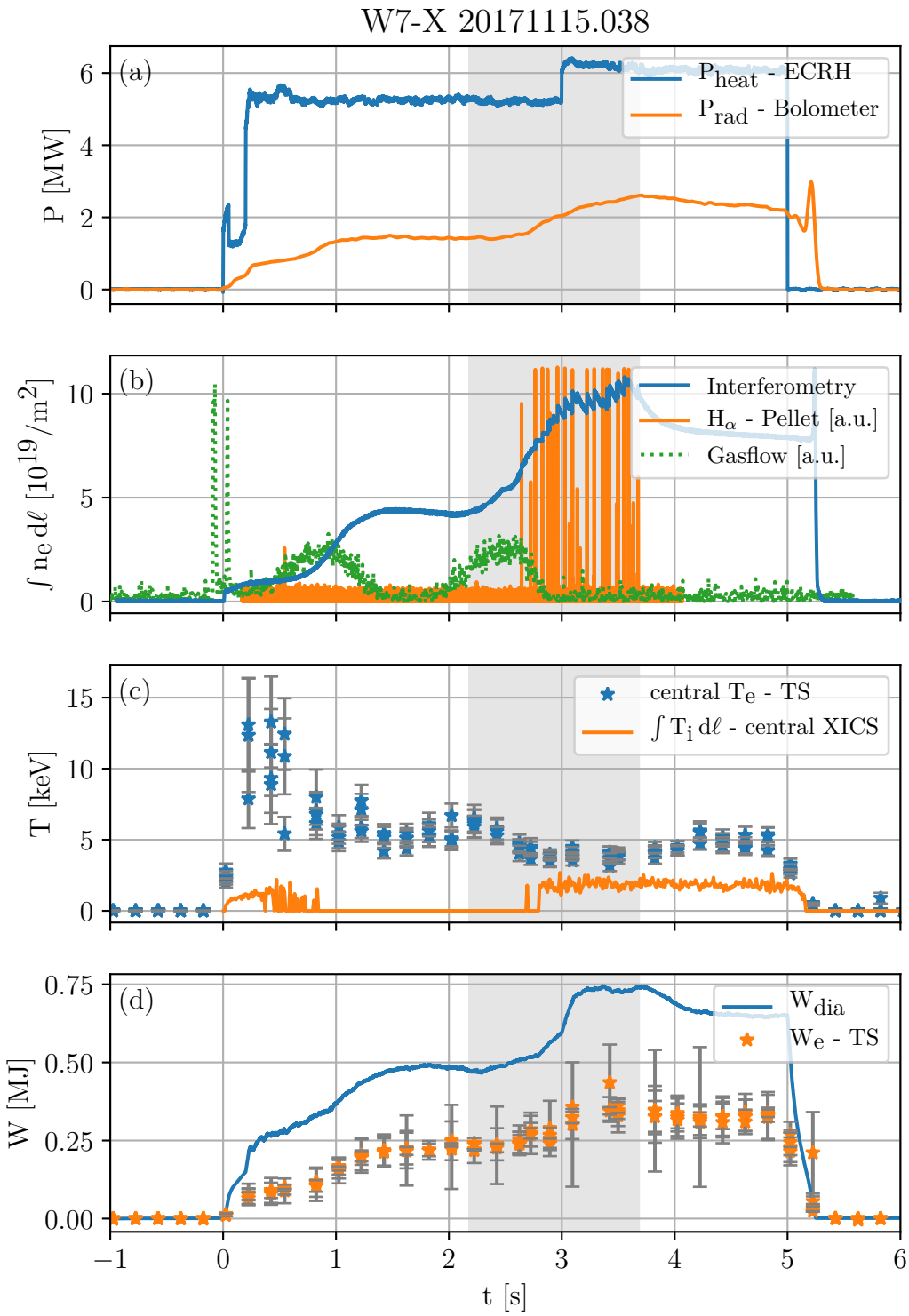

Fig. 4.2.9.: W7-X discharge 20171115.038 overview plot. The time interval of the analysed gas fuelling and the later pellet injection is indicated by the grey shading.

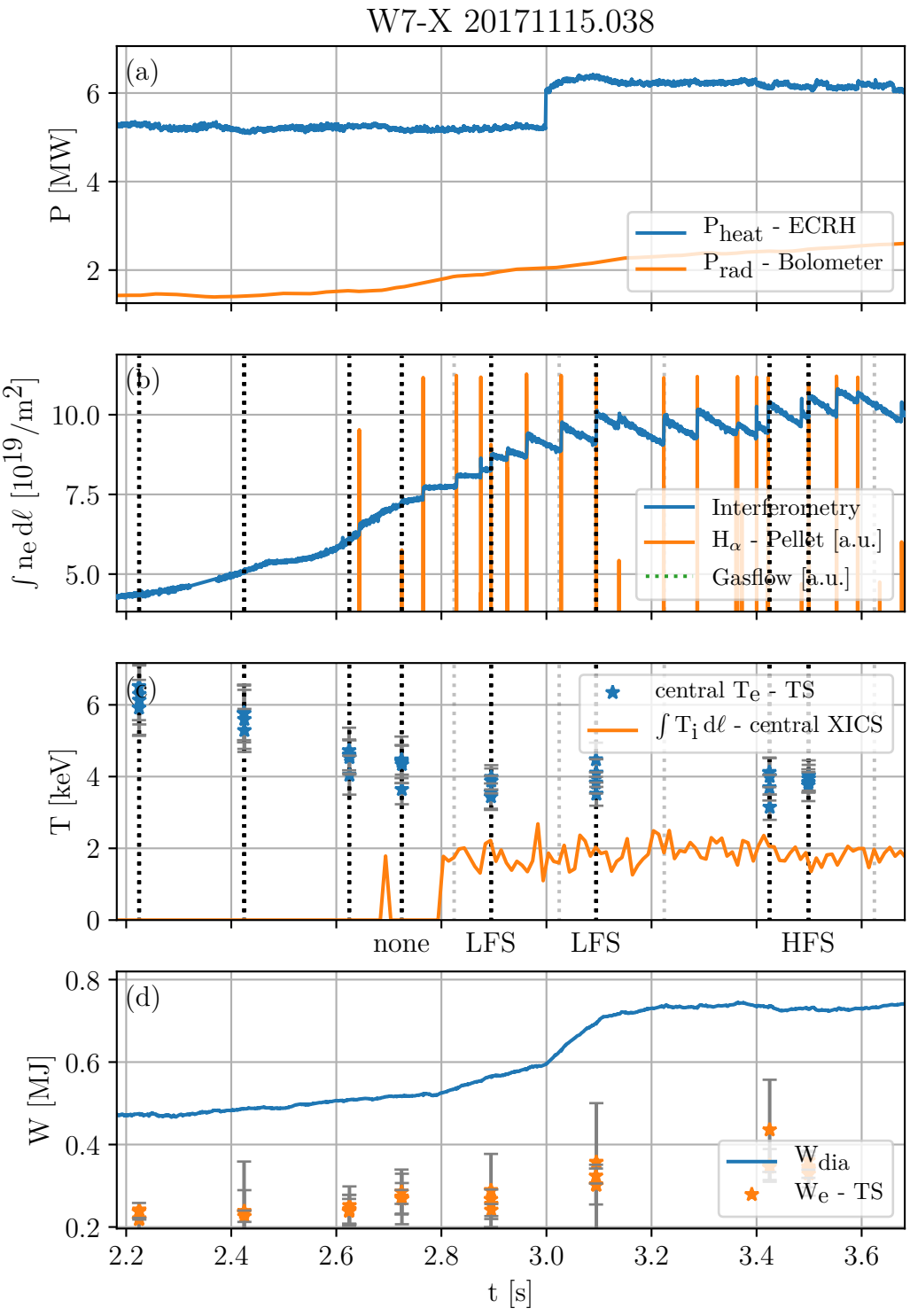

Fig. 4.2.10.: W7-X discharge 20171115.038 overview plot during the pellet injection phase. The dashed black lines indicate the timing of the Thomson scattering measurements; dashed grey lines indicate the uniform standard trigger. If the Thomson scattering diagnostic was triggered by a pellet the lines do not overlap. The pellet injection side is indicated by HFS (high field side) or LFS (low field side).

4.3. Profile Studies Between two Pellets from a Series

The W7-X discharge 20171206.025 was a helium discharge until 8 hydrogen pellets were injected from HFS starting at 23.5 s. The discharge was heated with the X2-mode of 140 GHz microwave radiation. The incident ECRH power is displayed in fig. 4.3.2. The 1st and 2nd pellet were injected when the burst-mode Thomson scattering diagnostic could not accept an external event trigger (cf. section 3.2) and was triggered automatically by the standard trigger ≈ 2.3 ms after the second pellet. The 3rd pellet's trigger was accepted and hence the rare situation occurred where the time interval between two pellets within a series could be analysed. The line integrated density obtained from the interferometer measurements is shown for the corresponding interval in fig. 4.3.1.

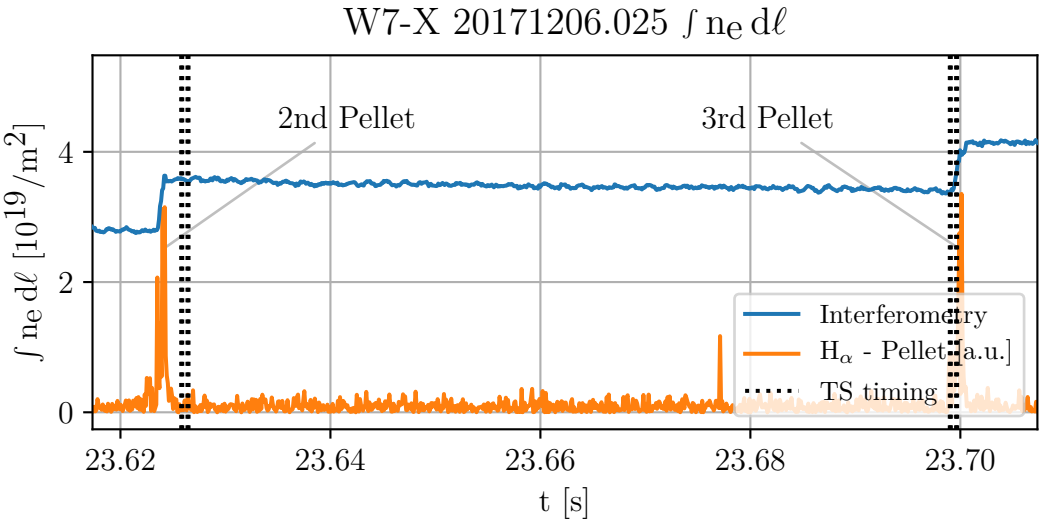

Fig. 4.3.1.: The line integrated electron density signal of W7-X discharge 20171606.025 plotted between the second and the third pellet. The dashed black lines indicate the timing of the Thomson scattering measurements; the H_α pellet ablation light diode-signal in arbitrary units is shown in orange for comparison.

In fig. 4.3.3 the electron density profile change induced by the first two pellets is shown at 2.3 ms. Similarly in fig. 4.3.4 the electron density profile change between 2.3 ms and 75.5 ms after the second pellet is shown depicting the 73.2 ms period where the interferometry signal does not change except for a small decrease.

The profile change introduced by the two pellets shown in fig. 4.3.3 is rather large, whereas in the period where no pellet was injected, shown in fig. 4.3.4, no

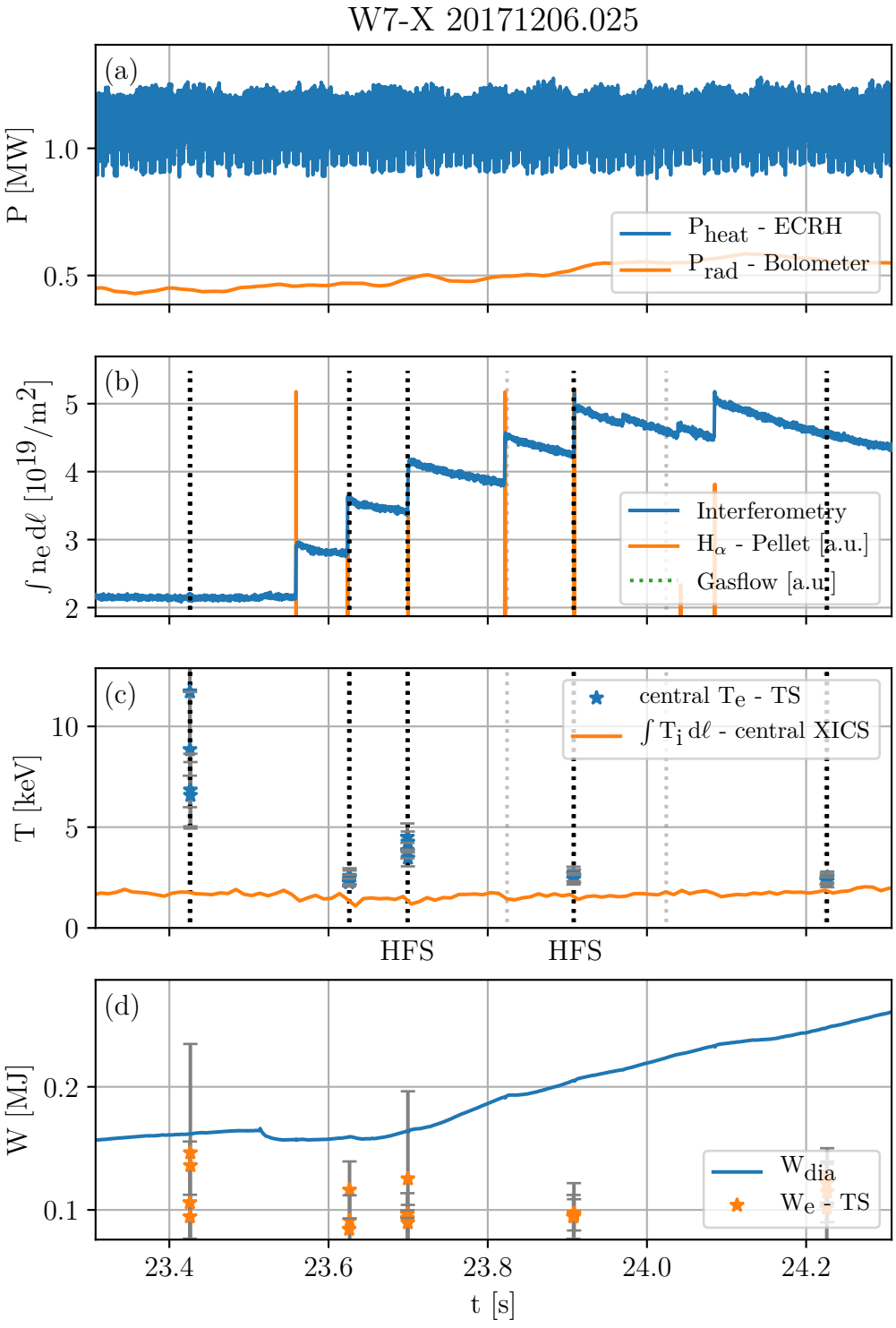

Fig. 4.3.2.: W7-X discharge 20171206.025 overview plot during the pellet injection phase. The dashed black lines indicate the timing of the Thomson scattering measurements; dashed grey lines indicate the uniform standard trigger. If the Thomson scattering diagnostic was triggered by a pellet the lines do not overlap. The pellet injection side is indicated by HFS (high field side) or LFS (low field side). The full overview plot can be found in the appendix.

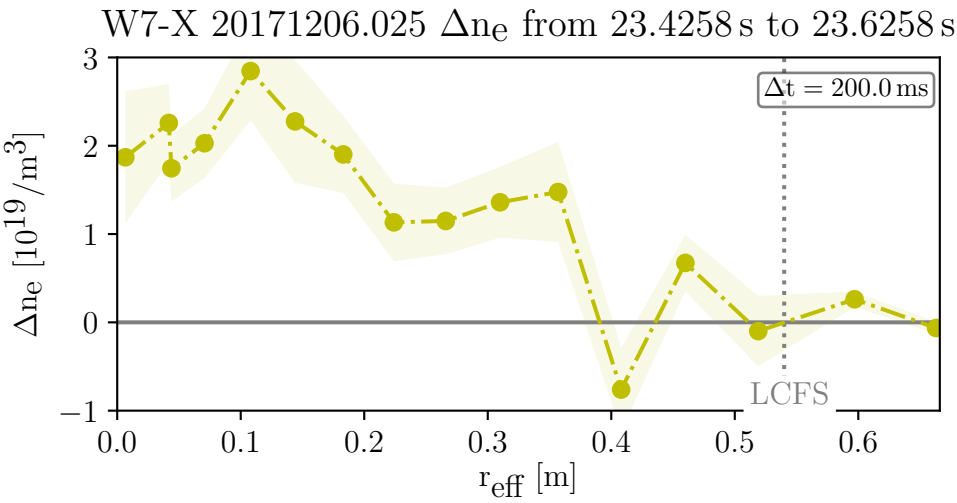

Fig. 4.3.3.: Electron density change in W7-X discharge 20171206.025 introduced by two pellets injected from HFS 2.3 ms after the second pellet was injected.

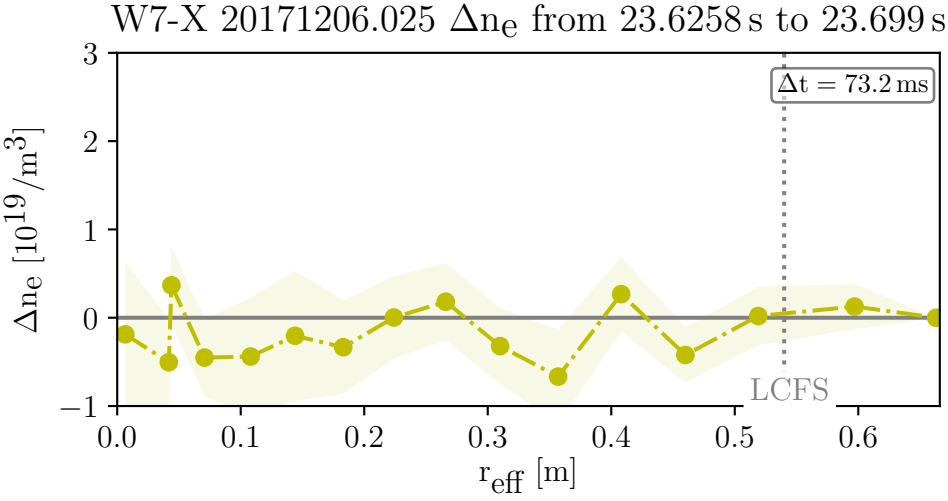

Fig. 4.3.4.: Electron density change in W7-X discharge 20171206.025 within 2.3 ms and 75.5 ms after the second pellet was injected. In the analysed 73.2 ms no further pellet was injected.

significant profile change was found except some small fluctuations that mainly lie within the uncertainties. From the two aforementioned plots and the mostly unchanged line-integrated density in the interval between the pellets, it is safe to say that the density profile rearrangement was finished within the 2.3 ms period after the second pellet.
Neoclassical particle transport was predicted to occur on much slower timescales on the order of 0.5 s in W7-X [59]. This experimental finding of much faster particle transport (< 2.3 ms) is rather remarkable, because it indicates the presence of anomalous transport mechanisms that dominate the neoclassical transport.
Additionally, this very quick equilibration is interesting with respect to the time interval of the a burst from the burst-mode Thomson scattering diagnostic being 1.2 ms. It seems like most of the profile change will be observable with the fully equipped burst-mode diagnostic in the next operational campaign. Moreover, it might be possible to rearrange the timing of the burst pulses such that ≈ 2 ms will be covered.

4.4. Pre-Cooling and Penetration Depth of Serial Pellets

The W7-X discharge 20171115.018 was a pure helium discharge until a mixture of 14 HFS and LFS hydrogen pellets was injected starting at 2.8 s. (Note: The 1st and 2nd pellets did not introduce a noticeable density increase but were clearly seen by the H_α monitoring diode.) The discharge was heated with the X2-mode of 140 GHz microwave radiation up until 2 s and with O2-mode (second harmonic ordinary mode) afterwards. The incident ECRH power during the injection of hydrogen pellets is displayed in fig. 4.4.2. The 6th and the 11th pellet were both injected from low field side and observed with the event-triggered burst-mode Thomson scattering diagnostic as shown in fig. 4.4.2 (c). The electron temperature profiles for the pellet injection time interval are shown as 3D plot in fig. 4.4.1.

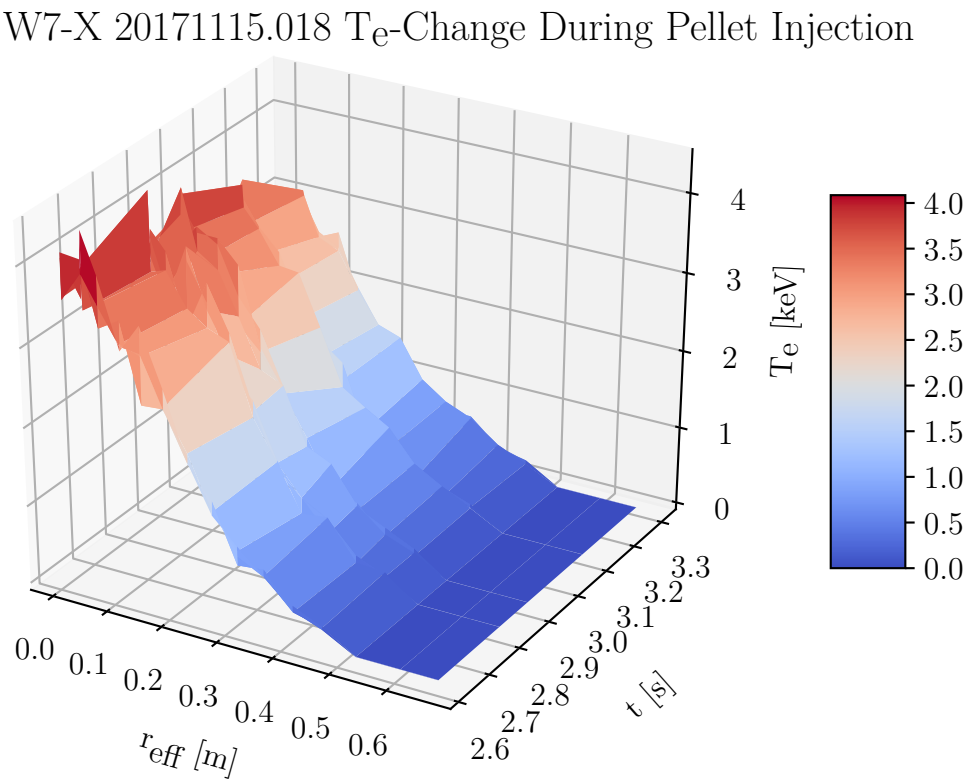

Fig. 4.4.1.: Electron temperature profile evolution of W7-X discharge 20171115.018 in the pellet injection time interval. Temperature spikes outside the LCFS exceeding the central temperature were set to zero.

As can be seen, the overall temperature decreases sightly; but more importantly,

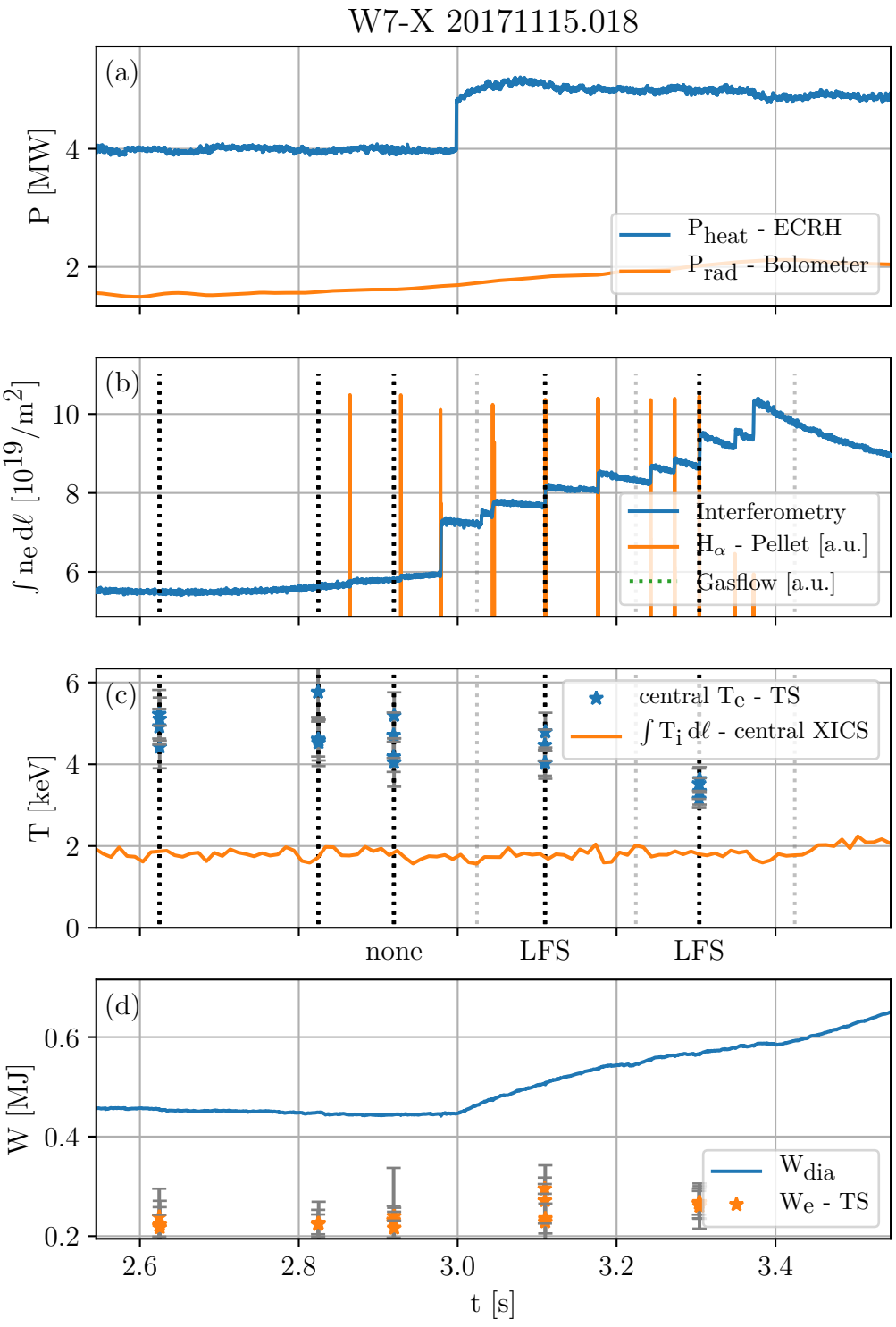

Fig. 4.4.2.: W7-X discharge 20171115.018 overview plot during the pellet injection phase. The dashed black lines indicate the timing of the Thomson scattering measurements; dashed grey lines indicate the uniform standard trigger. If the Thomson scattering diagnostic was triggered by a pellet the lines do not overlap. The pellet injection side is indicated by HFS (high field side) or LFS (low field side). The full overview plot can be found in the appendix.

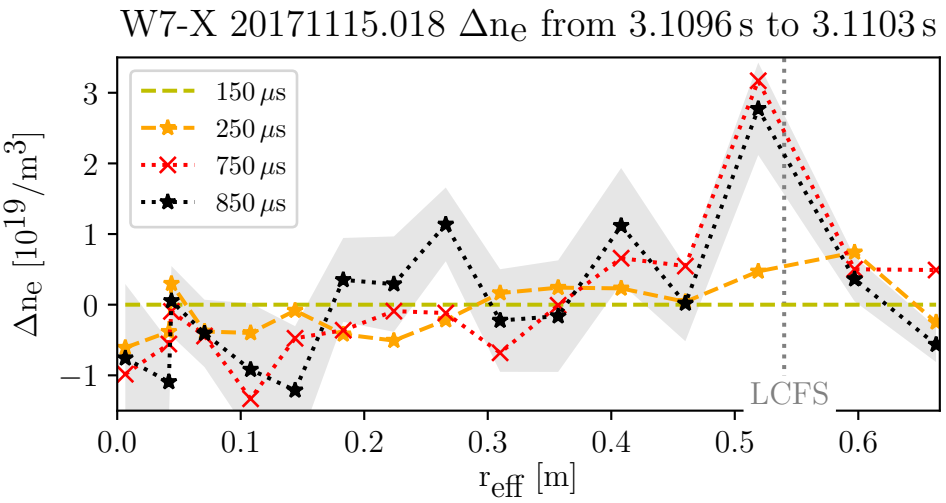

Fig. 4.4.3.: Electron density change induced by the 6th pellet (low field side) injected during W7-X discharge 20171115.018 relative to the first density profile from the burst.

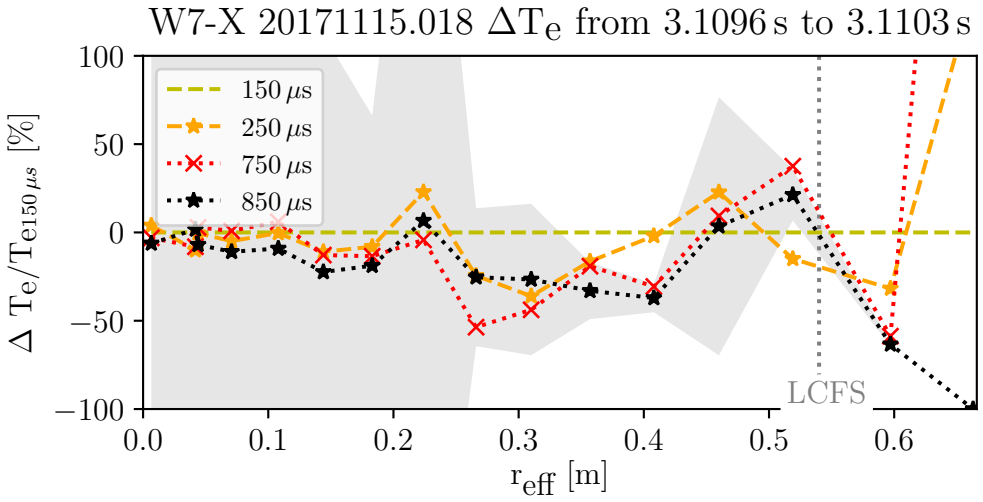

Fig. 4.4.4.: Electron temperature change induced by the 6th pellet (low field side) injected during W7-X discharge 20171115.018 normalized to the first temperature profile from the burst.

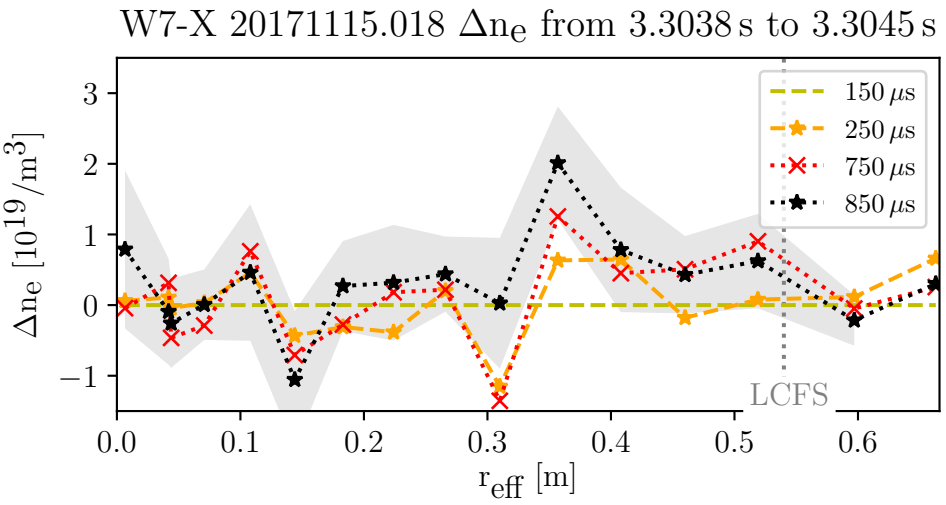

Fig. 4.4.5.: Electron density change induced by the 11th pellet (low field side) injected during W7-X discharge 20171115.018 relative to the first density profile from the burst.

the edge cools disproportionately as indicated by the light blue gradient region in fig. 4.4.1 shifting inward. Additionally, to investigate the change during the pellet ablation phase, which cannot be discretised with the low time resolution of fig. 4.4.1, the temperature change $\Delta T/T$ within the burst is shown in fig. 4.4.4. A temperature decrease of about 40 % can be found for the fourth burst (850 µs) between $r_{eff} \approx 0.25$ m and $r_{eff} \approx 0.45$ m. This "pre-cooling" allows the next pellet to penetrate deeper than the previous pellet because the pellet material ablation rate is smaller for lower background plasma temperature. Accordingly, the peak density increase introduced by the 11th pellet was found now penetrating deeper, up to $r_{eff} \approx 0.36$ m, as shown in fig. 4.4.5, whereas the peak increase of the 6th pellet was found further out at $r_{eff} \approx 0.52$ m as shown in fig. 4.4.3.

5. Conclusions and Outlook

The conclusions presented in this chapter cover the event-triggered burst-mode Thomson scattering diagnostic's upgrade as well as the pellet fuelling studies carried out employing the upgraded diagnostic. A short outlook to further applications and improvements is given subsequently.

5.1. Conclusions

To detect short transient events, it is necessary to synchronize event and measurement. With the developed trigger logic utilizing the pellet ablation H_α trigger signal, it succeeded in reliably triggering the Thomson scattering laser system, matching the timings of cryogenic pellets injected into the plasma. The laboratory tests showed the general applicability for other trigger events as well and demonstrated the logic circuit developed for the purpose of triggering meets all requirements. These requirements were filtering for events in a certain acceptance interval and blocking the regular trigger accordingly to maintain the original repetition frequency on average. Moreover, no harm was caused to the laser system confirming that it stayed within the thermal limits, as calculated employing the general heat equation, even for non-uniform laser pulse triggering.
The duration of the pellet ablation and depositions effects is approximately 1 ms. To provide several measurements in this time interval, the special burst-mode operation regime of the Thomson scattering lasers was employed. The potential risks accompanying the burst-mode laser operation were carefully assessed in the laboratory investigations. The laser configurations were optimized such that the beam profile and the beam pointing stability did not change compared to the normal operation. Laser self emission was impeded and the energies of individual burst pulses were maximized and balanced. The chosen burst contains four consecutive laser pulses with $\approx 1\,\mathrm{J}$ energy per pulse compared to the $\approx 1.5\,\mathrm{J}$ energy per pulse of normal mode operation. It was verified that the optical components employed in the laser and the beam path could withstand the loads of the burst-mode operation. The reliable operation of the Thomson scattering diagnostic in burst mode as whole was shown.
For the setup at W7-X, a fast energy monitor employing a pin diode and a diffusive reflecting quartz plate was set-up to surveil the individual pulse energies of the laser in burst-mode operation. Its proper functionality was validated by an absolutely-calibrated pyroelectric monitor. The not-yet fully understood energy fluctuation of each 2nd laser pulse generated by the repeated switching of the laser Pockels cell was identified by the fast energy monitor. Furthermore, indications of the later verified clipping of the laser beam as well as the thermal drift were found employing the energy monitor signal over the course of a day.
Nevertheless, one of the main unexpected difficulties of this work arose from the clipping of the laser beam beyond the plasma. It made the normalisation of the obtained data to the varying laser energy impossible. Therefore, an alternative calibration method, the cross-calibration to the interferometry, was applied. This method, initially introduced for the burst-mode operation only, will be applied to the normal-mode Thomson scattering density data as well to compensate for the

clipping of the laser beam that occurred during normal-mode operation.
With an appropriate calibration and the sufficient match of the pellet and Thomson lines of sight, the burst-mode provided 4 consecutive Thomson scattering measurements synchronised to pellet injection. The measurements were obtained at 150 µs, 250 µs, 750 µs, and 850 µs after the H_α ablation pellet trigger. Even with the lowered energy per pulse, the errors could be kept smaller than the observed effects, i.e. in the case of pellet injection studies. Thus, the event-triggered burst-mode Thomson scattering was confirmed to be a particularly useful tool for studying electron density and temperature profile effects introduced by the injection of cryogenic fuelling pellets on both 1 ms (burst) and 200 ms (inter-burst) timescales. The evaluation of single pellet events within the 1st ms after injection allowed for comparisons between the experimental data and the HPI2 code results [60]. The HPI2 [57] code was developed to model the behaviour of single cryogenic hydrogen pellets injected into plasmas. The diameter of the pellets injected into W7-X is typically 2 mm. A pellet penetration depth of up to 35 cm was measured while a depth of no more than 10 cm was predicted. Furthermore, experimental results show that the plasmoid, resulting from the ablation and consecutive ionisation of the pellet, expands up to 40 cm diameter radially measured along the Thomson line of sight. The determined plasmoid drift speed (≈ 1000 m/s) fits to the predicted values.
Fuelling efficiencies close to 100 % were obtained for all pellets, but this measurement suffered from a large uncertainty. Nevertheless the efficiencies of inboard and outboard side injected pellets did not deviate significantly as predicted from HPI2, and the deposition of the pellet material was found to be rather central. HPI2 gave maximum material deposition depths of 30 cm and 20 cm for inboard and outboard side injection, respectively. Although the inboard deposition apparently was more exclusively central than in the outboard case, core fuelling could be achieved by individual pellets for both injection geometries.
The density profile study carried out for the time between two consecutive injected pellets indicates that as quickly as 2.3 ms after a pellet was injected the profile equilibration had already ended. This finding does not match the neoclassical transport models and their respective timescales, indicating anomalously dominated transport mechanisms for current W7-X plasmas. Additionally, this means that the originally chosen burst-mode observation interval of 1.2 ms covers most of the interval of interest and only minor adjustments to the final system need to be implemented in the next campaign.
By employing pellet-triggered burst-mode Thomson scattering measurements, it was shown that the HPI2 code could not reproduce most of the profile changes introduced by the injection of cryogenic pellets into W7-X. Therefore, it can be emphasised that the W7-X adaption of the code does not yet include all physics

models that would be necessary to sufficiently describe the pellet ablation and deposition.
Series of injected pellets cannot be described by the code either but were studied using the upgraded diagnostic. Overall similar results were found for both pure inboard and mixed inboard & outboard pellet series. For series the central particle deposition additionally benefited from a pre-cooling effect that could be validated for W7-X based on both density and temperature profile measurements. This arises from the cooling of the plasma edge by former pellets of the series. The comparison of injection geometry for pellet series did show that efficient core fuelling is possible for both inboard and outboard injection. A future injector could therefore employ one injection geometry only; an outboard injection system would be preferable with respect to engineering constrains.
A comparable fuelling study for hydrogen gas puff fuelling showed a less favourable general density profile increase rather than the centrally dominated behaviour of pellet fuelling. Pellets therefore turned out to be more promising for high performance plasma operation than gas puff fuelling.

Finally, it can be stated that the understanding of the pellet processes advanced significantly by employing the event-triggered burst-mode Thomson scattering system in combination with the line integrated densities provided by the interferometer measurements.

5.2. Outlook

The future implementation of two additional lasers into the Thomson scattering diagnostic will increase the number of sampling points within $\approx 1\,\mathrm{ms}$ from the available 4 to 12 pulses. Thus the capabilities of the prototypical implementation described in this thesis will be increased. This will help to understand the underlying physics processes of pellet ablation and deposition in W7-X and therefore to improve the models employed by the HPI2 code. The aim is that the code can then be used to precisely describe pellet injection into W7-X varying parameters that cannot be changed in the experimental setup, e.g. the pellet speed, size, or injection geometry.
Application specific timings for the individual lasers can be chosen and delays can be added in the future. The available spacing between the lasers is mainly limited by the data acquisition system. The shortest time delay between two laser pulses will be $2\,\mu\mathrm{s}$. Longer delays will, for instance, allow for the investigation of the post-pellet density decrease that was found for some pellet series on a $\approx 10\,\mathrm{ms}$ timescale and is not yet investigated. To sustain the high densities achieved by pellet injection, it is obligatory to avoid this quick decrease. In principle, the delay has no upper limit but is only reasonable if lower than half of the time between two consecutive bursts.
In the next campaign measurements on the inboard side are planned, since 30 additional scattering volumes on this side of the plasma are designated. By this improvement, the results obtained for outboard side geometry can then be compared to inboard measurements. Moreover, full temperature and density profiles will be obtained, and thus profile symmetry studies can be performed.
Once the trigger timer event (TTE) system becomes fully available for the post-2020 experimental campaigns, other events can be employed as laser triggers. By then it will be possible to study various fast transient plasma events employing the trigger logic that was developed in the course of this thesis. Important candidates are: low frequency Alfvén Eigenmodes, a type of magnetohydrodynamic plasma waves; neutral beam and electron cyclotron resonance heating on/off-switching or modulation; laser blow-off experiments; and edge localized mode crashes.
For electron cyclotron current drive crashes, experiments have already been proposed for the next experimental campaign at W7-X. Without a dedicated trigger signal, though, these experiments rely on a sufficient crash predictability and reproducibility.

List of Figures

List of Tables

Bibliography

[1] F. Koechl et al., *Modelling of Pellet Particle Ablation and Deposition: The Hydrogen Pellet Injection code HPI2*, Preprint EFDA–JET–PR(12), vol. 57,

[2] Earth System Research Laboratory, U.S. Department of Commerce, *Full Mauna Loa CO2 record*, acessed: 09.04.2018. [Online]. Available: `https://www.esrl.noaa.gov/gmd/ccgg/trends/full.html`.

[3] S. Solomon et al., *Contribution of Working Group I to the Fourth Assessment Report of the Intergovernmental Panel on Climate Change*. Cambridge: Cambridge University Press, 2007.

[4] V. Ramanathan, *The Greenhouse Theory of Climate Change: A Test by an Inadvertent Global Experiment*, Science, vol. 240, pp. 293–299, 1988.

[5] L. S. Rothman et al., *The HITRAN 2008 molecular spectroscopic database*, Journal of Quantitative Spectroscopy and Radiative Transfer, vol. 100, pp. 533–572, 2009.

[6] C. W. Team et al., *Climate Change 2014: Synthesis Report. Contribution of Working Groups I, II and III to the Fifth Assessment Report of the Intergovernmental Panel on Climate Change*. Geneva, Switzerland: IPCC, 2014, pp. 151.

[7] Arbeitsgemeinschaft Energiebilanzen, *Endenergieverbrauch 2016 nach Sektoren und Energieträgern*, acessed: 09.04.2018. [Online]. Available: `https://www.umweltbundesamt.de/daten/energie/energieverbrauch-nach-energietraegern-sektoren`.

[8] Williams, David R., *Sun Fact Sheet*, acessed: 10.04.2018. [Online]. Available: `https://nssdc.gsfc.nasa.gov/planetary/factsheet/sunfact.html`.

[9] J. Eddy, *A New Sun: The Solar Results From Skylab*. Washington, D.C.: NASA, 1979, p. 37.

[10] F. F. Chen, *Introduction to Plasma Physics*. New York: Springer US, 1974.

[11] Tuli, Jagdish K., *Nuclear Wallet Card*, acessed: 10.04.2018. [Online]. Available: `http://www.nndc.bnl.gov/nudat2/`.

[12] R. Schlögl, *Zum Mechanismus der Oxidation von elementarem Kohlenstoff mit Sauerstoff*, Chemie in unserer Zeit, vol. 28, p. 166, 1994.

[13] E. A. Azizov, *Tokamaks: from A D Sakharov to the present (the 60-year history of tokamaks)*, Physics-Uspekhi, vol. 55, p. 190, 2012.

[14] L. Spitzer jr., *The Stellarator Concept*, The Physics of Fluids, vol. 1, p. 253, 1958.

[15] G. W. C. Kaye et al., *Tables of Physical and Chemical Constants*. London: Longmans, Green and Co, 1911.

[16] H. Craig, *Standard for Reporting Concentrations of Deuterium and Oxygen-18 in Natural Waters*, Science, vol. 133, pp. 1833–1834, 1961.

[17] JET Team, *Fusion energy production from a deuterium-tritium plasma in the JET tokamak*, Nuclear Fusion, vol. 32, p. 187, 1992.

[18] P. T. Lang et al., *Considerations on the DEMO pellet fuelling system*, Fusion Engineering and Design, vol. 96-97, pp. 123–128, 2015.

[19] P. T. Lang et al., *Refuelling performance improvement by high speed pellet launch from the magnetic high field side*, Nuclear Fusion, vol. 41, p. 1107, 2001.

[20] L. R. Baylor et al., *Pellet fuelling deposition measurements on Jet and TFTR*, Nuclear Fusion, vol. 32, p. 2177, 1992.

[21] T. S. Pedersen et al., *Key results from the first plasma operation phase and outlook for future performance in Wendelstein 7-X*, Physics of Plasmas, vol. 24, p. 055503, 2007.

[22] R. Yasuhara et al., *Short-interval multi-laser Thomson scattering measurements of hydrogen pellet ablation in LHD*, Review of Scientific Instruments, vol. 85, p. 11D822, 2014.

[23] R. Scannell et al., *Experimental investigation into ELM filament formation on MAST*, Plasma Physics and Controlled Fusion, vol. 49, pp. 1431–1446, 2007.

[24] M. Knoop et al., *Trapped Charged Particles: A Graduate Textbook With Problems And Solutions (Advanced Textbooks in Physics)*. Singapore; Hackensack, NJ: Advanced Textbooks in Physics (World Scientific), 2016.

[25] M. Hölzl, *Diffusive Heat Transport across Magnetic Islands and Stochastic Layers in Tokamaks*, Dissertation, p. 21, 2010.

[26] J. C. Maxwell, *Illustrations of the Dynamical Theory of Gases. Part I. On the Motions and Collisions of Perfectly Elastic Spheres*, Philosophical Magazine [4], vol. 19, pp. 19–32, 1860.

[27] J. P. Freidberg, *Plasma Physics and Fusion Energy*. Cambridge: Cambridge University Press, 2007.

[28] P. Debye, *Zur Theorie der spezifischen Wärmen*, Annalen der Physik, vol. 344, pp. 789–839, 1912.

[29] S.-D. Poisson, *Mémoire sur la distribution de l'électricité à la surface des corps conducteurs*, Mémoires de la Classe des Sciences Mathématiques et Physiques de l'Institut Impérial de France, vol. 12, pp. 1–92, 1812.

[30] H. Maaßberg et al., *Transport in stellarators*, Plasma Physics and Controlled Fusion, vol. 35, pp. B319–32, 1993.

[31] A. Einstein, *The Quantum Theory of Radiation*, Physikalische Zeitschrift, vol. 18, p. 121, 1917.

[32] J. E. Geusic et al., *Laser oscillations in Nd-doped yttrium aluminum yttrium gallium and gadolinium garnets*, Applied Physics Letters, vol. 4, p. 182, 1964.

[33] J. Eichler et al., *Laser*. Berlin, Heidelberg: Springer Vieweg, 2015, pp. 137–168.

[34] R. Clausius, *Über die bewegende Kraft der Wärme und die Gesetze, welche sich daraus für die Wärmelehre selbst ableiten lassen*, Poggendorffs Annalen der Physik und Chemie, vol. 79, p. 368–397 & 500–524, 1850.

[35] J. B. J. Fourier, *Theorie Analytique de la Chaleur*, Librairies pour Mathematiques, l'Architecture Hydraulique et la Marine, p. 92, 1822.

[36] Crystran Ltd, *Yttrium Aluminium Garnet (YAG)*, acessed: 19.03.2018. [Online]. Available: `https://www.crystran.co.uk/userfiles/files/yttrium-aluminium-garnet-yag-data-sheet.pdf`.

[37] I. Hutchinson, *Principles of Plasma Diagnostics*. Cambridge: Cambridge University Press, 1987, pp. 273–321.

[38] R. Pasqualotto et al., *High resolution Thomson scattering for Joint European Torus (JET)*, Review of Scientific Instruments, vol. 75, p. 3891, 2004.

[39] B. Kurzan et al., *Edge and core Thomson scattering systems and their calibration on the ASDEX Upgrade tokamak*, Review of Scientific Instruments, vol. 82, p. 103501, 2011.

[40] I. Yamada et al., *Current status of the LHD Thomson scattering system*, Journal of Instrumentation, vol. 7, p. C05007, 2012.

[41] T. N. Carlstrom et al., *Design and operation of the multipulse Thomson scattering diagnostic on DIII-D*, Review of Scientific Instruments, vol. 63, p. 4901, 1992.

[42] J. W. Hughes et al., *Thomson scattering upgrades on Alcator C-Mod*, Review of Scientific Instruments, vol. 74, p. 1667, 2003.

[43] J. H. Poynting, *On the Transfer of Energy in the Electromagnetic Field*, Philosophical Transactions of the Royal Society of London, vol. 175, pp. 343–361, 1884.

[44] C. F. Gauß, *Theoria motus corporum coelestium in sectionibus conicis solem ambientium*. Hamburg: sumtibus Frid. Perthes et I. H. Besser, 1809.

[45] C. Doppler, *Über das farbige Licht der Doppelsterne und einiger anderer Gestirne des Himmels*, Abhandlungen der k. böhm. Gesellschaft der Wissenschaften, vol. 5/2, pp. 465–482, 1842.

[46] J. Sheffield et al., *Plasma Scattering of Electromagnetic Radiation: Theory and Measurement Techniques*. Amsterdam: Academic Press, Elsevier Inc., 2011.

[47] S. A. Bozhenkov et al., *The Thomson scattering diagnostic at Wendelstein 7-X and its performance in the first operation phase*, Journal of Instrumentation, vol. 12, p. P10004, 2017.

[48] R. Fischer et al., *Thomson scattering analysis with the Bayesian probability theory*, Plasma Physics and Controled Fusion, vol. 44, pp. 1501–1519, 2002.

[49] O. Naito et al., *Analytic formula for fully relativistic Thomson scattering spectrum*, Physics of Plasmas, vol. 5, p. 4256, 1993.

[50] ——, *Erratum: Analytic formula for fully relativistic Thomson scattering spectrum*, Physics of Plasmas, vol. 1, p. 806, 1994.

[51] J. Howard et al., *Rotational Raman calibration of Thomson scattering*, Journal of Physics D: Applied Physics, vol. 12, p. 1435, 1979.

[52] E. Pasch et al., *The Thomson scattering system at Wendelstein 7-X*, Review of Scientific Instruments, vol. 87, p. 11E729, 2016.

[53] P. T. Lang et al., *ELM pacing and high-density operation using pellet injection in the ASDEX Upgrade all-metal-wall tokamak*, Nuclear Fusion, vol. 54, p. 083009, 2014.

[54] B. Pegourie, *Review: Pellet injection experiments and modelling*, Plasma Physics and Controled Fusion, vol. 49, p. R87, 2007.

[55] W. A. Houlberg et al., *Neutral and plasma shielding model for pellet ablation*, Nuclear Fusion, vol. 28, p. 595, 1988.

[56] S. Futatani et al., *Non-linear MHD modelling of ELM triggering by pellet injection in DIII-D and implications for ITER*, Nuclear Fusion, vol. 54, p. 73008, 2014.

[57] N. Panadero et al., *Experimental studies and simulations of hydrogen pellet ablation in the stellarator TJ-II*, Nuclear Fusion, vol. 58, p. 026025, 2018.

[58] M. Dibon et al., *Blower Gun pellet injection system for W7-X*, Fusion Engineering and Design, vol. 98–99, p. 1759–1762, 2015.

[59] Y. Turkin et al., *Neoclassical transport simulations for stellarators*, Physics of Plasmas, vol. 18, p. 022505, 2011.

[60] N. Panadero, *Private communication*, Greifswald, 2018.

[61] A. Iiyoshi et al., *Overview of the Large Helical Device project*, Nuclear Fusion, vol. 39, p. 1245, 1991.

[62] Max-Planck-Institut für Plasmaphysik, *Introduction – the Wendelstein 7-X stellarator*, acessed: 11.04.2018. [Online]. Available: `http://www.ipp.mpg.de/16931/einfuehrung`.

[63] M. Odenwald, *GRAFIK DER WOCHE Die Sonne auf die Erde holen In Greifswald startet ein Versuchsreaktor, der Atome verschmelzen soll*, Focus, vol. 6, 2016.

[64] P. T. Lang et al., *A pellet launcher tool optimized for the control of edge localized modes in ASDEX Upgrade H-mode plasmas*, Fusion Engineering and Design, vol. 82, p. 1073–1080, 2007.

[65] J. G. Leidenfrost, *De aquae communis nonnullis qualitatibus tractatus*. Duisburg: Ovenius, 1756.

[66] M. J. Gouge et al., *A combined microwave cavity and photographic diagnostic for high-speed projectiles*, Review of Scientific Instruments, vol. 61, p. 2102, 1990.

[67] E. Pasch, *Private communication*, Greifswald, 2018.

[68] J. Knauer et al., *A New Dispersion Interferometer for the Stellarator Wendelstein 7-X*, P. Mantica (Ed.), 43rd EPS Conference on Plasma Physics, European Physical Society, p. P4.017, 2016.

[69] S. P. Hirshman et al., *Preconditioned descent algorithm for rapid calculations of magnetohydrodynamic equilibria*, Journal of Computational Physics, vol. 96, pp. 99–109, 1991.

[70] G. Kocsis, *Private communication*, Greifswald, 2018.

[71] J. Baldzuhn et al., *Particle fueling experiments with a series of pellets in LHD*, Plasma Physics and Controlled Fusion, vol. 60, p. 035006, 2018.

[72] P. T. Lang et al., *High-Efficiency Plasma Refuelling by Pellet Injection from the Magnetic High-Field Side into ASDEX Upgrade*, Physical Review Letters, vol. 79, p. 1487, 1996.

Appendices

A. Trigger Transmission Line Delay

After the successful setup of the transmission path for the pellet trigger, an investigation on the total transit time of the H_α signal was carried out. In order to do so, a reference signal was transmitted via a copper cable to the location of the photo diode and back via the optical transmission line. Additionally, the signal was passed trough a logic circuit. The delay arising from the transmission line was determined using an oscilloscope. The resulting image is shown below:

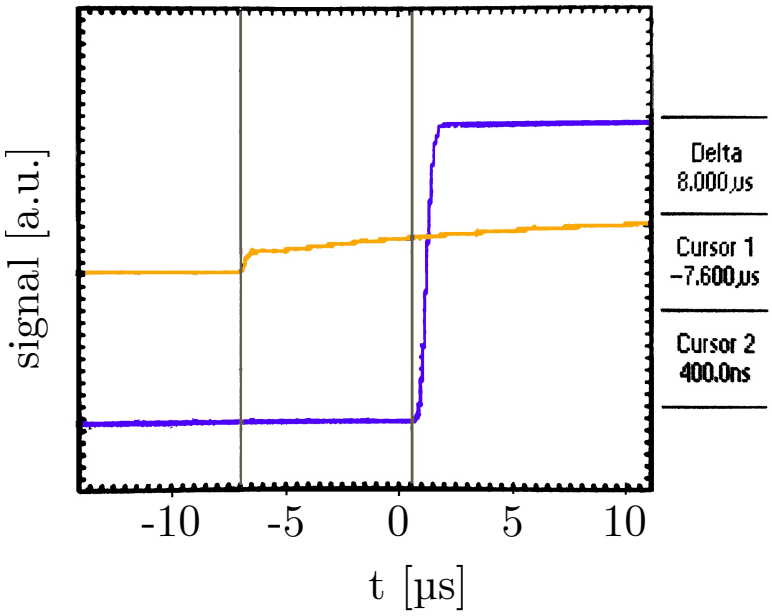

Fig. A.0.1.: Transit time of a signal transmitted via copper cable to the amplifier behind the H_α-signal detecting diode and back via the optical fiber transmission line including an amplifier and the Baumer fiber optic link "HEAG17x". The cursor lines and the related values on the right hand side where added later.

To obtain the correct transmission time for the real conditions, the delay from the copper cable needed to be subtracted. Unfortunately, the cooper cable was inaccessible after installation. Therefore, the delay was measured by comparing the reference signal with its own reflection at the cable's open end as shown in fig. A.0.2:

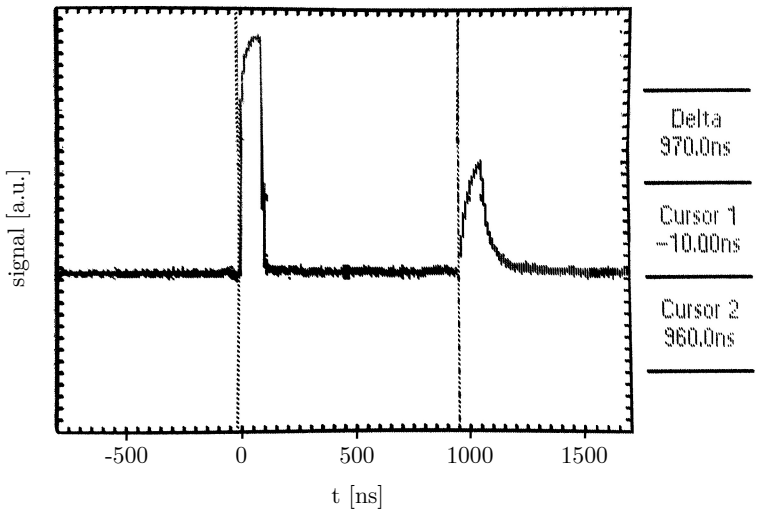

Fig. A.0.2.: Reference signal and its reflection at the open end of the copper cable.

The resulting 970 ns needed to be halved because the reflection passes trough the cable twice. Hence the delay between the pellets H_α emission start and the signal arriving at the lasers is $\approx 7.5\,\mu s$ which is neglectable compared to the time the lasers need to reach a sufficient population inversion (150 - 200 µs). H_α signals from real pellets transmitted throughout the experimental campaign are displayed below:

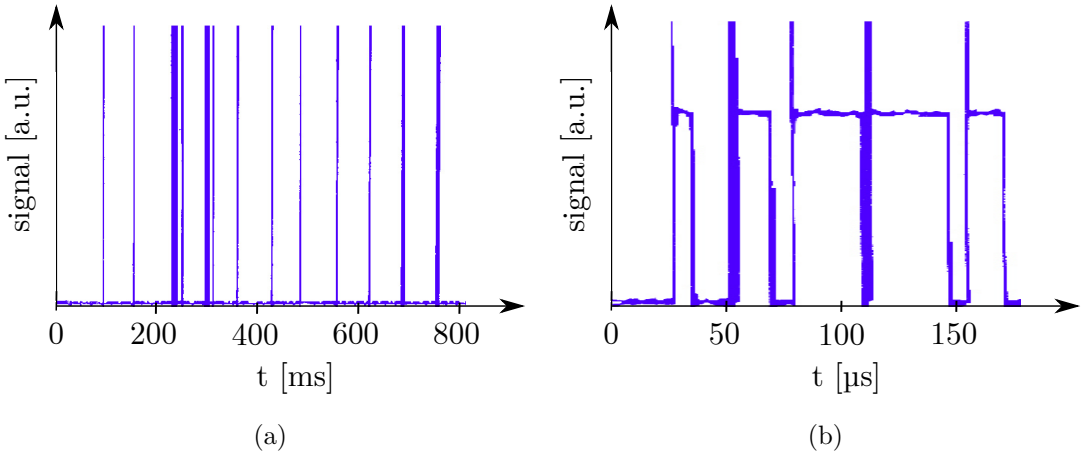

Fig. A.0.3.: All H_α signals throughout a normal pellet shot (a) and a version zoomed in a smaller time interval (b).

B. Visualisation of the Event-Trigger Scheme

A visualisation of the event-trigger scheme, taking the 5 Hz standard frequency of the burst mode as an example, is shown in fig. B.0.1. It is likewise applicable to the 10 Hz standard Thomson scattering laser frequency.

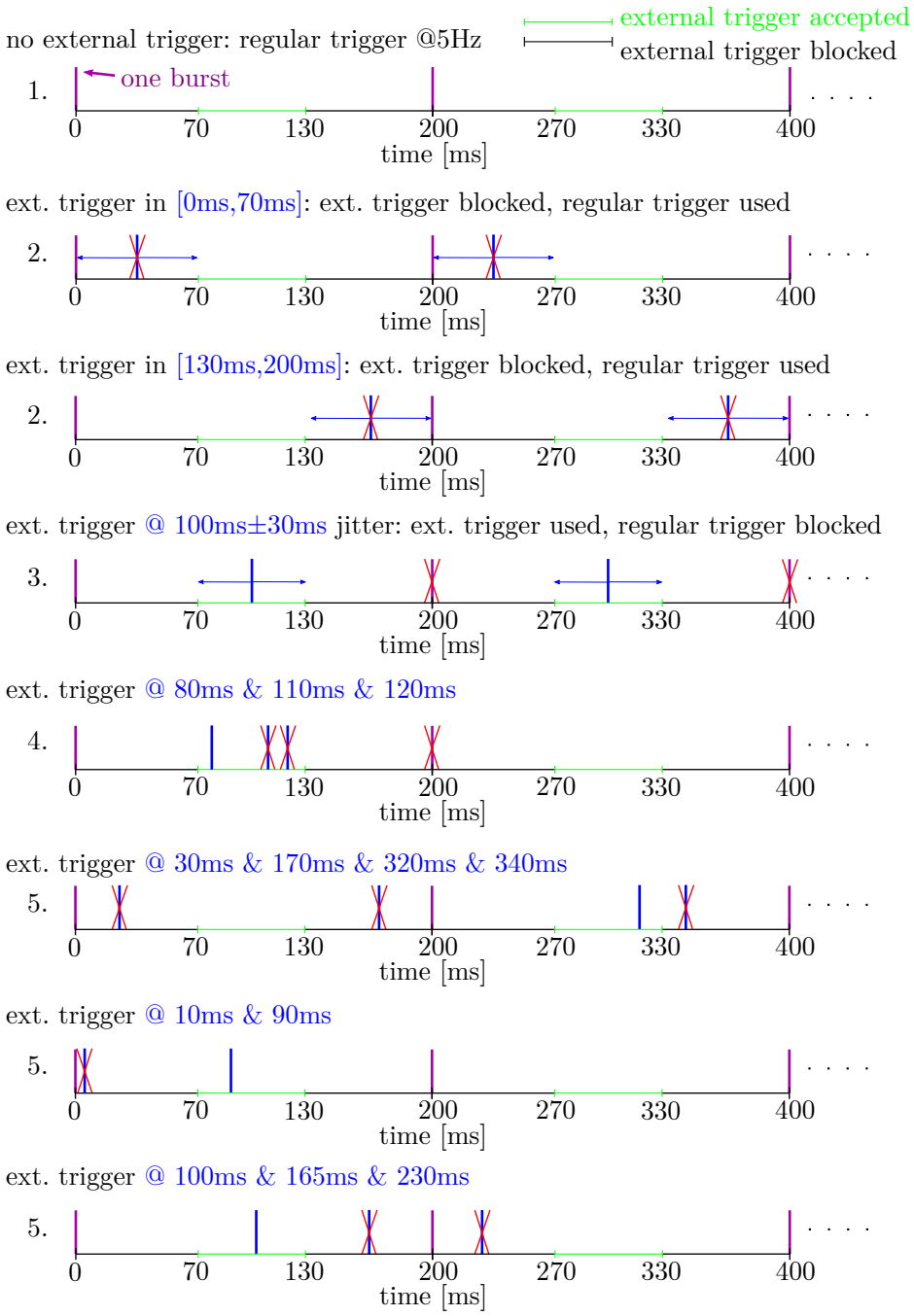

Fig. B.0.1.: Visualisation of the required trigger scheme.

C. Burst-Mode Laser Pulse Energy Calibration by Raman Scattering

During a Raman calibration, the Thomson diagnostic is operated independent instead of using the W7-X control system. This system would usually start the lasers a certain amount of time ahead of the measurements. Therefore one would not be able to find the ramp-up of the laser energy in the data. For the Raman calibration, this period was excluded by hand and is the reason why all plots start at 5 s. This is the energy ramp-up time required by the lasers.

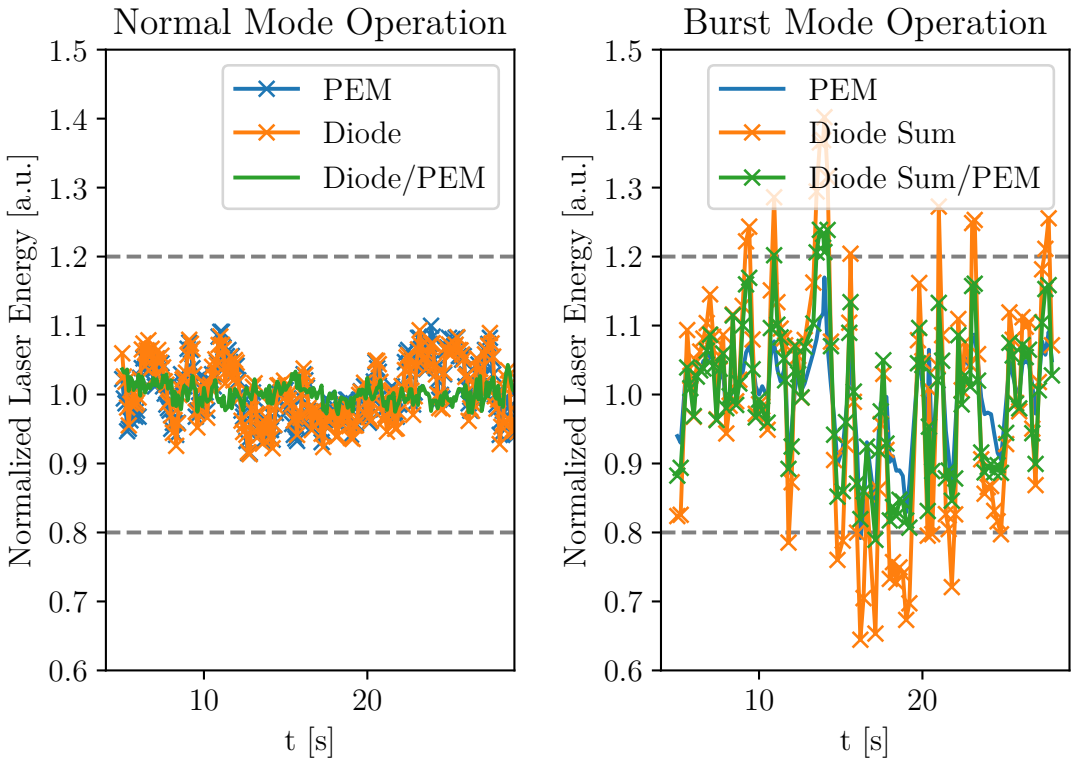

Fig. C.0.1.: Temporal evolution of the laser energy during a Raman calibration measurement determined using the PEM and the diode as well as their quotient during normal and burst-mode operation. For burst-mode operation, the sum of the four pulses per burst was taken to create a signal comparable to the PEM measurement.

As a sanity check, the normalized laser energy signal provided by the PEM and the diode as well as their quotient were plotted for normal and for burst-mode operation. For burst-mode operation the sum of the four pulses per burst was employed to gain a signal comparable to the PEM measurement. As shown in fig. C.0.1 and as expected from the study above, the quotient was approximately unity in the normal mode. The variation coefficient, defined as:

$$v = \frac{\text{standard derivation}}{\text{mean}}, \tag{C.0.1}$$

was $v = 1.5\,\%$. The slow fluctuation of the PEM and diode signal that could not be explained with the $1\,\%$ intrinsic energy scatter of the laser was unforeseen. This fluctuation as well as the quotients' deviation from unity ($v = 10.8\,\%$) were even larger during burst-mode operation. The fluctuations could be explained by a clipping of the laser beam combined with thermal drifts, mechanical vibrations and the beam pointing stability changing the amount of the laser energy reaching the energy monitors. This will be discussed in further detail throughout this section. The larger fluctuation during burst-mode operation implies that the beam pointing stability plays a leading role since the other two effects did not change for the burst mode.
Proceeding with the Raman calibration, the Raman signal normalized to the laser energy from both the PEM and the diode were plotted for normal operation in fig. C.0.2. The variation coefficients are $v = 8.6\,\%$ for the PEM normalisation and $v = 8.8\,\%$ for the diode normalisation, respectively.

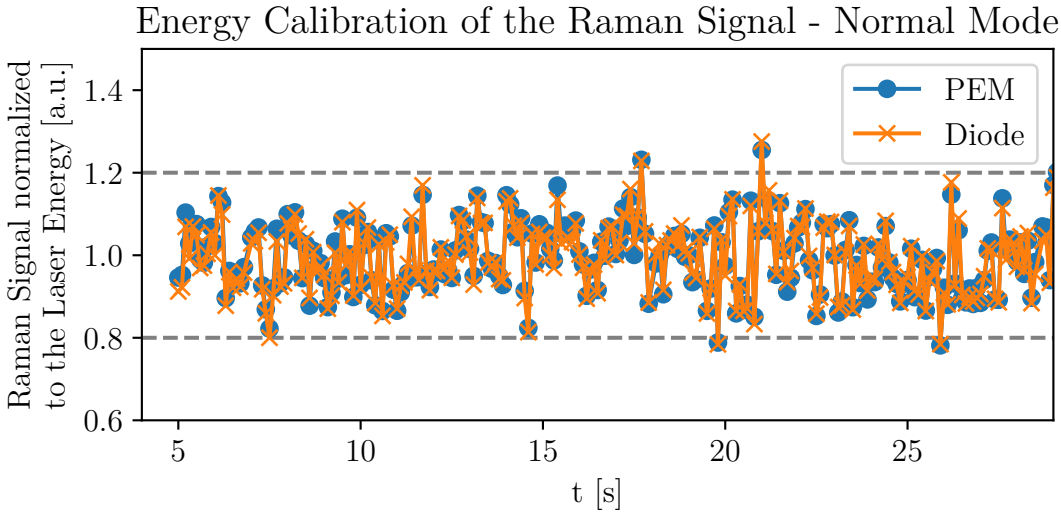

Fig. C.0.2.: Raman signal normalized to the laser energy from the PEM and the diode for normal operation.

The variation coefficient of the Raman signal normalized to its mean as plotted in fig. C.0.3 is $v = 7.6\,\%$ for normal mode and $v = 5.1\,\%$ for the burst mode.

The fluctuations of these signals arise from the Raman scattering process itself. It is a random variable, and therefore, no pattern or trend is visible in the signal. Moreover the scatter lies within the dashed lines introduced as "guide of the eye".

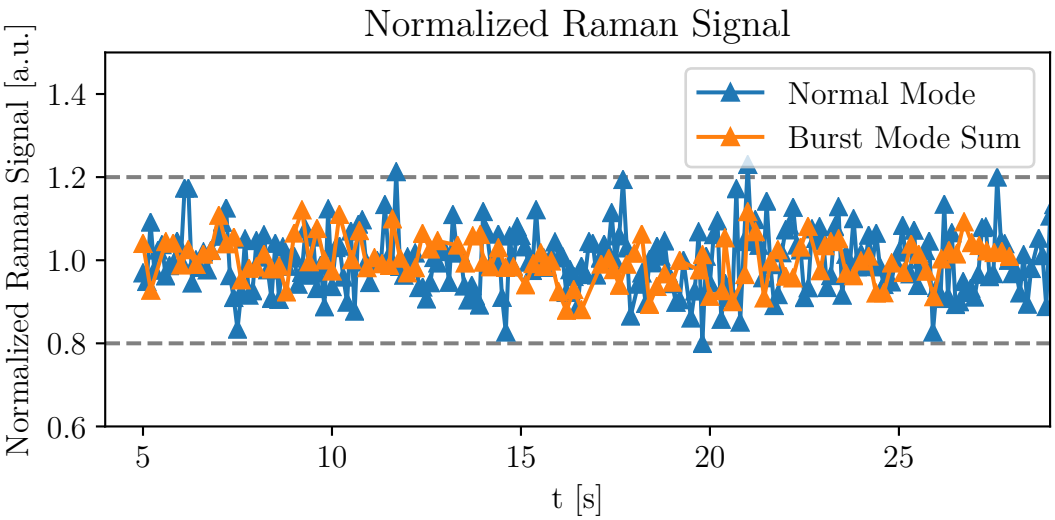

Fig. C.0.3.: Raman signal normalized to its mean for normal and burst-mode operation. The burst-mode Raman signal consists of the sum of the four pulses of one burst to have a signal level that is comparable to the normal mode signal.

Fluctuations of this size cannot be avoided for all analysed signals involving the Raman signal in any way. The signals' fluctuation in C.0.2 lay in the same range, and can therefore be understood as resulting from the Raman scattering measurement rather than from laser beam clipping. The laser must therefore be clipped after its propagation trough the plasma and before the location of the energy monitors, which has been cross-checked and will be shown later in this section. The reliability of the Raman calibration was an important finding because it means that the Raman calibration itself delivered sound results, which is essential for the validity of all Thomson data taken throughout the campaign.
The Raman signal scatter normalized to the diode-measured laser energy during burst-mode operation is rather large as shown in figure C.0.4. It can be explained as the combination of the Raman process and the larger laser energy variation shown in fig. C.0.1. From the plot and the variation coefficients $v_1 = 14.2\,\%$, $v_2 = 22.5\,\%$, $v_3 = 13.4\,\%$, and $v_4 = 23.2\,\%$, it can be inferred, that the error for the second Pockels cell pulses (2/4 and 4/4) is particularly large. This again indicates, that the beam pointing stability has a huge influence. In contrast to earlier assumptions, it is expected to be larger for Pockels cell double pulses which accordingly changed the beam clipping and hence the incident laser energy.

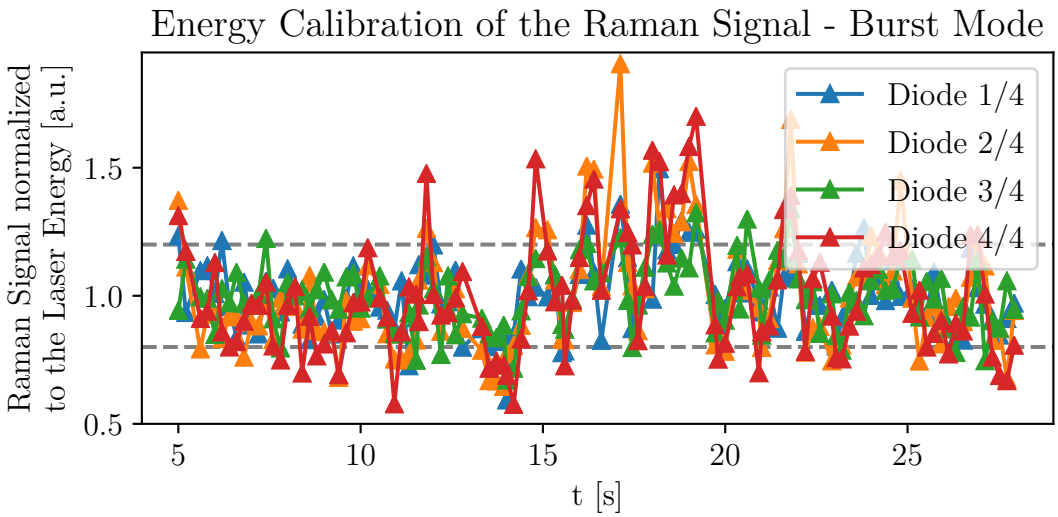

Fig. C.0.4.: Raman signal normalized to the diode measured laser energy for burst-mode operation.

This fact can be inferred from fig. C.0.5 which displays the sum of the Raman signals for the four pulses of a burst normalized to the PEM signal and the sum of the diode signals for the four pulses, respectively.

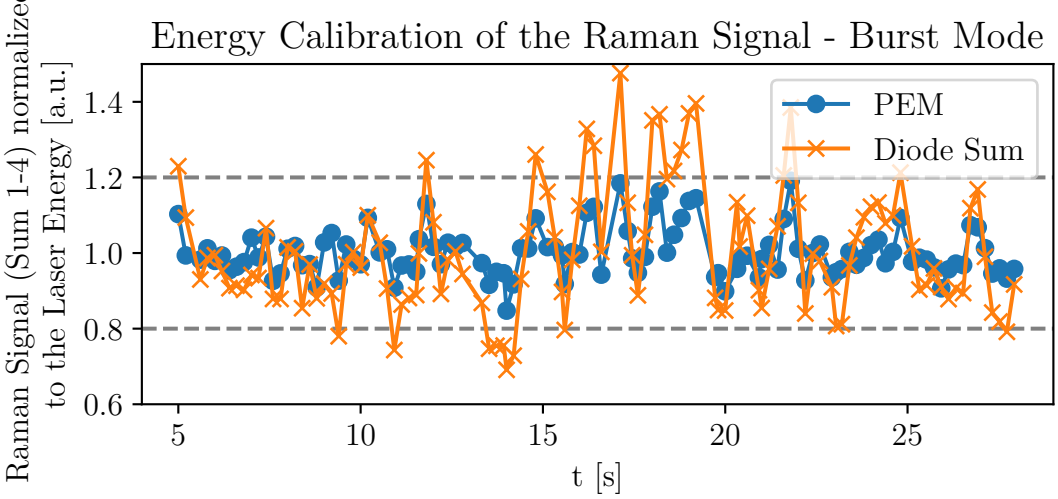

Fig. C.0.5.: Sum of the four Raman signals of a burst normalized to the PEM signal and the sum of the four diode signals.

The fluctuation of the diode normalized signal shows a deviation that fits the "1/diode signal" behaviour (cf. fig. C.0.1) with $v = 16.2\,\%$ exceeding the range of

the Raman scatter whereas the PEM normalized signal ($v = 6.3\,\%$) lies within the range. If the larger deviation did come from a clipping of the laser, no matter if it was introduced by thermal, mechanical or beam pointing fluctuations, the laser energy of pulses 1-4 in each burst normalized to the associated mean should be similar.

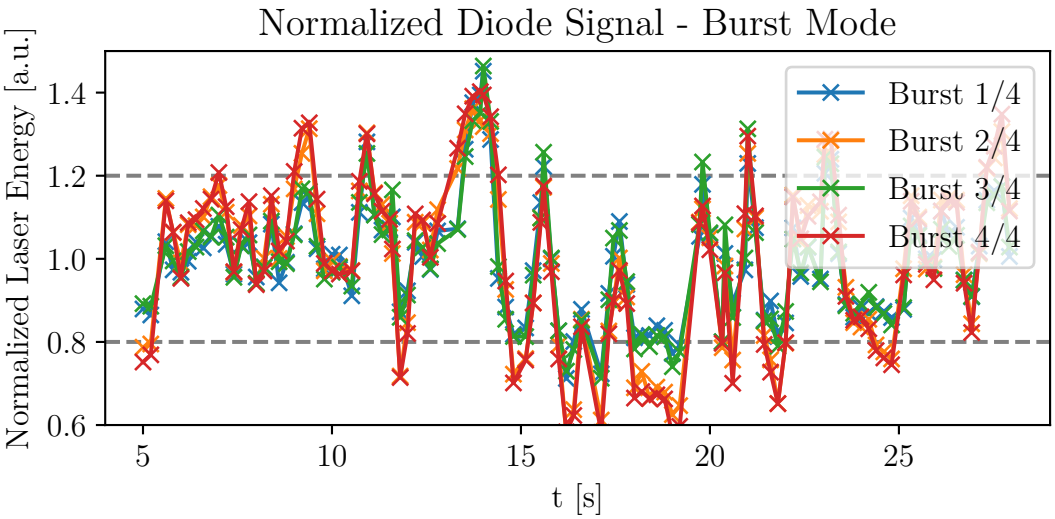

Fig. C.0.6.: Laser energy of pulse 1, 2, 3 and 4 in each burst normalized to the associated mean.

According to fig. C.0.6, the temporal evolution for the separated curves shows a good agreement. This indicates that the clipping of the laser beam plays a major role compared to the energy fluctuation per pulse. Therefore, normalizing the Raman signal to the average Raman signal, might better provide the desired energy normalisation than the actual energy monitor signal for every pulse that was clipped behind the plasma.
To cross-check this finding for data from a W7-X experiment discharge rather than for the Raman calibration alone, the central Thomson electron density was plotted together with the PEM and diode measured laser energy during a “flat-top” phase of a plasma experiment. In flat-top phases, the plasma is not disturbed by fuelling or other possible changes, and therefore the line integrated density and the density profiles should not change significantly. While the (clipped) laser energy signal changes noticeably as shown in fig. C.0.7, the electron density stays relatively constant as expected. Therefore, the energy normalisation of the Thomson scattering data employing the energy monitor signals is not possible and the Raman normalisation was chosen.

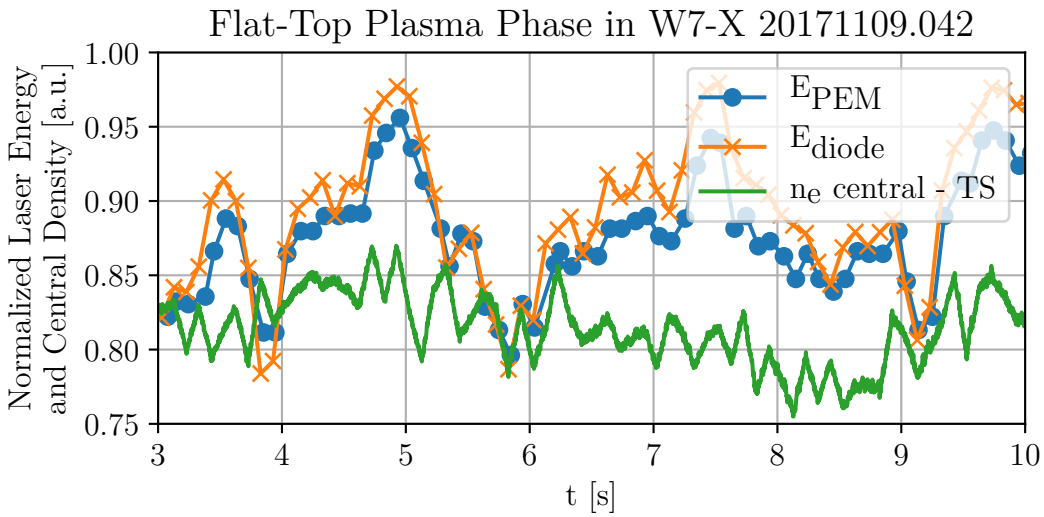

Fig. C.0.7.: Comparison between laser energy and central Thomson electron density during a "flat-top" plasma phase.

Applied to the Raman calibration during burst mode, this normalisation yields promising results as shown in fig. C.0.8, putting the Raman signal in the "guide of the eye"-range that denotes the scatter by the Raman process itself.

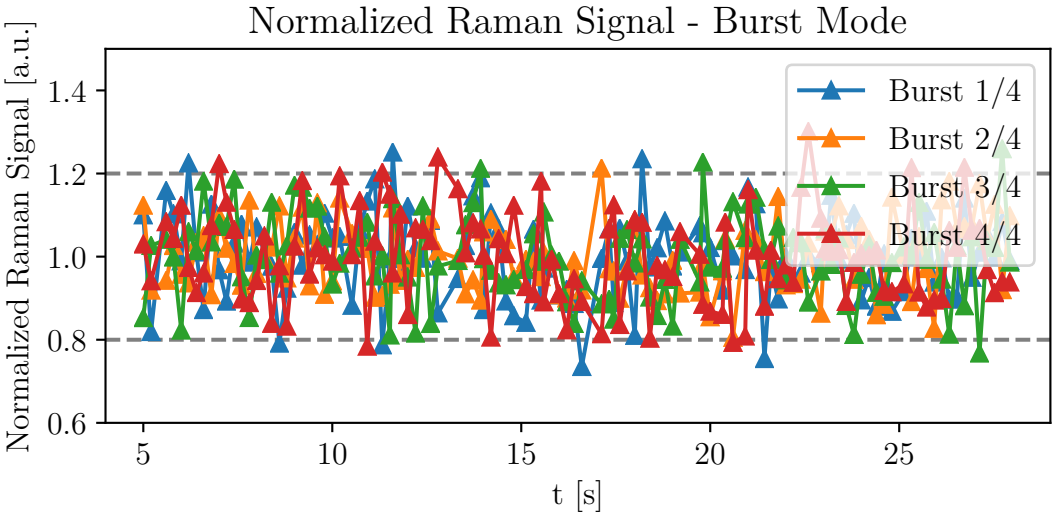

Fig. C.0.8.: Raman signal of pulses 1, 2, 3 and 4 in each burst normalized to the associated mean.

The variation coefficients $v_1 = 10.2\,\%$, $v_2 = 8.4\,\%$, $v_3 = 9.9\,\%$ and $v_4 = 11.0\,\%$ now become comparable to those from the Raman signal in normal mode operation

(cf. fig. C.0.2), which makes this normalisation preferable compared to the energy monitor normalisation presented in the context of fig. C.0.4.

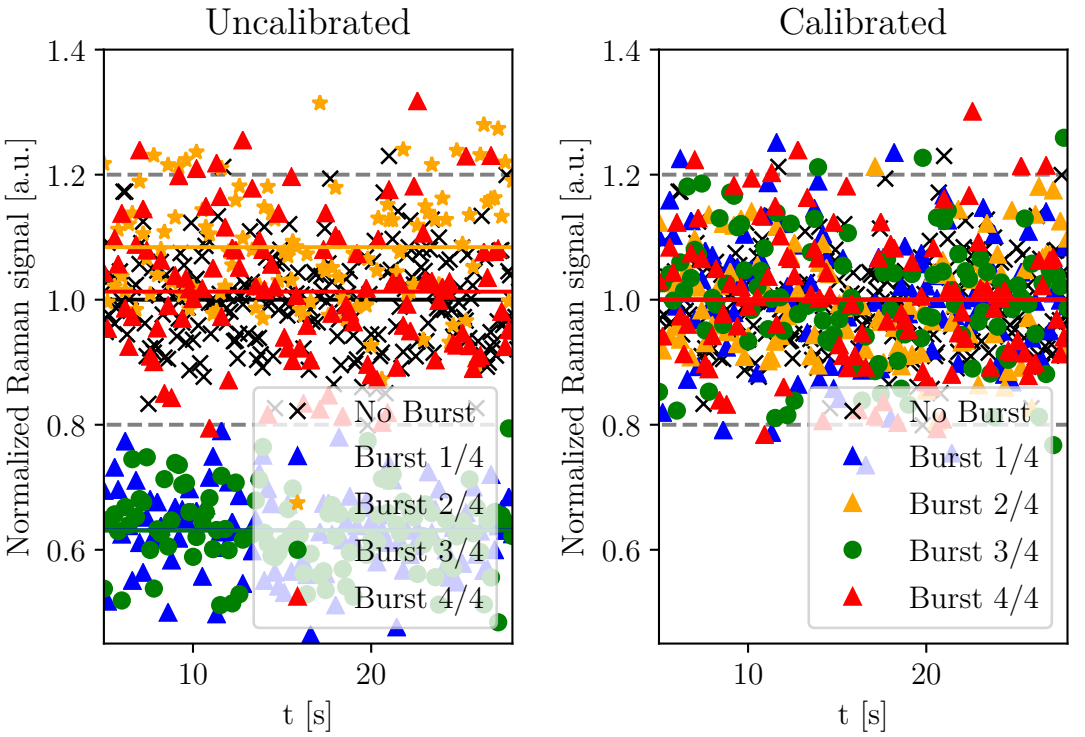

Fig. C.0.9.: Raman normalisation of the burst-mode Thomson scattering signal.

Finally the Raman normalisation factors were applied to the Raman signal and can be applied likewise to the Thomson scattering signal from normal plasma operation of W7-X. The non-normalised result for the Raman measurement is compared to the to the normalised data in C.0.9. The Raman signal from normal operation without burst, which needs no energy normalisation, is displayed as a reference. Additionally, the mean of all signals is indicated by a solid line in the associated colour. After the normalisation the lines are coalesced and the data lies almost entirely within the Raman fluctuation estimated by the normal mode Raman signal scatter and indicated by the dashed lines.

D. Clipping of the Laser Beam and Beam Alignment

Even before the Raman calibration, after the energy monitors were installed, unexpected fluctuations of the laser energy (cf. fig. C.0.7) and, more importantly, discrepancies between the densities measured with the Thomson scattering and the interferometry diagnostic (cf. fig. 3.4.5) were found. Often times the discrepancy increased during an experimental day and vanished the next morning.
To cross-check the energy stability of the experiment laser, which was not the one used during the preliminary experiments in the laboratory, the energy was checked with a PEM extracting a fraction of the beam right at the laser head. The energy fluctuation, as shown in fig. D.0.1(a), was negligible ($v = 1\,\%$) as stated by the manufacturer. In the M1 box a larger deviation ($v = 3.3\,\%$) and a greatly reduced mean energy was found as shown in fig. D.0.1(b).

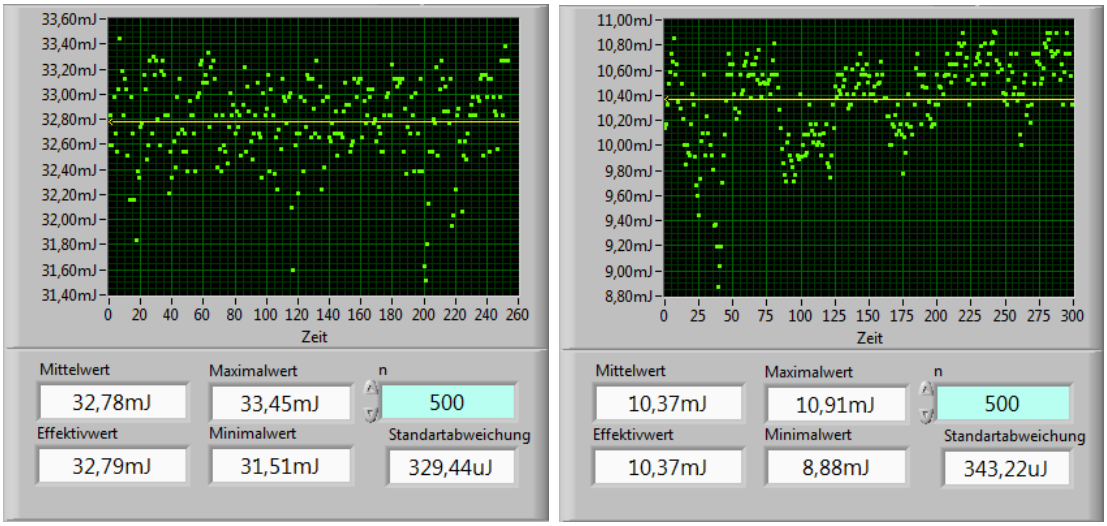

(a) (b)

Fig. D.0.1.: Laser energy fluctuation of the Thomson scattering laser in
(a) - the laser room.
(b) - the M1 mirror box at the entrance to the plasma vessel.

The fluctuations on top of the signal in the M1 mirror box appear similar to the ones detected with the regular energy monitor (PEM and diode) during experiment operation. This could only be explained by a clipping of the laser beam, which had been adjusted carefully before, implying that something in the setup must have changed. Visualized on photographic paper mounted in mirror box M1, the beam clipping was identified to happen right at the entrance port of the box, indicated by a sharp cut going trough the laser's burn pattern. If the clipping would occur further away from the paper, the cut would appear more blurry.

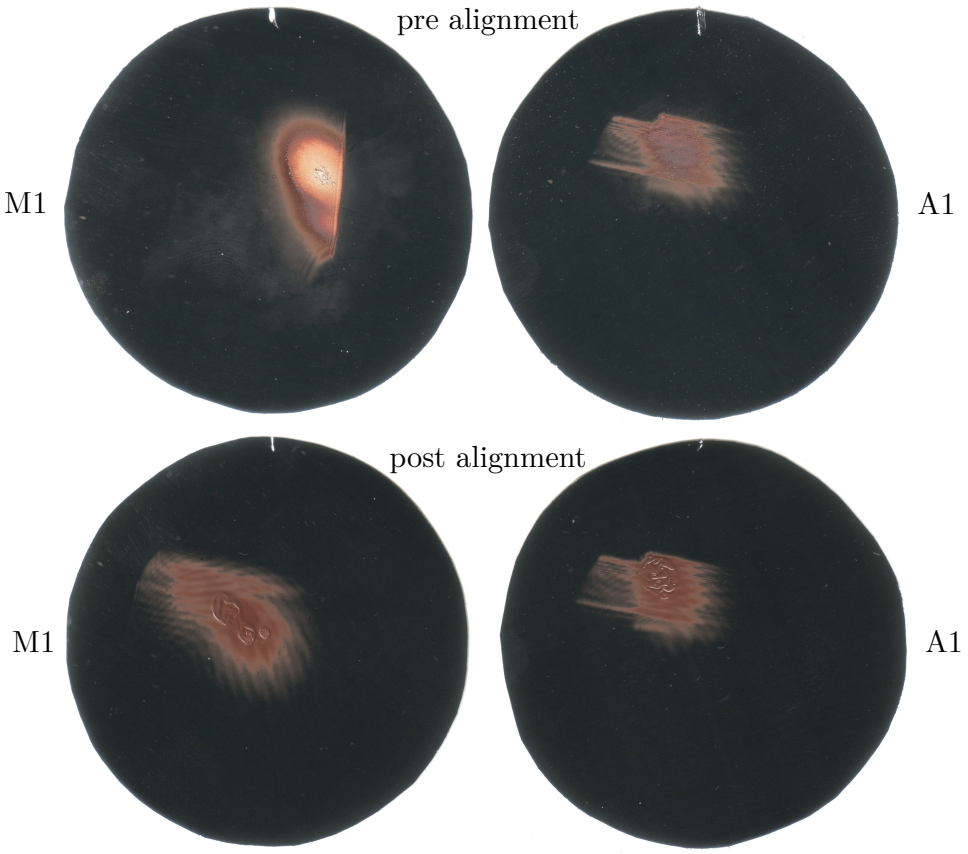

Fig. D.0.2.: Thomson scattering laser beam profiles, visualized on photographic paper. Brighter colours relate to higher intensities - darker colours to lower intensities.

A second piece of paper was installed in the exit mirror box A1 where another sharp cut was identified, indicating another clip closer to the side of the plasma vessel where the laser exits. With the procedure shown in fig. D.0.3 the laser was set back to the ideal alignment position which was determined before the start of the campaign by ensuring the propagation of the laser beam trough the scattering volumes during vessel access. A mock-up used to model the scattering volume sizes and positions was put into the plasma vessel for this purpose. Although the clipping of the beam in the M1 mirror box could be remedied, the attempt to do so for the A1 exit mirror box failed. The sharp edge was still present in the post alignment burn pattern. To remove this edge, the port opening needs to be widened or the entire beam path, and therefore, the optics defining the scattering volumes, would need to be realigned. Both of which were impossible during the

ongoing operational campaign. For the latter, even plasma vessel access would have been needed. The energy measurement therefore can only be taken as a rough estimate and not as a precise tool to sufficiently normalize the Thomson data.

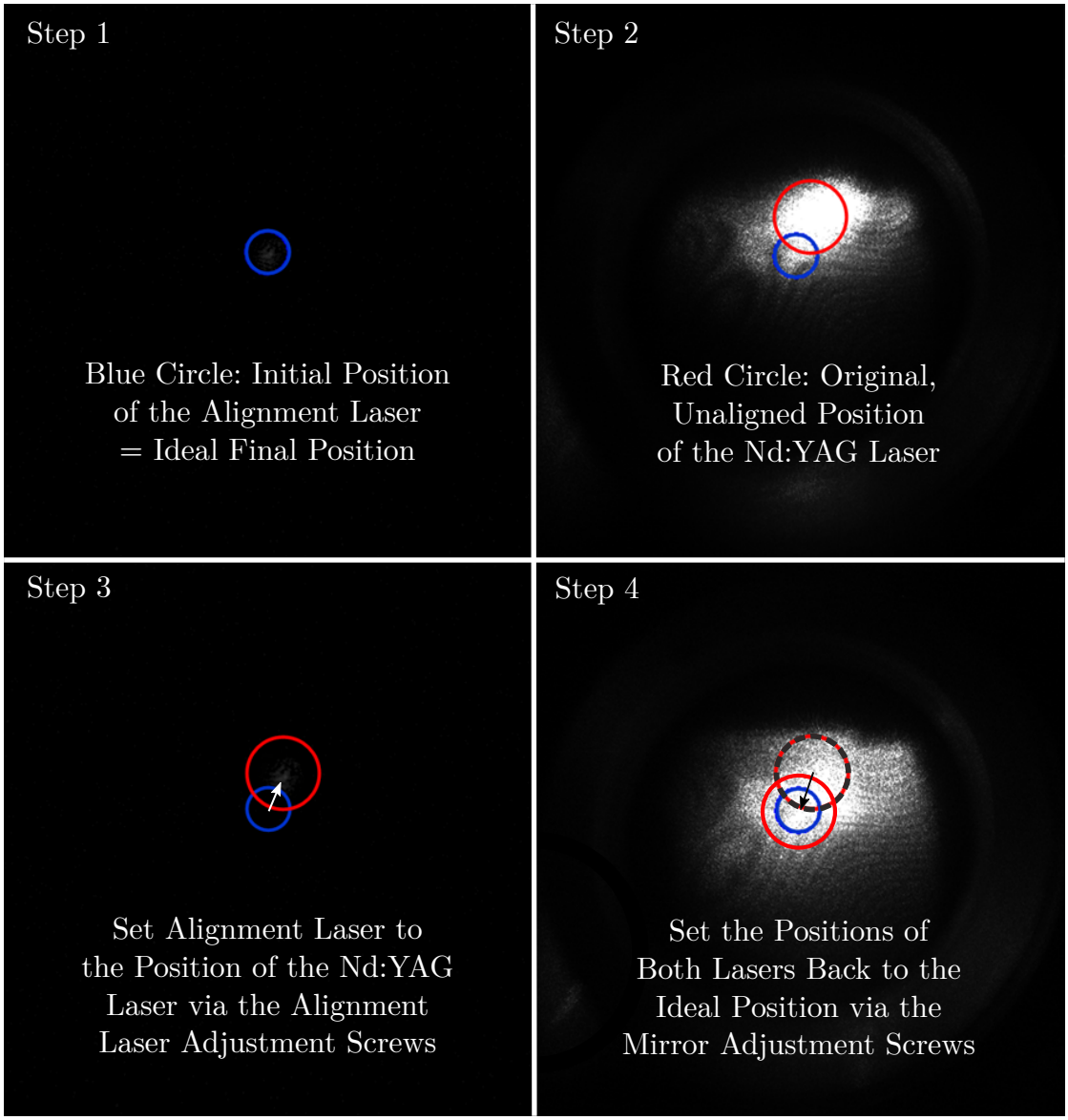

Fig. D.0.3.: The steps to align the alignment laser to the Nd:YAG laser (1-3), and both to the ideal position (4). The alignment was performed employing camera pictures, if no torus hall access was possible.

To find the source of the slow, persistent misalignment throughout a day, the decision was made to install the already planned alignment control cameras (cf.

fig. 2.3.5) which could not be installed before the beginning of the campaign. Together with the "Picomotor Piezo Clear Edge Mount 8822" (mirror mounts with piezoelectric stepper motors produced by "Newport"), it is possible to manually or automatically align the laser such that it stays in a predefined position indicated by the red cross in fig. D.0.4.

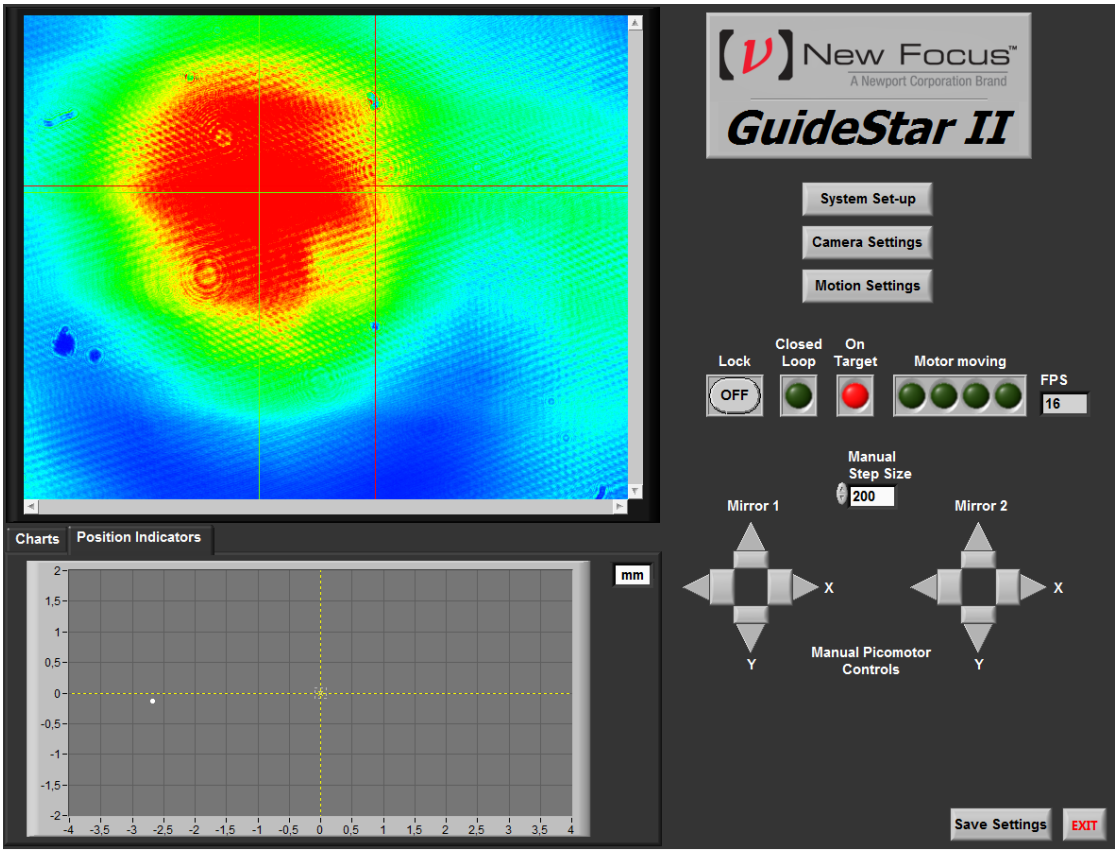

Fig. D.0.4.: Newport mirror control and alignment system used for control of the W7-X Thomson scattering laser. The small white dot in the lower plot relates to the current position of the alignment laser centre (green cross in the upper plot) whereas the ideal position (red cross in the upper plot) is the point of origin of the lower plot. The scale in the lower plot is millimetre.

Meanwhile, temperature fluctuations in the laser room have been identified to cause the drift throughout the day. Different heat sources, such as computers, lighting and laser operators, were present during experiment days but not on service days, which made the identification of the error difficult. To reduce the temperature increase all possible heat sources were removed from the room; the lasers were

prepared for remote operation in the control room, and the drift was only monitored with the alignment control cameras. The temperature increase after these changes was much slower, and consequently, the drift of the laser beam was as well. If the drift exceeded a certain threshold (a few millimetres), an air conditioner in the laser room was switched on manually, reducing the temperature to its value from the morning and bringing the beam back to its desired position. The change of the mean laser energy was noticeable decreased but still present as shown in fig. D.0.5. The fluctuations of the energy monitor signal throughout a shot caused by the mechanical vibrations changing the intensity of the beam clipping, and hence the laser energy, in the A1 box could not be eliminated by this procedure.

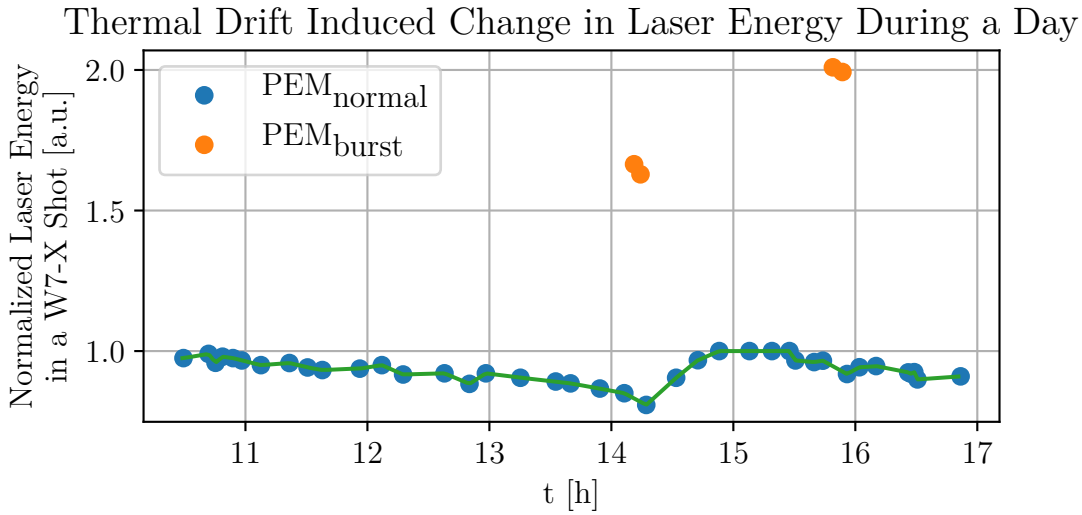

Fig. D.0.5.: Change in the average laser energy per W7-X shot monitored with the PEM in the A1 mirror box throughout the day.

Although the change in the average energy monitor signal between the shots is large, this does not mean that the laser energy passing trough the scattering volumes changes; the laser energy remains constant for a misalignment of a few millimetres. The change can rather be explained by beam clipping at the A1 box in the morning, causing small variations in the position to result in a large intensity change as seen by the energy monitors. The switch-on of the air conditioner at 2:15 pm is clearly visible in the signal.
Unfortunately, the optimized beam alignment did not result in a sufficient agreement between the densities from the Thomson scattering and the interferometry diagnostics. The discrepancy for both normal and bust mode was still 30 - 50 % (cf. fig. 3.4.5). The reason for this discrepancy is an open question for the Thomson and the interferometry groups. However, recently the spectral calibration of the Thomson polychromators has been discussed as a possible error source. Even

though it is not yet clear how significant the irregularities were, and if they fully explain the discrepancy, it is believed that the interferometry signal is correct, hence no interferometer calibration issues were identified so far. Therefore, the line integral of the Thomson density will be adjusted to the line-integrated interferometry density signal for the whole campaign, assuming the profile shape to be correct. This adjustment method is explained in the next chapter.
A general overview of the W7-X interferometer and its functionality is given in "A New Dispersion Interferometer for the Stellarator Wendelstein 7-X" by J. Knauer *et. al.* [68].

E. W7-X Discharge Overview Plots

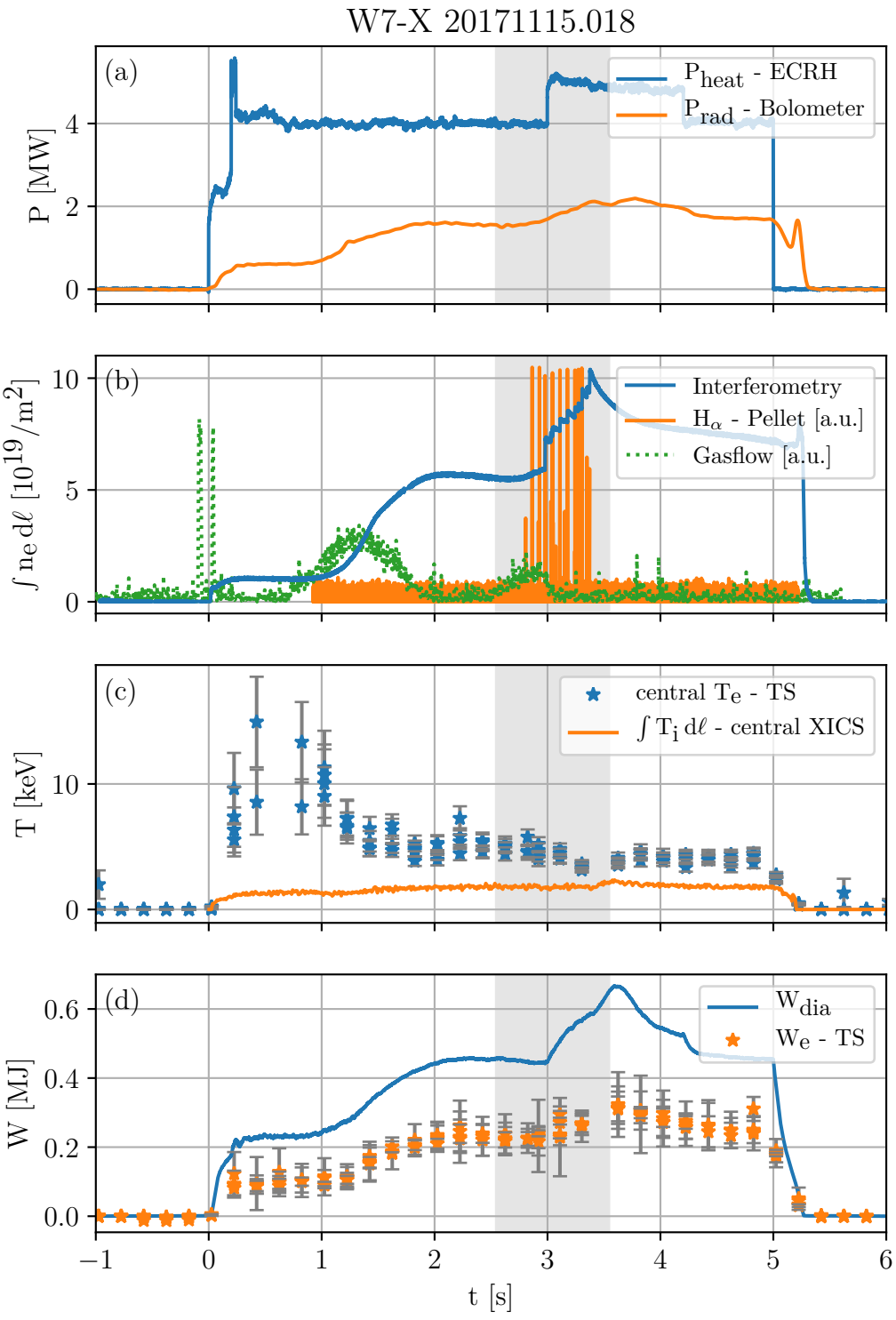

Fig. E.0.1.: W7-X discharge 20171115.018 overview plot. The time interval of pellet injection is indicated by the grey shading.

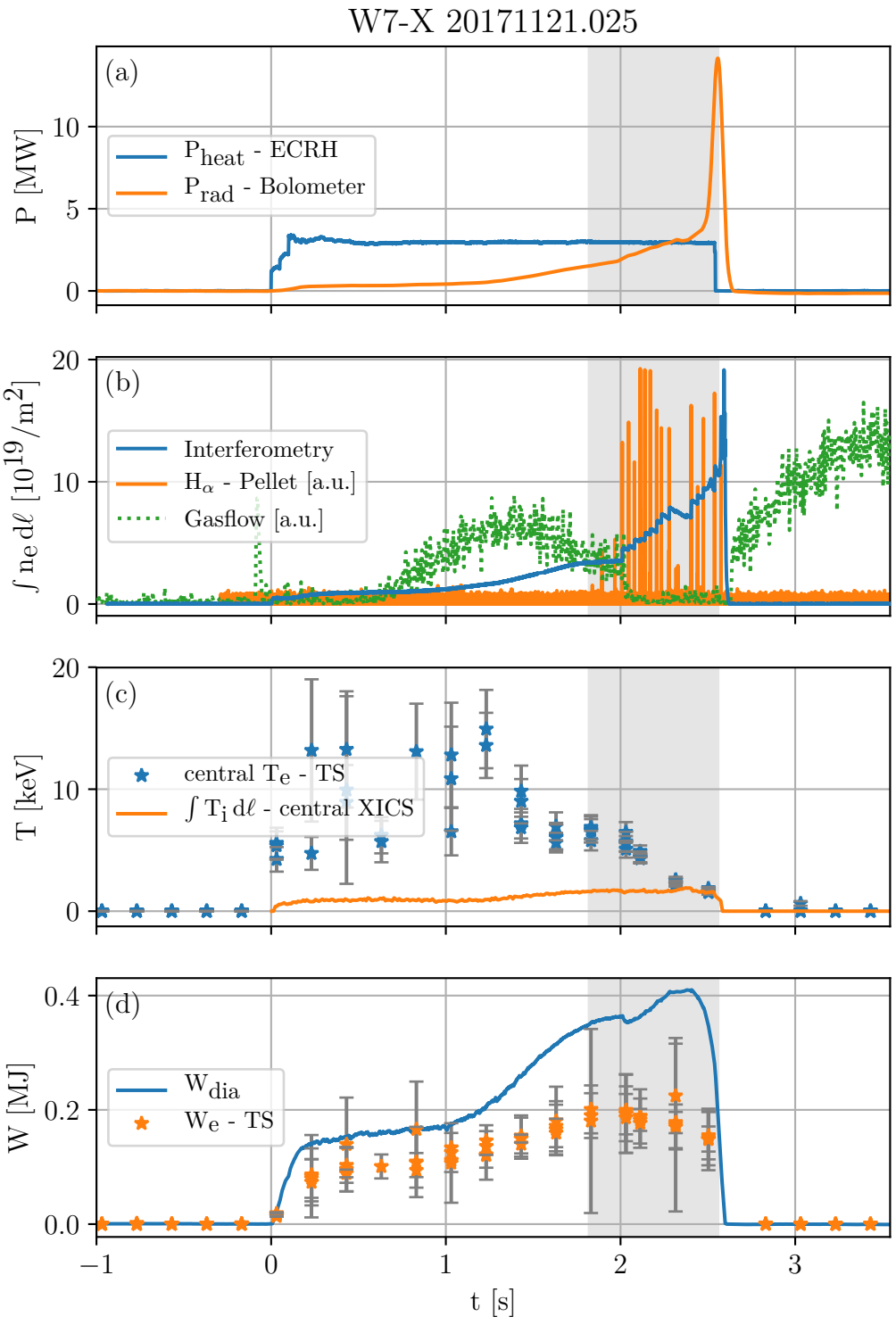

Fig. E.0.2.: W7-X discharge 20171121.025 overview plot. The time interval of pellet injection is indicated by the grey shading.

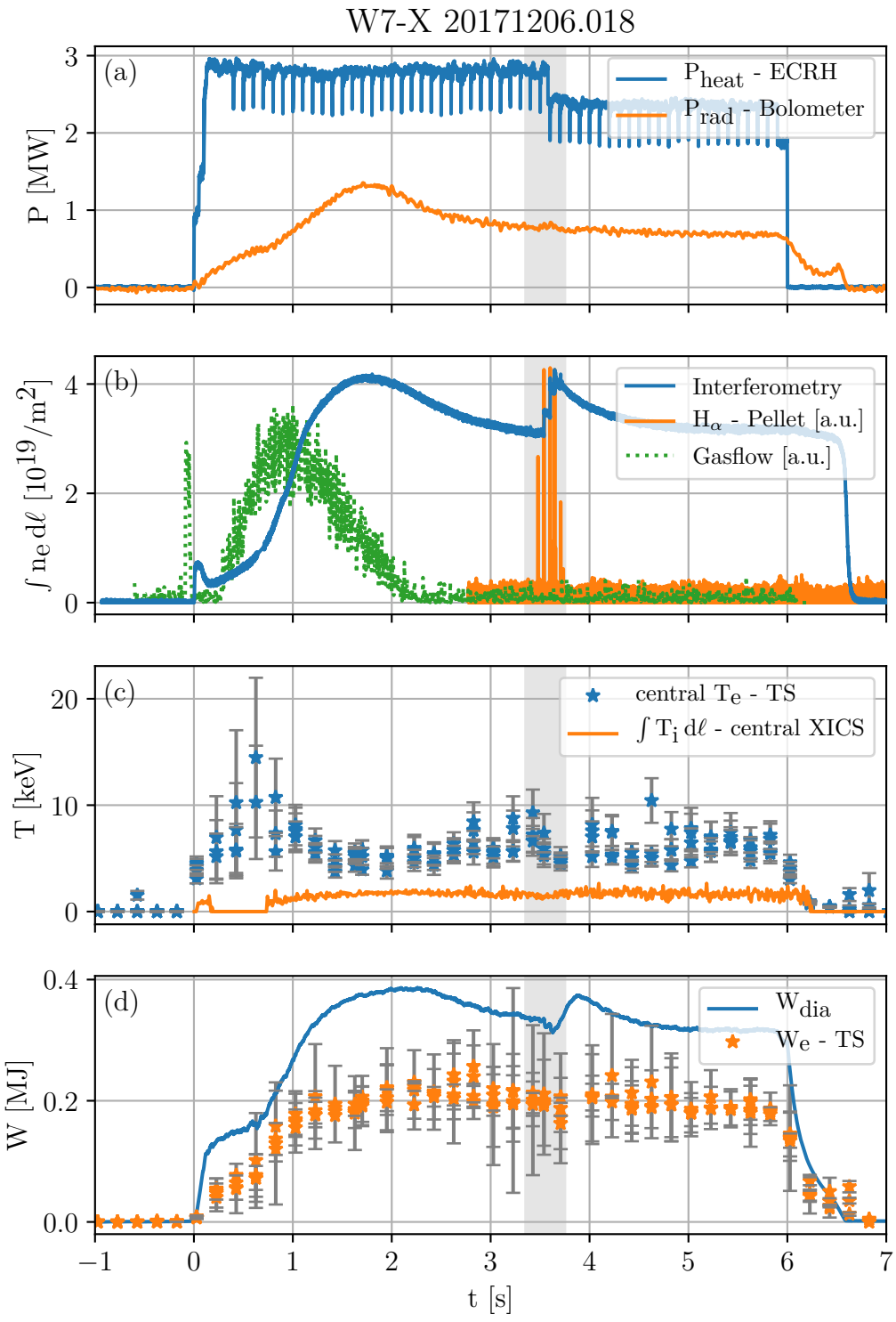

Fig. E.0.3.: W7-X discharge 20171206.018 overview plot. The time interval of pellet injection is indicated by the grey shading.

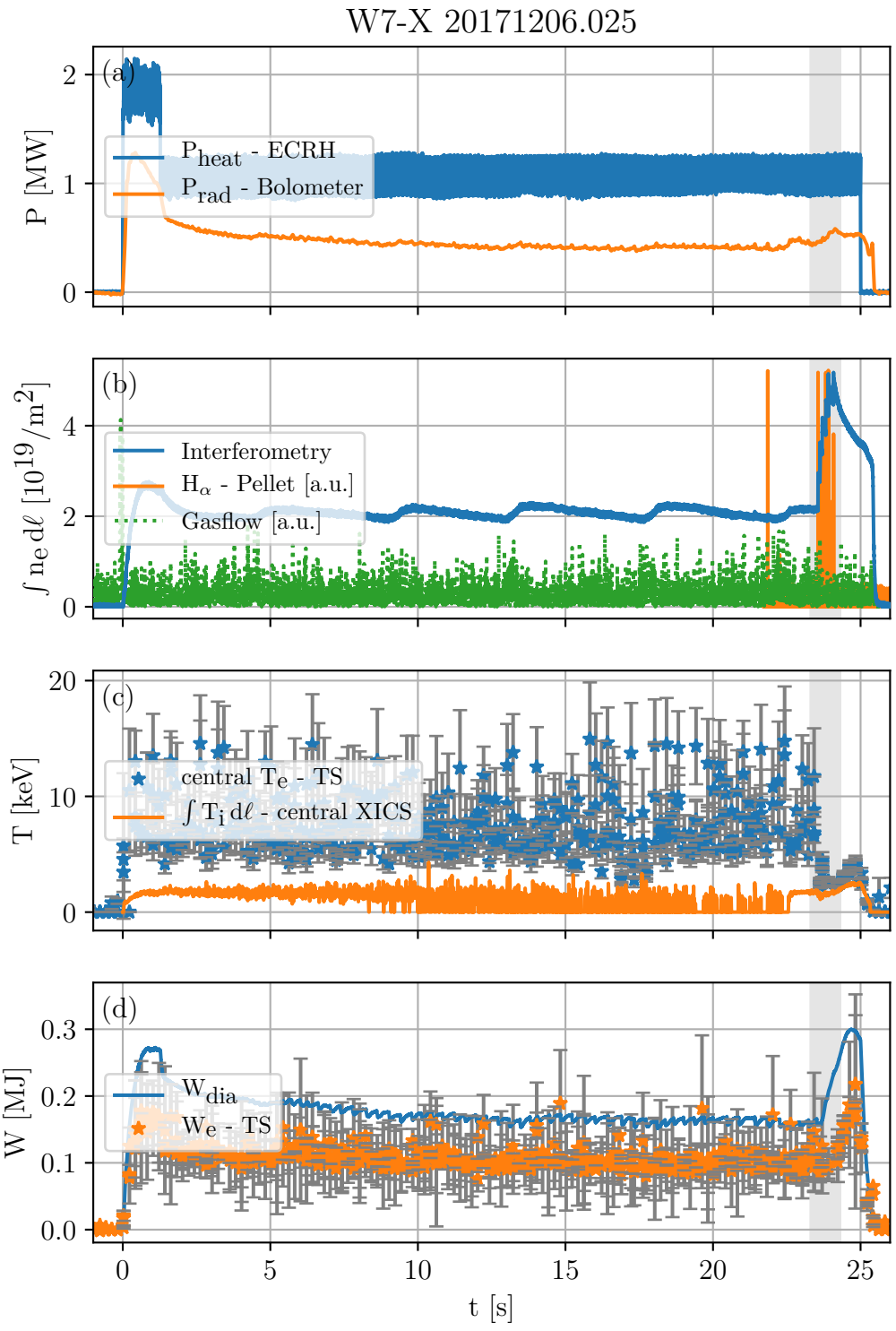

Fig. E.0.4.: W7-X discharge 20171206.025 overview plot. The time interval of pellet injection is indicated by the grey shading.

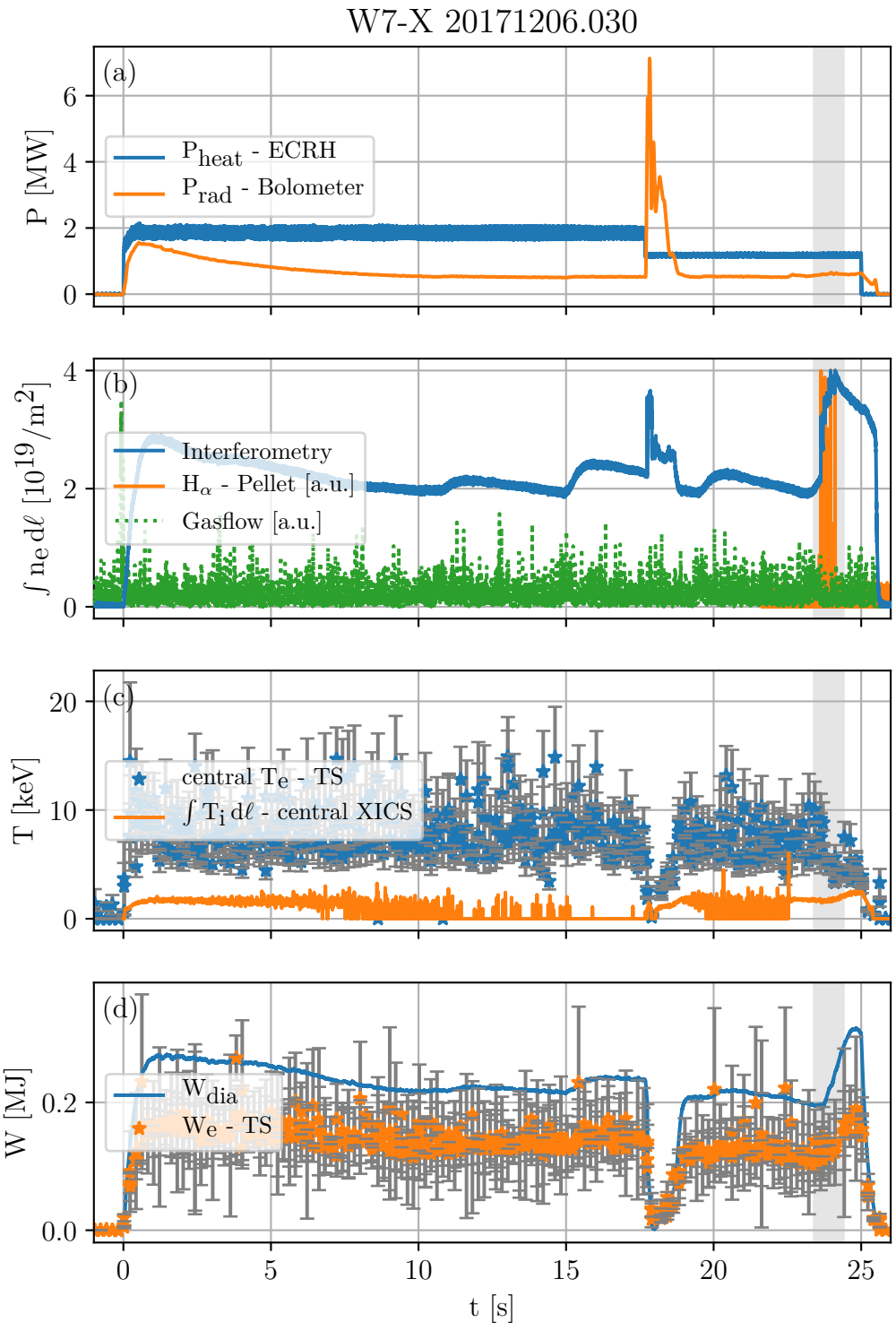

Fig. E.0.5.: W7-X discharge 20171206.030 overview plot. The time interval of pellet injection is indicated by the grey shading.

F. Technical Information on the Event-Triggered Burst-Mode Thomson Scattering Diagnostic

The Wendelstein 7-X Event-Triggered Burst-Mode Thomson Scattering System

- A Manual -

Version 0.3

Hannes Damm

May 2, 2018

Contents

1 General Setup

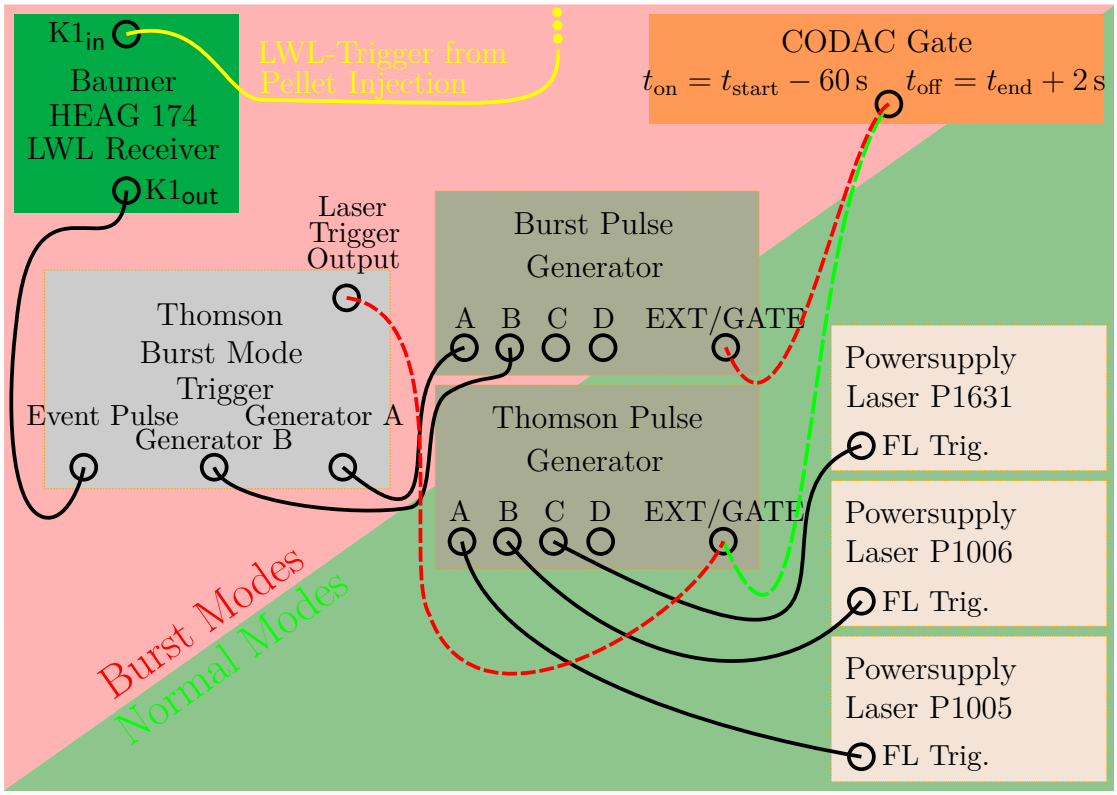

Fig. 1.0.1: Thomson-Trigger wiring: Green connections needed for normal laser modes, red connections for any burst mode operation. Black wires are permanent.
Note: Additional changes to the pulse generators and lasers are necessary to switch between the different modes!

One of the major improvements of this setup, as compared to the one from OP1.1, is the full implementation of the CODAC provided gate shown in fig. 1.0.2. The gate starts 60 s before plasma ignition and lasts until 2 s after the switch-off of the ECRH; no matter how long the experiment lasts, the pulse generators will start and quit operation without any further manual handling.

For now, the shutters of the lasers need to be opened and closed(!) by hand via the "Splitlight GUI" in a time slot of 30 s − 10 s before/after the start of a W7-X shot. This is under negotiation with CODAC and automation might be implemented at the start of OP1.2b. The Thomson diagnostic should then have fully automated operation via the CSS with no user input needed (apart from switching on the lasers and starting the pulse generators).

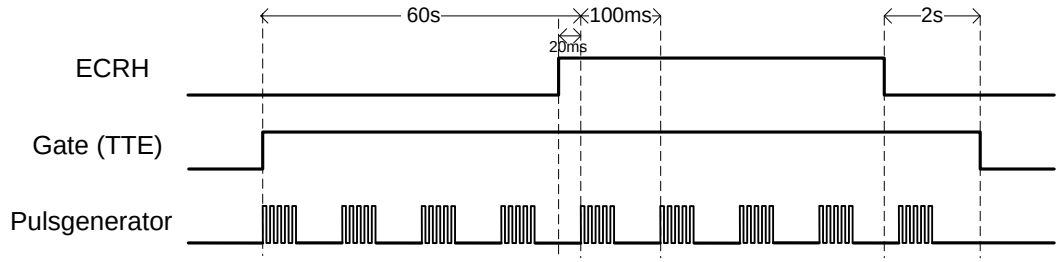

Fig. 1.0.2: CODAC-provided 3.3 V gate that allows the laser flash lamps to build-up the thermal lens in the Nd:YAG rods before plasma start-up and stop 2 s after plasma termination.

The schematic circuit diagram of the "Thomson burst mode trigger", shown in fig. 1.0.1, including logic chips and part numbers is displayed in fig. 1.0.3 in the latest version.

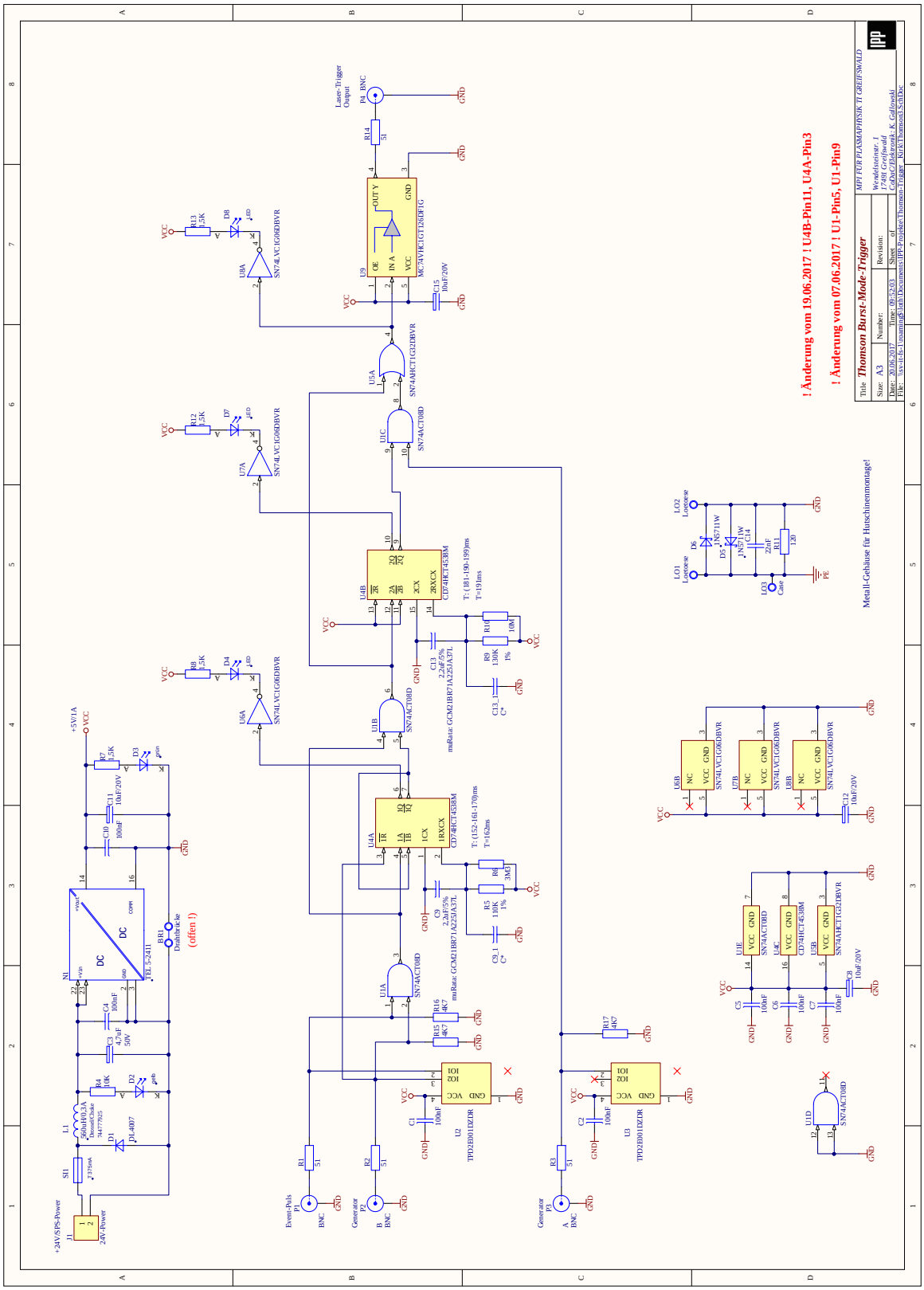

Fig. 1.0.3: Technical W7-X Thomson scattering event trigger circuit.

2 Software and Pulse Generator Setup

In this section the setup of the pulse generators and lasers for the different operation modes is explained in detail.

Two “Quantum Plus Pulse Generators Model 9514” from “Schulz Electronic” are used. The one called “Thomson Pulse Generator” in fig. 1.0.1 is used to trigger the flash lamps of the lasers. The other one in fig. 1.0.1 called “Burst Pulse Generator” is used to set the 5 Hz laser pulse frequency of the laser burst modes (rather than the 10 Hz in normal modes) and defines the time gate in which occurring events are passed to the lasers for an immediate measurement rather than being blocked.

Usually the modes described below do not need to be configured by hand. They will be stored using the pulse generators storing functionality and just need to be loaded via FUNCTION → RECALL ...

(for both generators, if in burst mode; else just for the “Thomson Pulse Generator”).

... and the store/recall function in the SplitlightGUI for the lasers.

This is a list of the available modes and their stored configuration files:

- **Normal Modes**
  - **10 Hz Mode:**
    Thomson Pulse Generator: “Store#: 1”, “Name: 10 Hz Mode”
    Laser SplitlightGUI: “10Hz_normal_mode_ca.1.5J(untested).ini”
  - **20 Hz Mode:**
    Thomson Pulse Generator: “Store#: 2”, “Name: 20 Hz Mode”
    Laser SplitlightGUI: “10Hz_normal_mode_ca.1.5J(untested).ini”
  - **30 Hz Mode:**
    Thomson Pulse Generator: “Store#: 3”, “Name: 30 Hz Mode”
    Laser SplitlightGUI: “10Hz_normal_mode_ca.1.5J(untested).ini”
  - **High Power Mode - 10 Hz, up to 6 J per Pulse:**
    NOT YET AVAILABLE
    Thomson Pulse Generator: “Store#: 4”, “Name: High Power”
    Laser SplitlightGUI: “10Hz_normal_mode_ca.1.5J(untested).ini”
- **Burst Modes**
  - **Event Triggered 2 Laser Burst Mode -** $8 \times$ **10 kHz @ 5 Hz:**
    Thomson Pulse Generator: “Store#: 5”, “Name: Normal Burst”
    Burst Pulse Generator: “Store#: 1”, “Name: Burst Mode”
    Laser SplitlightGUI: “10Hz_normal_mode_ca.1.5J(untested).ini” & “burst_old_OP1.2a.ini”
  - **Event Triggered 3 Laser Burst Mode -** $8 \times$ **10 kHz @ 5 Hz:**
    Thomson Pulse Generator: “Store#: 5”, “Name: Normal Burst”
    Burst Pulse Generator: “Store#: 1”, “Name: Burst Mode”
    Laser SplitlightGUI: “burst_old_OP1.2a.ini”
  - **Event Triggered Asymmetric Burst Mode** $8/12\times \approx$**10 kHz @ 5 Hz:**
    Thomson Pulse Generator: “Store#: 6”, “Name: Asym. Burst”
    Burst Pulse Generator: “Store#: 1”, “Name: Burst Mode”
    Laser SplitlightGUI: “burst_old_OP1.2a.ini”

2.1 Normal Modes

For the normal modes only the upper left corner of fig. 1.0.1 shaded in green is relevant.
The CODAC gate needs to be connected to “EXT/GATE” of the “Thomson Pulse Generator”!

2.1.1 10 Hz Mode - 1 . . . 2 J per Pulse

The following user inputs are needed to configure the W7-X Thomson scattering system to this mode:

“Thomson Pulse Generator”

- FUNCTION → GATE/TRIG: “Gated: 2 V”, “Active High”
- FUNCTION → MODE: “continuous”
- FUNCTION → RATE: “Per: 0.1”
- Channel A: “Enabled”, “Source: T_0”, Wid: 1 µs, Dly: 0 s, “Pol: Active High”, “Out: Adujustable”, “Out: 12 V”, “Mode: Normal”, “Gate: disabled”, “Wait: 0 Pulses”, “Mux: -0001-”
- Channel B: disabled
- Channel C: disabled
- Channel D: disabled

“Laser”

Start and connect laser if not yet done. “Login” → “Login as privileged user” → PW: “******”. “File” → “Load userparameters” → “1 JSP...”.

2.1.2 20 Hz - 1 . . . 2 J per Pulse

The following user inputs are needed to configure the W7-X Thomson scattering system to this mode:

“Thomson Pulse Generator”

- FUNCTION → GATE/TRIG: “Gated: 2 V”, “Active High”
- FUNCTION → MODE: “continuous”
- FUNCTION → RATE: “Per: 0.1”
- Channel A: “Enabled”, “Source: T_0”, Wid: 1 µs, Dly: 0 s, “Pol: Active High”, “Out: Adujustable”, “Out: 12 V”, “Mode: Normal”, “Gate: disabled”, “Wait: 0 Pulses”, “Mux: -0001-”
- Channel B: “Enabled”, “Source: T_0”, Wid: 1 µs, Dly: 0.05 s, “Pol: Active High”, “Out: Adujustable”, “Out: 12 V”, “Mode: Normal”, “Gate: disabled”, “Wait: 0 Pulses”, “Mux: -0010-”
- Channel C: disabled
- Channel D: disabled

“Laser”

Start and connect laser if not yet done. “Login” → “Login as privileged user” → PW: “******”. “File” → “Load userparameters” → “1 JSP...”.

2.1.3 30 Hz Mode - 1 . . . 2 J per Pulse

The following user inputs are needed to configure the W7-X Thomson scattering system to this mode:

“Thomson Pulse Generator”

- FUNCTION → GATE/TRIG: “Gated: 2 V”, “Active High”
- FUNCTION → MODE: “continuous”
- FUNCTION → RATE: “Per: 0.1”
- Channel A: “Enabled”, “Source: T_0”, Wid: 1 µs, Dly: 0 s, “Pol: Active High”, “Out: Adujustable”, “Out: 12 V”, “Mode: Normal”, “Gate: disabled”, “Wait: 0 Pulses”, “Mux: -0001-”
- Channel B: “Enabled”, “Source: T_0”, Wid: 1 µs, Dly: 0.033 333 333 s, “Pol: Active High”, “Out: Adujustable”, “Out: 12 V”, “Mode: Normal”, “Gate: disabled”, “Wait: 0 Pulses”, “Mux: -0010-”
- Channel C: “Enabled”, “Source: T_0”, Wid: 1 µs, Dly: 0.066 666 666 s, “Pol: Active High”, “Out: Adujustable”, “Out: 12 V”, “Mode: Normal”, “Gate: disabled”, “Wait: 0 Pulses”, “Mux: -0100-”
- Channel D: disabled

“Laser”

Start and connect laser if not yet done. “Login” → “Login as privileged user” → PW: “******”. “File” → “Load userparameters” → “1 JSP...”.

2.1.4 High Power Mode - 10 Hz, up to 6 J per Pulse

NOT YET AVAILABLE

The following user inputs are needed to configure the W7-X Thomson scattering system to this mode:

“Thomson Pulse Generator”

- FUNCTION → GATE/TRIG: “Gated: 2 V”, “Active High”

- FUNCTION → MODE: “continuous”
- FUNCTION → RATE: “Per: 0.1”
- Channel A: “Enabled”, “Source: T_0”, Wid: 1 µs, Dly: 0 s, “Pol: Active High”, “Out: Adujustable”, “Out: 12 V”, “Mode: Normal”, “Gate: disabled”, “Wait: 0 Pulses”, “Mux: -0001-”
- Channel B: “Enabled”, “Source: T_0”, Wid: 1 µs, Dly: 0 s, “Pol: Active High”, “Out: Adujustable”, “Out: 12 V”, “Mode: Normal”, “Gate: disabled”, “Wait: 0 Pulses”, “Mux: -0010-”
- Channel C: “Enabled”, “Source: T_0”, Wid: 1 µs, Dly: 0 s, “Pol: Active High”, “Out: Adujustable”, “Out: 12 V”, “Mode: Normal”, “Gate: disabled”, “Wait: 0 Pulses”, “Mux: -0100-”
- Channel D: disabled

“Laser”

Start and connect laser if not yet done. “Login” → “Login as privileged user” → PW: “******”. “File” → “Load userparameters” → “1 JSP...”.

This mode is not yet available.

Fast trigger adapters for timing jitters <1 ns are ordered but not yet installed. The trigger signal cables would then be directly wired to the laser-head rather then the power supplies.
Another concern is the unknown “Laser Induced Damage Threshold” of the mirrors for such high simultaneous laser irradiation.

2.2 Burst Modes

For the burst modes the full setup introduced in fig. 1.0.1 is relevant. The CODAC gate needs to be connected to "EXT/GATE" of the "Burst Pulse Generator", and the "Laser Trigger Output" from the "Thomson Burst Mode Trigger" needs to be connected to the "EXT/GATE" of the "Thomson Pulse Generator"!

2.2.1 Event Triggered 2 or 3 Laser Burst Mode - $8 \times 10\,\text{kHz} @ 5\,\text{Hz}$, 1 J per Pulse

The following user inputs are needed to configure the W7-X Thomson scattering system to this mode:

"Thomson Pulse Generator"

- FUNCTION → GATE/TRIG: "Triggered: 2.5 V", "Rising Edge"
- FUNCTION → MODE: "single shot"
- Channel A: "Enabled", "Source: T_0", Wid: 1 µs, Dly: 0 s, "Pol: Active High", "Out: Adujustable", "Out: 12 V", "Mode: Normal", "Gate: disabled", "Wait: 0 Pulses", "Mux: -0001-"
- Channel B: "Enabled", "Source: T_0", Wid: 1 µs, Dly: 200 µs, "Pol: Active High", "Out: Adujustable", "Out: 12 V", "Mode: Normal", "Gate: disabled", "Wait: 0 Pulses", "Mux: -0010-"
- Channel C: "Enabled", "Source: T_0", Wid: 1 µs, Dly: 400 µs, "Pol: Active High", "Out: Adujustable", "Out: 12 V", "Mode: Normal", "Gate: disabled", "Wait: 0 Pulses", "Mux: -0100-"
- Channel D: disabled

"Burst Pulse Generator"

- FUNCTION → GATE/TRIG: "Gate: 2 V", "Active High"
- FUNCTION → MODE: "continuous"

- FUNCTION → RATE: “Per: 0.2”
- Channel A: “Enabled”, “Source: T_0”, Wid: 1 µs, Dly: 0 s, “Pol: Active High”, “Out: TTL/CMOS”, “Mode: Normal”, “Gate: disabled”, “Wait: 0 Pulses”, “Mux: -0001-”
- Channel B: “Enabled”, “Source: T_0”, Wid: 60 ms, Dly: 70 ms, “Pol: Active High”, “Out: TTL/CMOS”, “Mode: Normal”, “Gate: disabled”, “Wait: 0 Pulses”, “Mux: -0010-”
- Channel C: disabled
- Channel D: disabled

“Laser”

Start and connect laser if not yet done. “Login” → “Login as privileged user” → PW: “******”. “File” → “Load userparameters” → “1.3 JDP...”.

(Note 1: The 2- and the 3- laser burst modes all have the same pulse generator settings. The only difference applies to the laser setting, where the “PC delay” (delay between the Pockels Cell switching) is set to 400 µs for the 2 laser burst modes and to 600 µs for the 3 laser burst modes via the “Splitlight GUI”.)

Note 2: The Gate set by “Channel B” defines the time interval in which occurring events are passed to the lasers for an immediate measurement rather than being blocked. This immediate measurement could be interpreted as a singular (slight) change of the laser-pulse frequency. This is by no means harmful for the laser, if kept in a certain range. Indeed, the 60 ms/70 ms configuration is a very conservative one. During our lab tests we verified a range of configurations up to 140 ms/30 ms not causing any damage to the lasers. Moreover, the 140 ms/30 ms threshold is given by the logic circuit that is used for the event signal processing after the pulse generator. Different electronic components would easily access other ranges, but, due to the limitations of the circuits used so far, there is no validated information about the lasers’ behaviour beyond the provided range. Regardless a gate of 60 ms is sufficient for the measurement of pellet injections in W7-X because the nominal injection frequency is ≈25 Hz, which relates to 1 pellet every 40 ms.

2.2.2 Event Triggered Asymmetric Burst Mode $8/12 \times \approx$10 kHz @ 5 Hz, 1 J per Pulse

The settings for the asymmetric burst mode equal the ones above, the only change is made to "Channel B" of the "Thomson Pulse Generator" where a delay of Dly: 190 µs rather than 200 µs is chosen.

The following user inputs are needed to configure the W7-X Thomson scattering system to this mode:

"Thomson Pulse Generator"

- FUNCTION → GATE/TRIG: "Triggered: 2.5 V", "Rising Edge"
- FUNCTION → MODE: "single shot"
- Channel A: "Enabled", "Source: T_0", Wid: 1 µs, Dly: 0 s, "Pol: Active High", "Out: Adujustable", "Out: 12 V", "Mode: Normal", "Gate: disabled", "Wait: 0 Pulses", "Mux: -0001-"
- Channel B: "Enabled", "Source: T_0", Wid: 1 µs, Dly: 190 µs, "Pol: Active High", "Out: Adujustable", "Out: 12 V", "Mode: Normal", "Gate: disabled", "Wait: 0 Pulses", "Mux: -0010-"
- Channel C: "Enabled", "Source: T_0", Wid: 1 µs, Dly: 400 µs, "Pol: Active High", "Out: Adujustable", "Out: 12 V", "Mode: Normal", "Gate: disabled", "Wait: 0 Pulses", "Mux: -0100-"
- Channel D: disabled

"Burst Pulse Generator"

- FUNCTION → GATE/TRIG: "Gate: 2 V", "Active High"
- FUNCTION → MODE: "continuous"
- FUNCTION → RATE: "Per: 0.2"
- Channel A: "Enabled", "Source: T_0", Wid: 1 µs, Dly: 0 s, "Pol: Active High", "Out: TTL/CMOS", "Mode: Normal", "Gate: disabled", "Wait: 0 Pulses", "Mux: -0001-"

- Channel B: “Enabled”, “Source: T_0”, Wid: 60 ms, Dly: 70 ms, “Pol: Active High”, “Out: TTL/CMOS”, “Mode: Normal”, “Gate: disabled”, “Wait: 0 Pulses”, “Mux: -0010-”
- Channel C: disabled
- Channel D: disabled

“Laser”

Start and connect laser if not yet done. “Login” → “Login as privileged user” → PW: “******”. “File” → “Load userparameters” → “1.3 JDP...”.

3 Known Issues and Possible Improvements

3.1 Known Issues

3.1.1 Filthy pellet trigger signal

During the trigger tests it was found that the amplifier used to process the pellet ablation signal does not behave as expected.

So far no further corrections are necessary because the "Thomson Burst-Mode Trigger" logic remedies this problem, but it would be beneficial to find the wrong settings and correct them at some point.

Jürgen Baldzuhn has been informed about this issue and will try to fix it. Testing of the fixed system might be possible during single pellet injection shots.

3.2 Possible Improvements

3.2.1 Automated shutter control

To avoid the manual switching of the laser shutter in the correct time window via the "Splitlight GUI" before and after each W7-X shot, the switching could be implemented by CODAC via the remote control client interface of the lasers. The shutter could always be opened ≈50 s after the rising edge of the gate and closed with the falling edge. The necessary commands in the remote control client interface are "Get-Shutter_State" and "Set_Shutter_State".

This would substantially reduce the risk of potential data loss due to human input errors.

This is under negotiation with CODAC and automation might be implemented at the start of OP1.2b. The Thomson diagnostic should then have fully automated operation via the CSS with no user input needed (Apart from switching on the lasers and starting the pulse generators).

3.2.2 High Power Mode

As mentioned above, in theory, a high-power, low-density option is possible via firing the 3 available lasers simultaneously.

Further investigation on the laser induced damage threshold of the mirrors is necessary as well as the installation and validation of the fast trigger adapters to implement this mode within the W7-X Thomson scattering system.

3.2.3 Pre-Triggering of Pellets

Rather than other statistical occurring plasma events, pellet injection is intentionally made and could therefore (theoretically) be exactly predicted. In real situations, the pellets will have a jitter in time and velocity which makes the prediction of their ablation time not only harder but also spread over some interval.

To gain reliable information about the timing, two light gates are installed in the flight path of the pellets. For unknown reasons they do not work with D-pellets, but

they do for H-pellets. If this could be fixed, the implementation of the pellet-event triggering should be revised.

3.2.4 Pellet Counter

With the current system it is theoretically possible to define which pellet out of a series of pellets one wants to observe with high time resolution. To implement this, one only needs to synchronize the pellet injection to the CODAC gate which determines the laser pulse timing. Even though the pellets do have an unpredictable jitter, this jitter only results in ± 20 ms for the ablation timings. At 25 Hz, though, the gap between each pellet is 40 ms; therefore, it would be possible to match the injection time and the laser trigger in a way that one knows which pellet number out of a series of pellets has been observed. Cross-checking via the H_α ablation signals or the fast cameras would also be conceivable.

3.2.5 FPGA Trigger

Using a "Field Programmable Gate Array" instead of a hard-wired physical logic circuit would increase system flexibility as well as make it a single device system. One could for instances setup a combined burst/non-burst mode where one runs one laser in the normal mode and two in the burst mode. This is not possible without adding an extra pulse generator to the current system due to the base frequency differences of both modes (5 Hz for the burst and 10 Hz for normal modes).
Furthermore, one could spread the event gate as mentioned in section 2.2.1 in note 2 or react on laser development, i.e. if the manufacturer provides 20 Hz Nd:YAG laser systems for new diagnostic applications.
Other than the still incomplete list of advantages due to increasing flexibility, only having one device creating errors rather than several would also increase the reliability of the system as a whole and reduce its costs.